The Effect of Model and Human Synovial Fluid Chemistry on Wear of CoCrMo in Bench Tests

by

Harriet Stevenson

A thesis submitted to Imperial College London

for the degree of Doctor of Philosophy

and Diploma of Imperial College (D.I.C.)

September 2018

Tribology Group

Department of Mechanical Engineering

Imperial College London

Abstract

Prostheses, for example hips and knees, are used to relieve pain and restore function in degenerated synovial joints. They are tribological devices and are susceptible to wear of the bearing surface which can lead to early failure. Human synovial fluid (HSF) is produced to lubricate the joint, however in tribological testing of implants 25%w/w Bovine Calf Serum (25BCS) is used as a screening fluid, although the composition is different. The key questions addressed in this thesis are: the lubrication and wear mechanisms similar? Is 25BCS an appropriate replacement for HSF in wear tests?

A ball-on disc CoCrMo wear test was developed to use small lubricant volumes suitable for HSF, which was supplied by the Musculoskeletal Group at Imperial College. Post-test the wear was measured, and surface deposits analysed to provide insights into lubrication mechanisms. Friction and wear of HSF samples were compared to BCS and model fluids comprising of proteins (albumin and globulin), lipids and hyaluronic acid. The wear depth for most HSF samples was significantly higher (up to 77%) compared to 25BCS.

Deposited films were observed in and around the wear scar and the pattern was similar for all protein-containing fluids including HSF. The deposits appeared to be viscous, insoluble and adherent to the surface. Micro-IRRAS analysis showed they were formed of denatured proteins although in some instance lipids were present. Analysis of the amide I band showed the protein secondary structure was transformed to an increased native β-sheet content with some fibular β-sheet structures. Thioflavin T (ThT) was used to confirm the presence of β-sheet amyloid fibrils.

The research showed that 25BCS isn't an appropriate substitute for HSF. The lubrication and wear mechanisms are similar, however 25BCS has a greater tendency to form high β-sheet content deposits due to their chemical composition that protect surfaces from wearing.

Acknowledgements

Foremost I would like to express my deepest thanks to my Supervisor Dr Philippa Cann for her advice, encouragement and guidance throughout my PhD. I am grateful to Pip who has been a huge inspiration and I continue to learn from each day. She has given me the opportunities to present both at home and abroad. Thank you. I hope we stay in touch.

Dr Mathew Jaggard and the MsK group whom collected and prepared the HSF samples and provided vital surgical knowledge and support.

Dr Connor Myant for encouraging me to do this PhD in the first place.

I must acknowledge the UK EPSRC for funding this project "Tribology of Artificial Articular Joints" (EP/M506345/1).

I would like to thank all the staff and students in the Tribology group for their advice, help and understanding. You have all made my time in the group truly unforgettable. A particular mention must go to Ruby, Zhench, Elze and Annelise who I have shared my PhD experience with, the highs, the lows and the many bottles of wine. Chrissy Stevens for who no problem is insurmountable and Pawel Orzlowski for his invaluable support in the lab.

To Nora and Guy who I have known me since the first week at Imperial and have never failed to make me laugh. Nora you have always been there for me. Guy, I can rely on you for a gossip over a cheeky shandy. One day between the two of you, you may finally persuade me to do a marathon! Secondly, the lovely ladies Jess and Elly, my housemates, who have provided me with much needed distractions and laughter with over the past three years.

A huge thank you to my Mum and Dad who without their support I would never have been in the fortunate position to have undertaken this PhD. They have encouraged me throughout my education particularly in science and engineering.

My sisters, Laura and Erin who are a constant inspiration and help me become the best person I can be. Last but not least Freddie, whilst only a year old he never fails to put a smile my face.

Disclaimer

This thesis is a description of work carried out in the Tribology Group of the Department of Mechanical Engineering, Imperial College London under the supervision of Dr Philippa Cann. The material presented is the original work of the author and no part has been submitted for a degree at this or any other university. Some of the work described in this thesis has been previously published in peer reviewed journals and conference proceedings.

The work carried out was performed under human ethics REC reference 15/LO/0388 and patient consent was obtained for all human samples testing.

Some of the figures and tables in Chapters 3, 4, 5 and 6 have been reprinted from Stevenson, H., Parkes, M., Austin, L., Jaggard, M., Akhbari, P., Vaghela, U., Williams, H.R.T., Gupte, C. and Cann, P., 2018. The development of a small-scale wear test for CoCrMo specimens with human synovial fluid. *Biotribology*, *14*, pp.1-10.

The copyright of this thesis rests with the author and is made available under a Creative Commons Attribution Non-Commercial No Derivatives licence. Researchers are free to copy, distribute or transmit the thesis on the condition that they attribute it, that they do not use it for commercial purposes and that they do not alter, transform or build upon it. For any reuse or redistribution, researchers must make clear to others the licence terms of this work

Contents

Abstract 2
Acknowledgements 3
Disclaimer 4
List of Figures 10
List Tables 19
Nomenclature 24
1 Prosthetic Joints and Tribology 27
Summary 27
1.1 General Introduction 27
1.2 Research Objectives 32
1.3 Thesis Outline 32
2 Tribology of Artificial Hips 34
Summary 34
2.1 Introduction 34
2.2 THR: Materials and Operating Conditions 35
2.2.1 Materials 35
2.2.2 Bearing Couples 37
2.2.3 Implant Size and Choice 38
2.2.4 Physiological Motion and Loads 38
2.2.5 Physiological Pressures 43
2.3 Classical Tribology 45
2.3.1 Lubrication Regimes 45
2.3.2 Wear Mechanisms 47
2.4 SF Chemistry and Properties 49
2.4.1 Proteins 53
2.4.2 Hyaluronic Acid 58
2.4.3 Glycoproteins 58
2.4.4 Lipids 59
2.5 Artificial Joint Tribology 61
2.5.1 Tribology Related Problems in Hip Joints 61
2.5.2 Wear of Artificial Hip Joints: Tribology Test Methods 61
2.5.3 Model Fluids for Tribology Tests 62
2.5.4 SF Lubrication Mechanisms of MoM hips 64

2.5.5 Wear Mechanisms of CoCrMo Interfaces 71
2.6 Conclusions 72
3 Development of a Small Scale Wear Test 74
Summary 74
3.1 Introduction 74
3.2 Experimental Programme 76
3.3 Materials and Methods 77
3.3.1 The High Frequency Reciprocating Rig (HFRR) 77
3.3.2 Material Selection 78
3.3.3 Test Fluids 78
3.3.4 Test Condition Considerations 79
3.3.5 Redesign of Ball and Fluid Holders 82
3.3.6 Friction and Wear Tests 83
3.3.7 Validation of Test Protocol 84
3.3.8 Wear Scar Analysis 86
3.3.9 Determining Test Repeatability 87
3.4 Results 87
3.4.1 Effect of Volume on CoF and AWD 87
3.4.2 Effect of Protein (BCS) Concentration on COF and AWD 92
3.4.3 Effect of Extended Test Time and N_2 Purge on CoF and AWD 95
3.5 Discussion 96
3.5.1 Test Development 96
3.5.2 Determining Test Repeatability 98
3.5.3 Final Test Protocol 99
3.6 Conclusion 100
4 The Effect of Model and Human SF on Friction and Wear 101
Summary 101
4.1 Introduction 101
4.2 Experimental Programme 103
4.3 Materials and Methods 103
4.3.1 Test Fluids 104
4.4 Results 107
4.4.1 Effect of Saline on CoF and AWD 107
4.4.2 Model SF's on CoF and AWD 109
4.4.3 HSF on CoF and AWD 116

4.4.4 Effect of pH on AWD 118
4.5 Discussion 121
4.5.1 The Effect of Saline in 25BCS 121
4.5.2 The Effect of Total and Specific Protein Concentration 121
4.5.3 The Effect of the Addition DPPC to Proteins 122
4.5.4 The Effect of the Addition of HA and DPPC to Proteins 122
4.5.5 The Effect of HSF on Friction and Wear 123
4.5.6 The Effect of pH on Wear 123
4.6 Conclusions 124
5 Optical Imaging of Wear Scars 125
Summary 125
5.1 Introduction 125
5.2 Experimental Programme 127
5.3 Materials and Methods 127
5.3.1 Optical Microscopy 127
5.3.2 Scanning Electron Microscope (SEM) 128
5.3.3 Wear Scar Analysis 128
5.4 Results: Optical Microscopy 129
5.4.1 Effect of Increasing BCS Concentration 130
5.4.2 Effect of the Addition of Saline 132
5.4.3 Effect of Protein Concentration 132
5.4.4 The Effect DPPC 133
5.4.5 Effect of HA 135
5.4.6 HSF 136
5.4.7 Roll Formation 137
5.5 Results: SEM imaging 139
5.5.1 Deposited Films 139
5.6 Results: Wear Scar Analysis 142
5.7 Discussion 146
5.7.1 Optical and SEM Imaging 146
5.7.2 WLI Analysis of Test Surfaces 149
5.7.3 Lubricating Mechanisms 150
5.8 Conclusions 151
6 Micro IRRAS Examination of Wear Scar Deposits 152
Summary 152

6.1 Introduction 152
6.1.1 FTIR Theory 153
6.1.2 Infrared Spectroscopy of SF's and Components 155
6.2 Experimental Programme 158
6.3 Materials and Methods 159
6.4 Results: Untested Fluid Reference Spectra 161
6.4.1 Model Fluid Components: BSA, γ-G and DPPC 161
6.4.2 25BCS and 25salBCS 165
6.4.3 Model Fluids without DPPC 167
6.4.4 Model Fluids with DPPC 170
6.5 Results: Spectra from Wear Scar Deposits 173
6.5.1 25BCS and 25BCSsal 173
6.5.2 Model Fluids without DPPC 176
6.5.3 Model Fluids with DPPC 179
6.6 Results: HSF Samples 182
6.6.1 HSF: Untested Samples 182
6.6.2 HSF: Wear Test Deposits 185
6.7 Discussion 188
6.7.1 Summary of Results 188
6.7.2 Amide I Peak Position and Protein Secondary Structure 189
6.7.3 Comparison of Untested BCS, Model and HSF Fluids 189
6.7.4 Wear Test Deposits 190
6.7.5 Effect of Amide I Position on AWD 193
6.8 Conclusions 195
7 Fluorescence Imaging 196
Summary 196
7.1 Introduction 196
7.2 Fluorescence Imaging of Amyloids 198
7.2.1 Theory 198
7.2.2 ThT Fluorescence 200
7.3 Experimental Programme 201
7.4 Materials and Methods 201
7.4.1 HFRR Bench Top Wear Test 202
7.4.2 Optical and Fluorescent Imaging 202
7.4.3 Micro-IRRAS Analysis 202

7.4.4 Test Fluids 202
7.5 Results 204
7.5.1 Wear 204
7.5.2 Optical and Fluorescent Imaging of Wear Scar Deposits 205
7.5.3 Micro-IRRAS Analysis 209
7.6 Discussion 216
7.6.1 AWD Measurements 216
7.6.2 Optical Imaging 217
7.6.3 Micro-IRRAS Analysis 218
7.7 Conclusions 220
8 General Discussion and Future Work 222
Summary 222
8.1 CoCrMo Wear Test 222
8.1.1 Matching Physiological Conditions 222
8.1.2 Test Repeatability 223
8.1.3 Future Work 223
8.2 Clinical Implications 225
8.2.1 Development of SF Implant Risk Analysis 225
8.2.2 Future Work 227
8.3 Lubrication and Wear Mechanisms 227
8.3.1 Evidence on Explanted Joints 228
8.3.2 Amyloid Fibres? 230
8.3.3 What Initiates Fibril Formation? 232
8.3.4 Possible Lubrication Mechanisms 234
8.3.5 Future Work 238
8.4 Conclusions 238
8.4.1 HFRR Wear Test 238
8.4.2 Effect of Chemical Composition 239
8.4.3 Lubrication and Wear Mechanisms 239
9 References 241
10 Appendices 266
10.1 Code of Practice 470 Contaminant Level 2 266
10.2 Bio1 Form 271
10.3 Peak Positions from Deconvoluted Micro IRRAS Spectra 286

List of Figures

Figure 1.1 - Examples of artificial joints a) total hip b) hip resurfacing c) total knee d) total ankle e) total shoulder f) total elbow..... 28

Figure 1.2 - a) A radiograph of 26-year follow-up of first generation Charnley low friction arthroplasty (4) (with permission form Elsevier) b) X-ray showing a Hip resurfacing (12) c) X-ray showing THR (12). 29

Figure 2.1 - Types of hip prosthesis categorised by bearing type. 37

Figure 2.2 – Types of motion experienced by the hip joint (adapted from (59)). 39

Figure 2.3 – Coordinate system of the left femoral head (59). 40

Figure 2.4 – Walking gait cycle a) Range of motion b) Loads experienced (adapted from (59, 60)).... 41

Figure 2.5 – Running gait cycle (adapted from(61)). 42

Figure 2.6 – Contact pressure distribution (MPa) at bearing surfaces of a 50 mm diameter hip resurfacing prosthesis and a 28 mm diameter THR (74) 45

Figure 2.7 - a) Full film b) Mixed c) Boundary lubrication regimes. 46

Figure 2.8 - a) Abrasive wear b) Surface fatigue adapted from (86) (87). 48

Figure 2.9 – Two body abrasion a) Hard surface asperities b) Hard particles embedded into surface c) Third body abrasion (adapted from (87)). 48

Figure 2.10 - a) Adhesion wear b) Tribo-chemical wear adapted from (86) (87). 49

Figure 2.11- Schematic of hip joint. Adapted from (98). 50

Figure 2.12 –a) Upper and lower bounds of viscosity vs shear rate for H, OA and RA pathologies. Adapted from (39, 106) b) Stress vs time for a shear rate of 0.05 s^{-1} for BSA, bovine SF and model SF (18 mg/ml protein concentration A/G =1.6). Adapted from (36). 52

Figure 2.13 - a) Ribbon structure of albumin with the subdomains shown in different colours (adapted from (122)) b) Molecular structure of γ-G (adapted from (98)). 54

Figure 2.14 - Amino acid structure. Adapted from (114)..... 54

Figure 2.15 – Schematic of the protein structure hierarchy. Adapted from (114). 55

Figure 2.16 - a) α-helix b) β-sheet. (128) 56

Figure 2.17 –β -sheet configurations a) Antiparallel i) Separate ii) Folded, b) Parallel i) Separate ii) Folded. Adapted from (114)..... 57

Figure 2.18 - Diagram of typical phosphatidylcholine (PC). Adapted from (146). 59

Figure 2.19 - a) Bilayer b) Unilamellar vesicle. Adapted from (98). 61

Figure 2.20 – a) Lambda ratio for MoM hip joint prosthesis ($R_{a\ head}$ = 10 nm and $R_{a\ cup}$ = 5 nm) for increasing D_h and Cl (84) b) film thickness using transient loads and speeds. Adapted from (9). 65

Figure 2.21 – Changes in potential indicating surface separation for a 36 mm femoral head for a simplified and physiological walking cycle. Adapted from (171). 66

Figure 2.22 – Sliding contact showing viscous inlet phase (200). 70

Figure 3.1 - A schematic of the HFRR (left) and a photograph of the loaded ball and fluid bath (right). 77

Figure 3.2 – Microstructure of Stellite 21 from disc specimen. 78

Figure 3.3 - Oxygen partial pressure over time for nitrogen purging. 82

Figure 3.4 - Left: modified lower specimen holder, Right: Original lower specimen holder. 82

Figure 3.5 - Left: Modified upper specimen holder Right: Original upper specimen holder. 83

Figure 3.6 – a) WLI contour map showing section line and regions AWD were measured b) Sectioned region of wear scar and places where AWD is measured. 86

Figure 3.7 - Example of a CoF traces for 25% w/w BCS for a) 0.5 ml b) 1 ml c) 1.5 ml d) 2 ml. 88

Figure 3.8 - Average CoF vs fluid volume. 88

Figure 3.9 - WLI wear scar images for a) 0.5, b) 1.0, c) 1.5 and d) 2 ml. 89

Figure 3.10 - Example profiles of wear scar width a) 0.5 ml b) 1 ml c) 1.5 ml d) 2 ml. 90

Figure 3.11 – Example profiles of wear scar length a) 0.5 ml b) 1 ml c) 1.5 ml d) 2 ml. 90

Figure 3.12 – AWD and AWV for varying fluid volumes. 91

Figure 3.13 - CoV of increasing fluid volumes. 91

Figure 3.14 – Summary of average friction values for different BCS concentrations, 1 and 2 ml fluid volumes. (with N2 Purge). 92

Figure 3.15 - Wear scar images for a) 1 ml b) 2 ml at i) 10%, ii) 25%, iii) 50% and iv) 100% BCS. 93

Figure 3.16 - Average wear scar depth for BCS at different concentrations, 1 and 2 ml. Approximate protein concentration ranges for "healthy" and "diseased" SF are indicated on the graph. 93

Figure 3.17- AWV for BCS at different concentrations, 1 and 2 ml. Approximate protein concentration ranges for "healthy" and "diseased" SF are indicated on the graph. 94

Figure 3.18 - CoV of increasing BCS concentration at both 1 and 2 ml. 94

Figure 3.19 - Effect of purge and preheat delay times on friction, AWD and AWV for 2 ml fluid tests 25 wt% BCS. 95

Figure 3.20 – CoV for the three HFRR test conditions. 96

Figure 4.1 - Example CoF traces for 25% w/w BCS and 25% w/saline BCS. 108

Figure 4.2 – Average CoF and AWD for 25% w/w BCS and 25% w/saline BCS. 108

Figure 4.3 - Example CoF traces for model fluids with and without DPPC a) saline b) mH. 109

Figure 4.4 - Average CoF for all model fluids with and without DPPC. 110

Figure 4.5 - AWD for all model fluids with and without DPPC. 111

Figure 4.6 – a) Average CoF vs total protein content, b) AWD vs total protein content, c) Average CoF vs A/G, d) AWD vs A/G. 112

Figure 4.7 – Example CoF traces for saline, saline + 0.5 mg/ml DPPC and saline + 2 mg/ml HA. 113

Figure 4.8 – a) Average CoF and b) AWD for saline, saline + 0.5 mg/ml DPPC and saline + 2 mg/ml HA. 114

Figure 4.9 - a) Average CoF and b) AWD for 25salBCS, mBCS, mBCS + 0.5 mg/ml DPPC, mBCS + 2 mg/ml HA and mBCS + 0.5 mg/ml DPPC +2 mg/ml HA. 115

Figure 4.10 – A plot of the CoF Vs AWD for all model fluids tested. 116

Figure 4.11 - Example CoF trace for a HSF compared to 25BCS. 116

Figure 4.12 - Average CoF for HSF samples compared to reference fluid 25BCS. 117

Figure 4.13 - AWD of HSF samples compared to reference fluid 25BCS. 117

Figure 4.14 - A plot of the average CoF Vs AWD for all model fluids and HSF. 118

Figure 4.15 - A plot of the AWD vs pH before testing. 119

Figure 4.16 - A plot of the AWD vs the pH after testing. 120

Figure 4.17 - A plot of the AWD vs change in pH before and after testing. 120

Figure 5.1 - Macroscopic visible deposited films on a explanted prosthesis a) Femoral head b) Acetabular cup c) microscopic image of rainbow interference fringes at transition zone on the femoral head in (a). (170). 126

Figure 5.2 - An example wear scar showing the areas inside and outside the wear scar used to measure surface roughness. 129

Figure 5.3 – Imaging of wear scars and surface deposits using a low power microscope for 1 ml 25BCS a) ball b) disc. 130

Figure 5.4 – Close up of deposits from mBCS fluid at the end of the stroke. 130

Figure 5.5 – Images of wear scars on balls for 2 ml BCS a) 10BCS b) 25BCS c) 50BCS d) 100BCS. 131

Figure 5.6 – Wear scar volume on ball vs BCS concertation. 131

Figure 5.7 – Images of wear scar on balls for a) 2ml 25BCS and b) 2 ml 25salBCS. 132

Figure 5.8 - Images of wear scar on balls with and without DPPC present a) i) Saline ii) Saline + DPPC b) i) 25BCS w/saline ii) 25BCS w/saline + DPPC c) i) mBCS ii) mBCS + DPPC d) i) mH ii) mH + DPPC e) i) mOA ii) mOA + DPPC f) I mPP ii) mPP + DPPC. 135

Figure 5.9 a) HA b) mBCS + HA c) mBCS + HA + DPPC. 136

Figure 5.10 – Wear scar and surface deposits on a) HSF 113 (low wear) i) Central ii) Side b) HSF 156 (high wear) i) Central ii) Side. 137

Figure 5.11 –Roll formation inside wear scars a) mBCS i) Ball ii) Disc b) mOA i) Ball ii) Disc c) mPP i) Ball ii) Disc. 138

Figure 5.12 - Disc scars with roll formation of low AWD specimens a) HSF041 b) HSF113. 139

Figure 5.13 – Black deposits on ball from 25BCS a) x1000 b) x6000. 140

Figure 5.14 – Black deposits on disc at end of wear scars from 25BCS. 140

Figure 5.15 – Black deposits at the end of the wear scar for 25BCS a) Agglomerated fibres b) Singular fibres. 141

Figure 5.16 – Fibril deposits inside the wear scar for 25BCS. 141

Figure 5.17 – Deposits inside the wear scar on the disc for HSF110 a) x250 b) x4000. 142

Figure 5.18 – Surface topography of an untested disc a) 3-D image b) Graphical profile. 142

Figure 5.19 - Surface topography of an untested ball a) 3-D image b) Graphical profile. 143

Figure 5.20 –Example of surface topography of the disc wear scar a) 3-D image b) Graphical profile for i) 25BCS ii) Saline iii) HSF164. 144

Figure 5.21 - Example of plucked carbide from the disc wear scar a) 3-D image b) Graphical profile for a) 25BCS b) HSF110. 145

Figure 5.22 – Surface roughness (r_q) of an untested disc, unworn and worn areas of the disc samples 25BCS, Saline and HSF samples. 146

Figure 6.1 – a) Path of visible beam for viewing a sample in reflectance b) Path of infrared beam for collecting spectra in reflectance. Adapted from (293) 155

Figure 6.2 – Structure of a fatty acid. Adapted from (114). 157

Figure 6.3 - Structure of DPPC. Adapted from (279, 306). 157

Figure 6.4 - Micro-IRRAS analysis of organics deposits on the ball. 160

Figure 6.5 – A typical spectra from the residual films with the regions 1750-1450 cm^{-1} and 3000 – 2800 cm^{-1} outlined. 161

Figure 6.6 - Micro-IRRAS analysis comparing the untested fluids of 12Alb and 6Glob in the range 1750-1450 cm^{-1} 162

Figure 6.7 - Micro-IRRAS analysis comparing the untested fluids of 12Alb and 6Glob in the range 3000-2800 cm^{-1} 163

Figure 6.8 - Micro-IRRAS analysis of the untested film 0.5 mg/ml DPPC in the range 1800-1450 cm^{-1}. 164

Figure 6.9 - Micro-IRRAS analysis of the untested film 0.5 mg/ml DPPC in the range 3000-2800 cm^{-1}. 165

Figure 6.10 - Micro-IRRAS analysis of untested films comparing 25BCS and 25salBCS in the range 1750-1450 cm^{-1} 166

Figure 6.11 - Micro-IRRAS analysis of untested films comparing 25BCS and 25salBCS in the range 3000 - 2800 cm^{-1}. 167

Figure 6.12 - Micro-IRRAS analysis of untested films comparing mBCS, mH, mOA and mPP in the range 1750-1450 cm^{-1}. 168

Figure 6.13 - Amide I peak position vs A/G ratio. 169

Figure 6.14 - Micro-IRRAS analysis of untested fluids comparing mBCS, mH, mOA and mPP in the range 3000 - 2800 cm^{-1}. 170

Figure 6.15 - Micro-IRRAS analysis of untested films comparing mBCS and mBCS + DPPC in the range 1750-1450 cm^{-1}. 171

Figure 6.16 - Micro-IRRAS analysis of untested films comparing mBCS and mBCS + DPPC in the range 3000 - 2800 cm^{-1}. 172

Figure 6.17 - Micro-IRRAS analysis of tested films comparing 25BCS black &rainbow deposits in the range 1800-1450 cm^{-1}. 174

Figure 6.18 - Micro-IRRAS analysis comparing spectra from untested fluids to both black and rainbow tested deposits for 25BCS in the range 3000 - 2800 cm^{-1}. 175

Figure 6.19 - Micro-IRRAS analysis comparing spectra from untested fluids to both black and rainbow deposits for mOA in the range 1800-1450 cm^{-1}. 177

Figure 6.20- Micro-IRRAS analysis comparing spectra from untested fluids to both black and rainbow tested deposits for mOA in the range 3000 - 2800 cm^{-1}. 178

Figure 6.21 - Micro-IRRAS analysis of wear deposits comparing mBCS + DPPC black and rainbow deposits in the range 1800 - 1450 cm^{-1}. 179

Figure 6.22 - Micro-IRRAS analysis comparing tested films and untested fluids of mBCS + DPPC and mPP + DPPC of 1800-1450 cm^{-1}. 180

Figure 6.23- Micro-IRRAS analysis comparing spectra from untested fluids to black and rainbow deposits for mBCS + DPPC in the range 3000 - 2800 cm^{-1}. 181

Figure 6.24 - Micro-IRRAS analysis of untested fluids 25BCS, HSF77, HSF110 and HSF113 in the range 1800-1450 cm^{-1}. 183

Figure 6.25 - Micro-IRRAS analysis comparing untested fluids 25BCS, HSF 77, HSF110 and HSF 113 in the range 3000 - 2800 cm^{-1}. 184

Figure 6.26 - Micro-IRRAS analysis comparing the untested fluid, black and rainbow deposits from HSF041 in the range 1800-1450 cm^{-1}. 186

Figure 6.27 - Micro-IRRAS analysis comparing the untested fluid, black and rainbow deposits from HSF164 in the range 1800-1450 cm^{-1}. 186

Figure 6.28 - Micro-IRRAS analysis comparing spectra from untested fluids to both black and rainbow tested deposits for HSF41 in the range 3000 - 2800 cm^{-1} 187

Figure 6.29 – AWD Vs amide I major peak position for BCS and Model fluids. 194

Figure 6.30 - AWD Vs amide I major peak position for model fluids + DPPC and HSF fluids. 194

Figure 7.1 - Schematic illustration of protein aggregation. Adapted from (313). 197

Figure 7.2 - Joblonski diagram showing three stages of fluorescence. Adapted from (98). 199

Figure 7.3 – a) A Schematic of a filter cube b) Transmission wavelengths of the excitation and barrier filters used. Adapted from (326) 200

Figure 7.4 – a) Molecular structure of ThT (327) b) The two planes of rotation about the shared carbon bond (329). 201

Figure 7.5 – AWD for the model and HSF samples. 205

Figure 7.6 - Optical Images taken with fluorescence set up of untested fluids a) 25BCS and b) HSF128. 206

Figure 7.7 - Optical Images taken with i) Navitar set up ii) Zeiss Axioscope for a)ThT b) 25BCS, c) 25salBCS + DPPC d) 12Alb e) 6Glob f) HSF105 g) HSF108 h) HSF128 j) HSF163. 208

Figure 7.8 - Optical Images of black deposits taken with i) Navitar set up ii) Zeiss Axioscope for a) HSF105 b) HSF108. 209

Figure 7.9 - Micro-IRRAS analysis comparing the untested fluids and tested films of 25BCS and 25BCS + ThT in the range 1800-1450 cm^{-1}. 210

Figure 7.10 - Micro-IRRAS analysis comparing the untested fluids and tested films of 12Alb + ThT and 6Glob + ThT in the range 1800-1450 cm^{-1}..... 211

Figure 7.11 - Micro-IRRAS analysis comparing the untested fluids of 25BCS, HSF105, HSF108, HSF128 and HSF 163 with ThT the range 1800-1450 cm^{-1}..... 213

Figure 7.12 - Micro-IRRAS comparing untested fluids and tested films of HSF105 with ThT the range 1800-1450 cm^{-1}. 214

Figure 7.13 - Micro-IRRAS comparing the untested fluids and tested films of HSF108 with ThT the range 1800-1450 cm^{-1}. 215

Figure 7.14 -Micro-IRRAS comparing the untested fluids and tested films of HSF163 with ThT the range 1800-1450 cm^{-1}. 215

Figure 8.1 - Mean contact pressure vs ball diameter for a range of loads. 224

Figure 8.2 - CoF and AWD of MoM and MoC bearing couples for 25BCS. 225

Figure 8.3 - Amide I peak position of untested samples vs AWD for HSF samples. 226

Figure 8.4 – a) Photograph of femoral head from DARF simulator study with rain bow films and black particulate b) zoomed in rainbow deposit from FH1 c) Zoomed in black deposit from FH1 d) Zoomed in gel deposit from FH2. 228

Figure 8.5 – Spectra from micro-IRRAS analysis in the region 1450 – 1800 cm^{-1} black, rainbow and gel films..... 229

Figure 8.6 - Spectra from micro-IRRAS analysis in the region 2800 – 3000 cm^{-1} black, rainbow and gel films..... 230

Figure 8.7 – Fluorescence image of initial state for 25BCS + ThT. 233

Figure 8.8 - Fluorescence image of sheared state for a) 25BCS + ThT b) HSF106 + ThT. 233

Figure 8.9 – DIC image of 25BCS a) Initial state b) Unidirectional sliding c) Cross shear sliding. 234

Figure 8.10 – Proposed mechanism of globular proteins captured and entrained into contact. 236

Figure 8.11 – Proposed lubrication mechanism showing the deposit morphology observed from tests and possible chemical interactions..... 237

List Tables

Table 2.1 - Material properties of hip joint materials (46). 35

Table 2.2 - Chemical composition of CoCrMo alloys (42, 43). 36

Table 2.3 - Hardness of CoCrMo alloys and carbide inclusions (48). 37

Table 2.4 – D_h and Cl for different material combinations (46). 38

Table 2.5 – The loads experienced and range of motion of an artificial hip for the most common activities (59-62). 43

Table 2.6 – Peak contact pressures reported in literature (74-80). 44

Table 2.7 – Lubrication regimes predicted by lambda ratio (85). 47

Table 2.8 - Healthy and diseased SF composition and pH (35, 37-41, 103, 104). 51

Table 2.9 – Buffer solutions used to make model SF. 63

Table 3.1 – Physiological conditions in a MoM hip joint. 76

Table 3.2 – Young's Modulus and Poisson's Ratio of ASTM F75-12 and Stellite 21 (46, 50, 59, 236). 78

Table 3.3 - Mean and maximum contact pressures and the contact area for two ball sizes on a flat contact. 80

Table 3.4 - Oxygen partial pressure in HSF. 81

Table 3.5 – HFRR test conditions. 84

Table 3.6 – Test protocols for testing effect of evaporation during nitrogen purge. 85

Table 3.7 – Initial protein concentration and estimated protein concentration after evaporation of fluids. 98

Table 3.8 – Final test protocol. 99

Table 4.1 - HFRR test conditions. 103

Table 4.2 –NaCl and protein concentration of model SF's tested. 105

Table 4.3 – NaCl, protein and DPPC concentration. 105

Table 4.4 - NaCl, Protein, DPPC and HA concentrations. 106

Table 4.5 - Gender, age and disease and volume of human samples 107

Table 4.6 - Total protein concentration and A/G ratio of model SF's. 112

Table 4.7 - Pathology and starting pH of HSF fluids. 119

Table 6.1 - Secondary structures associated with amide I and II peaks combined from (277, 278, 294-303). 156

Table 6.2 - Approximate band assignment for lipids (279). 157

Table 6.3 – Approximate band assignment for lipids (279, 306). 158

Table 6.4 - Summary of IR peaks from deconvolution and secondary structure assignment untested fluids of 12Alb and 6Glob in the range 1750 - 1450 cm^{-1}. (Bold type represents most intense peak). 162

Table 6.5 - Summary of IR peaks from deconvolution for untested 12Alb and 6Glob for 3000 - 2800 cm^{-1}. (Bold type represents the most intense CH_2/CH_3 peak). 163

Table 6.6 - Summary of IR peaks from deconvolution for untested 0.5 mg/ml DPPC. (Bold type represents the most intense CH_2/CH_3 peak). 165

Table 6.7 - Summary of IR peaks for untested 25BCS and 25salBCS for 1750-1450 cm^{-1}. (Bold type represents most intense peak). 166

Table 6.8 - Summary of IR peaks from deconvolution for untested 25BCS and 25salBCS for 3000 - 2800 cm^{-1}. (Bold type represents the most intense CH_2/CH_3 peak). 167

Table 6.9 - Summary of IR peaks from deconvolution and secondary structure assignment for untested 25salBCS, mBCS, mH, mOA and mPP for 1750 - 1450 cm^{-1}. (Bold type represents most intense peak). 168

Table 6.10 - Summary of IR peaks positions from deconvolution for untested 25salBCS, mBCS, mH, mOA and mPP for 3000 - 2800 cm^{-1}. (Bold type represents the most intense CH_2/CH_3 peak). 170

Table 6.11 - Summary of IR peaks from deconvolution and secondary structure assignment for untested 25salBCS + DPPC, mBCS + DPPC, mH + DPPC, mOA + DPPC and mPP + DPPC for 1750 - 1450 cm^{-1}. (Bold type represents most intense peak). 171

Table 6.12 - Summary of IR peaks from deconvolution for untested 25salBCS, mBCS and mBCS + DPPC for 3000 - 2800 cm^{-1}. (Bold type represents the most intense CH_2/CH_3 peak). 173

Table 6.13 - Summary of IR peaks from deconvolution and secondary structure assignment for tested black and rainbow deposits for BCS fluids in the region 1800 - 1450 cm^{-1}. (Bold type represents most intense peak, ^{w} denotes a weak peak). 174

Table 6.14 - Summary of IR peaks from deconvolution of spectra for black and rainbow deposits from the BCS samples for 3000 - 2800 cm^{-1}. (Bold type represents the most intense CH_2/CH_3 peak, no bold indicates similar peak heights). 176

Table 6.15 - Summary of IR peaks from deconvolution and secondary structure assignment for tested black deposits for model fluids in the region 1800 - 1450 cm^{-1} 177

Table 6.16 - Summary of IR peaks from deconvolution of spectra for black deposits from the model samples for 3000 - 2800 cm^{-1}. (Bold type represents the most intense CH_2/CH_3 peak, no bold indicates similar peak heights). 178

Table 6.17 - Summary of IR peaks from deconvolution and secondary structure assignment for model fluids + DPPC for the black deposits in the range 1800 - 1450 cm^{-1}.(Bold type represents most intense peak, ^{w} denotes a weak peak). 180

Table 6.18 - Summary of IR peaks from deconvolution for tested model fluids with DPPC for the black deposits in the range 3000 - 2800 cm^{-1}. (Bold type represents the most intense CH_2/CH_3 peak, no bold indicates similar peak heights). 182

Table 6.19 - Summary of IR peaks from deconvolution and secondary structure assignment for all untested HSF fluids and 25BCS in the range 1800 - 1450 cm^{-1}. (Bold type represents most intense peak, ^{w} denotes a weak peak). 183

Table 6.20 - Summary of IR peaks from deconvolution for all untested HSF fluids in the range 3000 - 2800 cm^{-1}. (Bold type represents the strongest peak). 184

Table 6.21 - Summary of IR peaks from deconvolution and secondary structure assignment for all tested HSF samples in the range 1800 - 1450 cm^{-1}. (Bold type represents most intense peak, ^{w} denotes a weak peak). 187

Table 6.22 - Summary of IR peaks from deconvolution for all tested HSF samples for the black deposits in the range 3000 - 2800 cm^{-1}. (Bold type represents the most intense CH_2/CH_3 peak, no bold indicates similar peak heights). 188

Table 6.23 – Model fluids, A/G ration, major amide I peak position with and without DPPC and ΔAWD. 191

Table 7.1 - Model fluids with ThT. 203

Table 7.2 - Gender, age and disease and volume of human samples. 204

Table 7.3 - Summary of IR peaks from deconvolution and secondary structure assignment for untested fluids and tested black deposits of 25BCS and 25BCS + ThT in the range 1800 - 1450 cm^{-1}. (bold most intense peak, ^{w} denotes a weak peak). 210

Table 7.4 - Summary of IR peaks from deconvolution and secondary structure assignment untested fluids and tested black deposits of 25BCS and 25BCS + ThT in the range 1800 - 1450 cm^{-1}. (bold represents strongest peak, ^{w} denotes a weak peak). 212

Table 7.5 - Summary of IR peaks and secondary structure assignment untested fluids of 25BCS + ThT, HSF105 + ThT, HSF108 + ThT, HSF128 + ThT and HSF163 + ThT in the range 1800 - 1450 cm^{-1}. (bold strongest peak). 213

Table 7.6 - Summary of IR peaks and secondary structure assignment for untested fluids of 25BCS + ThT, HSF105 + ThT, HSF108 + ThT, HSF128 + ThT and HSF163 + ThT in the range 1800 - 1450 cm^{-1}. (bold: strongest peaks, ^{w} denotes a weak peak). 216

Table 10.1 - Summary of IR peaks for untested 25BCS and 25salBCS for 1750-1450 cm^{-1}. (Bold type represents most intense peak) 286

Table 10.2 - Summary of IR peaks from deconvolution and secondary structure assignment for untested 25salBCS, mBCS, mH, mOA and mPP for 1750 - 1450 cm^{-1}. (Bold type represents most intense peak) 286

Table 10.3 - Summary of IR peaks from deconvolution and secondary structure assignment for untested 25salBCS + DPPC, mBCS + DPPC, mH + DPPC, mOA + DPPC and mPP + DPPC for 1750 - 1450 cm^{-1}. (Bold type represents most intense peak) 287

Table 10.4 - Summary of IR peaks from deconvolution and secondary structure assignment for tested black and rainbow deposits for model fluids in the region 1800 - 1450 cm^{-1}. (Bold type represents most intense peak, ^{w} denotes a weak peak) 288

Table 10.5 - Summary of IR peaks from deconvolution for tested mOA black and rainbow deposits for 3000 - 2800 cm^{-1}. (Bold type represents the most intense CH_2/CH_3 peak, no bold indicates similar peak heights) 289

Table 10.6 - Summary of IR peaks from deconvolution and secondary structure assignment for model fluids for both black and rainbow deposits in the range 1800 - 1450 cm^{-1}. (Bold type represents most intense peak, ^{w} denotes a weak peak) 290

Table 10.7 - Summary of IR peaks from deconvolution for tested model fluids with DPPC for both black and rainbow deposits in the range 3000 - 2800 cm^{-1}. (Bold type represents the most intense CH_2/CH_3 peak, no bold indicates similar peak heights) 291

Table 10.8 - Summary of IR peaks from deconvolution and secondary structure assignment for all untested HSF fluids and 25BCS in the range 1800 - 1450 cm^{-1}. (Bold type represents most intense peak, ^{w} denotes a weak peak) 292

Table 10.9 - Summary of IR peaks from deconvolution and secondary structure assignment for all tested HSF samples for both black and rainbow deposits in the range 1800 - 1450 cm^{-1}. (Bold type represents most intense peak, ^{w} denotes a weak peak) 293

Table 10.10 - Summary of IR peaks from deconvolution for all tested HSF samples for both black and rainbow deposits in the range 3000 - 2800 cm^{-1}. (Bold type represents the most intense CH_2/CH_3 peak, no bold indicates similar peak heights) 294

Nomenclature

10BCS	10% w/w Bovine Calf Serum
25BCS	25% w/w Bovine Calf Serum
50BCS	50% w/w Bovine Calf Serum
100BCS	100% Bovine Calf Serum
Λ	Lambda ratio
ν	Poisson's Ratio
γ-G	γ-globulin
A/G	Albumin/γ-Globulin Ratio
AWD	Average Wear Depth
AWV	Average Wear Volume
BCS	Bovine Calf Serum
BMI	Body Mass Index
BSA	Bovine Serum Albumin
BW	Body Weight
Cl	Diametrical Clearance
CMC	Carboxy Methyl Cellulose
CoC	Ceramic-on-Ceramic
CoF	Coefficient of Friction
CoP	Ceramic-on-Polymer
CoV	Coefficient of Variation
CoCrMo	Cobalt Chromium Molybdenum
D_H	Femoral Head Diameter
DI	Deionised

DIC	Differential Interference Contrast
DLPC	Dilauroylphosphocholine
DPPC	Dipalmitoylphosphatidylcholine
E	Young's Modulus
EHL	Elastohydrodynamic Lubrication
F-β	Fibril β-sheet
FWHM	Full Width Half Maxima
H	Healthy
HFRR	High Frequency Reciprocating Rig
HSF	Human Synovial Fluid
K	Wavenumber
LHMoM	Large Head Metal-on-Metal
N-β	Native β-sheet
Micro-IRRAS	Micro InfraRed Reflection Absorption Spectroscopy
mBCS	Model 25% w/w Bovine Calf Serum
mH	Model Healthy
mOA	Model Osteoarthritis
mPP	Model Periprosthetic
MoM	Metal-on-Metal
MoM_{HR}	Metal-on-Metal resurfacing
MoP	Metal-on-Polymer
MTM	Mini Traction Machine
OA	Osteoarthritis
PAGE	Polyacrylamide gel Electrophoresis

PLPC	Palmitoyllauroylphosphocholine
POPC	Palmitoyloleoylphosphatidylcholine
PP	Periprosthetic
R_a	Surface roughness – arithmetic mean
RA	Rheumatoid Arthritis
SEM	Scanning Electron Microscopy
SF	Synovial Fluid
SLPC	Stearoyllinoleoylphosphocholine
SRR	Slide-Roll-Ratio
TEM	Transmission Electron Microscopy
ThT	Thioflavin T
THR	Total Hip Replacement
UHMWPE	Ultra High Molecular Weight Polyethylene
UHXLPE	Ultra High Cross-Linked Polyethylene
ZTA	Zirconia Toughened Alumina; Biolex®delta

Chapter 1 Prosthetic Joints and Tribology

Summary

This chapter provides an introduction to the research project. It gives a brief overview of the evolution of the modern hip prosthesis and outlines the tribological performance of past and present material combinations. Wear of the bearing surfaces remains a limiting factor on implant life, despite nearly half a decade of redesign. Severe wear was widely reported in some MoM hips leading to revision of the joint, which has only partly been explained by edge loading or misalignment. However, some cases have shown excellent survivorship particularly in young adult males. It was identified that minimal work on the effect of SF chemistry on tribological performance had been carried out and suggested that this could be a possible reason for increased wear in some patients. Finally, objectives for the thesis were formalised.

1.1 General Introduction

In 2016 over 210,000 (1) joint replacement (hips, knees, shoulders, elbow and ankle) operations were performed in the United Kingdom. In 2010, for the UK, it was estimated that the cost of hip and knee replacements exceeded £850 million which represented a 66% increase from 2000 (2). The procedures are used improve the living standards of a patient by restoring function and relieving pain in synovial joints which have been damaged due to disease, trauma or infection. The replacement joints must fulfil a number of requirements: have an extended operational life (~ 20 years), allow easy movement and emulate natural gait as closely as possible.

Artificial joints are essentially tribological devices as the bearing surfaces articulate under load and as such they are susceptible to the usual tribological problems of high friction, wear and corrosion. These issues can cause early failure leading to revision surgery which accounted for over 7.1 % of procedures in 2016 (1). Devices are gradually being implanted into younger patients increasing the performance demand on the joint due to higher activity levels and longer operational life.

Implant procedures are routinely performed for the hips, knees, ankles, shoulders and elbows (Figure 1.1) ; the most common of which are the hips and knees totalling 48% and 50% (1) of recorded procedures in the United Kingdom respectively since 2003. Osteoarthritis (OA) is the leading cause of joint replacement surgery in the hips and knees accounting for 90% and 99% of procedures

respectively (1). Hip and knee replacements represented 85% of the direct cost of OA (2). The primary focus of the PhD research is hip joint tribology and the rest of the thesis will concentrate on this aspect.

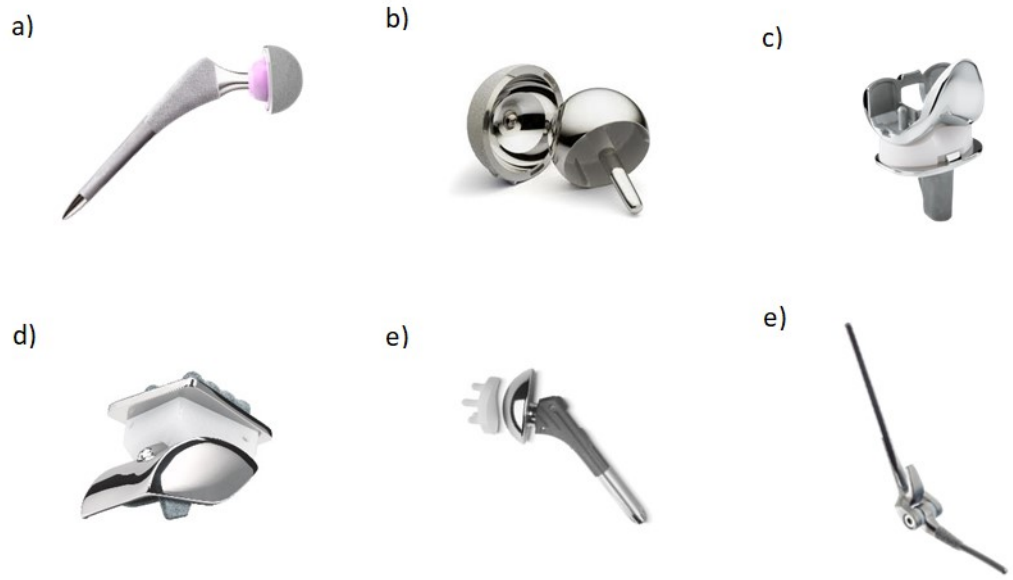


Figure 1.1 - Examples of artificial joints a) total hip b) hip resurfacing c) total knee d) total ankle e) total shoulder f) total elbow.

The first generation of the modern total hip replacement (THR), the *low friction arthroplasty*, was designed by Sir John Charnley in the early 1960's and is identical in principle to the prosthesis used today (3) (Figure 1.2a) (4). The joint used a metal (CoCrMo) femoral head and a thicker polyethylene acetabular cup (MoP). The joint was thought to operate in the boundary lubrication regime, which meant the bearing surfaces came into contact during articulation. To reduce the wear Charnley advocated the use of a small femoral head, minimising the surface area in contact and consequently the sliding distance (5). Although the joint was successfully used for over two decades the production of polyethylene wear debris could cause osteolysis in the periprosthetic bone, which is a chronic inflammatory response to a foreign body (6). Osteolysis is the destruction or disappearance of bone tissue causing fixation failure and aseptic loosening (7). Additionally the use of a small femoral head increased the risk of dislocation making the hip unsuitable for active patients (8).

Metal-on-Metal (MoM) replacements became popular in the 1990's with the Birmingham Hip Resurfacing (MoM_{HR}) prosthesis. This procedure removes diseased bone and cartilage from the joint, the femoral head is capped with a metal covering and a metal shell is inserted into acetabular cup.

The MoM_{HR} provides minimal bone loss, excellent stability, a wider range of motion and relative ease of revision (7). A MoM_{HR} replacement can be seen in Figure 1.2b.

Initial success of the MoM_{HR} lead to a revival in the use of MoM in the THR prosthesis. Prior to Charnley's *low friction arthroplasty,* MoM implants were used regularly and considered successful having a reported survival rate of 74% at 28 years. However in the 1970's they grew unpopular due to negative local effects caused by metal particles, this was only observed in patients with failed prosthesis undergoing revision surgery and therefore was attributed to poor design and improper implantation technique (3). In this new prosthesis (Figure 1.2c) large femoral components were used, unlike conventional MoP devices, as this was thought to promote fluid film lubrication (EHL) that reduced the wear (9). Similar to MoM_{HR}, larger heads increased stability and allowed a greater range of movement (10). The wear rate of the MoM implants were initially estimated at 60 times less than MoP implants as the metallic surfaces could be engineered to be smooth and hard (11). The increased stability and reduced wear made both MoM_{HR} and MoM devices suitable for more demanding patients.

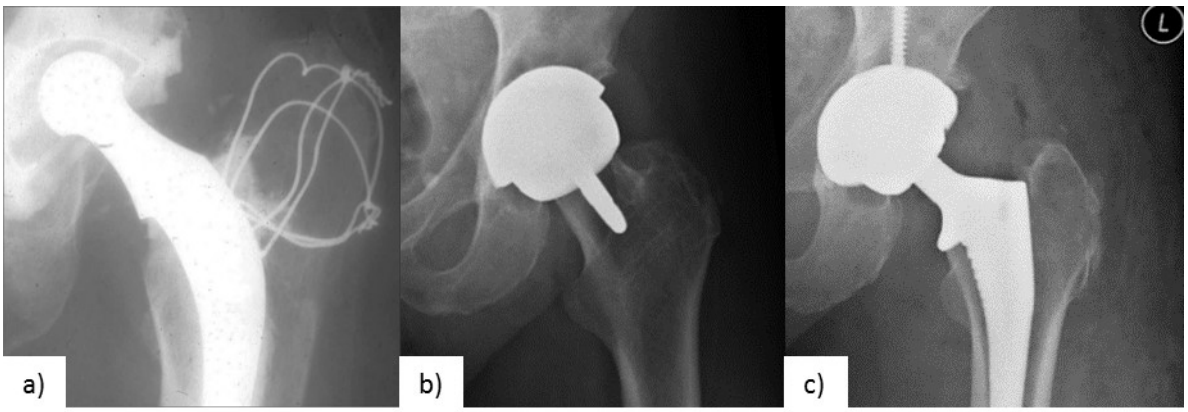


Figure 1.2 - a) A radiograph of 26-year follow-up of first generation Charnley low friction arthroplasty (4) (with permission form Elsevier) b) X-ray showing a Hip resurfacing (12) c) X-ray showing THR (12).

In 2008 it became clear from the NJR that that MoM bearings had a higher than expected revision rate (1). Approximately 13% of resurfacing joints required revision 10 years after primary surgery compared to less than 4% in MoP. Furthermore approximately 20% of MoM hip replacements required revision 10-13 years after insertion (10). It was found that although wear rates were reduced particles sizes were much smaller (~ 50 - 116 nm) than that produced in MoP bearings (0.1 – 8 µm) (13-15). This resulted in an increased total number of particles by more than two orders of magnitude. The surface area of metal particles was larger giving a greater potential for corrosion and biological activity leading to cell death and in excess adverse tissue reactions (16). Complications include

inflammatory pseudotumors, aseptic lymphocytic vasculitis associated lesion, metallosis and osteolysis (10, 16). As a result there were 578 recalls of MoM components from six major manufactures between 2002 – 2013 due to manufacturing defects (17). This led to over 28,000 lawsuits filed against companies who had made defective implants. To date over $6 billion has been paid in law suit settlements. In 2018 over 14,000 hip cases were still pending (18).

As a result by 2016 implantation of MoM THR reduced to less than 0.1 % and MoM_{HR} accounts for ~ 1% of all procedures (1).

In 2016 MoP prostheses account for 58% of hip replacements in the UK making them the most common (1), however osteolysis remains the main cause of failure (1). Wear rates, have been effectively reduced by using cross-linked (gamma radiation/thermal treatment) UHMWPE (Ultra High Molecular Weight Polyethylene) (7). In 1998 this bearing surface (Ultra High Cross-Linked Polyethylene; UHXLPE) was used clinically for the first time and initial follow ups and simulator tests (10 – 22 years) have shown significantly reduced wear (19-21). However, the crystalline and mechanical properties of UHMWPE were affected due to free radicals and polyethylene oxidation. A second generation UHXLPE bearing addressed these issues using two different methods; sequential annealing to saturate free radicals and the use of vitamin E as a free radical scavenger (7). Initial results are promising however long-term clinical results are not yet available (22, 23).

Ceramics (Biolex®delta; Zirconia Toughened Alumina (ZTA)) are a promising alternative bearing surface as they are bio-compatible, corrosion resistant (24) and debris is relatively inert in the body (25). Compared to metal surfaces they have a greater resistance to scratching, lower friction coefficient and better joint lubrication (7, 24). However the cost of operation and components is significant compared to MoP and therefore only cost effective in younger patients (26). Ceramics are brittle and catastrophic *in vivo* failure provides a serious concern (27). Chipping can occur on insertion or as a result of dislocation that can lead to third body wear therefore high surgical precision is required (28).

In 2016, 29% of hip replacements were CoP making them second most popular bearing couple (1). Linear wear tests and hip simulator studies have shown a 50% reduction in wear when compared to MoP (27, 29) and clinical studies have shown an 80% survivorship at 20 years (30). The use of UHXLPE is a promising breakthrough; clinical and laboratory data have shown wear is reduced by 10-50% (7).

The CoC device has the best wear properties of any bearing couple with reported linear wear rates of < 5 µm/year in comparison to CoP with wear rates of < 100 µm/year (27). A clinical study done at a 10 year follow up showed osteolysis was absent in all CoC devices and occurred in 26% of MoP cases (31).

Despite these promising results CoC configuration does not come without complications; squeaking noises, stripe wear, fracture (rare) and chipping during insertion. Complications are usually associated with acetabular component malposition, smaller femoral heads, edge loading and non-adherence to meticulous surgical technique (7).

Throughout the evolution of hip arthroplasty wear has been and still remains a major cause of failure. Particularly apparent in some MoM devices, the poor performance has been attributed to translational or rotational misalignment of the femoral head and acetabular cup resulting in edge loading. This is when the contact area is displaced from the centre of the cup, when perfectly concentric, to the rim. It has been reported that this can increase the wear and metal ion level by 10-fold (16, 17, 32, 33)

Not all failures have been explained by this and it accepted that MoM THR works very well for younger male patients. However a review by De Smet et al. (34) reported that of the 3313 MoM_{HR} performed by a single surgeon since 1998, the known revision rate was 1.5%. Additionally, 110 (44 males, 66 females, mean age 49.9 years) cases were studied in more detail, it was shown that there was no difference in outcome between genders. A possible reason for this could be the synovial fluid (SF) chemistry, which has not been widely studied.

The focus of the majority of implant tribology testing is the effect of implant design and material wear. The effect of SF chemistry on implant wear is rarely studied. SF is the natural lubricant found in articular joints. It is rarely available and only attainable in small quantities, certainly less than the large volumes required for simulator tests. Therefore, the lubricant model most communally used is BCS diluted concentration of 25% w/w (25BCS). It has been shown to have a similar total protein content (18-21 mg/ml) when compared to healthy SF (H) (35-37). However, the overall chemical composition is different (35-37). In addition diseased joints show large increases in total protein content not mirrored by the model (37-41).

The chemical composition and physical properties of HSF varies between patients and healthy or diseased fluids (37-41). The most abundant components of SF are proteins, particularly albumin and γ-globulin (γ-G) and their relative and total concentration can vary widely depending on the fluid pathology (37, 38, 40).

The vast majority of implant tribology testing uses BCS as the model SF lubricant: There are very few instances of HSF being used.

It is apparent from literature that the effect of SF chemistry on the lubrication and wear mechanisms, particularly use of HSF, has been rarely studied for MoM devices. This highlights deficiencies in our understanding of lubrication of prosthetic joints which raises the following questions:

- What is the effect of HSF composition on CoCrMo wear?
- Are some patients/diseases at a higher risk of implant failure though increased wear?
- Is 25BCS a suitable model lubricant to replace HSF?

1.2 Research Objectives

This thesis aims to develop an understanding of how both model and HSF lubricate artificial joints and the associated wear mechanisms. The study combines friction and wear tests with optical and organic chemical analysis in an attempt to replicate *in vitro* simulation of *in vivo* conditions and understand the role of macromolecules in SF.

The specific objectives are to:

- Develop a small-scale wear test for CoCrMo materials with small volumes for use with both model and HSF
- Investigate the effect of model and HSF on friction and wear of implant materials
- Investigate the fundamental mechanisms of SF lubrication:
    - Analyse the chemical composition of wear deposits and untested fluids
    - Examining deposited films on the wear scar surfaces

1.3 Thesis Outline

Chapter 2 begins by concentrating on the artificial hip joint. The current materials used for these prostheses are outlined followed by the operational conditions. The second section looks at classical tribology, specifically the lubrication and wear mechanisms. Thirdly, an anatomical description of the synovial hip joint is given joint and the composition of both healthy and diseased joints is explained. A detailed description of the most abundant macromolecules present in SF and those thought to be important in the lubrication of artificial joints is reviewed. Finally, the tribology related problems, test methods, model lubricants and lubrication and wear mechanisms are looked at.

A new bench top wear-test is developed for use with HSF in Chapter 3. It was important to replicate physiological conditions in an artificial hip joint and to use only a small amount of fluid allowing use of HSF. Initially tests were performed using 25BCS as the screening fluid to ensure that results were robust and repeatable. Once the final test protocol was finalised Chapter 4 used model fluids to further

investigate how the SF chemistry affected the wear of MoM artificial joint implants. Initially fluids comprised albumin and γ-G only, different total and specific protein concentrations were used to replicate healthy and diseased HSF. The fluids were made more complex with the addition of phospholipids and hyaluronic acid.

The residual deposited films were observed by use of optical and SEM imaging in Chapter 5 and the wear scar mechanisms were investigated by use of white light interferometry. Chapter 6 used Micro-IRRAS analysis to investigate the organic chemistry of the deposited films and compared this to the untested fluids. Chapter 7 uses fluorescence microscopy to visualise the presence of high β-sheet content deposits and compares the results to the AWD and the Micro-IRRAS spectra of the deposits.

In Chapter 8 the results from this work are discussed in terms of how they advance the current understanding of how the SF chemistry, particularly the role of proteins and lipids, effects the lubrication and wear mechanisms. The clinical relevance is discussed and if the of wear of MoM implants can be predicted once the chemistry of the SF is known. In each section of this chapter future work is considered. Finally, Chapter 9 draws conclusions of this study.

Chapter 2: Tribology of Artificial Hips

Summary

In this chapter a review of the current literature is presented, providing context to this thesis. The different materials and operating conditions of the THR and resurfacing prosthesis are reviewed including the implant size, joint kinematics and physiological loads. Classical lubrication and wear mechanisms are then reviewed. The structure of the articular hip joint and properties of the natural lubricant, SF, are described. Lastly artificial joint tribology is reviewed outlining current lubrication and wear mechanisms.

2.1 Introduction

This review provides context for thesis, it begins with background information on the materials and operating conditions of the THR and hip resurfacing prosthesis. A brief overview of the different types of materials, bearing couples used and prosthesis geometry are reported. The thesis focuses on the MoM hip therefore the chemical composition and microstructure of the surgical grade CoCrMo alloy (42, 43) is reviewed in more detail. A primary objective of the project was to develop a suitable MoM material wear test. When designing a wear test, it is important to understand the *in vivo* operating conditions so that they can be replicated. Therefore, the physiological motion, loads and pressures of the most common types of activities are reviewed.

Classical tribological models of lubrication and wear are often applied to these complex biological systems and therefore a brief overview of the Stribeck curve and the three lubrication regimes; i.e. boundary, mixed and full film, are given. All four types of wear mechanism; abrasion, surface fatigue, adhesion and tribo-chemical may occur in the prosthesis and are therefore reviewed.

The review then considers the properties of SF as this is the natural lubricant of healthy, diseased and post-operative joints. The rheology is briefly discussed before concentrating on the chemical composition. The main components of SF are: proteins, hyaluronic acid (HA), glycoproteins and lipids, which are reviewed in more detail.

Finally, artificial hip tribology has been extensively studied throughout the years, therefore the lubrication and wear mechanisms that have been reported are reviewed with regard to MoM prostheses.

The research project has focussed on CoCrMo alloy joints. However, it is recognised that the use of this bearing couple has rapidly declined to ~ 1% in recent years due to the risk of early revision (1). However, the reasons for this were not fully understood, although it was often attributed to the use of large heads (44) and transition or rotational misalignment (16, 17, 32, 33). However, other studies (34) have shown that MoM resurfacing and THR work well for younger male patients, and a possible reason for this could be the SF chemistry.

2.2 THR: Materials and Operating Conditions

The hip joint has a ball on socket conformation, the loaded femoral head represents the ball, which articulates within the acetabular cup that sits within the pelvis. For a THR the femoral head is removed and replaced whilst a hip resurfacing procedure caps the femoral head with a metallic surface. The prosthesis should restore the natural gait cycle as closely as possible and must be durable having *in vivo* lifespans that, preferably, outlive the life of a patient.

2.2.1 Materials

A range of materials are used for the bearing surfaces in these devices including polymers (Ultra High Molecular Weight Polyethylene; UHMWPE, Ultra Highly Cross-linked Polyethylene; UHXLPE), metal alloys (Cobalt Chromium Molybdenum; CoCrMo) and ceramics (Biolex delta; zirconia toughened alumina; ZTA). These materials must be resistant to wear and fatigue, biocompatible, corrosion resistant, easily manufactured to high specifications and have an appropriate strength (45). The material properties are outlined in in Table 2.1.

Table 2.1 - Material properties of hip joint materials (46).

Material	E (GPa)	ν	Ra (µm)
CoCrMo	230	0.3	0.01-0.05
Biolex Delta	350	0.26	0.1-2
UHMWPE	0.5-1	0.4	0.001-0.005

The focus of this research is CoCrMo implants and only this material that will be discussed in more detail. The family of CoCrMo alloys is used due to its superior hardness and wear resistance compared to stainless steel which was used in earlier designs (47). Cast or wrought (with low carbon or high carbon contents) CoCrMo alloys can be used and the properties are outlined in BS ISO 5832-4:2014

(42) BS ISO 5832-12:2007 and (43). The chemical composition of the implant must be in the range outlined in Table 2.2.

Table 2.2 - Chemical composition of CoCrMo alloys (42, 43).

Element	Mass fraction %		
	Low Carbon Alloy (Wrought)	High Carbon Alloy (Wrought)	Cast Alloy
Chromium	26.00 – 30.00	26.00 – 30.00	26.50 – 30.00
Molybdenum	5.00 – 7.00	5.00 – 7.00	4.50 – 7.00
Iron	0.75 max	0.75 max	1.00 max
Manganese	1.00 max	1.00 max	1.00 max
Silicon	1.00 max	1.00 max	1.00 max
Carbon	0.14 max	0.15 – 0.35	0.35 max
Nickel	1.00 max	1.00 max	1.00 max
Nitrogen	0.25 max	0.25 max	-
Cobalt	balance	balance	balance

The microstructure of the implant is important as this can strongly influence the durability and physical properties of the material; the standards for metallic implants outline a specification for this (43).

The high carbon content of the alloys produces a structure with a significant carbide distribution which can be adjusted in the production or through thermochemical processing. A carbide is a chemical compound whereby carbon is combined with a metallic compound. The carbides found in CoCrMo are $M_{23}C_6$ (M: Cr, Co) and M_6C (M: Mo, Cr) (48). The carbide phase has been determined to occupy between 4 – 5 % of the field of view and have a large blocky morphology when observed using an Scanning Electron Microscope (SEM) (49). The size of the carbides have been observed on an artificial joint surface to be 2 – 3 μm long, 10 – 30 μm wide and protrude from the surface by ~ 100 nm (49). The average hardness values of the carbides has been reported to be higher than that of the metal matrix (48) and are outlined in Table 2.3.

Table 2.3 - Hardness of CoCrMo alloys and carbide inclusions (48).

Material	Hardness
CoCrMo	434 ± 30 (HV0.05)
$M_{23}C_6$ (M: Cr, Co)	1170 ± 1300 (HV0.05)
M_6C (M: Mo, Cr)	518 ± 11 (HV10)

It has been reported that the increase in carbides in the high-carbon alloys give a superior wear performance, as a coarse carbide distribution gave better resistance against abrasion (50). Conversely McMinn (51) attributed the high carbon alloy responsible for early failure in some MoM_{HR} components. Other studies have found no difference in wear performance of high carbon alloys with different microstructures (52-54).

The roughness (Ra) of the bearing surface of new CoCrMo implants has been reported to be about r_a = 10 nm (55).

2.2.2 Bearing Couples

Bearing couples can consist of a combination of materials that can be further subcategorised as hard-on-hard or hard-on-soft. Hard-on-hard devices are made of metals and/or ceramics (Metal-on-Metal; MoM, Ceramic-on-Ceramic; CoC) whereas hard-on-soft (Metal-on-Polymer; MoP, Ceramic-on-Polymer; CoP) devices uses a polymer articulating against a metal or ceramic. The material combination chosen depends on the patient characteristics such as age, gender and size. A diagram of types of bearing surface is given in Figure 2.1

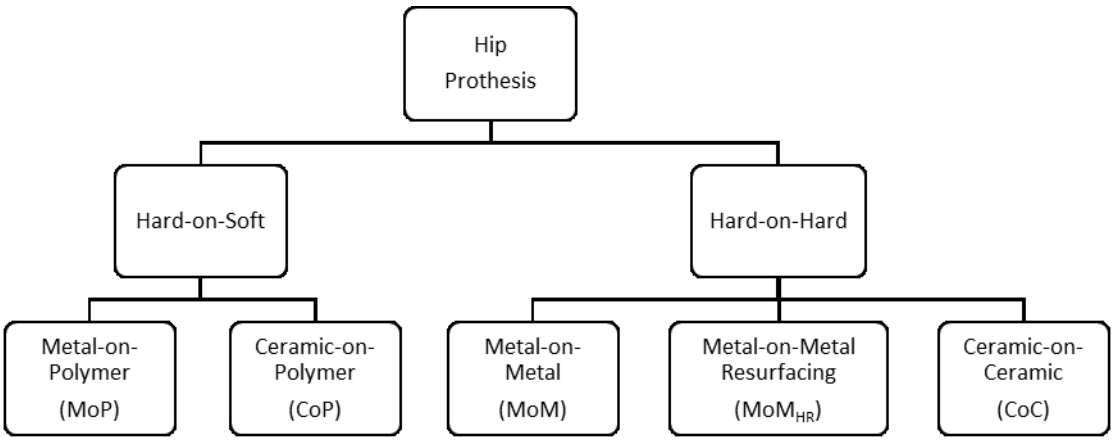


Figure 2.1 - Types of hip prosthesis categorised by bearing type.

2.2.3 Implant Size and Choice

Commonly used head diameter, D_h, and diametrical clearance, Cl, are outlined in Table 2.4 for different material combinations. The cup thickness is important for MoP and CoP designs and can range from 5-18 mm (46).

The primary choice of prosthetic implant size is the patient and their activity level. Large heads ($D_h \geq$ 36 mm) are favourable as studies have shown to have a greater range of motion, greater stability at higher levels of function and reduced risk of dislocation in older patients (56).

A secondary consideration is the lubrication Hard-on-Soft joints are often predicted (57) to operate in the boundary or mixed lubrication regime and therefore the articulating surfaces are susceptible to wear. A small femoral head is used to minimise the contact area, sliding distance and wear (5, 58). On the other hand, for Hard-on-Hard implants large femoral heads are used, as this is thought to promote EHL lubrication. If the articulating joints are fully separated, as in EHL, it follows that wear would be reduced (9).

Table 2.4 – D_h and Cl for different material combinations (46).

Head/Cup	D_h (mm)	Cl (μm)
MoP	22.2-44	160-400
CoP	22.2-36	160-400
MoM	22.2-54	50-150
MoM_{HR}	42-62	50-300
CoC	22.2-44	20-100

2.2.4 Physiological Motion and Loads

The ball and socket conformation of the natural joint has a wide range of movement and it is important that an artificial joint emulates this. The motion in a hip joint can be categorised as three general movements, shown in Figure 2.2: flexion/extension, abduction/adduction and external/internal rotation. Flexion/extension moves the thigh forwards and backwards, it is the main range of movement when walking or running in a straight line. Abduction/adduction describes a sideways motion, which forces the leg out away from the centre of the body and back towards the centre. Finally external/internal rotation describes the movement of the thigh along its long axis outwards away from the centre of the body and inwards towards the centre (59). The major direction of motion is flexion/extension which is a bi-directional linear motion.

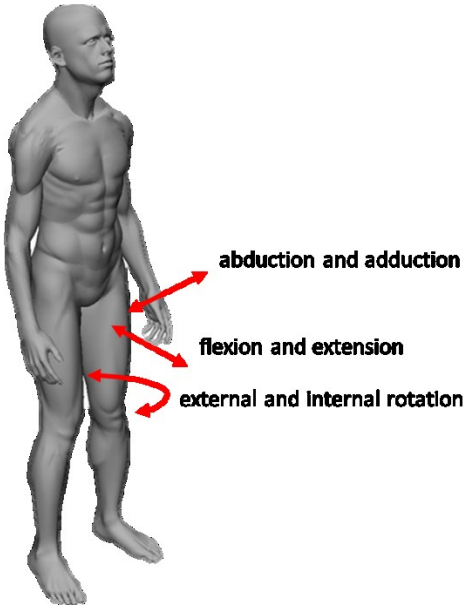


Figure 2.2 – Types of motion experienced by the hip joint (adapted from (59)).

The range of movement varies for different activities and the contact forces can extend to many times the body weight (BW). In her thesis Hadley (59) reviewed the literature of the kinematics of the most common types of activity; data was taken from researchers reporting the loading and motion in gait studies from several different activities. The results were also compared to other studies for verification. The broadest range of motions was reported by Bergmann et al. (60-62).

Two different methods are used to evaluate the loading and motion over the gait cycle for an artificial hip. The first implements modelling using force data plates on the ground and derivation of muscle action across the joint. This method is easy to perform on a wide range of subjects; however, the results can vary widely depending upon the model used. The second uses instrumented *in vivo* implants, this method is more accurate but can only be performed on a limited number of subjects (59). Comparisons of these techniques report discrepancies ranging from 10-23 % of the peak load, which is a similar range to the cycle-cycle variation in a single patient (63, 64).

The contact loads are often reported in three axes, which is based on a coordinate system fixed to the femoral head as shown in Figure 2.3 (59).

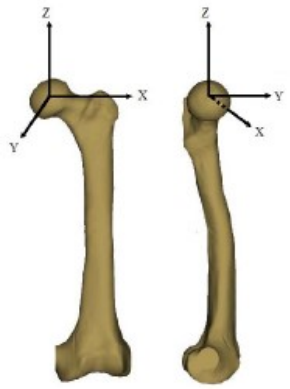


Figure 2.3 – Coordinate system of the left femoral head (59).

Bergmann et al. (60) used instrumented implants to measure the load and a fixed camera system to monitor markers placed on the body to analyse the motion. Results were averaged for four patients at least 11 months post-surgery. Figure 2.4 shows the range of motion for each type of movement and the loads along each axes as a percentage of BW during a walking gait cycle (adapted from) (59, 60).

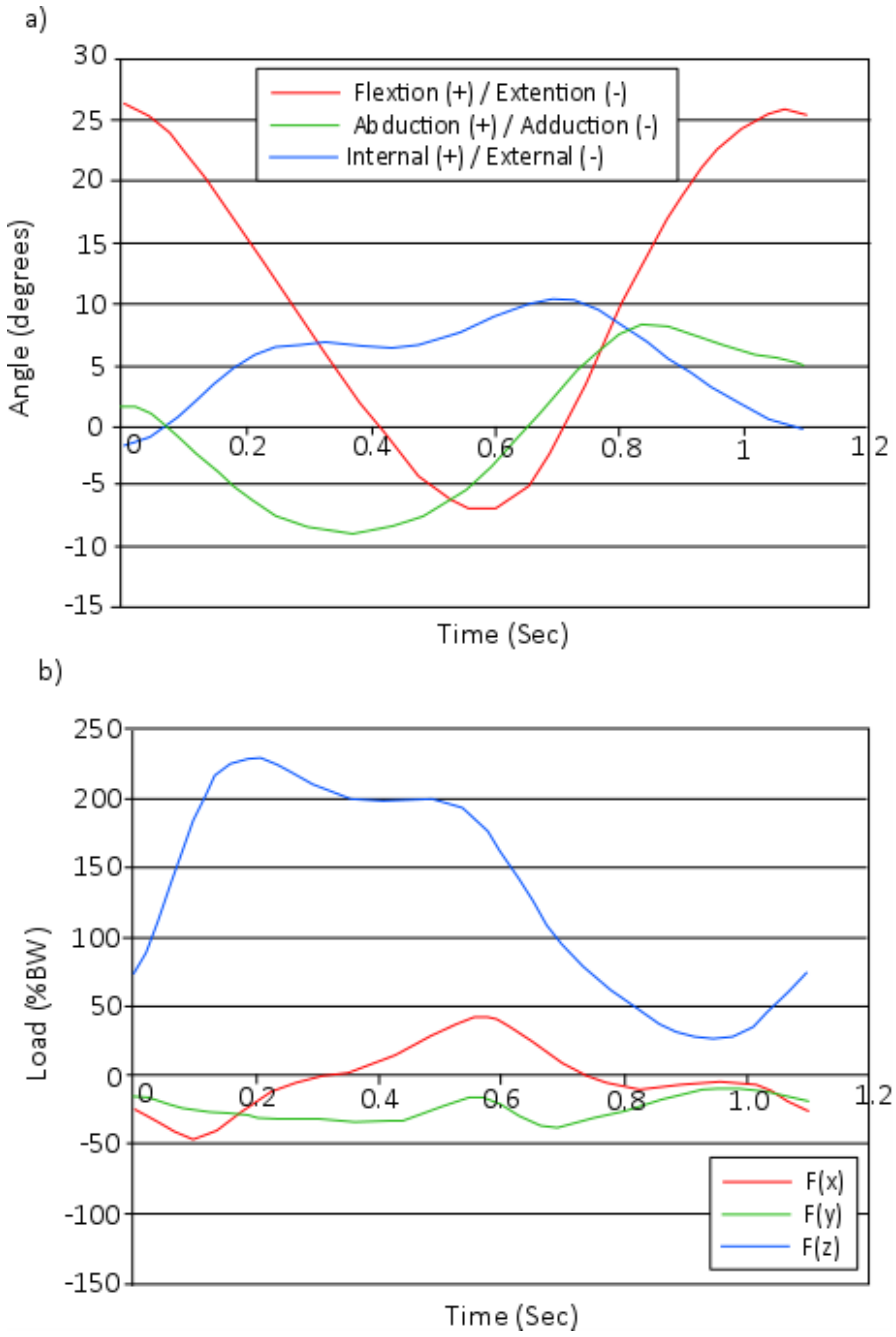


Figure 2.4 – Walking gait cycle a) Range of motion b) Loads experienced (adapted from (59, 60)).

It is generally accepted that during a walking gait cycle the load has a twin peak profile with the major motion being flexion and extension (65). The kinematics have been shown to change significantly with both age and walking velocity.

It was reported that a study using force plates to analyse the gait cycle that an increase in velocity form 0.3 to 1.2 m/s increased the peak contact force from 3.5BW to 4BW and 5BW in patients aged

60-80 years and 20-30 years respectively (66). Other studies have shown an increase in the hip contact force from 4.9BW to 7.6BW with an increase in walking velocity from 1.5 to 2 m/s (67) and from 0.28BW to 4.8BW for a velocity increase of 0.27 to 1.35 m/s (61). The latter two studies did not detail if differences were observed with the age of the patient.

Similarly, there was an increase in the range of hip flexion for an increase in velocity. Crowninshield et al. (66) reported that an increase in velocity from 0.3 to 1.2 m/s increased the hip flexion from 20^0 to 30^0 and 40^0 for patients aged 60-80 years and 20-30 years respectively. Another study reported an increase in hip flexion from 42^0 to 48^0 for an increase in velocity from 1.5 to 2 m/s (67).

As the velocity increases towards jogging, 2-3 m/s, the gait cycle is similar; however, certain characteristics become more pronounced. During walking the twin peaks have a similar magnitude of force, whereas during running the gait is dominated by a single peak controlled by the forces following the heal strike. This occurs at the same time during the cycle as the first load peak in walking. Figure 2.5 shows the running gait cycle when jogging at 2.2 m/s on a treadmill where the loads were measured by instrumented implants, the range of motion was not measured in this study. The peak loads experienced in this cycle were at 5BW which was similar to a study by Van den Bogert et al. who used force plates and found the peak contact load to be 5.2BW (68).

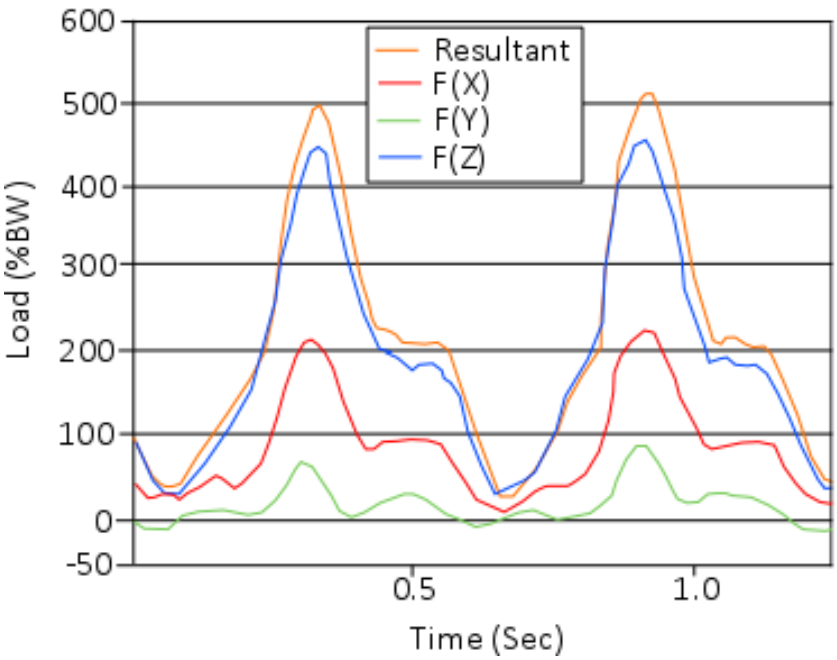


Figure 2.5 – Running gait cycle (adapted from(61)).

Table 2.5 summaries the peak loads and the range of motions experienced in the most common activities (60-62). The range of motion for running was not reported in this study and therefore is not included in the table, however other studies have reported a flexion and extension range of 36^0 / -12^0 (67), calculated using simplified muscle models. The ISO standards is shown for reference (69).

Table 2.5 – The loads experienced and range of motion of an artificial hip for the most common activities (59-62).

Motion	Peak Load (BW %)	Flexion (+) – Extension (-)	Abduction (+) – Adduction (-)	External (+) – Internal Rotation (-)
standing	0.8 – 1			
walking	2.3 - 7.6	27^0 / -7^0	8^0 / -9^0	10^0 / -2^0
running	5.0 - 5.2			
assent	2.5 -7.2	55^0 / -5^0	10^0 / -5^0	28^0 / 12^0
descent	2.6 - 7.1	22^0 / -10^0	11^0 / 0^0	20^0 / 11^0
sitting down	1.6	60^0 / 2^0	18^0 / 8^0	21^0 / 10^0
standing up	1.8	65^0 / 10^0	18^0 / 5^0	18^0 / 8^0
stumbling	8.7	-	-	-
ISO standard	3.4	25^0 / -18^0	7^0 / -4^0	10^0 / -2^0

If possible wear tests should be designed to simulate these loads and motions, which is done in hip simulators for millions of cycles. The ISO standards (69) outlines the loads and range of motion that should be tested in a hip joint simulator. It states a peak load of 3 kN is required which equates to 3.4BW for a man of average height with 28.8 BMI (Body Mass Index) (1, 70, 71), the average of patients undergoing this type of surgery. The forgoing review has shown that this is not representative of the worst case scenarios, particularly those that will be experienced in younger patients or at high velocities.

Sliding speeds vary in the range of 2-49 mm/s dependent upon age (72, 73) and activity; it is also dependent upon height, BW, fitness and terrain.

2.2.5 Physiological Pressures

Whilst it is interesting to understand what activities impart the greatest load and range of motion on these prostheses, ultimately it is contact mechanics that dictate the tribology of the prosthesis. Predicting the Hertzian pressure is complex as this is dependent upon characteristics of the entire tribological system: load, material properties, prosthesis size, radial clearance, anatomical positioning and fixation mechanisms/properties (74). Finite element analysis is used to model the full system (74-78) along with more simplistic ball on plane models (79, 80), which are cheaper to compute. A

summary of the contact pressures and conditions in MoM joints reported in literature are outlined in Table 2.6.

Table 2.6 – Peak contact pressures reported in literature (74-80).

Author	Contact Pressure	Details
Liu et al. (74)	MoM: 47 MPa (Dia – 28 mm, Cl – 120 μm)	FE model Anatomically positioned
	MoM_{HR}: 22 MPa (Dia – 50 mm, Cl – 145 μm)	
Besong et al. (75)	MoM: 31 MPa (Dia – 28 mm, Cl – 60 μm)	FE model Anatomically positioned Only half of cross section modelled due to symmetry
Yew et al. (76)	MoM: 20 – 55 MPa (Dia – 35 mm, Cl – 79 μm)	FE model Anatomically positioned Increased with acetabular cup thickness from 1.5 – 4.5 mm
	MoM: 10 – 30 MPa (Dia – 35 mm, Cl – varied)	FE model Anatomically positioned Decrease in radial clearance from 0.158 – 0.0395 mm decrease the contact pressure
Liu et al. (77)	MoM: 47 MPa (Dia – 28 mm Cl - 60 μm)	FE model Anatomically positioned Acetabular cup with a UHMWPE backing
Liu et al. (78)	MoM_{HR}: 20 MPa (Dia – 54.6 mm, Cl – 50 μm)	FE model Anatomically positioned
Mattei et al. (80)	MoM: ~50 MPa (Dia – 28 mm, Cl – 60 μm)	Ball-on-plane model
Wang et al. (79)	MoM: ~50 MPa (Dia – 28 mm, Cl – 60 μm)	Ball-on-plane model

Finite element analysis maps the location of the maximum contact pressure, this is often found at the edge (74, 76, 77) as illustrated in Figure 2.6 (74).

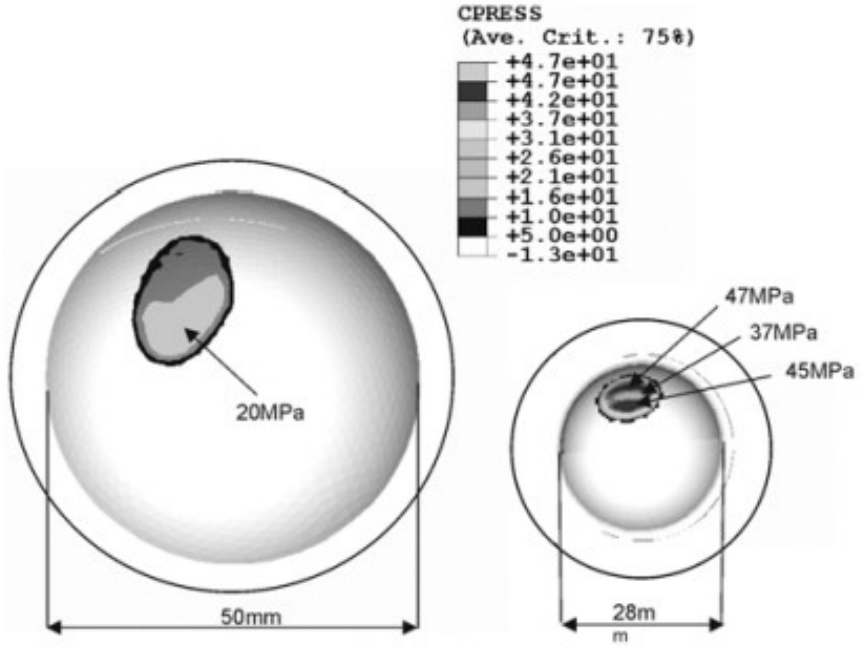


Figure 2.6 – Contact pressure distribution (MPa) at bearing surfaces of a 50 mm diameter hip resurfacing prosthesis and a 28 mm diameter THR (74)

A fixed contact load is often used in these models, stated to be 4-5 BW (3000 – 3200 N) (74, 75); however, Hadley et al. (59) suggests loads could be up to 8.7BW. Additionally the NJR reports the average BMI of patients to be 28.8 (overweight) (1). From this the BW for a man of average height can be calculated to be 88.2 kg (70, 71), which represents 3.4BW.

2.3 Classical Tribology

2.3.1 Lubrication Regimes

Current understanding of implant tribology is derived from classical lubrication knowledge which is briefly reviewed in this section. A lubricant is an important element of many engineering systems where its primary function is to form a separating film between the articulating surfaces which optimises wear and friction. Depending on the lubricant properties and operating conditions the mechanism of film formation may vary, and this is often summarised in the form of a Stribeck curve. This is shown in Figure 2.7 where the coefficient of friction (CoF) is plotted against $\mu v/F_N$ where μ is

the lubricant viscosity, v is the sliding speed of the surfaces and F_N is the normal force. Three regions are shown on the Stribeck curve corresponding to the classical lubrication regimes associated with engineering contacts: full film, mixed and boundary.

Full film lubrication occurs when the articulating surfaces are completely separated by a load carrying film thus there is very little contact between surface asperities. Under these conditions friction is mainly due to shearing of the lubricant film (81, 82). Hydrodynamic lubrication is a form of full fluid lubrication, the articulating surfaces form a shallow wedge causing the relative motion to entrain lubricant and force it to high pressures which are large enough to support external loads. The CoF is influenced by the viscosity of the fluid, the sliding speed and the normal force. There is a drag force associated with the entrained fluid which is dependent on the viscosity. The more viscous the fluid or the higher the sliding speed the larger the drag force and the CoF increases. (83).

Mixed lubrication occurs when the fluid film has reduced due to decreasing speed or increasing load pushing the articulating surfaces together. In the mixed regime the load is partially supported by a fluid film however some of the surface asperities come into contact resulting in increased friction and wear.

Boundary lubrication occurs when the hydrodynamic film thickness is negligible, so the surface asperities come into contact. Under these conditions adsorbed or reacted lubricant additives play an important role in determining friction and wear.

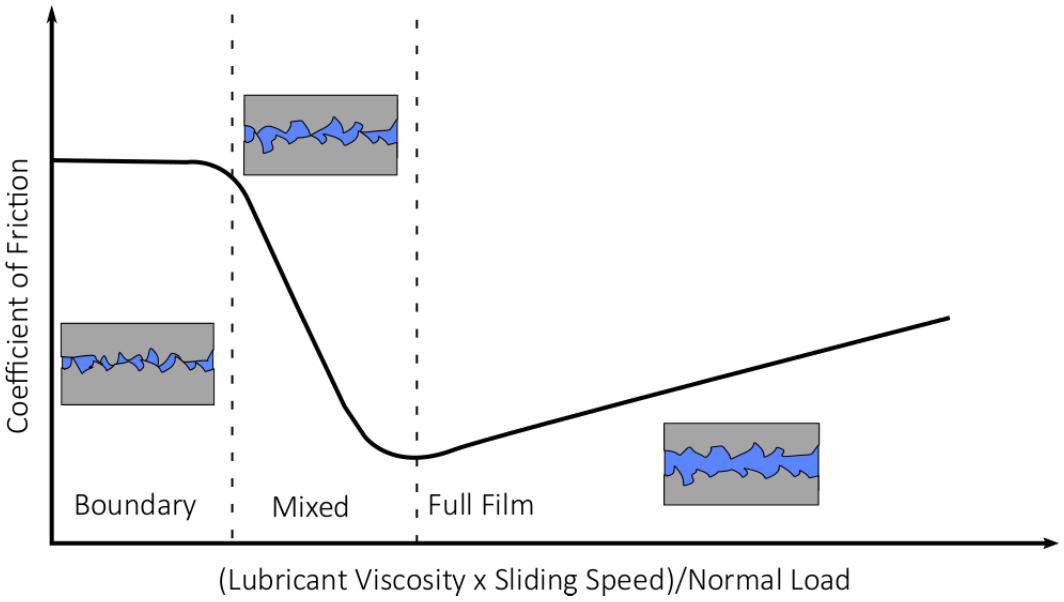


Figure 2.7 - a) Full film b) Mixed c) Boundary lubrication regimes.

The lambda ratio, Λ, is the ratio of the calculated Elastohydrodynamic minimum film thickness, h_{min}, to composite surface roughness (R_a) as shown in Equation 1.1 (84). This dimensionless number can give an indication of the lubrication regime shown in Table 2.7.

$$\Lambda = \frac{h_{min}}{\sqrt{(R_a)^2{}_{head} + (R_a)^2{}_{cup}}} \qquad (1.1)$$

Table 2.7 – Lubrication regimes predicted by lambda ratio (85).

	Lubrication regime
Λ < 1	Boundary
1 < Λ < 3	Mixed
3 < Λ	Full film

2.3.2 Wear Mechanisms

Wear is the damage of a solid body by deformation combined with progressive loss of material due to relative motion with a solid, liquid or gaseous counter body (86-89). Sometimes wear mechanisms are required for smooth operation for example facilitating running-in (3). However loss of material usually has deleterious effects in most engineering systems loss of efficiency (89), durability and reliability (87) with the potential for catastrophic failure. Wear debris can cause contamination of the lubricant, prevention of normal function of the system or increased wear. In non-human applications this can require maintenance and machine downtime, which whilst potentially costly (89) is trivial compared to the consequences in biological applications.

Wear and failure of an artificial joint can be critical causing severe pain and reduction in mobility of a patient often resulting in revision surgery (90). Wear debris can have catastrophic and irreversible effects; polyethylene particles can cause osteolysis (91) bone loss and loosening of the prosthesis. Although the estimated wear of a MoM joint is less than that of a MoP, the particle size is smaller

therefore many more particles are released. CoCrMo metallic particles have been linked to metallosis (5) and necrosis (92) damaging periarticular bone and soft tissue.

There is no single mechanism that can be used to describe wear and often multiple mechanisms are present in a system. They can be divided into two categories, those dominated by the mechanical behaviour of the solids and those dominated by the chemical behaviour of the materials (86) (87).

Mechanical wear is due to a stress interactions which is a combination of loading and frictional forces which can lead to abrasive wear and surface fatigue (Figure 2.8 adapted from (86) (87)).

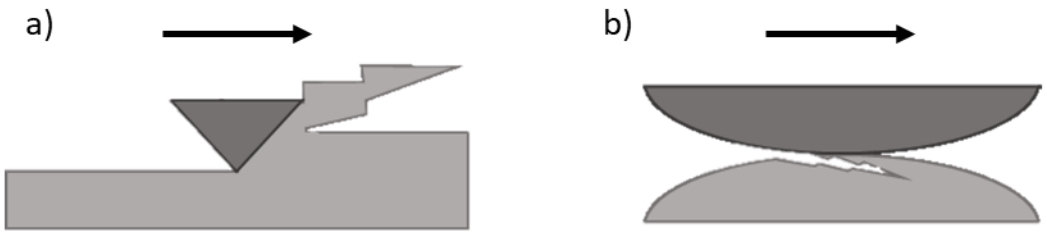


Figure 2.8 - a) Abrasive wear b) Surface fatigue adapted from (86) (87).

Abrasive wear (Figure 2.8a) is the result of micro-ploughing, micro-cutting and micro-cracking (86). It occurs during direct contact between two articulating interfaces when one has considerably harder surface asperities or if hard particles are present in the contact. This can be further categorised into two body or three body abrasion. In two body abrasion one of the articulating surfaces has harder surface asperities or embedded particles (88). When in contact these are forced into the softer surfaces causing plastic deformation, during articulating the harder material removes the softer material (86). In three body abrasion hard particles are trapped in the contact between the two bodies but are free the move with respect to the two surfaces (3). A schematic of these three mechanisms are shown in Figure 2.9.



Figure 2.9 – Two body abrasion a) Hard surface asperities b) Hard particles embedded into surface c) Third body abrasion (adapted from (87)).

Surface fatigue (Figure 2.8b) is the result of repeated stress cycles in a contact which leads to microstructural changes (86). This manifests itself as crack formation, crack growth and particle detachment causing generation of wear debris (88). This mechanism particularly takes effect in a rolling contact; however, during sliding asperities also undergo cyclic stressing. The wear process only starts after a prolonged number of cycles (86) (87).

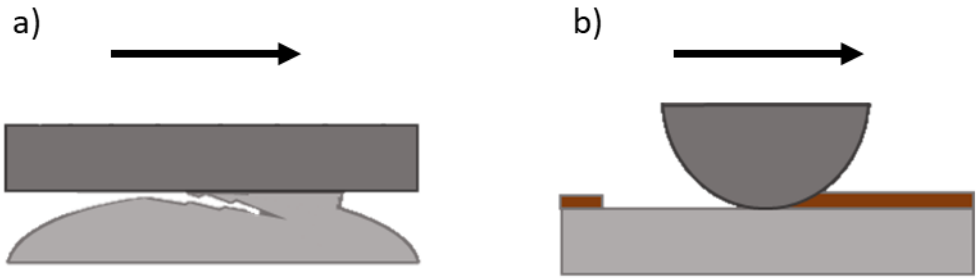


Figure 2.10 - a) Adhesion wear b) Tribo-chemical wear adapted from (86) (87).

Adhesive wear (Figure 2.10a) occurs in the contact interface when the adhesion between the two bodies is stronger than that of the atomic bonds in one of the solid bodies causing resistance in relative motion (88). Under compression and shearing plastic deformation takes place initiating a crack which then propagates under tensile and shearing. When the crack fully runs across the interface the wear particle is adhesively transferred to the opposing surface (87).

Tribo-chemical or corrosive wear (Figure 2.10b) occurs when one or both of the two surfaces chemically react with the lubricant or environment (88). Chemical reaction products adhere to the surface (87), this layer is then removed as the two surfaces pass before reformation of the chemical layer occurs resulting in a continuous cycle of material loss (86, 88). Lubrication factors that contribute to corrosive wear in hip joints include temperature (93), pH (94), SF composition (95), electrolytes (96) and oxygen content (97).

2.4 SF Chemistry and Properties

The hip is a synovial joint which consists of a femoral head and acetabular cup covered in a layer of articular cartilage creating a tough, elastic but smooth surface. The joint is enclosed by a stiff and elastic fibrous tissue lined with a synovial membrane forming a capsule. The capsule contains a biological lubricant, SF, produced by the body (39) a schematic of the joint is shown in Figure 2.11.

During arthroplasty the synovial membrane is broken draining the SF out of the joint. After implantation the membrane reattaches itself restoring the function and regenerating SF. Post-implantation SF is called Periprosthetic Fluid (PP) (39).

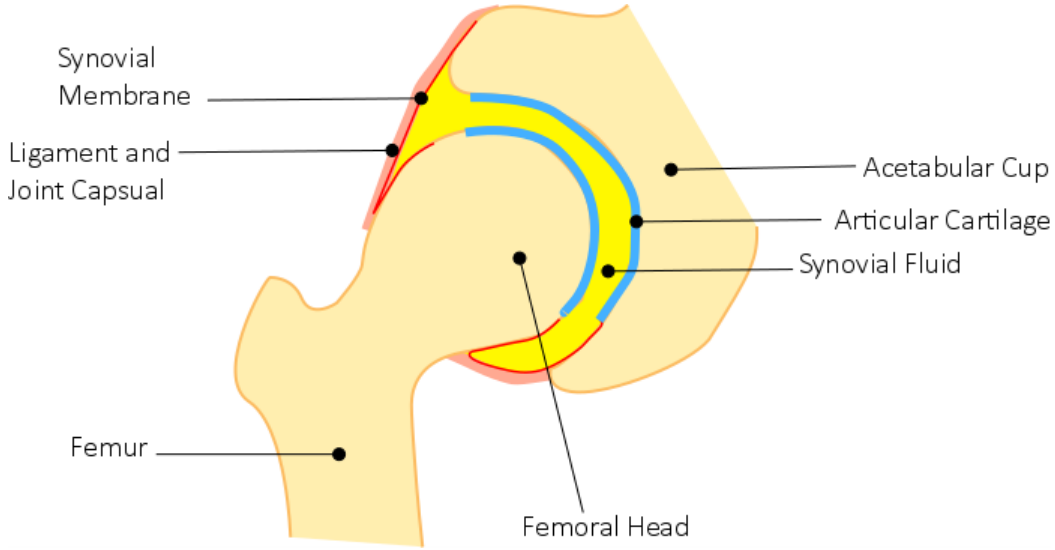


Figure 2.11- Schematic of hip joint. Adapted from (98).

SF is a dialysate of blood plasma filtered by the synovial membrane into the capsule. It comprises of four main constituents: proteins (mainly albumin and γ-G), hyaluronic acid (HA), glycoproteins and phospho/lipids (99). The protein and lipid content of the SF is derived from the blood plasma, although the filtration process reduces the concentration to nearly one third allowing only smaller molecules to pass into the capsule (100). Hyaluronic acid and glycoproteins are produced by the cells in the synovial membrane (98). Lubricin is a highly purified glycoprotein and is considered the primary boundary lubricant of articular cartilage (101). Cytokines, collagen, enzymes, proteoglycans, phospholipids and fibronectin are also present in small amounts in healthy SF and at elevated levels in diseased joints (102). The composition (concentration and albumin/γ-G (A/G) ratio) and pH of healthy, OA, Rheumatoid Arthritis (RA) and PP SF is summarised in Table 2.8. Bovine calf serum diluted to 25% w/w (25BCS) is the most commonly used screening fluid and therefore the chemical composition is shown for reference.

Table 2.8 - Healthy and diseased SF composition and pH (35, 37-41, 103, 104).

	Albumin	γ-G	A/G	Lubricin	Phospholipid	HA	pH
Healthy (H)	7-18	0.5-2.4	2.9-36.0	0.05-0.35	0.13-0.15	0.35-4.22	7.3-7.4
Periprosthetic (PP)	20–39	4.6 – 15.4	1.3-8.5		0.5-1	2.7-4.1	7.5-8.5
Osteoarthritis (OA)	17.8-18.5	12.9-13.4	1.3-1.4	0.05-0.35	0.26-0.98	1.06-3.48	7.4-8.1
Rheumatoid Arthritis (RA)	18.6-28.0	4.8-23.5	0.8-5.8		0.26-0.98	0.19-3.74	6.6-7.6
25BCS	8.75	5.5	1.6		0.80	0	7.0-8.1

SF has non-Newtonian flow properties; shear rates up to 10^3 s^{-1} Healthy SF exhibits shear thinning rheology where the viscosity decreases under strain (105). Figure 2.12a plots the upper and lower boundaries of viscosity plotted against shear rate for H, OA and RA pathologies up to 10^3 s^{-1} (106). At shear rates between ~5000 – 30,000 s^{-1} viscosity has been reported to be within the Newtonian regime (107). Other studies have shown shear rates of HSF to be rheopectic (Figure 2.12b), which is defined as an increasing stress with a function of time at a constant shear rate, it was concluded that this was due to protein aggregation (36). Previous work in our group have reported the appearance of high viscosity phase in the inlet region which is attributed to protein aggregation in model SF (108-112).

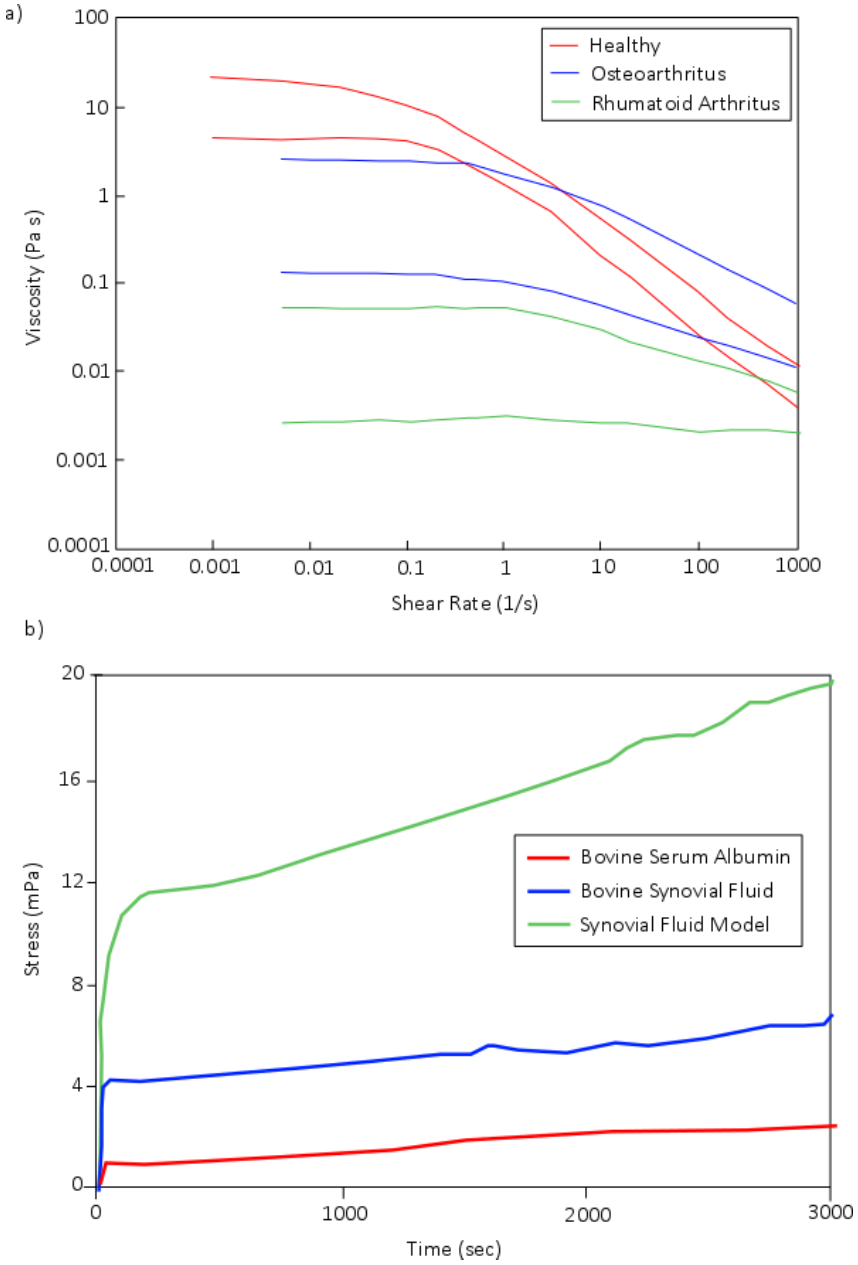


Figure 2.12 –a) Upper and lower bounds of viscosity vs shear rate for H, OA and RA pathologies. Adapted from (39, 106) b) Stress vs time for a shear rate of 0.05 s^{-1} for BSA, bovine SF and model SF (18 mg/ml protein concentration A/G =1.6). Adapted from (36).

Schurz et al. (106) reported that in OA and RA fluids the viscosity was significantly reduced when compared to healthy SF. The viscosity at zero shear rate for H, OA and RA SF, was in the range of 1-40, 0.1-1 and 0.004 – 0.07 Pa s. This was attributed to a decrease in the HA concentration and molecular weight (39). Studies on primary and revision joint replacements are limited; however, they indicate that PP fluids show further reductions in viscosity and HA concentration (113).

2.4.1 Proteins

Proteins are highly complex macromolecules with unique three-dimensional arrangements. They are the most abundant and functionally diverse molecules in a living system with almost every life function dependent upon them (114). The proteins in SF are derived from an ultra-filtrate of blood plasma and cells within the joint tissues.

The proteins present in SF have a low molecular weight (Albumin ~66.5 kDa (115), γ-G ~ 150 kDa (116)) any larger proteins are present in insignificant amounts as they have been filtered out as the plasma crosses the synovial membrane (Fibrinogen ~340 kDa (117)). Albumin and γ-G are present in the highest concentrations making up 60-75 % and 15-19 % of the proteins in SF respectively (118).

Albumin is a simple flexible protein synthetized in the liver and comprises of 585 amino acids (119), it has a molecular weight of 66.5 kDa (115). Literature reports that albumin takes different shapes when in solution or crystals. In a solution the shape is described as '*cigar-shaped form of an ellipsoidal of revolution'* of dimensions 14 x 4nm. (120). The structure in crystals is heart shaped with dimensions 3x 3 x 8 nm as seen in Figure 2.13a (121). It was suggested by Peters et al. (120) that the difference could be due to the flexibility of the protein allowing it to take different forms when tightly packed into a crystal or free to flow in a solution.

Globulins are a group of proteins within SF which further divide into four subgroups α_1, α_2, β and γ – G (39), the latter accounts for over half (98). The most significant subclass of γ-G are immunoglobulins, also known as antibodies, type G (IgG). IgG is a large Y shaped molecule, with a molecular weight of approximately 150 kDa. It consists of two sets of identical polypeptide chains called the heavy and light chain weighing approximately 50 k Da and the other 25 k Da respectively. They are bonded by disulphate bonds and are arranged as shown Figure 2.13b. The arms region of the Y shape has a length of 8.9 nm and the upright region has a length of 7.7 nm and width of 4nm (116).

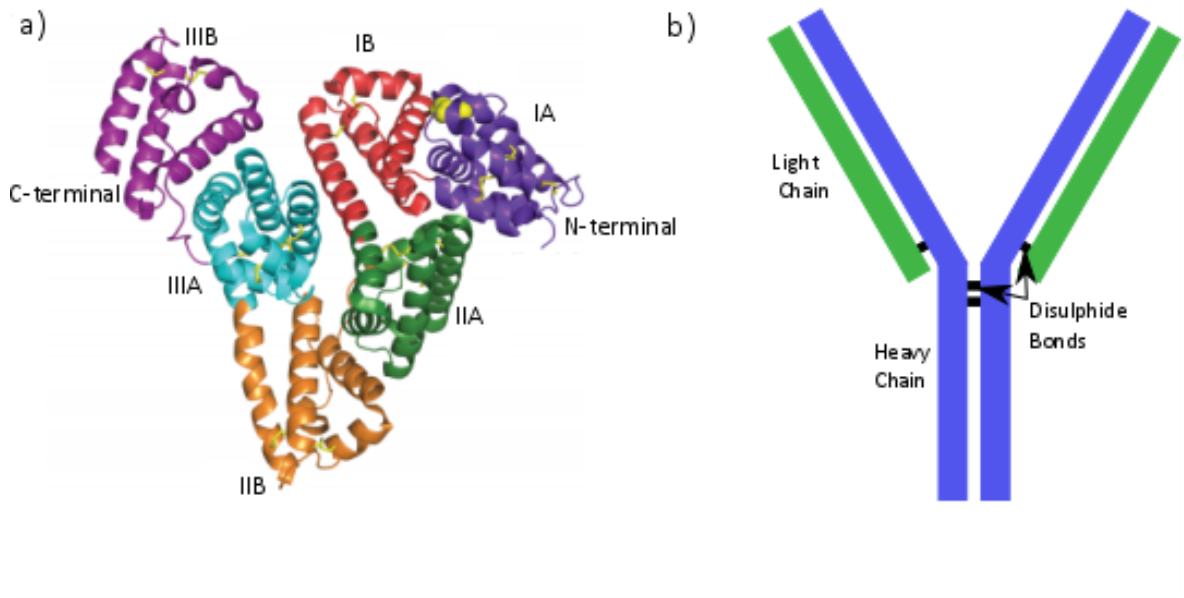


Figure 2.13 - a) Ribbon structure of albumin with the subdomains shown in different colours (adapted from (122)) b) Molecular structure of γ-G (adapted from (98)).

2.4.1.1 Protein Structure

Amino acids are the building blocks of proteins and there are over 300 different types described in nature however only 20 are commonly found in mammals. Each amino acid comprises of a carboxyl group, amino group and a side chain all bonded to the α-carbon (114). The free amino end is called the N-terminal whereas the free carboxyl end is called the C-terminal. A schematic structure of an amino acid is shown in Figure 2.14. These singular amino acids, also named peptides, form polypeptide chains where the carboxyl and amino groups are covalently bonded meaning neither are available for chemical reactions. Therefore it is the side chain that interacts with other molecule and dictates the physiochemical properties and hence the function of the protein such as the shape, hydrophobicity, charge and pH (102) (114).

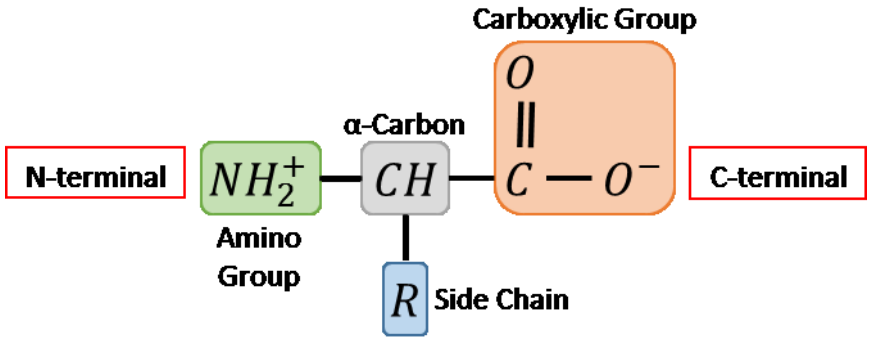


Figure 2.14 - Amino acid structure. Adapted from (114).

Amino acids are joined together by covalent bonds to form polypeptides and the sequence in which they are linked determines the three-dimensional shape. To best explain this, the molecule is analysed in terms of four hierarchical groups of increasing complexity; primary, secondary, tertiary and quaternary and a schematic is shown in Figure 2.15 (114, 123).

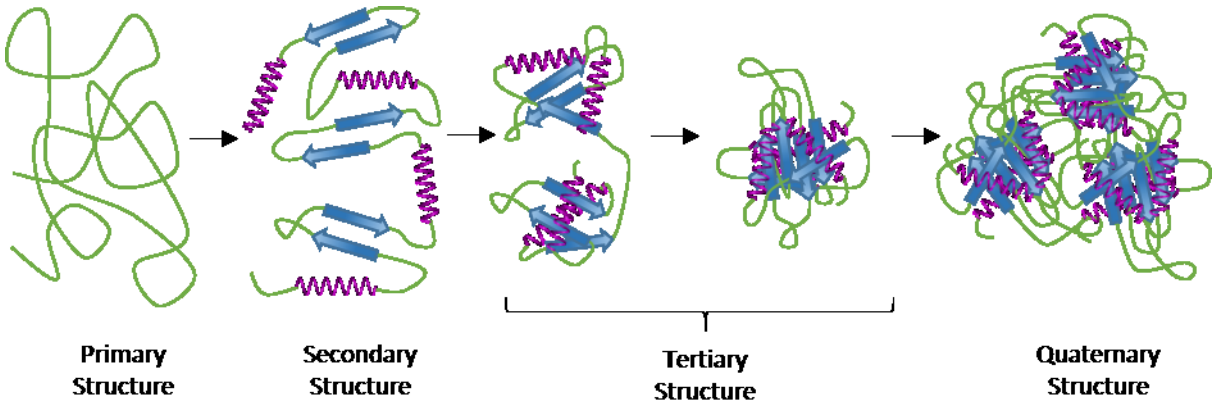


Figure 2.15 – Schematic of the protein structure hierarchy. Adapted from (114).

The primary structure of a protein is the sequence that amino acids are bonded forming the backbone of the molecule (123). Within the chain -C=0 and –N-H are polarized and therefore are able to form hydrogen bonds (114). Other charged groups consist of ionized groups present in the side chain. It is therefore important to understand the primary structure as it is the interactions between these side chains that will dictate how the protein will fold. Abnormalities in the sequence can cause improper folding and loss of normal function which are the root of many genetic diseases (114).

Regions within the polypeptide backbone are organised into regular localised three-dimensional arrangements due to the hydrogen bonding between –C=O and –N-H. This is the secondary structure of the protein (114, 123). Whilst a single hydrogen bond is intrinsically weak, the combined force of multiple bonds acts to stabilise the structure. Common examples include the α-helix, β-sheet and β-turn which are described in more detail below.

The α-helix has a spiral structure, the backbone is tightly packed into a coil stabilised by hydrogen bonds (124, 125). These bonds lay parallel to the spiral and link every fourth amino acid ensuring all but the first and last peptides are linked. The side chains of each amino acid extend outwards from

the central core as not to interfere with each other sterically. Each turn of an α-helix contains 3.6 amino acids (124). A schematic of the structure is shown in Figure 2.16a (125).

Certain amino acids can disrupt the helical shape if either the side chain is not geometrically compatible, or the amino acid is charged causing ionic bonds to form or repel each other.

β-Sheets are composed of two or more separate polypeptide chains, named β-strands, or segments of a polypeptide chain folding back on itself. The surfaces of the sheets appear to be pleated and the stabilising hydrogen bonding act perpendicularly to the backbone. The side chains are perpendicular from the face of the sheet (126). A schematic of this secondary structure is shown in Figure 2.16b (127).

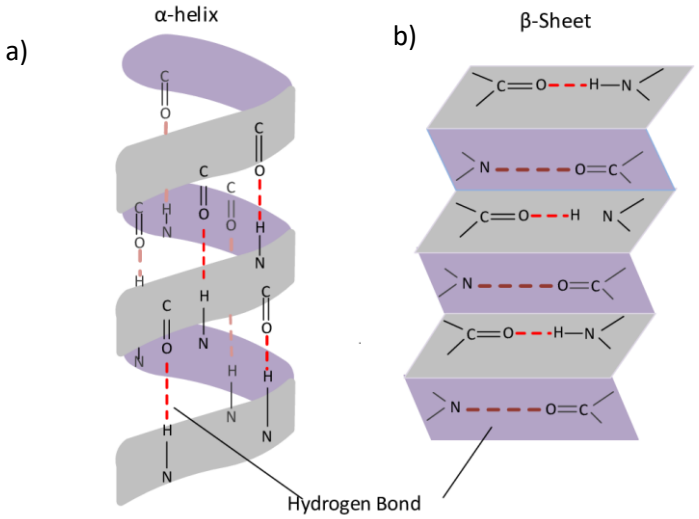


Figure 2.16 - a) α-helix b) β-sheet. (128)

β-sheets can be arranged in either an antiparallel or parallel arrangement (114, 123, 126). In the antiparallel structure the N-terminal and the C-terminal of the β-strands alternate direction whereas in the parallel structure they are orientated in the same direction (114, 123). Diagrams of these are given in Figure 2.17 for both separate and folded peptides where the β-strands are represented as broad arrows with the C-terminal is represented by the pointed end. The antiparallel β-sheet arrangement is more stable and therefore more easily formed as the hydrogen bonds present are less constrained and are in the preferred linear configuration (129).

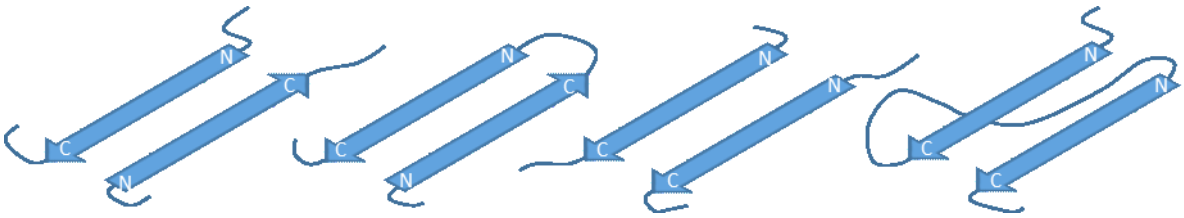


Figure 2.17 –β -sheet configurations a) Antiparallel i) Separate ii) Folded, b) Parallel i) Separate ii) Folded. Adapted from (114).

Whilst roughly a half of a globular protein are arranged into highly ordered structures the remainder of the chain is described as loops and coils. They are not entirely random but have less structure than the α-helix and β-sheet and are described as "unordered". Loops connect the α-helix and β-sheet conformations (114). A loop containing four amino acids is called a β-turn as they are usually found connecting successive antiparallel β-sheets (Figure 2.17aii), reversing the direction of a polypeptide chain, helping globular proteins from. They are stabilised by the formation of hydrogen and ionic bonds (114).

Albumin and γ-G are globular proteins, which are constructed by combining secondary structural elements to produce specific patterns. This forms the core of the molecule connected by loops and turns at the surface of the protein. In aqueous solutions they are closely packed at the core of the molecules. Hydrophobic side chains become hidden in the interior, whereas hydrophilic groups are found on the surface (114).

The tertiary structure of a proteins is its 3-dimensional shape and describes how the polypeptide chain (built from a pattern of secondary structures) fold and interact (130). It will bend and twist to achieve maximum stability or the lowest energy state (114). Disulfide bonds, hydrophobic interactions, hydrogen bonds and ionic interactions all act to stabilise the folding. These interactions occur between the side chains and it is therefore the primary structure that is responsible for the three dimensional structure (114). The quaternary structure is how each of the tertiary structures interact (114).

Proteins easily denature, whereby the secondary and tertiary structures unfold and become disorganised without hydrolysis (i.e. without breakdown of covalent bonds) of the polypeptide backbone. Denaturation can be caused by excessive heat, organic solvents, strong acid or bases, detergents, shear forces or ions of heavy metals (114) (131, 132). Aggregation occurs due to non-native interactions between misfolded proteins, they are often insoluble, precipitate from the solution

and are metabolically stable (133). Denaturation is often reversible once the cause is removed however the aggregation process is irreversible (134).

Denaturing and deposition of SF proteins could occur within the loaded contact and may contribute to the lubrication process. It is one aspect of the SF lubrication mechanism which will be examined in this thesis. Earlier work has suggested that denatured unfolded proteins are more readily absorbed onto a surface which lead to an increase in CoF affecting the boundary lubrication properties (135).

2.4.2 Hyaluronic Acid

Hyaluronic acid is a polysaccharide produced by the synovial lining of the cells, it is polydisperse with a healthy sample having a lower bound and median value molecular weight of 4 MDa and 6-7 MDa respectively (100). It is thought that HA gives SF its characteristic viscosity and in diseased fluids reductions in the MW and concentration results in a lower viscosity (106). The rheological behaviour of SF is heavily influenced by HA (39).

HA concentration has been shown to be a function of age with the highest concentration occurring in the 18-23 age group after which it decreases until the age of 30. Between the ages of 30-80 no changes are observed in healthy joints. This means after the age of 23 the viscosity of the SF will also decrease and this could negatively impact the lubrication and wear properties (136).

2.4.3 Glycoproteins

Glycoproteins are proteins with one or more carbohydrate groups attached (137). There are several types of glycoprotein in SF however lubricin, LGP-1, was found to be the most significant. It is thought to adsorb onto the articular cartilage acting as the boundary lubricant in SF (138). It has also been shown that lubricin prevents excessive accumulation of proteins, cells and other components of the SF at the joint surfaces as well as cartilage-cartilage integration (139). Decreased levels of lubricin are associated with symptoms which relate to arthritic diseases such as joint malformation, decreased joint lubrication and increased cartilage wear (139).

Lubricin is encoded by the gene PRG4 (140) and is composed of 41.5-44.3 % protein and 45.9-55.4 % carbohydrate (141) and 9.2-13 % phospholipid (142). It has a molecular weight of 227 kDa and is relatively monodisperse (138). This glycoprotein is secreted by cells in the synovial membrane and chondrocytes in articular cartilage (140).

During joint arthroplasty the cartilage is removed reducing the amount of lubricin produced and therefore it is not considered to contribute to the lubrication of artificial joints however this does not

affect the concentration of glycoproteins from blood plasma dialysate such as alpha-1-acid glycoprotein (AGP) and alpha-1-antitrypsin (A1AT) (143). Roba et al. (143) investigated how AGP, A1AT and albumin influence the lubrication of a CoP joint. Results show that both glycoproteins enhanced the lubrication by reducing the friction however albumin had the opposite effect. When a mixture of albumin with AGP or A1AT was used the albumin dominated the behaviour giving a response similar to that of pure albumin (143).

2.4.4 Lipids

In SF the lipid content is derived from the blood plasma; however, the concentration is much lower, as the lipids cannot freely move into the synovial cavity (41, 143-145). Phospholipids account for roughly 0.14-0.52 mg/ml (143) (41) of SF, of which 45 % are phosphatidylcholine (PC) (146).

The head of PC is hydrophilic and made of a chlorine, phosphate and glycerol; the tail is hydrophobic and made of two fatty acid chains which may be saturated or unsaturated (contains one or more double bonds between the carbon atoms) as shown in Figure 2.18. It is a zwitterionic lipid, meaning that the hydrophilic head contains both a positive and negative electrical charge but the net charge is neutral (98).

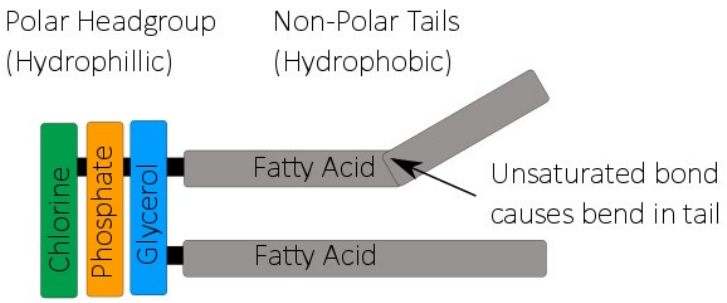


Figure 2.18 - Diagram of typical phosphatidylcholine (PC). Adapted from (146).

Dipalmitoylphosphatidylcholine (DPPC) accounts for 45% of the total lipid content (147), is the most surface active PC (148) and is also thought to contribute to the boundary lubrication of articular cartilage (149). Only recently other PCs (saturated and unsaturated) have been considered (150). Analysis carried out using high performance liquid chromatography (HPLC) identified specific lipid molecules on articular cartilage (151, 152) and artificial joint surfaces (150). A summary of PC's detected on different surfaces is given in Table 3. They are primarily unsaturated and liquid at body temperature and thus more readily absorbed.

Table 3 - PC's found on joint surfaces (150-152).

Lipid	Cartilage (%)	UHMWPE (%)	Metallic (%)
PLPC (unsaturated)	30	28	24
DLPC	23	13	5.5
POPC (unsaturated)	17.5	33	27
SLPC (unsaturated)	16	27	28
DPPC (saturated)	8.3	11	15

There have been numerous studies carried out investigating phospholipids as boundary lubricants (146, 153, 154). This was first proposed by Hardy and Butler (146); they suggested that polysaccharides incorporated in the cartilage provide negative sites to attract hydrophilic zwitterionic heads, hence orientating the hydrophobic fatty acid chains outwards towards the SF (146). However, this is energetically unfavourable; when phospholipids are exposed to an aqueous environment they self- orientate into bilayers (Figure 2.19a). When exposed to water lipid bilayers are formed, weak forces form between their hydrophobic tails protecting them from water and exposing the hydrophilic head (155). This stable conformation exhibits low friction attributed to a layer of water (153). It has been shown by AFM (156) and hip simulator tests (99) that the presence of a lipid bilayer reduces the CoF. A low CoF at the joint surfaces are associated a single or several stable bilayer(s) (156).

Alternate models suggest that these bilayers curve to from a sphere known as a vesicle which can consist of one layer (unilamellar) or several (multilamellar) (155) (Figure 2.19) tightly packed layers that adsorb onto the joint surface. These structures cause the system to have a low CoF due to hydration lubrication of the head groups (153).

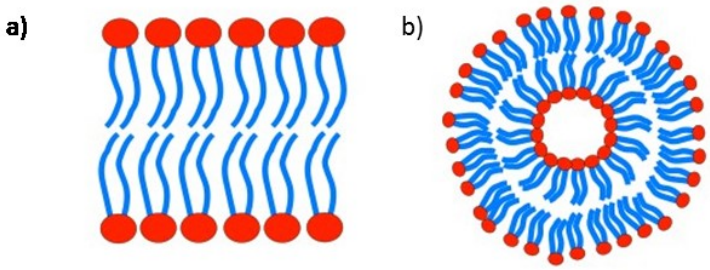


Figure 2.19 - a) Bilayer b) Unilamellar vesicle. Adapted from (98).

2.5 Artificial Joint Tribology

2.5.1 Tribology Related Problems in Hip Joints

After the initial success of MoM implants it became clear from the NJR there was a higher than expected revision rate and therefore by 2016 less than 0.1% and ~1% of procedures used MoM THR and MoM_{HR} respectively (1). Although the leading cause of MoM failure of THR was aseptic loosening, due to wear of the bone over time (44), the production of harmful cobalt and chromium wear debris/ions is a major concern (157) which can lead to cell death and adverse tissue reactions (16).

The linear wear rates of MoM bearing surfaces are reportedly low (157) and in a hip simulator predicted to be up to ~100 fold less than for UHMWPE (158, 159). However, the CoCrMo debris was typically 50 – 116 nm (13-15) in size and thus the number of wear particles increased compared to UHMWPE which has a particle size in the range 0.1 – 8 μm (13, 14, 157, 160). Due to the nm size both ions and particles can be transported around the body in the lymphatic (161, 162) and possibly the vascular system (163, 164). Cobalt and chromium debris/ions have been reported be the cause of local tissue reactions (165). Limited evidence has reported toxicological responses in the following areas of the body: blood, immune system, liver, kidney, respiratory system, nervous system, heart and vascular system, musculoskeletal system, endocrine system, visual and auditory system, skin, reproductive system (157).

2.5.2 Wear of Artificial Hip Joints: Tribology Test Methods

The wear of implant materials are usually evaluated in bench top and joint simulator tests (15, 48, 54, 55, 166-174). Bench-top tests (15, 48, 166-170) focus upon material response to rubbing rather than the joint design factors. The tests have a simple geometric configuration, usually pin-on-disc (166-168), pin-on-plate (15, 169) or pin/flat-on-sphere (48, 170), which simulates in *vivo* contact pressures. The loading (usually constant) and kinematics (unidirectional/bidirectional sliding) are chosen to

provide a simple simulation of implant contact conditions. Wear of the pin or ball after a certain sliding distance and specific number of cycles (15, 48, 167-169) is usually evaluated by simple weight loss (15, 48, 167-169).

Hip joint simulators replicate the complex loading and kinematics experienced in a physiological gait cycle and are used to evaluate the effect of implant design or material combinations (15, 48, 54, 55, 166-174).The standard ISO 14242 specifies the range of movement, the transient load, speeds, duration, sample configuration and environment required for testing the wear of hip prosthesis (69). The test usually achieves millions of cycles before the cumulative wear is measured (54, 59, 171-174). The measurement of wear on either the head or cup components is based on small changes in mass (54, 59, 171-174) or white light interferometry (WLI) (175). This measurement can also be affected by the environmental conditions over the lifetime of the test (54, 59, 171-174) and so often has poor repeatability (59). The joint specimens are usually submerged in Bovine Calf Serum (BCS) which is changed regularly during the test, typically every 5x105 cycles (174). Thus completing a 5 million-cycle test requires very large amounts (~ 5litres) of fluid (54, 172).

2.5.3 Model Fluids for Tribology Tests

Human Synovial Fluid (HSF) is hard to procure and only attainable in small quantities; certainly much less than is required in tribological testing (176). Additionally, ethics approval is required for collection and laboratory work as well as a Bio-Hazard assessment for safe use. Due to these constraints HSF is rarely used. Instead 25BCS is the most commonly used screening fluid (69) as it is readily available in large volumes and relatively inexpensive making it suitable for use in joint simulators. BCS is different from SF in two ways; firstly, it contains the larger molecules/proteins that would usually be filtered by the synovial membrane, secondly molecules produced by the synovial membrane will be absent. Studies have shown that lubrication of SF is not closely replicated by BCS (177-179) and variations are observed between batches of BCS in both friction and wear studies (179).

The protein and lipid composition varies between patients and healthy and diseased joints (37-41, 103, 104). Whilst 25BCS has a similar total protein concentration as healthy SF the specific content is different (35, 37, 39). Osteoarthritic (OA) and Periprosthetic (PP) SF tend to have a higher protein concentration than both healthy SF and 25BCS; therefore, it is questionable that 25BCS is an appropriate substitute lubricant for implant screening.

An alternative approach of using a known concentration of molecules in a physiological solution has been adopted by several researches (36, 37, 98, 99, 111, 156, 180-184), as this allows a more

systematic approach to studying the role of specific protein and lipid concentration. It could also allow lubricants to be tailored to match patient's SF profile to test susceptibility of wear for certain material combinations.

A saline solution is the base of a model SF, it comprises of a salt or combination of salts dissolved in deionised (DI) water to a concentration that is isotonic with tissue fluids or blood. The most basic saline is made of sodium chloride (NaCl) only at a concentration of 154 mM (185). A change in the ionic strength alters the concentration of ions in the solution and will therefore affect the charge on proteins. A higher concentration will act to screen the charges, a lower concentration will cause the charges to become more predominant (186). The distance over which the charge is felt is the Debye Length, whose square is inversely proportional to the ionic strength (187). Changes in ionic charges will effect interactions between molecules (proteins, lipids and HA), protein folding-unfolding and aggregation (186).

In some cases researchers use a buffer which resists change in pH of pure water due to addition of an acid or a base ensuring it remains constant through a test (188). The amino acids, that are the building blocks of proteins, contain ionisable groups. Changes in pH can alter the charge carried affecting molecule interactions and protein conformation. The ionic strength of these solutions are adjusted to physiological levels using NaCl (188). Ringers solution is more complex, representing a more realistic isotonic solution it comprises of NaCl, KCl and $CaCl_2$ whist sodium bicarbonate is used to balance the pH (189).The range of ionic base solutions used in the literature is summarised in Table 2.9.

Table 2.9 – Buffer solutions used to make model SF.

Base	pH	Ionic Strength (mM)	Reference
Distilled/DI Water	5.6-7	0	(111, 156)
Normal Saline	5.8-7.5	150-154	(99, 180, 181)
Phosphate Buffered Saline	7.4	50-154	(36, 37, 182)
HEPES Buffered Saline	7.4	4-10	(183, 184)
Tris Buffered Saline	7.2	154	(156)
Tris Buffer	7.2-8.1	15-33	(37, 156)
Ringers solution	6.4	157	(189)

Once the base solution is made macromolecules can be added to match HSF. Proteins are the most abundant molecule and therefore the most important addition to the model fluid. The other main

constituents DPPC, HA and glycoproteins are added into the model fluid in attempts to further replicate native SF.

2.5.4 SF Lubrication Mechanisms of MoM hips

Three different lubrication mechanisms have been reported in literature:

1. EHL
2. Boundary lubrication
3. Protein aggregation

Evidence of these mechanisms comes from modelling, direct film measurement and analysis of deposits on explanted/tested hip joints and are discussed in more detail below.

2.5.4.1 EHL

The predominant lubrication model for MoM hips is based on classical EHL theory for an iso-viscous fluid (9, 84, 107, 190). In a series of papers Dowson and Jin (9, 84) modelled film thickness over the gait cycle for a range of operating conditions and implant geometries. For varying D_h and Cl it was calculated that this EHL condition was only satisfied for large diameter femoral heads with a small Cl for $R_{a\ head}$ = 10 nm and $R_{a\ cup}$ = 5 nm (Figure 2.20a adapted from (84)). A more sophisticated model used transient loads and speeds to replicate walking conditions to predict the film thickness and is shown in Figure 2.20b (adapted from (9)) (D_H = 28 mm, Cl = 120 μm). This predicts the minimum film thickness to fluctuate throughout the cycle, in the range ~ 0.04 – 0.055 μm and is slightly thicker than the minimum film thickness for static mean conditions, which is shown for reference.

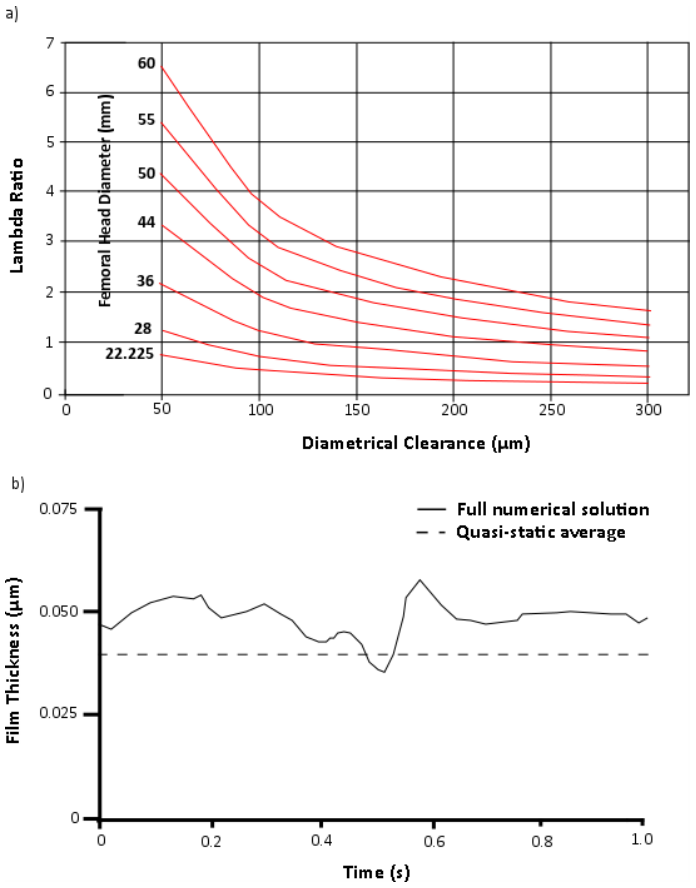


Figure 2.20 – a) Lambda ratio for MoM hip joint prosthesis ($R_{a\ head}$ = 10 nm and $R_{a\ cup}$ = 5 nm) for increasing D_h and Cl (84) b) film thickness using transient loads and speeds. Adapted from (9).

The effect of start-up conditions on film thickness was investigated by Jalali et al. (72). It was predicted that the load and speed did not have an effect on the predicted lubricant thickness and only 2-3 steps were required to establish a steady cyclic variation of the predicted film thickness.

Supporting evidence for the EHL model has come mainly from friction measurements in pendulum tests (191) and measuring surface separation in hip simulator wear tests (171, 192).

Vassiliou et al. (191) measured the friction before during and after wear testing in a hip joint simulator for a MoM_{HR} prosthesis. Initially joints operated in the boundary lubrication regime, however as the number of wear cycles increased a classical Stribeck curve was formed. At 2, 3 and 5 x 10^6 cycles friction results indicated an EHL film had formed for viscosities of 0.1 Pa s. The transition from boundary to the EHL regime was attributed to diminishing surface asperities from running in wear.

Smith et al. (171) used a hip joint simulator to measure the wear (gravimetrically) and surface separation (electrical resistivity) for MoM prosthesis subject to dynamic motion and loading cycles

with 25BCS as the lubricant. Four different femoral head sizes were used: 16, 22.225, 28 and 36 mm. Results showed that for the smaller head sizes (16 and 22.225 mm) surface separation was none existent, indicating boundary lubrication. This correlated to the high mean wear rates (4.85 and 6.30 $mm^3/10^6$ cycles respectively). For the 28 mm femoral head there was limited evidence of surface separation suggesting that this prosthesis operated in the mixed lubrication regime and had a mean wear rate of 1.62 $mm^3/10^6$. Finally, the mean wear rate for the 36 mm femoral head was significantly reduced to 0.07 $mm^3/10^6$ and it was stated that the surfaces were separated for considerable parts of each walking cycle. The surface separation is shown in Figure 2.21; (adapted from (171)), a potential difference of 0 mV indicated components were in contact and increased to a maximum of 50 mV when separated. A closer look at this figure shows that the surfaces are in contact for large periods of time for the physiological walking cycle. Other studies have shown, for a 36 mm femoral head, that surface separation was achieved (measured using electrical resistivity techniques) during the swing phase of the gait cycle and at times under severe conditions in the stance phase for protein based fluids (192).

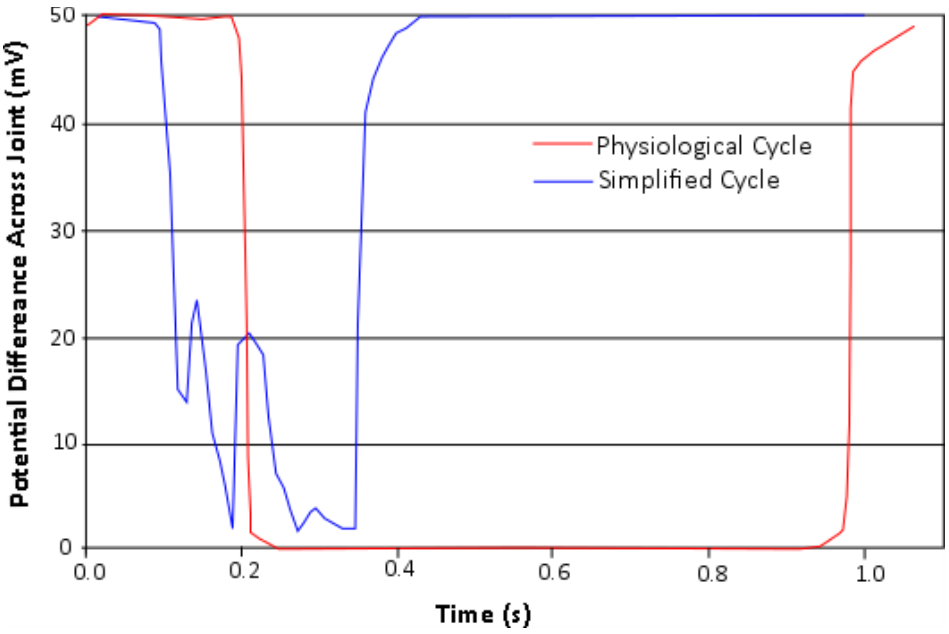


Figure 2.21 – Changes in potential indicating surface separation for a 36 mm femoral head for a simplified and physiological walking cycle. Adapted from (171).

A study by Scholes et al. (193) used a hip simulator to show that when using Carboxyl Methyl Cellulose (CMC), CoC operated under EHL conditions whilst MoM and MoP joints operated in the mixed lubrication regime. These findings correlated well with computational studies. However, when 25BCS was used the full fluid regime in the CoC joint was inhibited due to protein adsorption. The adsorbed protein layer appeared to reduce the friction in MoM joints but increase in CoC and MoP joints. The

use of pooled HSF further decreased the CoF for a MoM and MoP contact, whilst for CoC little difference was observed (194). It was concluded that the lubrication regime differed when a biological lubricant was present, and therefore non-biological lubricants should not be relied upon in the design of orthopaedic bearing surfaces (193, 194).

The EHL model appeared to predict performance and became the driver of MoM design. The influence of model SF composition upon implant wear (particularly MoM), in both simulation tests and *in vivo* is unclear and is rarely studied. In EHL regime lubricant film formation will not be affected by the biochemical properties of SF, such as protein content. The lubricant film thickness is predicted to scale with the high-shear rate viscosity of the fluid (9, 84) and the viscosity is fairly constant over the protein concentration range (195). Therefore, protein concentration will have little effect on predicted EHL film thickness and thus, by implication, wear. As discussed in Section 2.4, the viscosity is dependent upon the HA (39). At shear rates between ~3000 – 5000 s^{-1} it was shown that BCS and SF can be considered Newtonian (107), these results were used in the calculations to predict an EHL lubrication regime (9, 72, 84). However, these shear rates are not representative of physiological conditions (108) where shear thinning prevails. The high shear forces break down HA which is able to recover when the shear is reduced (38). Other studies have shown HA does not have a load bearing ability in the physiological joint (150) and that it does not have a beneficial effect on reducing the wear (196-198).

When early failure of these MoM devices became apparent a study was performed it establish if larger head sizes had an improved survival rates. Data from the NJR analysed, in a paper by Smith (44), 31,171 MoM stemmed prosthesis implanted between 2003 and 2011 (1). It was found that larger femoral heads were associated with high revision rates, it was predicted for every 1 mm increase in head size the risk of revision increased by 2% (44). This study contradicts all predicted calculated using the EHL models and Stribeck curve λ criterion (9, 72, 84).

The question should be asked whether this simple analysis, based on mineral oils, is transferable to biological systems such as artificial joints? The Stribeck curve was developed for journal bearings which operated under steady state loads and speeds; the lubricant was a simple Newtonian hydrocarbon oil. However, an artificial joint is lubricated by a complex multiphase fluid that exhibits shear-thinning operating under transient loads and speeds (39).

2.5.4.2 Boundary Lubrication

In contrast MoP hips are considered to operate in the boundary lubrication regime as the predicted film thickness (~0.125 – 0.25 µm (199)) is smaller than the surface roughness (1 µm (190)). The

articulating surfaces are in contact, therefore the wear is directly related to the sliding distance, thus wear increases for an increase in head size (5, 58).

If the prosthesis operates in the boundary regime the changing protein and lipid content might have an effect on wear (37). Proteins (albumin and γ-G) and lipids are thought to adsorb at the implant surfaces and act as boundary additives (146, 166, 200-203). Thus most studies of the effect of SF chemistry on implant friction and wear have been for UHMWPE components (166, 177, 197, 201, 204, 205).

A study by Roba et al. (143) investigated the ability of glycoproteins alpha-1-acid glycoprotein (AGP) and alpha-1-antitrypsin (A1AT), which are present in HSF, to absorb onto UHMWPE and Al_2O_3 in the presence of bovine serum albumin (BSA). Nanoscale Friction measurements were performed using an AFM, and the deposits were analysed. Results showed that AGP and A1AT had superior lubrication properties when compared to BSA which was attributed to their ability to adsorb via their hydrophobic backbone leaving the hydrophilic carbohydrate chains exposed to the aqueous solution providing a low-shear strength fluid film that lubricated the system. Additionally, the glycoprotein lubricin (LGP-1) has been attributed to be the active lubricating molecule in SF and that it can perform this function in the absence of other constituents. Lubricin binds to the surface and allows a layer of water at the tissue surface (138).

Schwarz et al. (142) isolated lubricin from bovine SF and analysed the lipid content by thin-layer chromatography phosphorus determination. Results revealed a phospholipid content of 11.1 ± 1.7 % and therefore it was proposed that it was the phospholipid responsible for the lubrication of the joints, not lubricin. It is thought that these phospholipids act as a boundary layer and the reduction in friction is due to the long hydrocarbon chains (203). Further studies have shown surface active phospholipids present on retrieved implants and are thought to act as the boundary lubricant. They were found on all bearing surfaces analysed including PE, stainless steel, CoCrMo, alumina, zirconia and titanium (202). Another study identified substantial amounts of different 8 types of PC adsorbed onto retrieved implants including SLPC, POPC, DPPC, PSPC, OSPC, DLPC and PLPC (150).

Conflicting results have been reported to whether this phospholipid containing boundary layer reduce the friction and wear. A hip simulator study by Bell et al. showed that PC phospholipids diluted in gelatine significantly reduced the wear of a UHMWPE/CoCrMo contact when compared to 25BCS (154). A reduction of 99% in the CoF was reported when PC phospholipids where acting as a boundary lubricant in comparison to dry sliding (146). On the other hand in a Trunfio-Sfarghio et al. (206) reported that phospholipids increased the CoF for a reciprocating steel/steel and steel/PE contact.

Phospholipids have been shown to readily adsorb to hydrophilic solids, which become hydrophobic surface active in reducing the surface tension of water. The adsorbed monolayers have been reported to reduce the CoF in the dry state under physiological loading by up to 99% (146).

Other studies have reported thick deposited films which are most often attributed to denatured proteins (48, 112, 207-210). They are thought to act as a solid lubricant and be protect the articulating surfaces from wear (170) of MoM implants. These have been found in both in *vitro* (48 , 112, 170, 208-211)and *vivo* conditions (170). Parkes et al. showed that a higher pH (which is found with diseased fluids) the rate of adsorption of proteins decreased and reduced the likelihood of protein aggregation and agglomeration (98).

Pourzal et al. (212) presented experimental evidence of the formation of "graphitised" carbon films which they suggested acted as the primary lubricant preventing wear and reducing friction. The surface analysis was performed on a series of explanted metal-metal hips joints and graphitised surface layers were found in 80% of the implants.

2.5.4.3 Protein Aggregation

Work in our group has identified an alternate type of lubrication mechanism based on protein-aggregation effects (110-112, 200, 213). In this work film thickness measurements with BCS fluids and solutions containing BSA and γ-G were made for a glass/CoCrMo head contact under pure sliding. Optical interferometry was implemented to measure the central film thickness and visualise the contact zone.

During shear proteins are thought to aggregate to form viscous, insoluble gels which can be entrained into the contact zone forming a separating film which reduces wear. The mechanism of shear denaturing and deposition contributes to the formation of a compacted, solid protein film (up to 20 nm thick) in the rubbed contact, which continues to separate the surfaces when motion has stopped (37, 108). This film is augmented by a much thicker, transient film that appeared to be a high-viscosity gel which was sporadically entrained into the contact creating larger than expected lubricating films (112). The type (albumin/γ-G) and concentration of proteins is thought to determine viscous gel formation and hence both lubricant film thickness/deposits and wear reduction (111, 200, 213). Figure 2.22 shows the interferogram of the contact zone showing the high viscosity inlet and bulk phase (200).

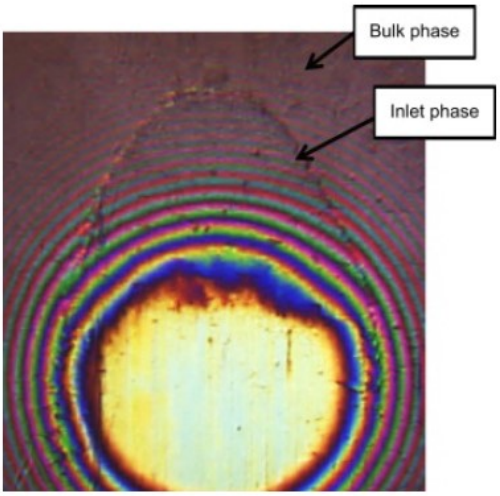


Figure 2.22 – Sliding contact showing viscous inlet phase (200).

Other researchers have provided evidence to support this mechanism using a ball on disc tribometer (198, 209, 214-217). Initial testing was performed by Vrbka and co-workers; instead of pure sliding, experiments were performed under pure rolling and a Slide-Roll-Ratio (SRR) of 1.5 and -1.5. Additionally, both glass/CoCrMo and glass/Al_2O_3 were used. Thicker films were formed on CoCrMo in comparison to Al_2O_3 (215). It was shown that the film formation was dependent upon the wettability of the rubbing surfaces, a chromium layer on the glass disc is hydrophobic which allows adsorption of proteins and therefore thick lubricating films were produced in comparison to a hydrophilic silica layer (216). Protein aggregation was not observed for a conformal contact in this set up (216).

The role of albumin and γ-G in protein aggregation in the presence of each other was assessed using the same ball on disc tribometer. Colorimetric interferometry was combined with fluorescent microscopy to tag albumin or γ-G; an Albumin/γ-G (A/G) ratio of 2:1 was used which is representative of healthy SF. It was found for a glass/CrCoMo contact that under pure rolling and positive sliding the film thickness was formed predominantly due to albumin. Under negative sliding the film thickness was strongly dependent upon sliding distance and at high speeds only the increase in film thickness was due to γ-G. Thick films in the inlet were attributed to aggregated proteins (209). For a glass/ceramic contact the film thickness from protein aggregation was attributed to albumin for pure rolling, positive sliding and negative sliding. However, γ-G had a great affinity to adsorb onto the rubbing surfaces. It was therefore suggested that γ-G formed a thin boundary layer which allowed thick albumin deposits to adsorb on top (217).

Further tests used the colorimetric interferometry with a pendulum hip simulator joint (198, 214) to allow the effects of real joint geometry and joint kinematics on film formation to be studied. It was found that the measured film thickness was considerably higher that what is predicted from film thickness estimations (9, 72, 84). This was attributed to protein aggregation and adsorption (214). These results showed the most important geometrical parameter to enhance tribological performance was the diametric clearance; a decrease from 318 to 40 µm on a 28 mm head increased the film thickness potentially protecting the surfaces. The femoral head diameter was not thought to be as critical (198).

2.5.5 Wear Mechanisms of CoCrMo Interfaces

The motion of the joint can be defined as reciprocating sliding wear as the contact area is smaller than the stroke length (170), therefore it is possible that all four major wear (abrasion, surface fatigue, adhesion and tribochemical reactions mechanisms will contribute to surface damage (48).

Wear mechanisms are usually identified by imaging the wear surfaces post-test. The main form of material loss is commonly attributed to abrasion due to the presence of grooves and scratches (52, 218, 219) and surface fatigue (48). However, understanding the initiating wear mechanism is challenging as it this will not be visible from the wear surfaces post-test.

It is widely accepted that abrasion is likely to be induced from foreign particles such as fractured carbides compacted wear debris or plastically deformed parts of the metal matrix (48). Wimmer et al. (48) suggested that the initiating wear particle could be produced in one of two ways. The first is that tribo-chemical reactions cause an oxide layer to form which begins to spall off once it has reached a critical thickness. The second mechanism suggests that a wear particle is generated by cyclic contact stresses. The interface between carbides inclusions and the metal matrix is weak (48) and therefore it is possible generation of wear particles from the cyclic stress is mainly torn off protruding carbide inclusions (48).

Further evidence of this was shown by Fan et al. (110, 112). The study used optical interferometry with a CoCrMo femoral head/glass contact to measure the film thickness, the femoral head was imaged prior to testing and revealed characteristic ‘blocky carbide’ structures across the surface. Surface typography revealed that they protruded out of the surface by 80 – 100 nm and typical had the dimensions 40 x 15 µm. After articulation of the femoral head and glass disc, the wear scar on the femoral head appeared smooth with almost complete loss of the carbide structures within a few minutes of the start of sliding suggesting that they have been removed from the metallic surface.

Assuming that the normal loads are not carried by the fluid, the generated particles come into contact with the articulating surfaces. Depending upon the particle size they may become dislodged into one of the surfaces. Articulation causes adhesion as the particle cuts and ploughs into the counter-surface creating scratches and grooves (48). Alternately the particles roll and cause surface fatigue by indenting the surfaces (220). The carbides present in the CoCrMo matrix have a micro hardness of 1170 – 1300 $HV_{0.05}$ and 434 ± 30 $HV_{0.05}$ respectively, therefore these hard torn off carbide fragments accelerate the wear of the softer metal matrix (48).

A study by Chan et al. (52) reported that during the first 1 million cycles the wear rate was elevated (run-in wear); this was followed by lower steady-state wear rate values. The accelerated run-in wear was attributed to both abrasion and adhesion, it was suggested that the steady state region was reached once a constant surface roughness was obtained.

Surfaces are protected from adhesion by tribochemical reactions that instantaneously cover the CoCrMo surface with a thin metal-oxide film of around 10-30 nm (221, 222). It is possible that high plastic deformation close to the surface could crack this oxide layer bringing about adhesion (221, 222), however a study by Wimmer et al. (48) reported no signs of adhesion despite the fact that the system is a self-mating MoM contact. In addition several *in vitro* studies have reported a solid film deposited on the surfaces which is thought to be due to denatured proteins that provides protection against adhesion and hinders surface fatigue (48, 52, 112, 207-210). Importantly these deposits have also been found *in vivo* (170).

In conclusion the loss of material in the MoM contact can usually be attributed to the mechanical wear mechanisms: abrasion and surface fatigue. Simultaneously tribochemical reactions generated from denatured proteins and/or oxide films have been reported to rigidly adhere to parts of the surface thus helping to reduce the wear.

2.6 Conclusions

The foregoing review has explored the tribology of artificial hip joints; including implant design and materials, gait and loading patterns and SF lubrication and wear. From the tribology perspective the problem is extremely complex because of the following:

1. Hip joint gait: transient loading and speed patterns with cross shear motion.
2. Lubricant: periprosthetic fluid which has a complex rheology and chemistry containing proteins, lipids and HA. Patient chemistry can vary depending on pathology.

3. Wear of bearing surfaces: can determine implant life and the requirement for revision operation.
4. Lubrication mechanisms: various film formation mechanisms have been suggested including EHL, boundary and protein-aggregation.
5. The effect of patient SF chemistry on lubricant film formation and wear has not been established.
6. Tribology test methods: usually use 25BCS as a screening fluid for wear tests, however this has a different specific protein profile compared to HSF
7. HSF is rarely used as it is only available in small quantities.

Initially MoM hips appear to solve the problem of limited MoP implant life. The LHMoM joints were predicted to operate in the full film λ>3 regime (223) and thus experience minimal wear. However, the very high failure rates have shown this prediction, which was based on classical EHL theory, to be flawed. Despite this, for some patients, these joints have worked well and this might be explained by the SF chemistry. The review has highlighted the need for more detailed understanding of the effect of patient SF chemistry on film formation and implant wear and this is the focus of the research. Key questions in for project were:

1. Is 25BCS an acceptable substitute for HSF in wear tests?
2. Are the lubrication and wear mechanisms the same for model and human SF?
3. Does SF chemistry (model, BCS, human) affect lubrication and wear?
4. What are the properties of lubricant films formed during wear tests?
5. Do some patient pathologies have an increased risk of wear and failure with CoCrMo?

To investigate these questions the research project comprised of the following:

1. Development of small-scale wear test for CoCrMo which used a very small fluid volume suitable for HSF samples.
2. Measurement of CoCrMo friction and wear for a range of model and human SF samples
3. Examination of the surface deposits formed during wear tests using optical microscopy and Scanning Electron Microscopy (SEM)
4. Analysis of the organic composition of deposited films using micro-IRRAS
5. Visualisation of protein denaturing during wear tests using ThT fluorescence.

Chapter 3 Development of a Small Scale Wear Test

Summary

The aim of this Chapter was to develop a robust and reliable wear test for implant materials with HSF using the High Frequency Reciprocating Rig (HFRR). The main requirement is that the test must use low volumes of lubricant (~ 1-2 ml) as HSF is only available in small amounts. The test uses a ball-on-disc configuration with a reciprocating motion. CoF was recorded throughout the test and average depth and volume of the wear scars on the disc were evaluated afterwards using a WLI. During the test development phase the effects of lubricant volume, protein concentration and the oxygen partial pressure were investigated. BCS at varying concentrations is used as the lubricant and CoCrMo couples are used as the test specimens.

3.1 Introduction

One of the problems hindering implant development is the lack of data on HSF wear with different materials. HSF is rarely available and only attainable in small quantities certainly much less than volumes required for joint simulator tests which typically require many litres of fluid over an extended time period (~5 litres) (54, 172). Volumes used in pin-on-disc/plate wear tests require at least 10 ml and in some cases as much as 250 ml (154, 166, 169), which is much lower but not close enough to volumes required. Pin-on-disk/plate bench tests usually have a low Hertzian contact area compared to stroke length which allows partial replenishment of the lubricant, if the contact area is similar to or larger than the stroke length, starvation of the lubricant may occur (190). It was shown that contact areas above a critical value resulted in starvation causing increased surface damage (224).

A small misalignment of as little as 0.5^0 in a pin-on-disk test for a hard on hard contact has been shown to have increased predicted contact pressures that may lead to scatter in wear data (225).

To test HSF a bench test that uses low volumes of fluid is required, however when using low volumes of fluid evaporation of test fluid is a concern (226) and therefore the test length should be minimised. A short time period means that the distance travelled during articulation will be much shorter than that reported in literature (15, 168, 227) and therefore the test should use a high frequency of

articulation and a long stroke length as to maximise this. Additionally, it should have a high contact area/stroke length ratio.

Cross-shear occurs in full hip joint motion (228) and can be replicated in hip simulators through complex loading and gait patterns (59) but absent in the majority of bench tests which provide uni-directional (pin-on-disk) (166-168) or bi-directional (pin-on-plate) (15, 169) motion. The importance of cross-shear in determining the wear of UHMWPE is well known (229), but is unclear for MoM joints.

Hadley (59) in her review of MoM hip simulator studies noted that the wear rate measured in *vitro* were often much lower than in *vivo* and suggested this was due to the continuous nature of the simulator motion rather than active and inactive periods typical of human behaviour. The increase of wear in *vivo* was attributed to the collapse of the EHL film at zero speed so that minimal surface protection was present due to inactivity. In her PhD Hadley (59) reported the development of simulator test profiles which incorporated a period of stance (stop-dwell-motion) under load which was found to increase the wear due to a collapse of the EHL film. The HFRR introduces a "stop" for each stroke and as such a collapse of the EHL film occurs before re-entering into the cavity and potentially provides a more severe wear condition compared to continuous motion tests. This stop-dwell-motion is present in bi-directional tests provided by the halt at each end of the stroke where the speed returns to zero before changing direction.

The use of MoM implants has reduced to less than 0.1% since 2014 (1) due to due adverse tissue reactions attributed to an increase in metal ions and wear debris. However, studies have shown that some MoM prosthesis are extremely successful with a with a known revision rate of 1.5% since 1998 (34). In some cases misalignment of the femoral head and acetabular cup resulting in edge loading has been reported (16, 32) as the cause; another possible reason for this could be the SF chemistry, which has not been widely studied.

The test conditions in *vitro* should be matched to in *vivo* as closely as possible, some parameters such as temperature are easily attainable where set-ups are heated to 37^0C (230). The sliding speeds in a hip joint varies from 2 - 49 mm/s (73), which can easily be replicated in a hip simulator (231), however for bench tests this is more complex. For uni-directional sliding the speed during the test is constant (apart from starting and stopping) (166-168) whereas bi-directional sliding varies from zero at turn around to a maximum (15, 169) at the centre of the stroke length, therefore by carefully selecting the stroke length and frequency the speed can cover the full range of speeds experienced in *vivo*. The reported sliding speeds for hip simulators and bench top tests are in the range of 20 – 50 mm/s and 10 – 100 mm/s respectively (232).

The reported contact pressures in both hip simulators and bench tests using a CoCrMo-CoCrMo couple are in the range 14 - 60 MPa and 2.4 – 370 MPa (169, 232). Contact pressures in *vivo* have been extensively studied and vary dependent upon materials, for MoM prosthesis it has been reported in the range 10 – 50 MPa (74, 78, 233, 234).

Table 3.1 summarises these physiological parameters.

Table 3.1 – Physiological conditions in a MoM hip joint.

Temperature	37^0C
Sliding Speed	2 – 49 mm/s
Contact Pressure	10 – 50 MPa

Volumetric wear is most often measured by means of a simple gravimetric measurement in both hip simulator (59, 171, 173, 174) and bench top tests (15, 48, 167-169). Alternate methods include mapping the surface typography using WLI (175).

Cleaning and fluid transfer are an additional consideration for the design of a wear test with HSF. All surfaces will have to follow protocol in accordance with ethics and health and safety and no sharps can be used to transfer fluids.

The forgoing review has highlighted that there is no single test suitable for the testing of HSF. Therefore, the overall aim of this chapter was to develop a reliable test to measure friction and wear using small volumes of fluid (< 3ml), as this would allow for some repeat testing of samples from a single patient. Physiological conditions should be replicated and procedures must use cleanable or disposable materials and equipment to allow testing with human fluids.

3.2 Experimental Programme

The overall aim was to design a reliable test to measure the friction and wear of implant materials for future use of HSF. The model SF BCS was used at a range of concentrations, although 25BCS is implemented as the reference fluid. The objectives of this chapter are as follows:

1. Develop a simple bench tests to study friction and wear of implant materials. The test should:
    a. Simulate physiological conditions of contact pressure, sliding speed, fluid temperature.
    b. Provide a high number of rubbing cycles in a short time period.
    c. Use very small fluid volumes (<3 ml) without being affected by evaporation loss.

d. The lubricant bath and specimen holder must be easy to clean/sterilise and be easy to assemble to reduce health and safety issues when using human samples.

2. Investigate the effect of fluid volume and protein concentration on friction and wear of CoCrMo couples.
3. Investigate the effect of the oxygen partial pressure in the lubricant.

3.3 Materials and Methods

3.3.1 The High Frequency Reciprocating Rig (HFRR)

A High Frequency Reciprocating Rig (HFRR), (PCS Instruments PLC; London) was used to measure the friction and wear properties of model SF's. As the fluid bath could be easily modified to use small volumes of lubricant. A schematic of the experimental set up is shown in Figure 3.1. The upper specimen consists of a CoCrMo ball oscillating against a stationary lower specimen (CoCrMo disc) using an electromagnetic vibrator. The upper specimen is loaded via a dead weight and a test fluid is injected into the lower specimen holder to lubricate the contact. The contact is subject to bidirectional reciprocation but no cross-shear, which occurs in full hip joint motion (228). The frequency of reciprocation and stroke length are controlled by a computer in the ranges 10-200 Hz and 20 µm – 2 mm respectively. A plate beneath the lower specimen can be used to heat the test up to 60 ^{0}C so that tests can be performed at above ambient temperature.

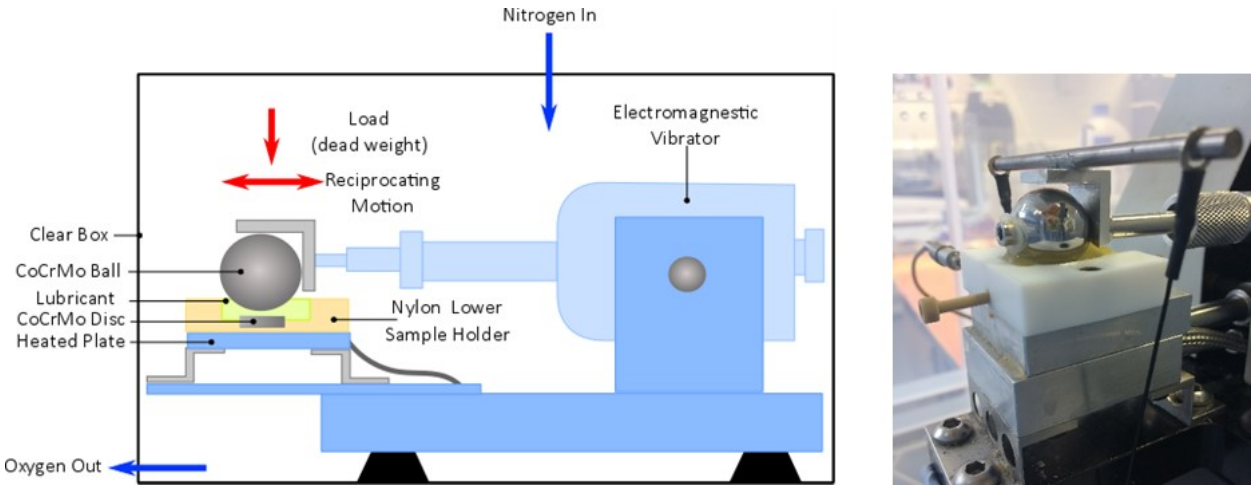


Figure 3.1 - A schematic of the HFRR (left) and a photograph of the loaded ball and fluid bath (right).

3.3.2 Material Selection

Metallic artificial joint materials made from Cobalt-28 Chromium-6 Molybdenum alloy (ASTM F75-12). The standard outlines a comprehensive list of material properties including the composition which comprises of Co (base), Cr (27-30 %), Mo (5 -7 %) and Ni (max 0.5%) (235). This alloy composition was originally based upon Stellite®21 (236) which is readily available and therefore it was chosen for the ball and disc test specimens due to the closeness in material composition. Stellite®21 is manufactured (as cast) by Deloro Stellite and comprises of Co (base), Cr (26-29 %), Mo (4.5-6 %), C (0.20-0.35 %) and Ni (2-3 %) (236). The surface roughness (R_a) of the disc and ball were measured by WLI to be 9.12 ± 1.9 nm and 39.6 ± 1.5 nm respectively. Important material properties of Cobalt-28 Chromium-6 Molybdenum and Stellite®21 are shown in Table 3.2. The microstructure on the disc is observed using optical interferometry in Figure 3.2.

Table 3.2 – Young's Modulus and Poisson's Ratio of ASTM F75-12 and Stellite 21 (46, 50, 59, 236).

	Cobalt-28 Chromium-6 Molybdenum	Stellite®21
Young's Modulus (GPa)	230	250
Poisson's Ratio, ν	0.3	0.3
Hardness (HRC)	25 – 35	27 – 40
Density (g/cm^3)	8.28	8.33

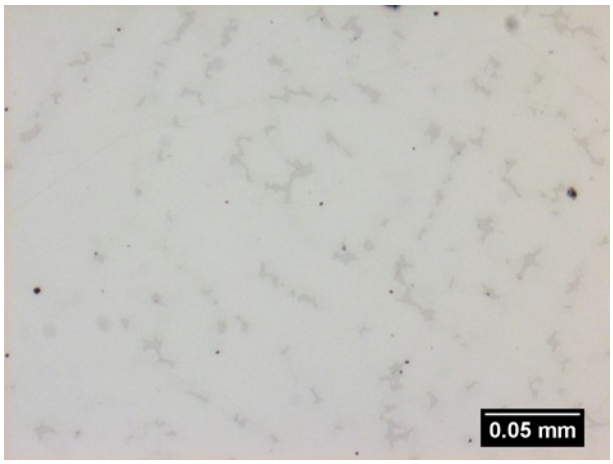


Figure 3.2 – Microstructure of Stellite 21 from disc specimen.

3.3.3 Test Fluids

BCS (Sigma Aldrich Poole, UK12133C sterile-filtered) was used as the reference test fluid. On receipt the 500ml sample was divided into 7 ml aliquots and then refrozen and stored at -40°C. An aliquot

was removed the day before testing, defrosted overnight in a refrigerator and then diluted with Deionised (DI) water to the required (10, 25, 50 or 100%) concentration before testing. The pH of all test fluids was 7.9.

3.3.4 Test Condition Considerations

In this section the contact pressure, speed of articulation, temperature and the partial pressure of oxygen in the test set-up are matched as closely as possible to in *vivo* conditions.

3.3.4.1 Pressure and Contact Area

Using the original set up the Hertzian contact pressures are much higher than those experienced physiologically.

It was important to match the contact pressure in the rig as closely as possible to what is experienced in real life. Assuming a point contact the mean and max contact pressure can be calculated using equation 3.2 and 3.3 respectively where F is the load and a is the semi contact width calculated using equation 3.4 (46).

$$p_{mean} = \frac{F}{\pi a^2} \tag{3.2}$$

$$p_{max} = \frac{3}{2} p_{mean} \tag{3.3}$$

$$a = \left(\frac{3Fr^*}{4E^*}\right)^{\frac{1}{3}} \tag{3.4}$$

The relative radius, r^*, and effective Young's modulus, E^*, can be calculated using equations 3.5 and 3.6. Bodies 1 and 2 have radius of curvature r_1 and r_2 and Young's modulus E_1 and E_2.

$$\frac{1}{r^*} = \frac{1}{r_1} + \frac{1}{r_2} \tag{3.5}$$

$$\frac{1}{E^*} = \frac{1-\nu^2}{E_1} + \frac{1-\nu^2}{E_2} \tag{3.6}$$

For the case of a ball on flat, as in the experimental set up, the relative radius of curvature is that of the curved body. For an artificial hip the convex (femoral head) surface is given a positive geometry and concave (acetabular cup) a negative geometry.

The maximum contact pressure in a hip joint arises when the surfaces are least conformal, i.e. a small femoral head with a large diametrical clearance (Cl). The contact pressures in a MoM range from 20 – 55 MPa (74-80).

The standard HFRR set up uses a 6 mm ball articulating against a flat disc, 19.05 mm balls were also readily available. The lowest useable force was 1N, the mean and maximum pressure for these two balls are shown in Table 3.3.

Table 3.3 - Mean and maximum contact pressures and the contact area for two ball sizes on a flat contact.

Ball diameter (mm)	p_{mean} (MPa)	p_{max} (MPa)	Contact area (mm^2)
6	467	700	2.1 (26.1 µm)
19.05	216	384	4.6 (38.4 µm)

The increase in ball size reduced the mean Hertzian pressure from 467 MPa to 216 MPa, this is higher than that experienced in the joint however the contact pressure will decrease as the contact area increases due to wear. Additionally edge loading provides a severe case and contact pressures have been reported to more than an order of magnitude higher (237).

3.3.4.2 Stroke Length, Frequency and Speed

The average sliding speed ranges form 2 – 49.0 mm/s (73). The sliding speed in the test setup is dependent upon the frequency of articulation and the stroke length. It was important to keep the stroke larger than the contact diameter to avoid starvation (190, 224) and therefore 1 mm was chosen. A frequency of 20 Hz was chosen so the sliding speed varies from 0 (at the end of the stroke) to approximately 40 mm/s.

3.3.4.3 Temperature

The temperature of the inside of the human body is 37^0C (230) and proteins start to thermally denature at temperatures above 40^0C, (114). Therefore, the temperature during testing should be at 37^0C, but care should be taken to ensure it never exceeds 40^0C.

3.3.4.4 Partial Pressure of Oxygen

The oxygen pressure in the human body is ⅛ to ½ of the normal atmospheric pressure (238) and the pressure in SF has extensively been reported in literature (239-241). The averages are summarised in Table 3.4.

Table 3.4 - Oxygen partial pressure in HSF.

Average Oxygen Partial Pressure in SF (mm Hg)	% of atmospheric
31.7 ± 20.0 (239)	19.3 ± 12.6
29.4 ± 11.2 (240)	16.6 ± 12.1
42.3 ± 20.2 (241)	26.6 ± 12.7

Therefore, the HFRR rig was placed into a sealed box and nitrogen was purged into the box. As oxygen is heavier than nitrogen a hole was cut at the bottom to allow oxygen to exit. Calculations were done iteratively using equation 3.7 to obtain the pressure of oxygen each minute in a 20 minute purge. Here p_n is the partial pressure at n minutes, the atmospheric partial pressure of oxygen (159.6 Hg mm) was used as p_0. V is the volume of the box and $\dot{V}$ is the volumetric flow rate.

$$p_n = p_{n-1} - \left(p_{n-1} - \frac{V}{\dot{V}}\right) \qquad (3.7)$$

Figure 3.3 shows the calculated partial pressure over time for three different flow rates (3, 5 and 7 L/min); the actual partial pressure was measured (GOX 100T Greisinger) for the flow rate 5 L/min. 5 L/min was initially chosen as this was a little below the desired range to account for losses. The oxygen content in this environment was recorded over the 20 minutes and then converted to partial pressures in Hg mm. For this flow rate the partial pressure did not decrease as quickly as the calculated values; however, it fell within the desired range, therefore a flow rate of 5 L/min was chosen for the initial purge followed by 1 L/min for the duration of the test.

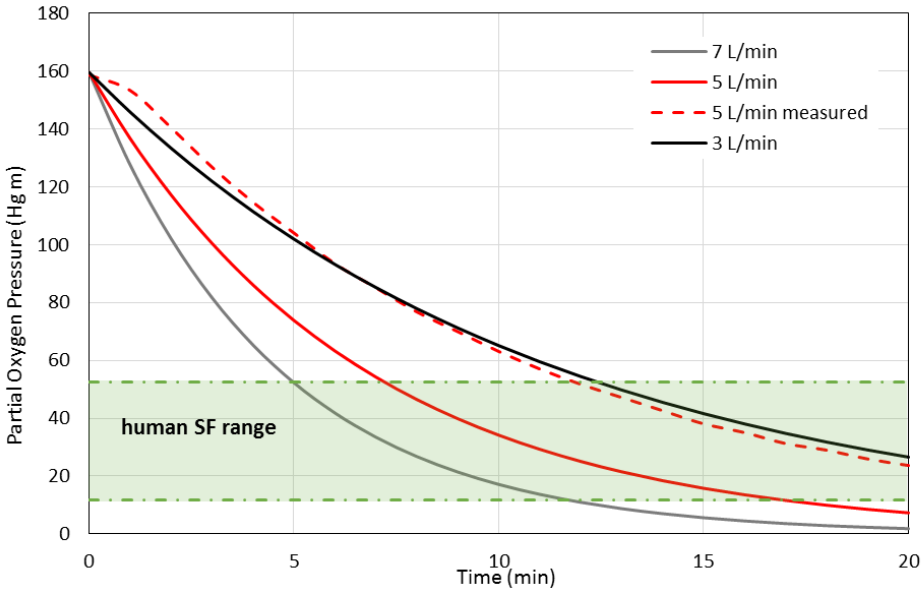


Figure 3.3 - Oxygen partial pressure over time for nitrogen purging.

3.3.5 Redesign of Ball and Fluid Holders

To accommodate the increased ball size a new upper specimen holder was required, and the machine had to be rebalanced. Figure 3.4 shows the original and modified upper specimen holder.



Figure 3.4 - Left: modified lower specimen holder, Right: Original lower specimen holder.

Currently the volume of fluid required to immerse the contact is larger than the volumes of HSF that can be collected from patients (< 3 ml). A new lower specimen holder was manufactured to reduce the volume of the recess, it was made from Teflon to avoid metal contamination of the test fluid. Figure 3.5 shows the original and modified sample holders. Both the new (left) and old (right) specimen holder are shown in Figure 3.5.

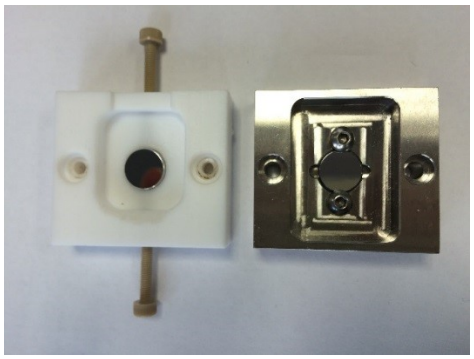


Figure 3.5 - Left: Modified upper specimen holder Right: Original upper specimen holder.

3.3.6 Friction and Wear Tests

Before testing the metal specimens were cleaned in 1% detergent solution and rinsed (3 times) in distilled water. The specimens were then stored under isopropanol. Just before testing they were air-dried and cleaned in an oxygen plasma (Diener) which removes organic contamination and leaves a hydrophilic surface (242).

The 19.05 mm CoCrMo ball was loaded and reciprocated against the disc to simulate joint articulation. A frequency of 20Hz and stroke length of 1mm were used. A load of 1N was used, this gives a mean Hertz pressure of 216 MPa. The test was run for 1 hour and were repeated a minimum of 3 tests per condition.

The temperature was set at 35^0C, 1.5^0C below body temperature, this is because Teflon has a low heat conductivity but high heat capacity causing a thermal lag triggering an overshoot of the fluid bath temperature. The thermocouple in the Teflon block will not be the same temperature as the heating thermal couple causing a temperature fluctuation of $\pm 1.5^0$C; therefore, the test temperature was maintained below 37^0C to avoid proteins denaturing from high temperatures. An additional thermocouple was used to monitor the fluid temperature. Details of the test conditions are shown in Table 3.5.

Table 3.5 – HFRR test conditions.

Test Length (hr)	1 (+ 20 mins pre heat)
Number of Wear Cycles	72000
Ball and Disc specimen Material	CoCrMo
Disc Dimensions (mm)	Diameter – 10, Depth - 3
Ball Dimensions (mm)	Diameter 19.05
Normal Load (g)	100
Mean Hertzian Pressure (M Pa)	216
Temperature (^{0}C)	35
Pre-test flow rate (L/min)	5
Test flow rate (L/min)	1

The contact is immersed in a small volume (1-2ml) of SF. The depth of fluid above the sample was approximately ~5 mm for the 2 ml volume. A lightweight cover placed over the fluid bath was used to reduce evaporation during the test. The test device was housed in a plastic box which ensured a stable temperature environment as one of the practical challenges was to establish an equilibrium temperature without significant loss of the fluid through evaporation. The ball and disc were assembled, and the fluid bath heated to the desired temperature. Once this was reached the test fluid was introduced. The box was then purged with N_2 for 20 minutes to reduce the atmospheric oxygen content to physiological levels (24 mm Hg, GOX 100T Greisinger) (239, 241). The disadvantage of this method was that it extended the total test time and the continued flow of gas also contributed to increased evaporation.

Friction was recorded throughout the test and the average CoF was obtained from the outputted data. At the end of the test the samples were drained of excess fluid. The fluid pH was measured by narrow range litmus paper (pH 6.5 – 10 VWR MColorHast) at the start and end of the test. This method was chosen as it only requires a very small amount of fluid and there are no cleaning/decontamination issues when using HSF.

3.3.7 Validation of Test Protocol

An initial series of tests were run to validate the test design; this included the effect of fluid volume, the effect pf protein concentration and the effect of extended test time/N_2 purge.

3.3.7.1 Effect of Fluid Volume

As HSF was only available in very small quantities (< 5 ml max) it was therefore advantageous to use smaller volumes to allow for repeat tests, however it was unknown the effect of volume on friction and wear. This was investigated using the reference lubricant 25BCS. Volumes were increased in 0.5 ml increments from 0.5-2ml and the friction and wear was recorded and compared.

3.3.7.2 Effect of Protein Concentration

The protein concentration in SF varies significantly between patients and is significantly higher in diseased fluids than in healthy. Therefore, the effect of protein (BCS) concentration was investigated by performing tests using both 1 and 2ml of 10%, 25%, 50% and 100% w/w BCS. The friction and wear were recorded and compared.

3.3.7.3 Effect of Extended Test Time/N_2 Purge

The test procedure outlined above purges the test environment with nitrogen to reduce the oxygen partial pressure. The disadvantage of this method was it extended the total test time and the continued flow of gas also contributed to increase evaporation. The effect of this was investigated by running tests without the purge but heating for the 20 minutes and omitting the 20 minute delay but running the test once the fluid was introduced (Table 3.6). The friction and wear were recorded and compared.

Table 3.6 – Test protocols for testing effect of evaporation during nitrogen purge.

	40 minutes before test	20 minutes before test	During test
Nitrogen	Heat to 35^0C End: Introduce fluid	Purge Nitrogen @ 5L/min Temperature @ 35^0C	Purge Nitrogen @ 1L/min Temperature @ 35^0C
20 Minute hold	Heat to 35^0C End: Introduce fluid	Temperature @ 35^0C	Temperature @ 35^0C
Final		Heat to 35^0C End: Introduce fluid	Temperature @ 35^0C

Once the test was complete both ball and disc were removed from the test set up and the remaining fluid was retrieved and frozen for future analysis. The ball and disc were lightly rinsed with DI water for 10 s to remove excess fluid. Once fully dried, surfaces were observed using a low power optical microscope (Axioscope, Zeiss; Germany) connected to an Infinity 2 (Lumenera Corporation; Ottawa); this will be reported in Chapter 5.

3.3.8 Wear Scar Analysis

White light interferometry is a non-contact optical method for measuring 3-D-profiles of rough or smooth surfaces (243). The light is collimated from the source and split into two beams by a beam splitter; one that reflects off the object being measured and the second off a reference mirror. They are then recombined at the beam splitter and are captured by a CCD camera. As the beams recombine the matrix of point wavelengths will either interfere in either constructive or unconstructive manner and each wavelength is assigned an intensity value. If the two beams have the same path length they will interfere constructively and be assigned a high intensity value, having different path length means a lower intensity value. Only the reference arm or the objective arm is moved relative to the beam splitter, so interferences are formed pixel by pixel when the object depth is scanned. To determine which object points are at the same height the images from the camera are compiled, analysed and the topographical structure of the sample is digitalised

WLI was used to measure the depth of the wear scar formed on the disc during frictional tests. WLI images were obtained using a Wyko NT9100 (Veeco; New York) with a 20x magnification objective. On each disc multiple images were taken and stitched together to enable the full length of the wear scar to be visualised an example of this is shown in Figure 3.6a. Two possible methods of wear analysis were investigated. The first of which was the wear depth; readings at 30%, 50% and 70% along the length of the scar were taken and averaged (Average Wear Depth, AWD). The section and locations of these are also shown in Figure 3.6b. The second was taking the entire wear volume using analysis directly from the software (Average Wear Volume; AWV). Before scans were performed any surface deposits on the discs were removed by soaking in 2% detergent solution followed by rinsing with water and isopropanol.

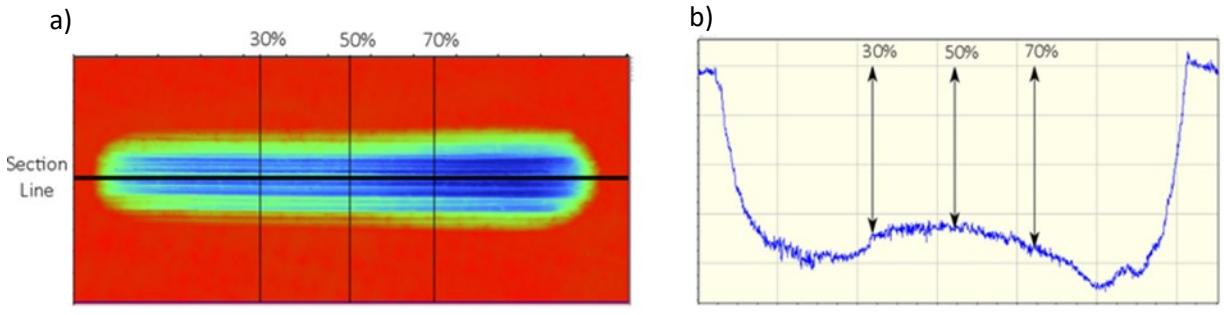


Figure 3.6 – a) WLI contour map showing section line and regions AWD were measured b) Sectioned region of wear scar and places where AWD is measured.

3.3.9 Determining Test Repeatability

It is important that the test is repeatable as only small volumes of HSF are available and repeat testing may not be possible. Therefore the repeatability of both AWD and AWV was assessed using the Coefficient of Variation (CoV) (Eq 3.8) a ratio between the standard deviation, σ, and the mean, μ, shown as a percentage (244).

$$CoV = \frac{\sigma}{\mu} x\ 100 \qquad (3.8)$$

The CoV is a measure of the dispersion of data points about the mean. It is a dimensionless number, independent of the unit in which it was measured, and therefore comparisons can be made between data sets with different units and a large range of means. In this case it is used to assess the repeatability of the test and investigate which measurement, AWD or AWV , is the most reliable (244).

3.4 Results

The aim of this chapter was to develop an extended wear test which only requires a small volume of fluid. To validate this method a series of tests were run investigating the effect of different factors on repeatability of the wear results.

3.4.1 Effect of Volume on CoF and AWD

Figure 3.7 shows example friction traces for 25 BCS at each volume. All volumes of BCS fluids gave a low, stable friction traces over the test period, typically the COF was in the range μ = 0.190-0.280. Figure 3.8 shows the average friction for the four volumes investigated; although variation is small, a clear increase in CoF is observed for increasing volume. The error bars show the standard deviation of the results, which will be continued where possible throughout this thesis.

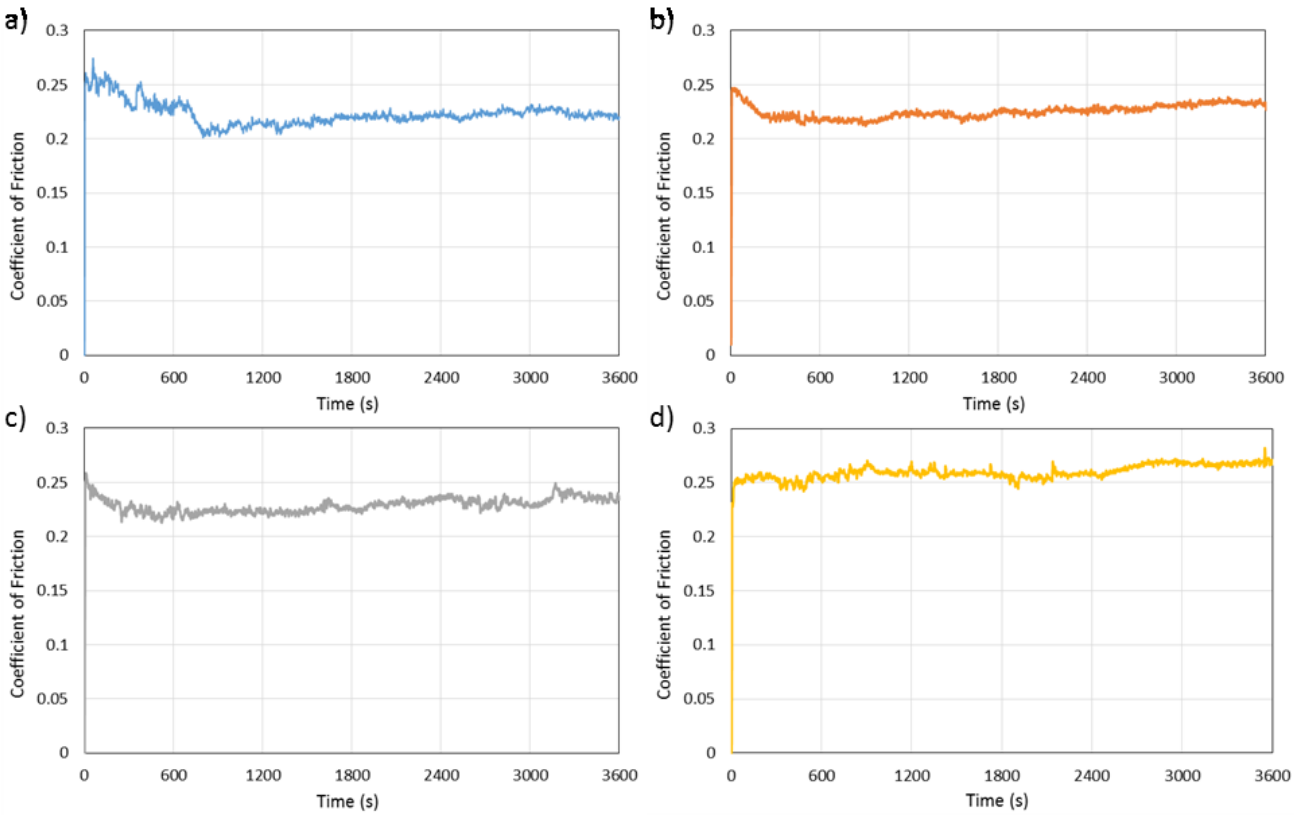


Figure 3.7 - Example of a CoF traces for 25% w/w BCS for a) 0.5 ml b) 1 ml c) 1.5 ml d) 2 ml.

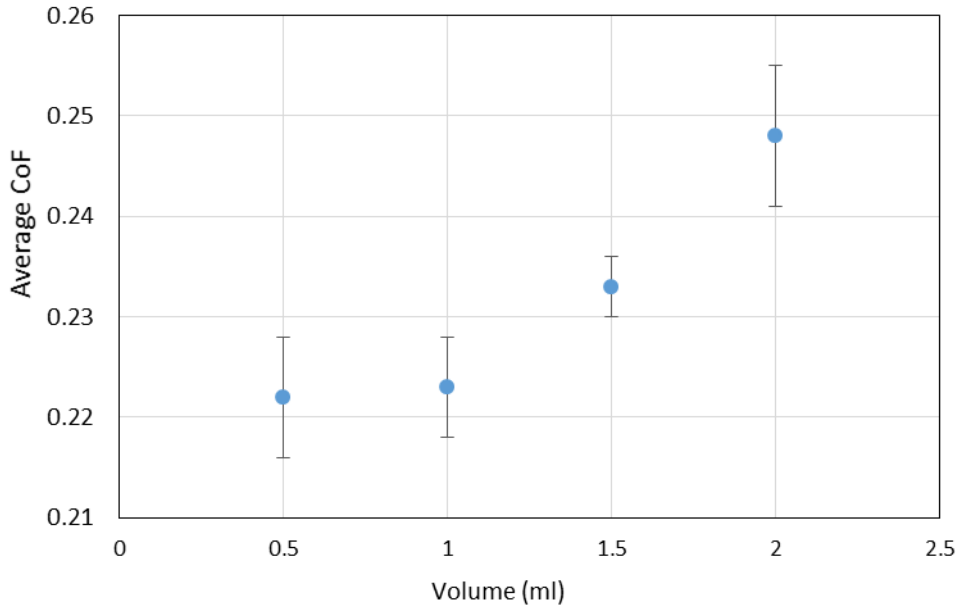


Figure 3.8 - Average CoF vs fluid volume.

WLI images of typical wear scars for each of the fluid volumes tested are given in Figure 3.9 and examples of the wear scar width and length are shown in Figure 3.10 and Figure 3.11 respectively. From 0.5-1.5 ml the wear scars become narrower (~ 160 to 50 µm) and shallower (~ -0.25 to -0.10 µm) however the 2ml wear is much wider (~ 240 µm) and deeper (~ 0.65 µm). This result is reflected in the AWD and AWV measurements as seen in Figure 3.12. For volumes less than 1.5 ml wear was found to decrease with increasing volume whereas the 2ml sample did not follow this trend and exhibited unexpectedly large amounts of wear.

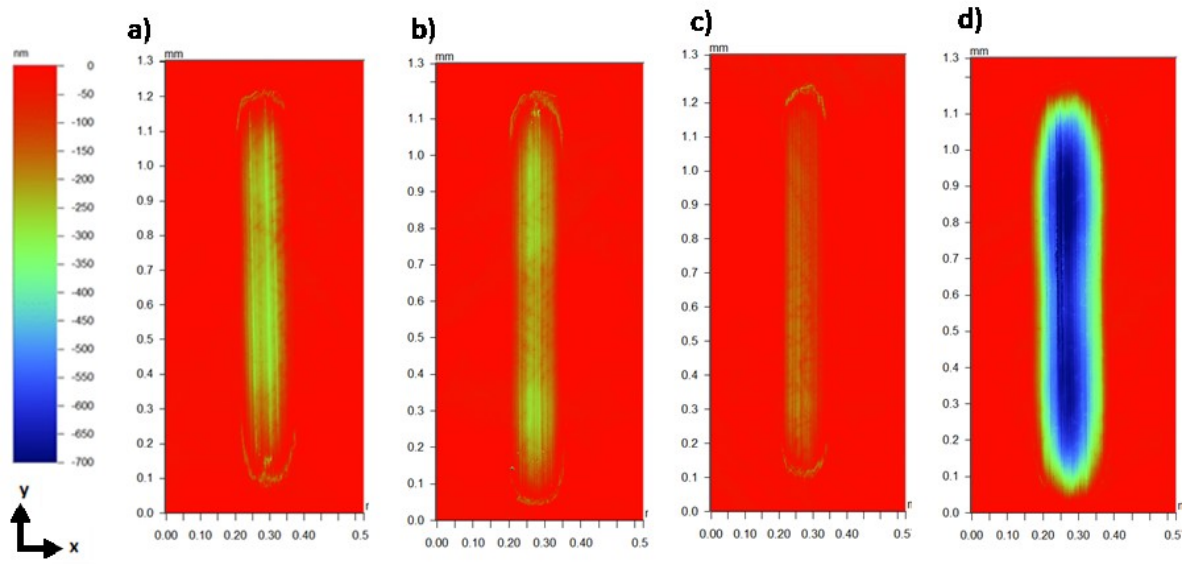


Figure 3.9 - WLI wear scar images for a) 0.5, b) 1.0, c) 1.5 and d) 2 ml.

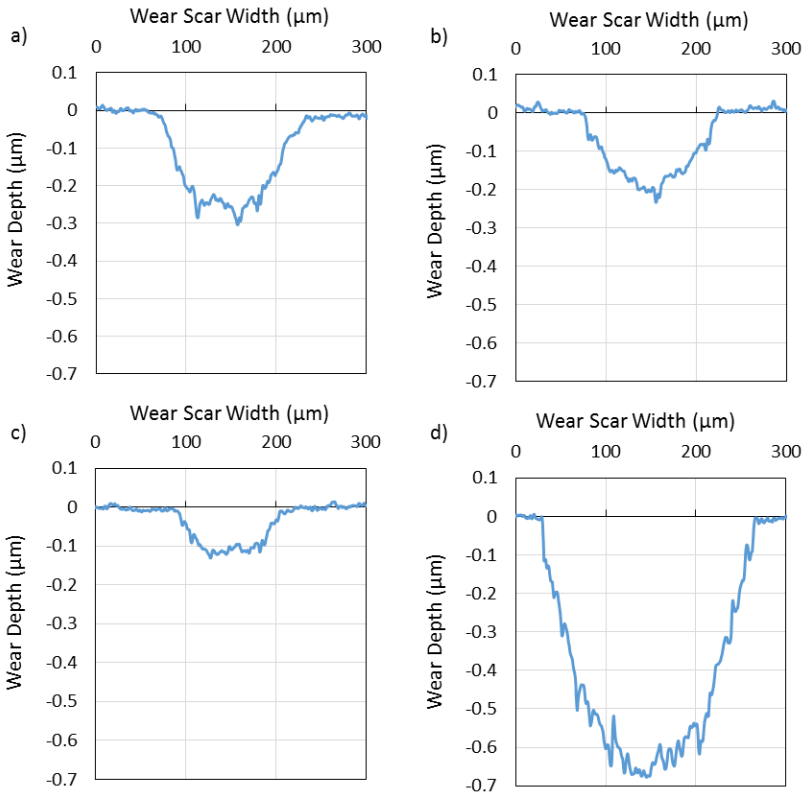


Figure 3.10 - Example profiles of wear scar width a) 0.5 ml b) 1 ml c) 1.5 ml d) 2 ml.

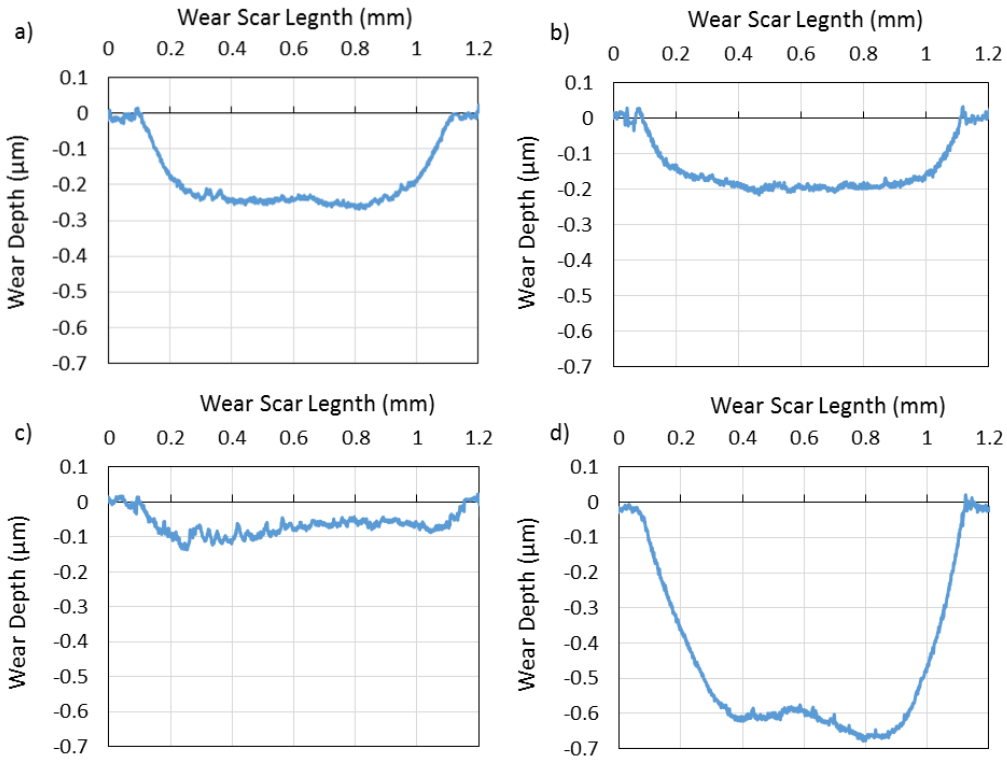


Figure 3.11 – Example profiles of wear scar length a) 0.5 ml b) 1 ml c) 1.5 ml d) 2 ml.

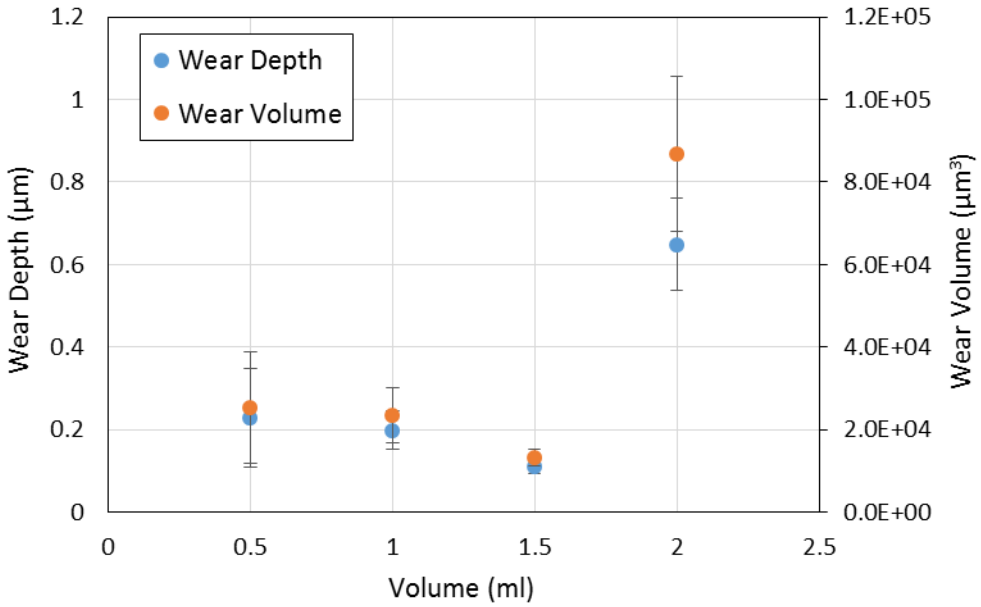


Figure 3.12 – AWD and AWV for varying fluid volumes.

The CoV for both AWD and AWV was calculated at each fluid volume and is shown in Figure 3.13. The repeatability was poor at 0.5 ml having a CoV of 53% for both AWD and AWV however this decreased significantly to 16% at 1.5 ml; 2ml again did not follow this trend and the CoV increased slightly. There was no difference in the CoV of AWD and AWV at 0.5 and 1.5 ml; however, at 1 and 2 ml AWD measurement was 5% more repeatable than AWV.

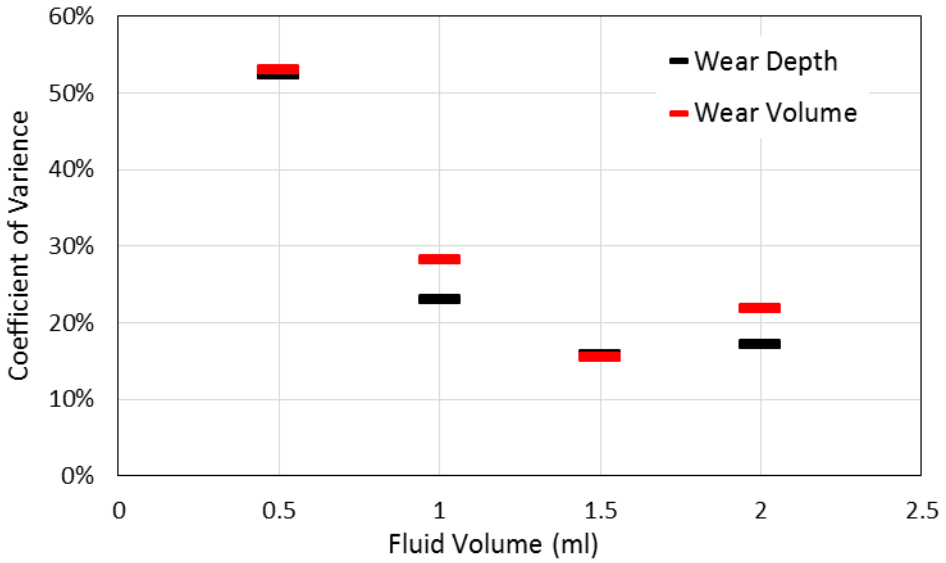


Figure 3.13 - CoV of increasing fluid volumes.

3.4.2 Effect of Protein (BCS) Concentration on COF and AWD

The effect of protein concentration was investigated by running a series of tests using 1 and 2 ml volumes for a range of BCS concentrations (10, 25, 50, 100 wt %). Average CoF results are summarised in Figure 3.14 for different BCS concentrations. At low BCS concentrations (10, 25 wt.%) $CoF_{1ml}<CoF_{2ml}$ but for the higher concentrations (50 and 100 wt.%) CoF was similar for both volumes.

Typical WLI images are shown in Figure 3.15, for the 2ml tests the WLI images gradually become thinner and narrower whereas there seems to be no correlation for the 1ml images, all wear scars are similar, narrow and thin. AWD and AWV are plotted against BCS concentration for different fluid volumes in Figure 3.16 and Figure 3.17 respectively. The wear results are similar for the high concentrations tests (50, 100 wt.%) but diverge significantly at low concentrations (10, 25 wt.%).

These results are in line with the CoF values shown in Figure 3.14 assuming these can be used as an indicator of wear, in this case higher average friction equates to higher wear. Generally, CoF cannot be used as an indication of wear, particularly for very different chemical systems; however for these BCS results there does appear to be a CoF/wear correlation. Indications are given on the AWD graph for approximate range of protein concentration for healthy and diseased SF.

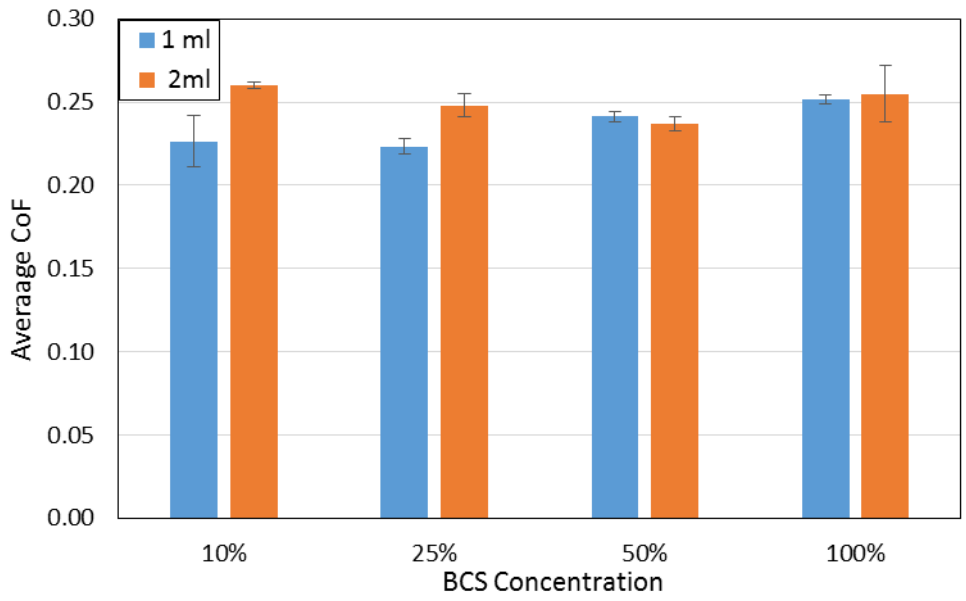


Figure 3.14 – Summary of average friction values for different BCS concentrations, 1 and 2 ml fluid volumes. (with N2 Purge).

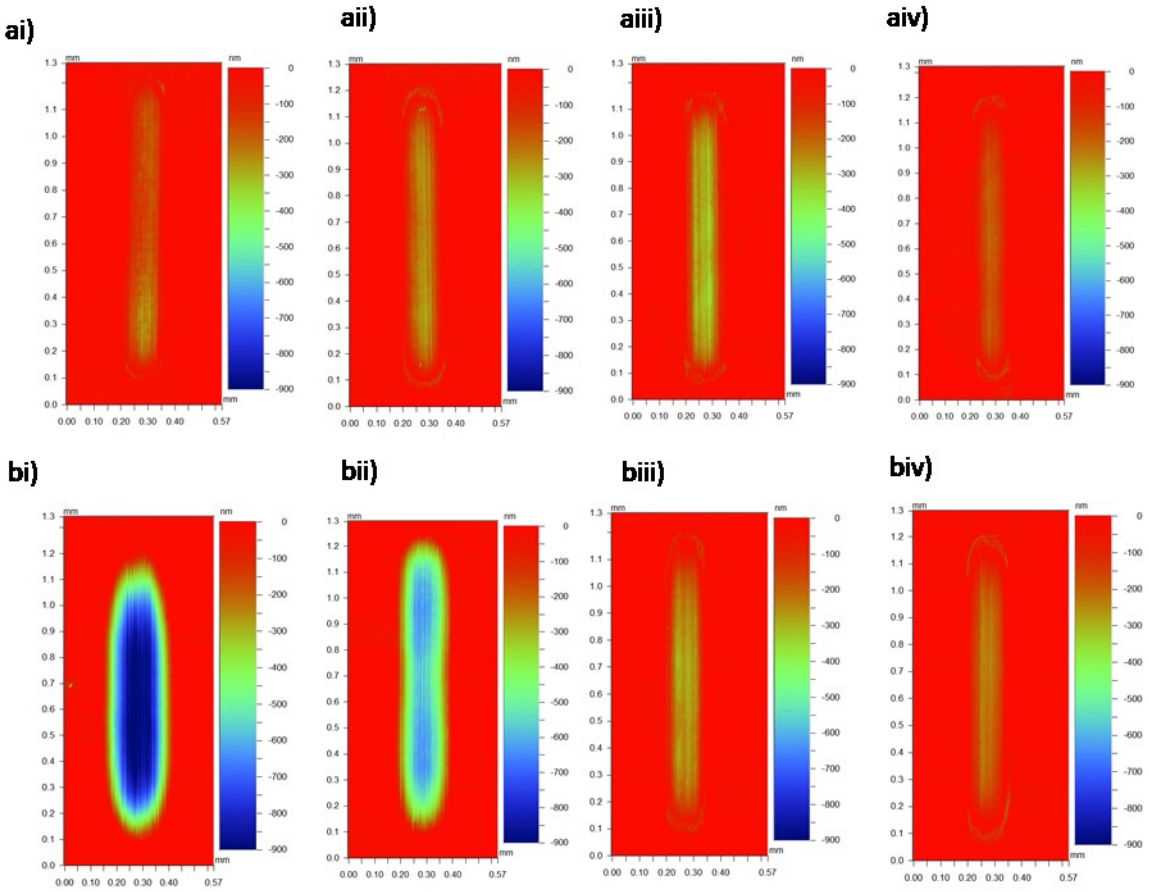


Figure 3.15 - Wear scar images for a) 1 ml b) 2 ml at i) 10%, ii) 25%, iii) 50% and iv) 100% BCS.

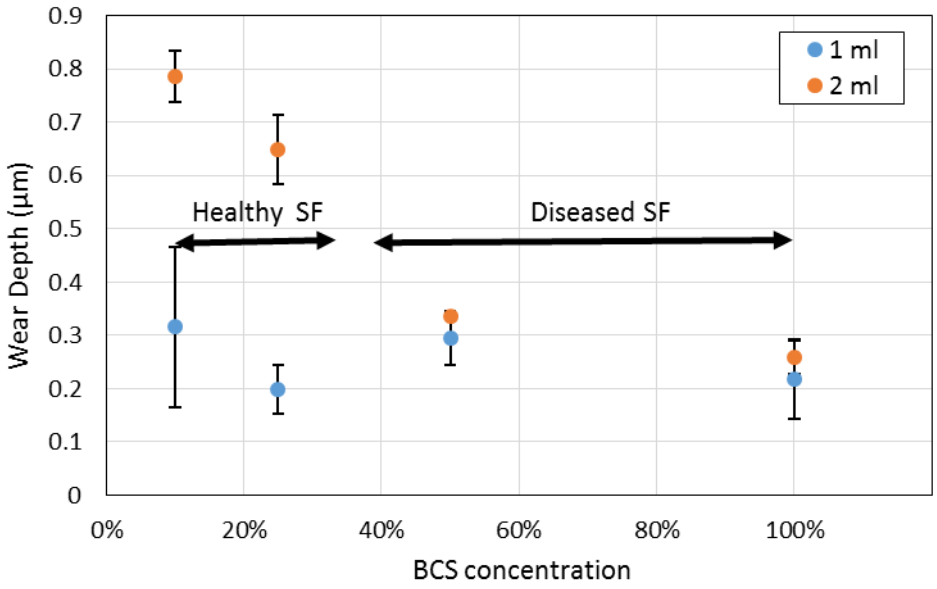


Figure 3.16 - Average wear scar depth for BCS at different concentrations, 1 and 2 ml. Approximate protein concentration ranges for "healthy" and "diseased" SF are indicated on the graph.

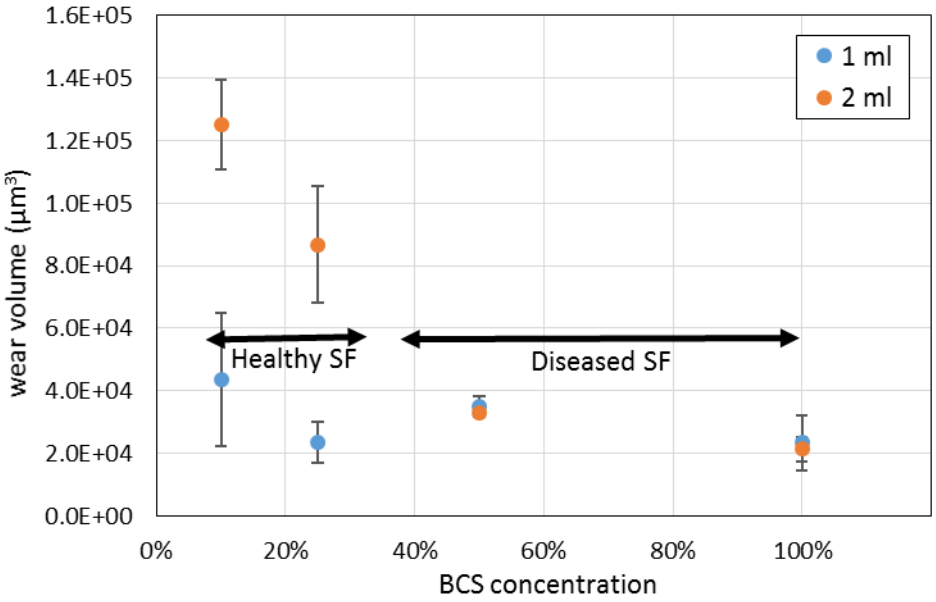


Figure 3.17- AWV for BCS at different concentrations, 1 and 2 ml. Approximate protein concentration ranges for "healthy" and "diseased" SF are indicated on the graph.

The CoV is shown in Figure 3.18 for AWD and AWV at both 1 and 2 ml for increasing BCS concentrations. For each concentration and volume, the CoV for AWD measurements are 2 – 12% lower than AWV showing higher repeatability. 50BCS using 1 ml of fluid is the exception where the CoV for AWV was 7% lower than AWD. The CoV for all concentrations at 2 ml is lower when compared to 1 ml volumes, showing tests at 2ml have a better repeatability. Thus the AWD measurement using 2 ml shows the best repeatability with all CoV values less than 12%.

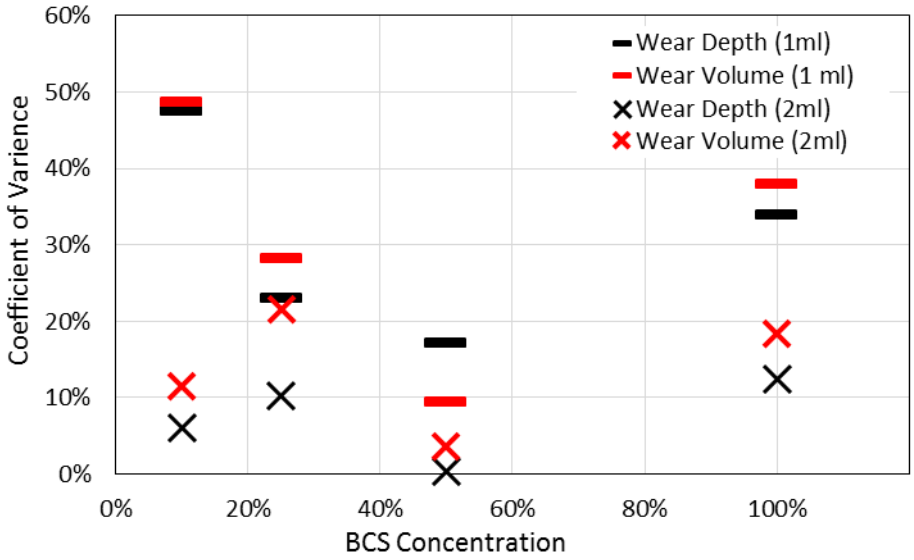


Figure 3.18 - CoV of increasing BCS concentration at both 1 and 2 ml.

3.4.3 Effect of Extended Test Time and N_2 Purge on CoF and AWD

Evaporation of the test fluid appeared to influence the measured wear for some test fluids. Purging nitrogen into the system could be contributing to evaporation due to the increased test period and the continued flow of gas. Tests were performed to see if this had a significant effect and the three protocols are outlined in Table 3.6. This will separate the effects of increased test length and the continued gas flow on friction and wear, to see if evaporation is a factor. Tests were performed using 25BCS at a volume of 2ml.

Figure 3.19 compares results from these protocols. The "nitrogen" protocol gave a slightly higher AWD however there was little difference in the AWV or CoF. Therefore, future tests ("Final" protocol) will be started immediately after test fluid is added with no nitrogen purge to reduce the potential of evaporation effects.

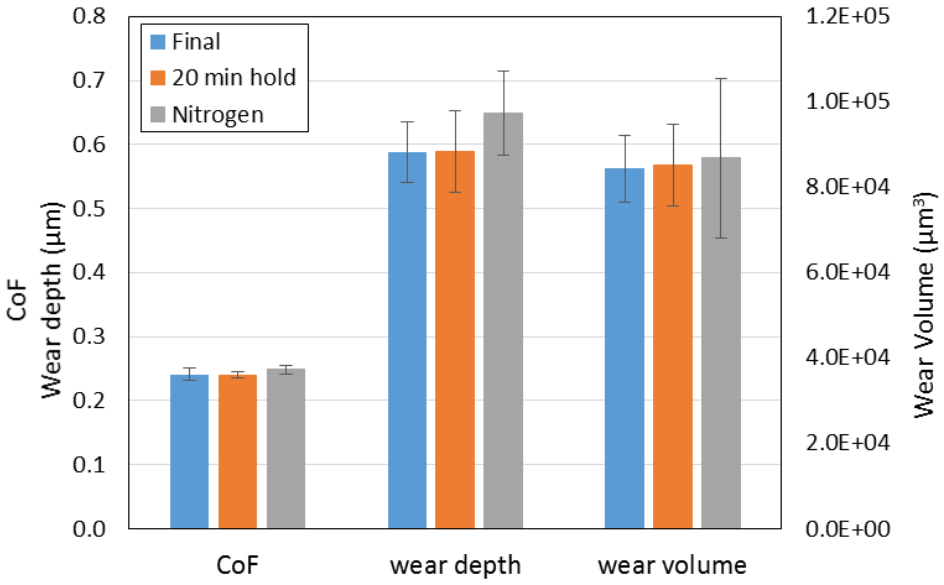


Figure 3.19 - Effect of purge and preheat delay times on friction, AWD and AWV for 2 ml fluid tests 25 wt% BCS.

The CoV for AWD and AWV measurements were in the range of 8-11% for all three HFRR conditions except the AWV of 'Nitrogen' which had lower repeatability with a CoV of 22%. There was little difference seen in the CoV between AWD and AWV under the 'Final' and '20 min hold' conditions.

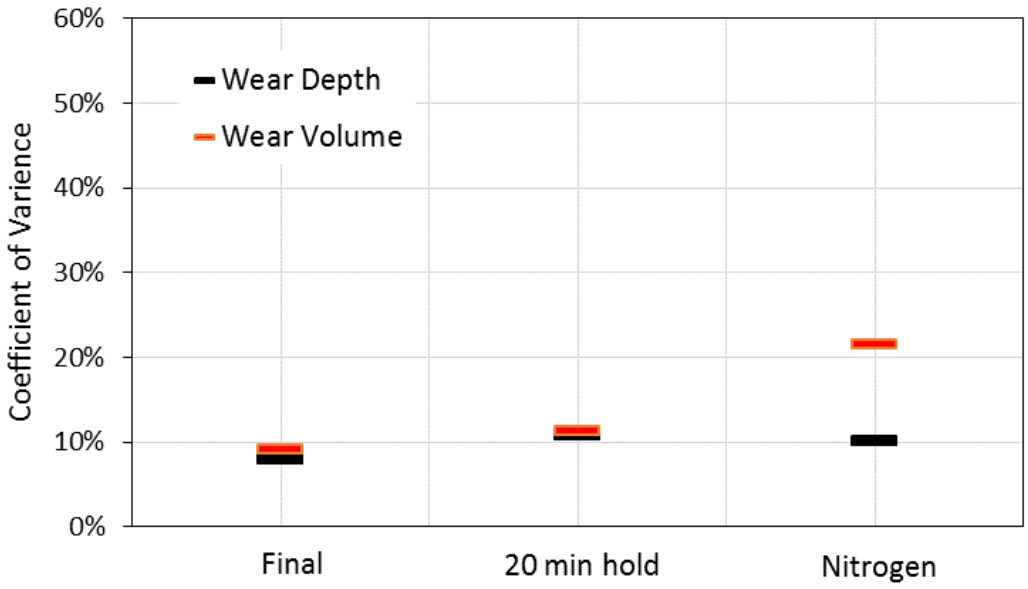


Figure 3.20 – CoV for the three HFRR test conditions.

3.5 Discussion

The test rig was designed to give robust repeatable wear measurements of artificial joint materials using a small volume of fluid under physiological conditions. As a low volume of fluid was used evaporation was a concern; therefore, the test procedure was developed to address this.

3.5.1 Test Development

The test development and repeatability has been reported on the effects of different factors. These were:

1. Effect of fluid volume
2. Effect of protein concentration
3. Effect of oxygen pp and heating time

3.5.1.1 Effect of Fluid Volume

To obtain measurable wear rates it was necessary to test for a large number of cycles, in this case 72,000. It was shown that for increasing fluid volumes the CoF also increases from $\mu = 0.222 – 0.248$ although changes are small. The effect of the fluid volume on the wear was more complex, for 0.5 – 1.5 ml both AWD and AWV were low and, although changes were small, decreased with increasing volume. Whereas the measured wear using 2 ml was elevated having an AWD and AWV 5.8 and 6.6

times larger respectively than the wear at 1.5 ml, both measurements are reflected in the WLI images and profiles. This result of greatest wear at the largest volume was not expected as at lower volumes starvation/dry sliding is more likely to occur and hence increase the wear (190, 224).

The tests were run at body temperature, 37^0C, which meant they are susceptible to fluid evaporation. As each test was run for the same time period and at the same temperature it follows that the same volume of lubricant will evaporate for each. This means that the species present in BCS, which have been attributed to wear protection (111, 143, 150, 170, 200, 202, 208, 209, 224), will be at elevated concentrations at lower volumes. Therefore, it was proposed at 2 ml volumes the BCS concentration is lower, possibly below a critical value, and provides less protection leading to much higher but true values of wear. Whereas at lower volumes (<1.5 ml) evaporation artificially increased the BCS content resulting in anomalously low wear values. An increase in BCS concentration has been reported to correlate with a decrease wear (177).

3.5.1.2 Effect of Protein Concentration

The effect of protein concentration on friction and wear was evaluated at both 1 and 2 ml volumes. For the 2ml volume tests showed wear decreasing with increasing protein concentration levelling off at >50BCS. For 1 ml volumes the wear was low and there did not appear to be any correlation with protein concentration however at concentrations >50BCS wear was similar to 2 ml results. The CoF at >50BCS concentrations were comparable for both 1 and 2 ml, whereas for concentrations less than 50BCS $CoF_{1ml}<CoF_{2ml}$.

It is clear that the wear and CoF is dependent upon both the volume and BCS concentration, and it is suspected that low volumes/BCS concentration are susceptible to evaporation effects. When evaporation does not have an effect (2ml) the wear decreases with increasing BCS concentration as seen in previous studies (177). At 1 ml evaporation of the fluid elevates the protein concentration to levels that can effectively protect the surfaces from wear. The role of proteins in forming a thicker and more protective lubricant film has been reported in a number of papers (108, 110, 111, 166).

Initially the fluid film above the disc was 3.1 and 6.2 mm for 1 ml and 2 ml volumes respectively, it was estimated that the 0.25 ml of fluid evaporated, this left a fluid film of 2.3 mm and 5.4 mm above the disc for 1 ml and 2 ml of fluid respectively. The estimated protein concentration before and after evaporation is shown in Table 3.7.

Table 3.7 – Initial protein concentration and estimated protein concentration after evaporation of fluids.

Initial w/w % BCS concentration	Total Protein Concentration (mg/ml)		
	Initial	1 ml	2 ml
10%	5.7	9.6	8.2
25%	18.0	24.0	20.6
50%	36.0	48.0	41.1
100%	72.0	96.0	82.3

3.5.1.3 Effect of Extended Test Time/N_2 Purge

Oxygen is present at lower partial pressures in SF (239, 241) than atmospheric conditions, therefore initial tests were performed at physiological levels however this increased the overall test time and provided a continuous flow of nitrogen therefore increased the possibility of evaporation. Results showed that there was little difference in the friction or wear with the addition of nitrogen or extended test time, and therefore this step was removed.

3.5.2 Determining Test Repeatability

This test set up was designed to measure wear of HSF, as this is only available in small quantities (~ < 3 ml) results must be highly accurate as repeat tests may not be possible for all samples. Wear in prosthetic joints has been extensively examined, using 25BCS, in literature for both hip simulator (54, 59, 171-174) and pin-on-disk (166-168, 225, 245) tests however they often have very high confidence intervals showing poor repeatability. In her thesis Hadley et al. used a new hip simulator which was validated using standard walking conditions and a MoM prosthesis. Although these results agreed with previous studies the 95% confidence limit was 73% and 66% of the average during the initial 'bedding in' and secondary 'steady state' phase respectively (59). Hip simulator studies are unsuitable for investigating the composition of lubricant due to unrepeatability of these tests. A pin-on-disk (UHMWPE on Stainless steel) test performed by Saikko et al. using BCS (~6-8.5% total protein concentration) calculated the wear factor for two different pin geometries, the CoV ranged from 12-53% (245).

Tests performed in this chapter showed for low volumes of fluid (< 1 ml) gave very low repeatability with the CoV as high as 53%, however this decreased to ~20% at 2 ml. There did not appear to be a correlation between repeatability and protein concentration; the test protocol did not seem to

significantly affect the repeatability. The 'final' protocol which will be used for future wear tests showed good repeatability with CoV of 8% for both AWD and AWV. Up to this point both AWD and AWV have been measured for each sample, the CoV's for the AWD were repeatedly lower than the values for AWV showing higher repeatability. Therefore, in future experiments only the AWD will be considered.

3.5.3 Final Test Protocol

A repeatable wear test has been developed using low volumes of fluid as required. The final test conditions are shown in Table 3.8. The test is at physiological temperature (230) and speed (73). The initial contact pressure, 216 MPa, is much higher than physiological conditions (74, 78, 233, 234) however this is quickly reduced due to the increase in contact area as the ball wears. The contact pressure at the end of the test, for 25BCS 'final' protocol, was calculated to be 23.7 ± 2.3 MPa from measuring the area of the wear scar on the ball (~30 mm^2) which is in line with physiological conditions. The sliding distance is 144 m whilst this much lower than that of typical bench top tests which are in the range 25 – 1500 km (15, 168, 227) the length of this test is restricted due to evaporation of the fluid. Additionally, the partial pressure of oxygen in the surrounding environment was not at physiological conditions as this was found not to make a significant difference to the friction and wear.

Table 3.8 – Final test protocol.

Test Length (hr)	1
Number of Wear Cycles	72000
Fluid Volume (ml)	2
Stroke length (mm)	1
Frequency of reciprocation (Hz)	20
Ball and Disc specimen Material	CoCrMo
Ball Dimensions (mm)	Diameter 19.05
Normal Load (g)	100
Mean Hertzian Pressure (M Pa)	216
Temperature (^{0}C)	35
Pre-test flow rate (L/min)	0
Test flow rate (L/min)	0

3.6 Conclusion

A bench-test, which uses a small volume of fluid, has been successfully developed to measure wear of CoCrMo specimens. The minimum fluid volume which can be used is 2ml, for volumes less than this evaporation increases the effective protein concentration which affects both the wear and friction. The wear of the disc decreased with increasing protein concentration levelling off at ~ 50BCS which is approximately 28 mg/ml total protein concentration. The partial pressure of oxygen did not seem to have much effect on wear measurements and therefore the test protocol was simplified to omit this step. The AWD measurement was shown to have higher repeatability than AWV and therefore this measurement will only be considered in future tests.

Chapter 4: The Effect of Model and Human SF on Friction and Wear

Summary

In this chapter the effect of model SF chemistry on friction and wear was investigated, implementing the test design outlined in Chapter 3. Initially model fluids consisting of only proteins (albumin, γ-G) were tested. The overall protein concentration and (A/G) ratio were varied to replicate levels in mH, mBCS, mOA and mPP SF. In later tests the effect of DPPC and HA addition to the protein solutions were investigated to more closely simulate physiological SF. Finally tests with HSF were carried out and the results compared to the model solutions.

4.1 Introduction

Synovial fluid is a complex mixture of macromolecules derived from blood plasma and partly produced by the synovial membrane (100, 102), the concentration can vary significantly between patients and is dependent upon pathology (37-41). Proteins (albumin and γ-G), phospho/lipids and HA are the most abundant molecules present (36-40, 246) and during articulation it is likely that some or all of these species are involved in the lubrication process. However this has been rarely studied, particularly in MoM joints, due to the belief they operate predominately in the EHL regime and the viscous nature of HSF, and therefore film formation is not affected by the bio-chemical properties of SF (9, 84). However, it was shown in Chapter 3 that reducing the concentration of BCS increased the wear for reciprocating CoCrMo couples showing that SF chemistry has an effect.

BCS is the most commonly used model SF as it is readily available in large quantities and has been shown to have a similar overall protein concentration when diluted to 25% w/w (~18-20 mg / ml) as healthy SF (35-37). However, the protein concentration in OA and PP fluids is elevated, and the specific content of albumin and γ-G is not replicated by 25BCS. Furthermore, the lipid content is not specified and HA is not present. Alternate model SF's comprise of SF species dissolved in a buffer which can control the pH and ionic strength of the solution (98, 109, 185). Proteins, lipids and HA can be added individually or in a varying concentrations and combinations to systematically investigate the tribological role of each species and how they interact.

Nečas et al. (247) investigated the effect of total and specific protein concentration using a Mini Traction Machine (MTM) with a CoCrMo pair. Tests were run for 300 second periods and measured the friction. It was concluded that the composition of model SF was not important as differences in the CoF were minor; however, results from Chapter 3 showed that small changes in the CoF lead to much larger differences in AWD, an additional aspect which should be studied for model SF's.

One of the few studies using HSF to investigate the influence of lubricant composition on friction was performed by Yao et al. (107). A pin-on-disk tribometer with a MoP pairing showed that HSF exhibited the lowest friction (~0.013) followed by DI water (~0.015) and surprisingly 25BCS gave the highest friction (~0.024). This direct comparison of HSF to 25BCS indicates fundamental differences in the lubricants affects their tribological properties.

Recent work by our group (111, 200) and Brno University (208, 209) reported formation of thick protein based films formed in sliding tests simulating hip function which is thought to contribute to wear protection in artificial joints (170, 224). It was shown by Nečas et al. (209) that the film is formed from a combination of albumin and γ-G and therefore a simple protein solution comprising of only one constituent cannot provide information about the complex fluid behaviour. Wang et al. (177) reported that the A/G ratio impacted prosthesis wear of MoP joints. Other studies have identified glycoproteins (143) and phospholipids (150, 202) as the active friction and wear reducing species in SF. The viscoelastic properties of SF are due to the HA content (136) and has been shown to reduce the CoF (197) and potentially wear (227) for MoP couples. All authors agree that the lubrication and wear mechanisms are complex and more than one species contributes. This review highlights three points for future studies:

1. Model fluids should replicate the complex chemistry of SF to include proteins, lipids and HA when investigating lubrication and wear mechanisms.
2. The specific role of each species and how they interact within in film formation is unknown.
3. Does 25BCS replicate HSF present in artificial joints? And are the missing species important?

A systematic study of the effect of model SF chemistry on friction and wear will be addressed in this chapter and compared to HSF, using the test procedure developed in Chapter 3. Model fluids were made to replicate protein concentrations of HSF for H, OA and PP pathologies; 25BCS is used as the reference fluid and an additional model mBCS was developed to imitate this. Initially tests concentrated on the protein concentration ensuring correct specific protein content, these gradually became more complex with the addition of phospholipids and HA. Finally HSF was employed and results compared to the model fluids.

4.2 Experimental Programme

The overall aim of this chapter was to investigate the friction and wear of CoCrMo implant materials using both model and human SF. More specifically to investigate the roles of proteins, lipids and HA within the fluid and if the concentrations and interactions between these constituents affect the wear. 25BCS is used as a reference fluid. The objectives were the following:

1. The study the effect of SF constituents on friction and wear
    - Proteins (albumin and γ-G)
    - Lipids (DPPC)
    - HA
2. To investigate the effects of HSF samples on friction and wear.
3. Compare model SF to HSF and investigate if 25BCS reference fluid gives comparative friction and wear measurements.

4.3 Materials and Methods

The adapted HFRR and 'final' protocol developed in Chapter 3 was implemented. Test conditions are outlined in Table 4.1.

Table 4.1 - HFRR test conditions.

Test Length (hr)	1
Number of Wear Cycles	72000
Frequency	20 Hz
Stroke Length	1 mm
Ball and Disc Specimen Material	CoCrMo
Disc Dimensions (mm)	Diameter – 10, Depth - 3
Ball Dimensions (mm)	Diameter 19.05
Normal Load (g)	100
Mean Hertzian Pressure (M Pa)	216
Temperature (^{0}C)	35

Post-test both ball and disc specimens are removed and lightly rinsed for 10 s with DI water to remove excess fluid. At this point the ball was retained for imaging and further analysis which is discussed in

Chapters 5 and 6. The disc was cleaned in order remove any residual film so that WLI analysis could be performed. Discs were soaked in 2% Decon90 solution in an ultrasonic bath for 10 minutes, before rinsing three times for 10s with distilled water. The specimens were then soaked in distilled water in the ultrasonic bath for a further 10 minutes. Once complete specimens were rinsed with isopropanol and air dried.

WLI is used to image the wear scar and to analyse the depth at 30%, 50% and 70% of its length and friction was recorded throughout the test. The fluid pH was measured by narrow range litmus paper (pH 6.5 – 10 VWR MColorHast and pH 5 – 10 VWR MColorHast) at the start and end of the test. Friction and wear results are reported in this chapter. Further examination (optical, SEM and Micro-IRRAS) of surface films is reported in Chapters 5 and 6 respectively.

4.3.1 Test Fluids

4.3.1.1 Model Fluids

Proteins (albumin and γ-G) are the most abundant constituent in HSF and therefore initial studies investigated the concentration and specific A/G ratio. Bovine Serum Albumin (BSA; Sigma Aldrich, A7906 ≥98% agarose gel electrophoresis) and γ-G from bovine blood (γ-G; Sigma Aldrich, G7516 ≥97% agarose gel electrophoresis) where dissolved by weight in saline solution at a physiological concentration (154 mM). The specific protein concentration varies between healthy and diseased fluids, neither of which is replicated by the most widely used screening fluid 25BCS. The protein concentration of diseased and healthy fluids have been widely reported in literature and were reviewed in Table 2.8 Section SF Chemistry and Properties, the median value of these ranges were chosen to replicate mH, mBCS, mOA and mPP SF concentrations.

25BCS (Sigma Aldrich Poole, 12133C sterile-filtered) was used as the reference test fluid. On receipt the 500ml sample was divided into 5 ml aliquots and then refrozen and stored at -32°C. An aliquot was removed the day before testing, defrosted overnight in a refrigerator and then diluted using DI water. A sample of 25BCS was also prepared by diluting 100BCS 1:3 with the saline solution. This is not the usual procedure but allowed direct comparison of the results. A 154 mM saline solution was also investigated to study the effect of ionic strength. A detailed list of NaCl and protein concentration is given in Table 4.2.

Table 4.2 –NaCl and protein concentration of model SF's tested.

	Solution	NaCl (mg/ml)	Protein Concentration (mg/ml)			A/G ratio
			BSA	γ-G	Total	
A	Saline	9	0	0	0	0
B	25BCS	0	~8	~10	~18	~0.8
C	25salBCS	9	~8	~10	~18	~0.8
D	mBCS	9	8	10	18	0.8
E	mH	9	12	6	18	2
F	mOA	9	18	12	30	1.5
G	mPP	9	30	10	40	3

Additional tests were run using 0.5 mg/ml 1,2-Dipalmitoyl-sn-glycero-3-phosphocholine (DPPC; Sigma Aldrich, P4329 ≥99% TLC) to examine the effect of phospholipids on friction and wear. DPPC is fully saturated with a gel-liquid transition temperature of 41^0C (the temperature at which the lipid bilayer melts from a gel into a liquid phase). The DPPC was dissolved directly into the 154mM saline solution and incubated to 60^0C for 30 minutes, vortexing at 3 rpm for 1 minute every 10 minutes. The solution was then sonicated for 30 minutes in a 50^0C water bath before being allowed to cool (98). Once the solution was at room temperature BCS, BSA and γ-G were added to the solutions to match the concentration of solutions C-G in Table 4.2. The DPPC saline solution was also tested to see the effect of lipids only. Table 4.3 outlines the NaCl, protein and DPPC concentration of tested solutions.

Table 4.3 – NaCl, protein and DPPC concentration.

	Solution	NaCl (mg/ml)	Protein Concentration (mg/ml)			DPPC (mg/ml)
			BSA	Γ-G	Total	
H	Saline + DPPC	9	0	0	0	0.5
I	25salBCS + DPPC	9	~8	~10	~18	0.5
J	mBCS + DPPC	9	8	10	18	0.5
K	mH + DPPC	9	12	6	18	0.5
L	mOA + DPPC	9	18	12	30	0.5
M	mPP + DPPC	9	30	10	40	0.5

Testing was expanded further to include HA, whilst it is considered to give SF its characteristic rheological properties. Hyaluronic acid sodium salt from Streptococcus equi (Sigma Aldrich, 53747 bacterial glycosaminoglycan polysaccharide) was used. For solutions N and O, HA was first dissolved by weight into 154 mM saline solution gently stirred every 20 mins for 1 hr at room temperature, for solution O to avoid shearing of proteins BSA and γ-G were added in the correct concentration once the HA had fully dissolved. For solution P DPPC was added first, as described earlier, followed by HA and BSA and γ-G. Only mBCS was tested here as this part of the test was to understand the effect HA has on friction and wear.

Table 4.4 - NaCl, Protein, DPPC and HA concentrations.

	Solution	NaCl (mg/ml)	Protein Concentration (mg/ml)			DPPC (mg/ml)	HA (mg/ml)
			BSA	Γ-G	Total		
N	Saline + HA	9	0	0	0	0.5	2
O	mBCS + HA	9	~8	~10	~18	0.5	2
P	mBCS + DPPC + HA	9	8	10	18	0.5	2

4.3.1.2 Human Fluids

HSFs have been collected in collaboration with Dr Matthew Jaggard (Imperial College MSk Lab). The samples were collected either during surgical procedures or via needle aspiration from a range of clinical arthroplasties, most commonly the knee joint. The SFs was placed in a sterile container and stored at 4^0C for no longer than 12 hours. The SF is mixed thoroughly to ensure homogeneity before placed into a centrifuge which is run for 15 minutes at 10000 G to remove large debris and cellular material. The sample is then divided into aliquots of ~1ml and frozen at -80^0C before being transported according to appropriate biosafety regulations to South Kensington Tribology laboratory. They are frozen at-32^0C until required for testing. All procedures from arrival at the Tribology Laboratory to disposal must be in line with the Code of Practice and Bio1 form in Appendix 11.1 and 11.2 respectively.

The past and current medical history of all 43 patients were received including the pathology, age, sex and ethnicity. This allowed the fluids to be further categorised for testing. Initially samples were chosen where larger volumes were available (≥ 4 ml) so that repeat tests could be performed (041, 77, 135 and 145). Patients were then grouped based on age and disease for sample volumes ≥ 2 ml, the age group 60-69 with only OA had 4 samples (110, 113, 156 and 164) with volumes of 2 ml or more and therefore chosen for testing. Table 4.5 outlines the gender, age, disease and the volume of fluid

available for each patient. The chemical composition analysis is ongoing and therefore is not reported in this thesis.

Table 4.5 - Gender, age and disease and volume of human samples

Sample	Gender	Age	Disease	Volume (ml)	# of tests
041	F	59	OA, RA	4	2
077	M	69	OA	4	2
110	M	64	OA	2	1
113	F	61	OA	2.5	1
135	-	-	-	6.5	3
145	F	78	OA RA	4	2
156	F	65	OA	2.5	1
164	F	60	OA	3	1

4.4 Results

The results are divided into four groups:

1. Effect of saline
2. Model SF's
    a. Effect of protein concentration with and without DPPC
    b. Effect of HA
3. HSF
4. Effect of pH

Section 4.4.1 compares the CoF and AWD of 25BCS and 25salBCS to see the effect saline has in comparison to DI water in a proteinaceous solution. The model SF section is subdivided; the first details the effect of all model solutions (saline, 25salBCS, mBCS, mH, mOA and mPP) with and without DPPC. These results are reported together to allow comparisons to be made. The second part of the model SF section investigates the effect of HA and compares results to protein and DPPC solutions. Finally Sections 4.4.3 and 4.4.4 reports the effect of HSF and pH on CoF and AWD respectively.

4.4.1 Effect of Saline on CoF and AWD

Figure 4.1 shows example friction traces comparing 25BCS and 25salBCS. Over the test period the traces were low and stable, CoF's for 25BCS and 25salBCS were in the range μ = 0.197-0.284 and μ =

0.199-0.297 respectively. Figure 4.2 shows the average CoF and AWD for these two fluids. Increasing the salt content increased the AWD from 0.59 to 0.75 μm, which is expected as tribo-corrosion (248) will increase material loss; this is mirrored in the CoF however, the difference is smaller.

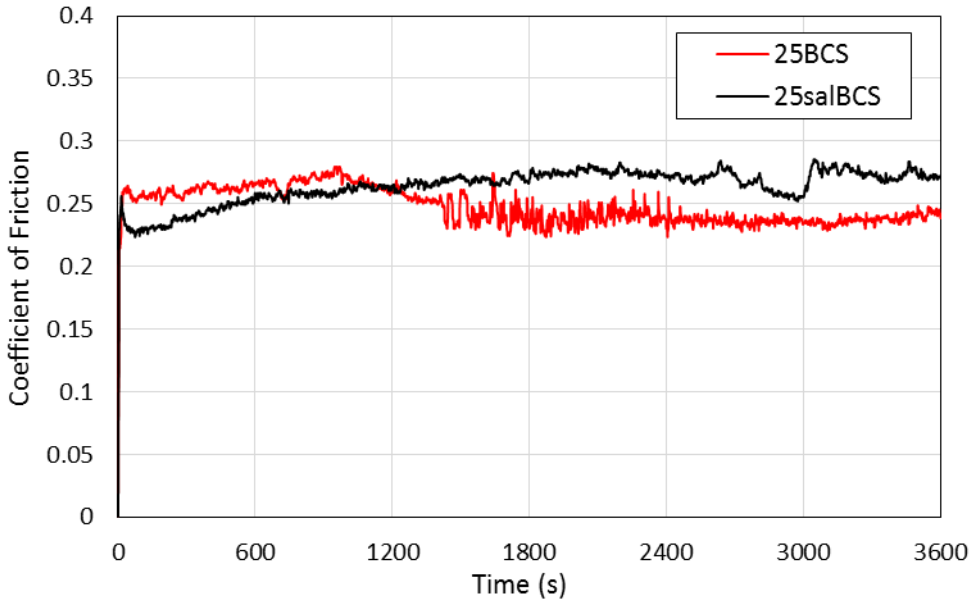


Figure 4.1 - Example CoF traces for 25% w/w BCS and 25% w/saline BCS.

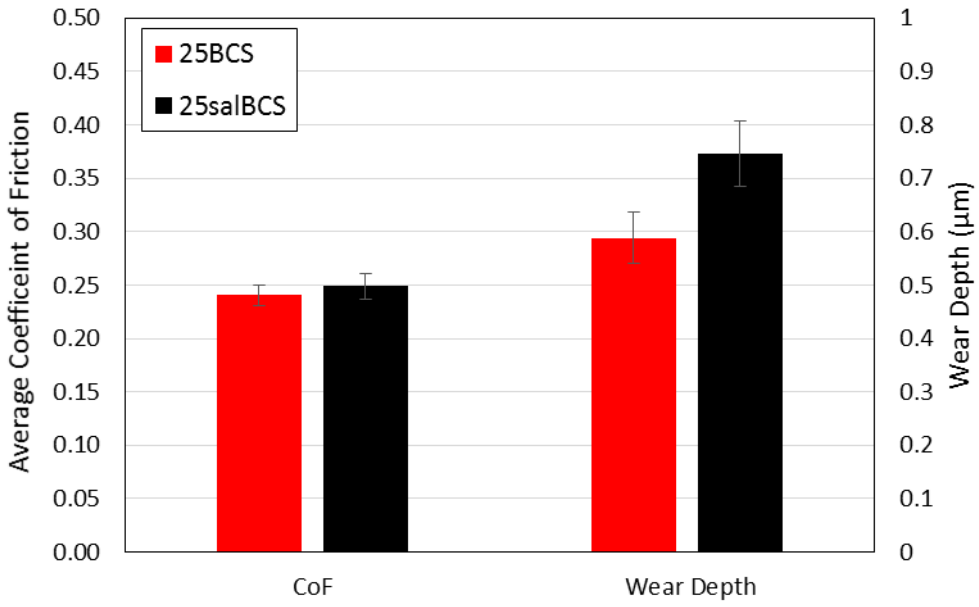


Figure 4.2 – Average CoF and AWD for 25% w/w BCS and 25% w/saline BCS.

4.4.2 Model SF's on CoF and AWD

4.4.2.1 Effect of Protein Concentration With and Without DPPC

Figure 4.3 gives example friction traces comparing solutions with and without DPPC for mH and mPP fluids to saline. Similar to 25BCS the model fluids with and without DPPC are low throughout the test period with CoF ranging from μ = 0.150 – 0.284 and μ = 0.174-0.284 respectively. For saline the CoF was initially high at μ = 0.616 before dropping to μ = 0.254 after 900 s.

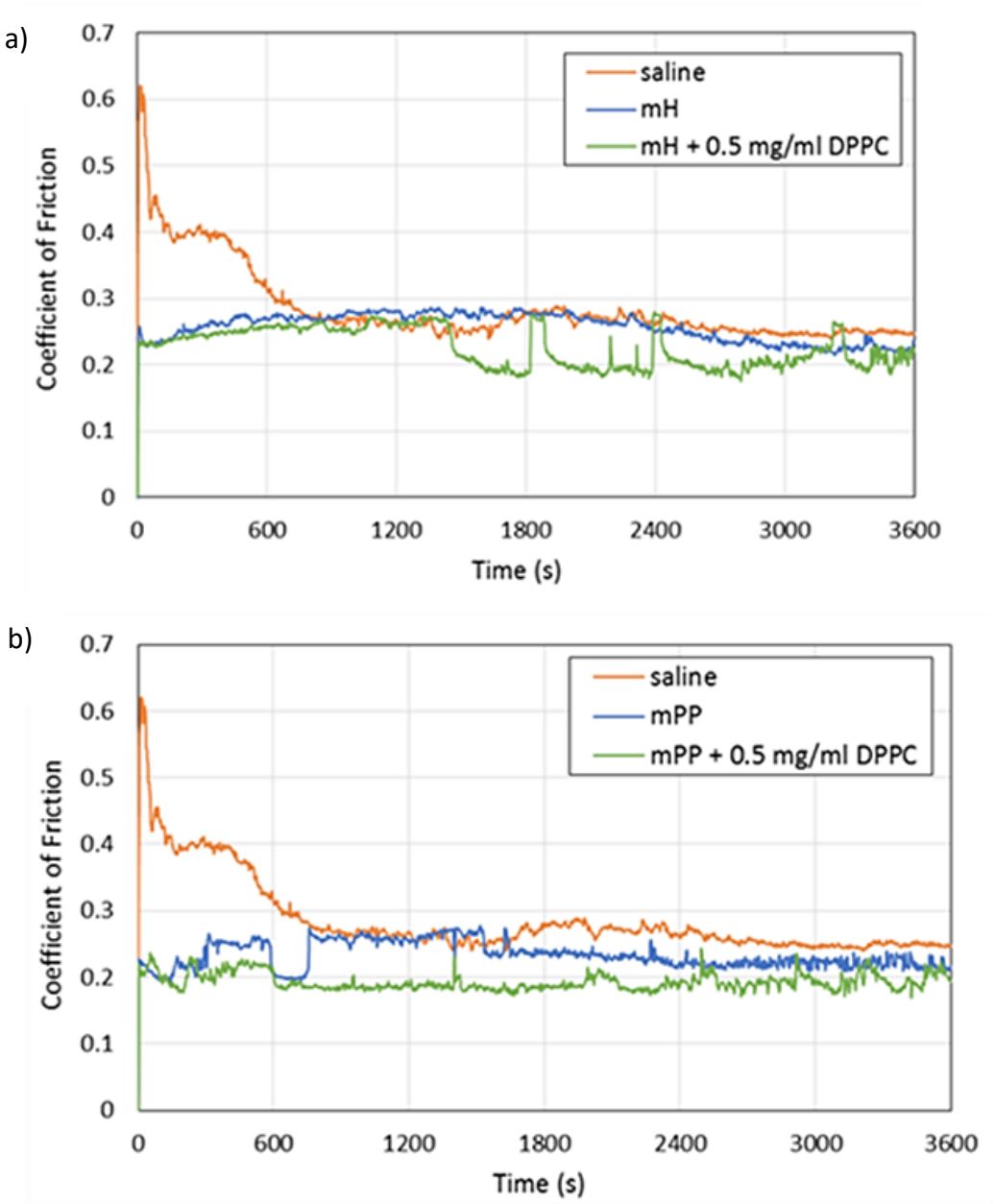


Figure 4.3 - Example CoF traces for model fluids with and without DPPC a) saline b) mH.

Figure 4.4 and Figure 4.5 show the average CoF and AWD of saline, 25salBCS and the four model fluids respectively. The average CoF is largest for saline with and without DPPC at μ = 0.281 and 0.290 respectively this can be attributed to the initial high CoF at the beginning of the test. The CoF of 25salBCS is around μ = 0.25 with and without DPPC whist all model fluids lie between μ = 0.20 – 0.25.

The AWD was highest for saline, 1 μm, which was to be expected as there were no proteins present and tribo-corrosion is expected to cause material loss (248). The AWD with DPPC for 25salBCS, the reference fluid, is comparable to mBCS with only a 0.008 μm difference however without DPPC there is a much larger difference of 0.135 μm. The lowest AWD for a model fluid occurred for mPP + 0.5 mg/ml DPPC with a depth of 0.251 μm and the highest was for mH with a depth of 0.907 μm. The effect of phospholipid addition is unclear.

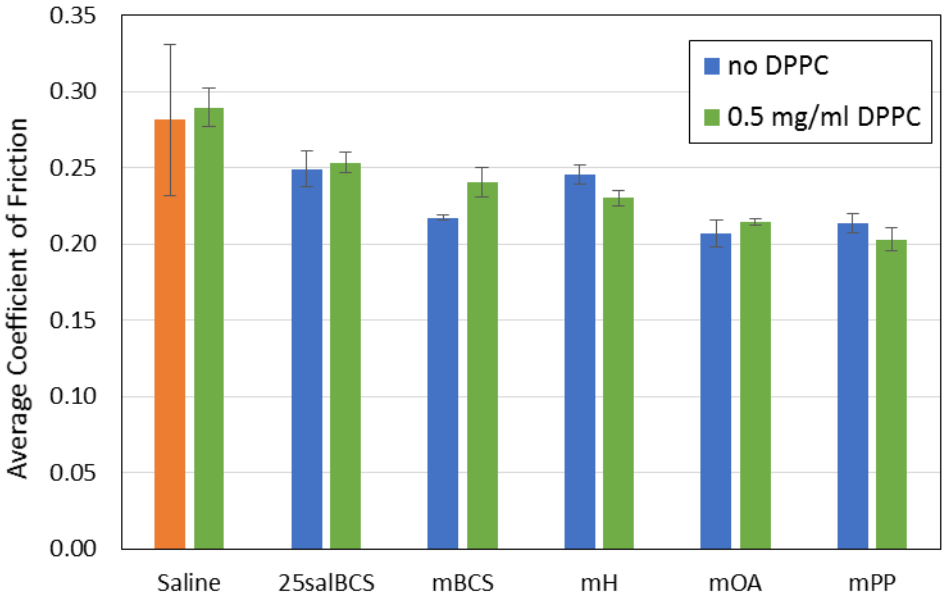


Figure 4.4 - Average CoF for all model fluids with and without DPPC.

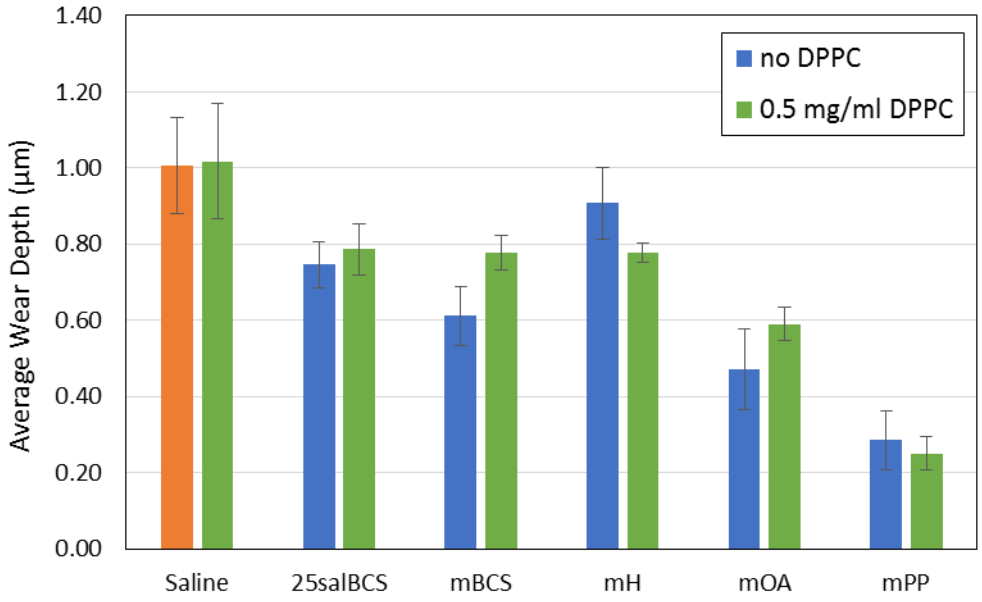


Figure 4.5 - AWD for all model fluids with and without DPPC.

The overall average CoF and AWD decreased with increasing protein content shown in Figure 4.6a and b respectively. The addition of phospholipid on friction and wear was not straightforward. For some fluids (saline, 25salBCS, mBCS and mOA) DPPC increased the AWD and slightly increased the average CoF whereas for mH and mPP the AWD and CoF decreased with addition of DPPC.

The effect of A/G profile on average friction and wear is shown in Figure 4.6c and d respectively. For an increasing A/G profile it is interesting to compare fluids with the same overall protein content but different protein composition. The fluids mH and mBCS have the same total protein concentration (18 mg/ml) but different A/G profile; for mH A/G = 2 and for mBCS A/G = 0.8. For solutions without DPPC the wear is much larger for mH (0.907 µm) compared to mBCS (0.611 µm), this limited evidence suggests that γ-G provides superior wear protection. Again the effect of DPPC addition is complex but could relate to the A/G ratio. For mBCS and mOA with a lower A/G of (0.8 and 1.5 respectively) the DPPC increased the average CoF and AWD whereas for mH and mPP which have a high A/G ratio (2 and 3 respectively) addition of DPPC decreased the average CoF and AWD, although decreases are small for mPP. From the limited evidence of this study it appears that DPPC inhibits the additional wear protection of high γ-G content fluids. The total protein content and A/G for each model fluid is given for reference in Table 4.6.

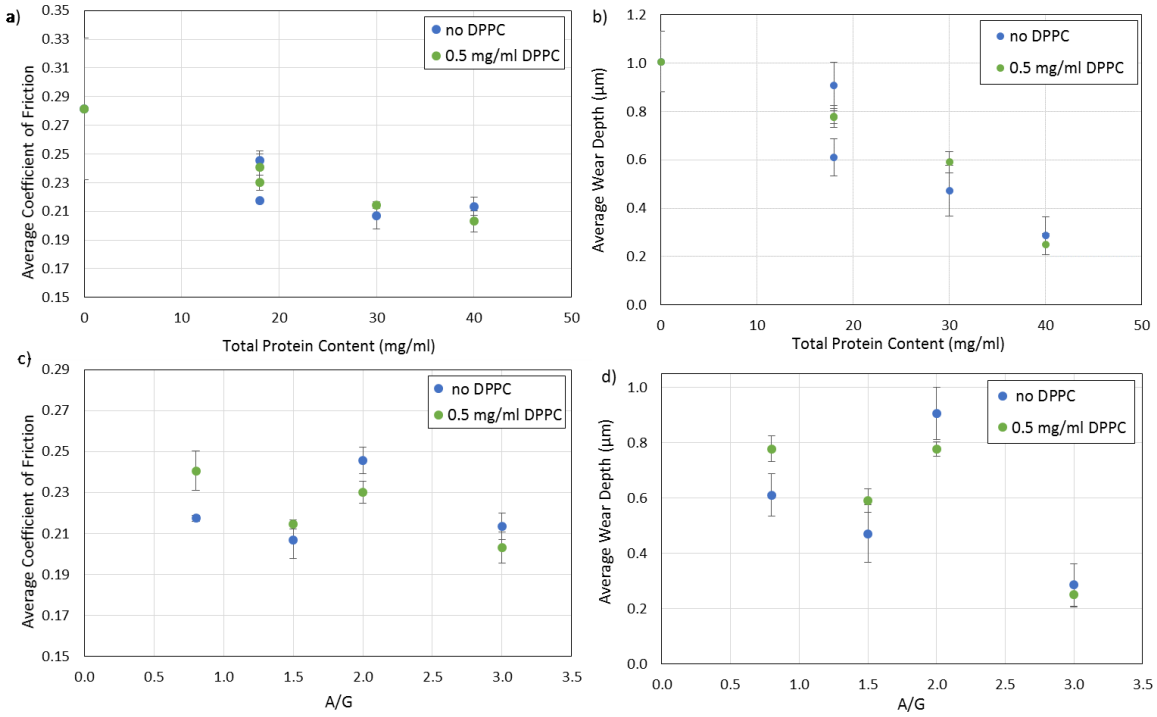


Figure 4.6 – a) Average CoF vs total protein content, b) AWD vs total protein content, c) Average CoF vs A/G, d) AWD vs A/G.

Table 4.6 - Total protein concentration and A/G ratio of model SF's.

	Saline	mBCS	mH	mOA	mPP
Total Protein (mg/ml)	0	18	18	30	40
A/G profile	-	0.8	2	1.5	3

4.4.2.2 Effect of HA

Figure 4.7 gives example friction traces comparing saline, saline with DPPC and saline with HA as this allows comparison of these species without the influence of the more abundant proteins. All three friction traces have a high starting CoF in comparison to model fluids with proteins present (~µ = 0.2 – 0.25). This was highest for only saline at µ = 0.607 followed by saline with DPPC, µ = 0.564, and lowest for saline with HA where µ = 0.472. The CoF of saline and saline with DPPC decreases and levels out at ~ µ = 0.2 - 0.25 by 1200 s until the end of the test. For saline with HA the CoF drops quicker to µ = 0.323 within 100s but steadily increased to µ = 0.408 at the end of the test. The CoF trace with saline as the lubricant appears 'smooth' in comparison to saline + DPPC which has large fluctuations in a small time period.

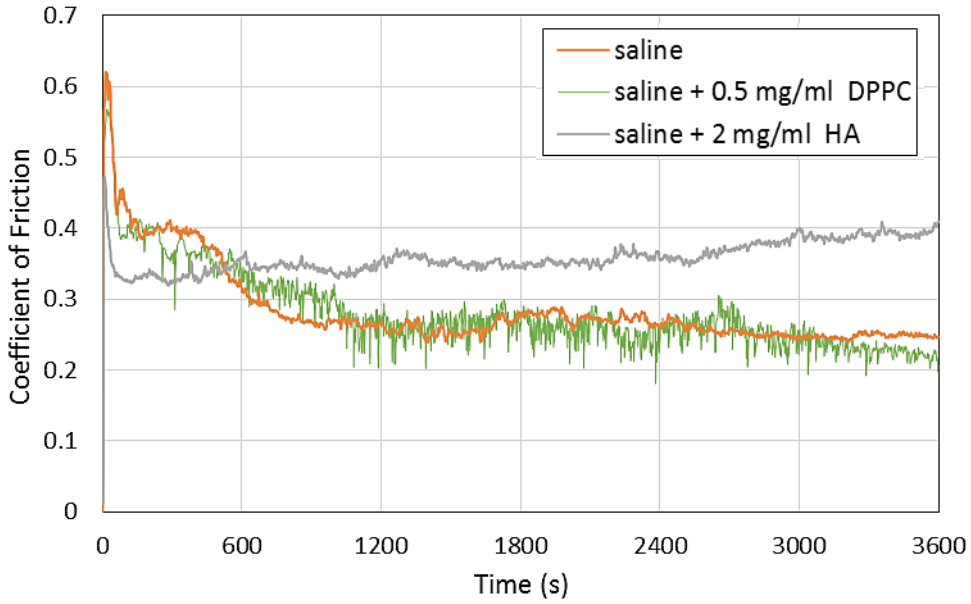


Figure 4.7 – Example CoF traces for saline, saline + 0.5 mg/ml DPPC and saline + 2 mg/ml HA.

Figure 4.8 shows the average CoF and AWD for saline, saline with DPPC and saline with HA compared to 25salBCS. The highest average CoF was for saline + 2 mg/ml HA at μ = 0.355. There was little difference in the CoF between saline and saline + 0.5 mg/ml DPPC with μ = 0.281 and μ = 0.290 respectively. These results were mirrored in the AWD, saline + 2 mg/ml HA had the highest wear at 1.2 μm and saline and saline + 0.5 mg/ml DPPC had similar values at 1.0 μm. All CoF and AWD were larger than 25salBCS results.

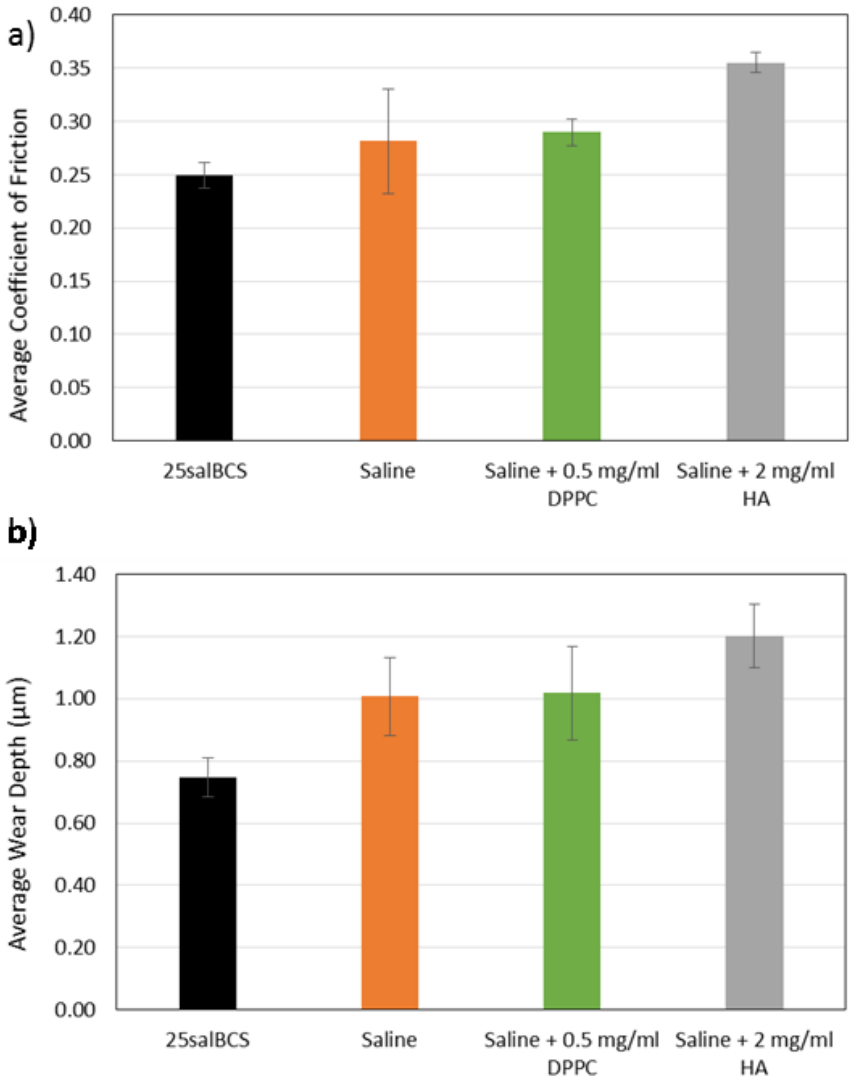


Figure 4.8 – a) Average CoF and b) AWD for saline, saline + 0.5 mg/ml DPPC and saline + 2 mg/ml HA.

Figure 4.9 compares the average CoF and AWD for mBCS, mBCS + DPPC, mBCS + HA and mBCS + DPPC + HA, the reference fluid 25salBCS is also shown. For all model fluids the average CoF (Figure 4.9a) ranged from µ = 0.217 - 0.257. The lowest value was for mBCS with no additional species and the highest for mBCS + 0.5 mg/ml DPPC + 2 mg/ml HA. The CoF of the reference fluid, µ = 0.249, 25salBCS is comparable to mBCS + 2 mg/ml HA, µ = 0.248. The AWD (Figure 4.9b) ranges from 0.611 to 0.922 µm for the model fluids and is 0.746 µm for 25salBCS. Similar to the average CoF the lowest AWD was from the mBCS with no additional species and the highest from mBCS + 0.5 mg/ml DPPC + 2 mg/ml HA.

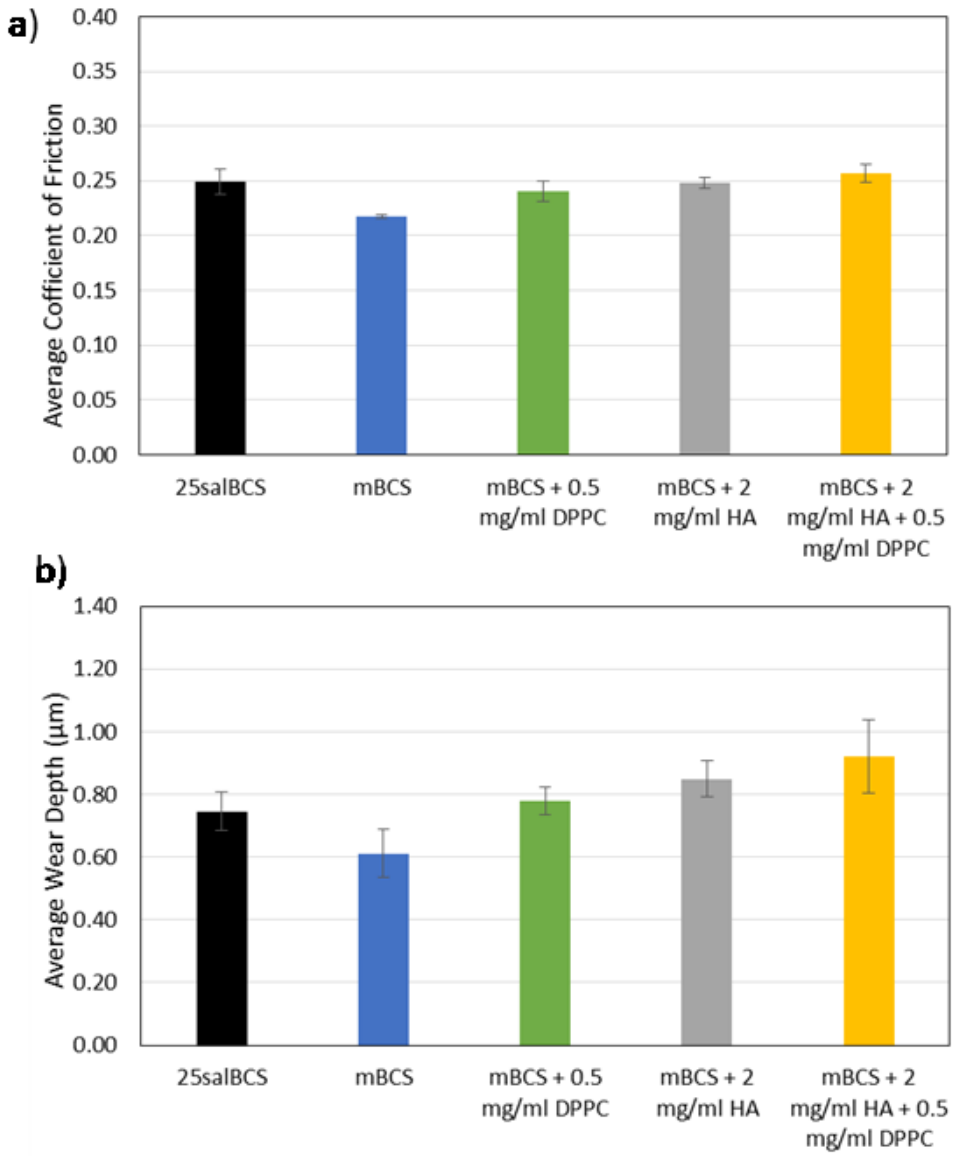


Figure 4.9 - a) Average CoF and b) AWD for 25salBCS, mBCS, mBCS + 0.5 mg/ml DPPC, mBCS + 2 mg/ml HA and mBCS + 0.5 mg/ml DPPC +2 mg/ml HA.

The average CoF was plotted against the AWD for all model fluids in Figure 4.10, showing a correlation between the two. The AWD increased for increasing CoF. This is not too surprising as all the model fluids are made using the same chemicals and therefore should correlate.

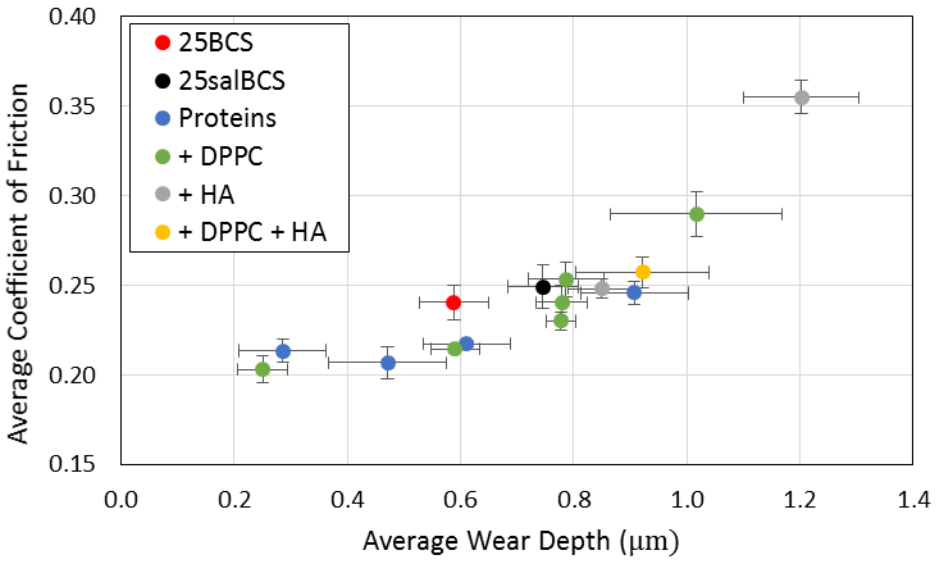


Figure 4.10 – A plot of the CoF Vs AWD for all model fluids tested.

4.4.3 HSF on CoF and AWD

Figure 4.11 shows an example CoF trace for a human sample compared to the reference fluid 25BCS (without saline). Both traces were low and stable throughout the duration of the test, for the human sample shown is 135/3 the CoF gradually increases to an end value of µ = 0.299; however, this is not true for all HSF samples. The CoF for all human samples were in the range of µ = 0.213 - 0.323 compared to µ = 0.224 – 0.279 for 25BCS.

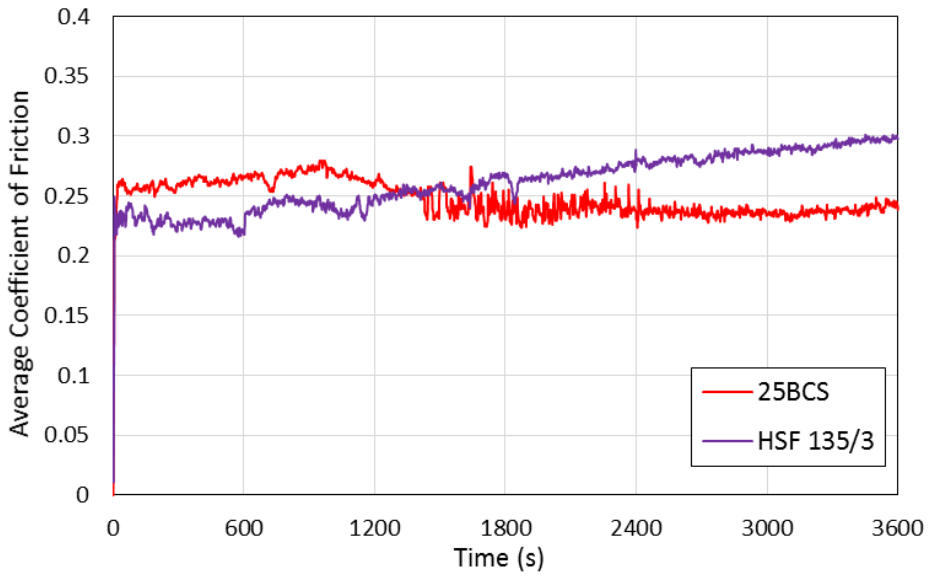


Figure 4.11 - Example CoF trace for a HSF compared to 25BCS.

Figure 4.12 shows the average CoF for all HSF samples tested, results are fairly constant ranging from μ = 0.241 - 0.268, this is comparable to 25BCS with μ = 0.240. Figure 4.13 shows the AWD for all HSF samples, values vary somewhat and range from 0.58 – 1.04 μm. The AWD of 25BCS, 0.589 μm is comparable to only HSF41 and HSF113, for all other samples the AWD is > 0.8 μm. The total and specific protein content of the HSF samples is unknown and therefore this could be the cause.

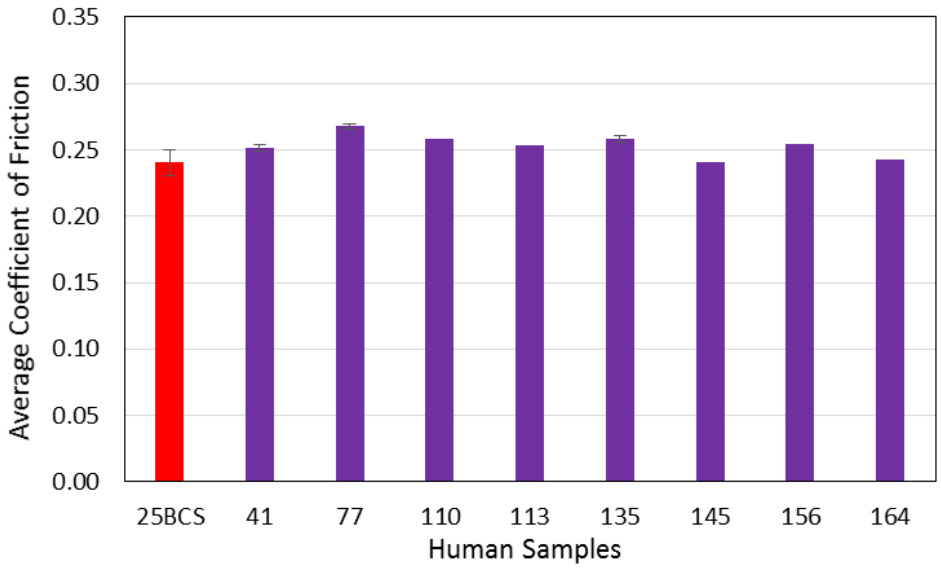


Figure 4.12 - Average CoF for HSF samples compared to reference fluid 25BCS.

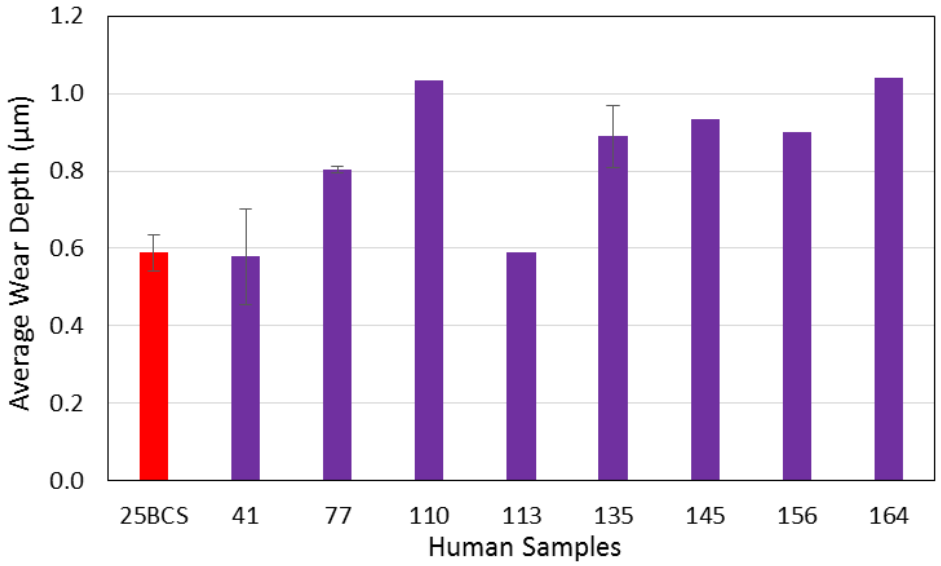


Figure 4.13 - AWD of HSF samples compared to reference fluid 25BCS.

Figure 4.14 plots the average CoF against the AWD, for all HSF samples and model fluids. There does not appear to be a correlation between the HSF samples however they are located in the centre of the graph showing HSF results are repeatable and are comparable to the reference fluids which are most commonly used for testing implants, 25BCS and 25salBCS. The variation in CoF is small in comparison to the large spread in AWD results and therefore using CoF as an indication of wear is not appropriate.

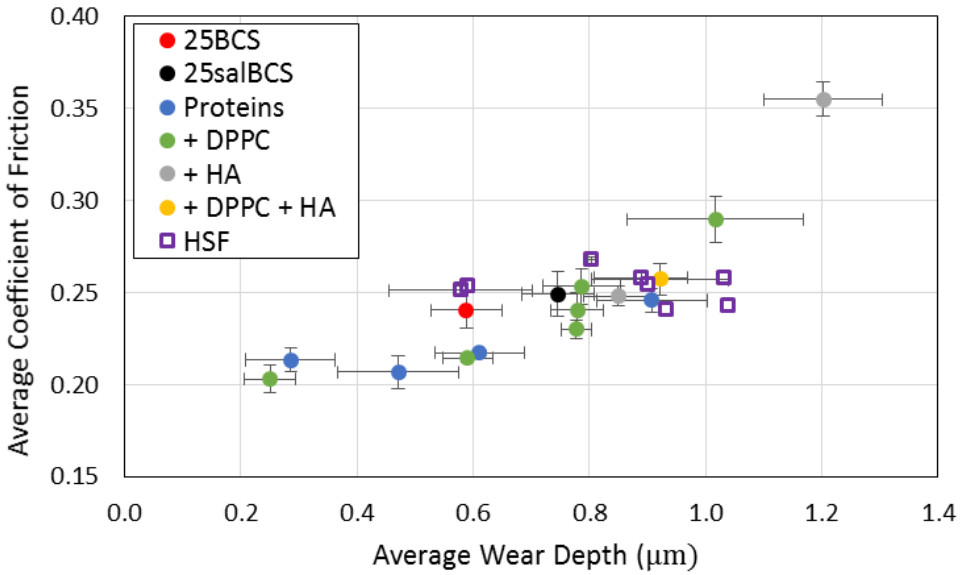


Figure 4.14 - A plot of the average CoF Vs AWD for all model fluids and HSF.

4.4.4 Effect of pH on AWD

An increase in pH was recorded at the end of the test for each of the fluids. For all model fluids, with and without DPPC, the pH increased from 6 to 6.5. For HSF and fluids containing BCS (with water, saline and DPPC) this was more complex and the starting pH was different for each test. Figure 4.15 and Figure 4.16 shows a plot of the AWD vs the pH before and after the wear test respectively. Before testing for all samples with BCS the starting pH was 7.9, for HSF the pH was within the range 7.7 – 8.5. There was no correlation between the starting pH and AWD. After testing the pH for the BCS fluids were lower than HSF, they were in the ranges 8.1 – 8.5 and 8.5 – 9.5 respectively. There was no correlation between the post-test pH and the AWD. The starting pH for repeat samples of HSF was the same; Table 4.7 shows the pathology and the pH of each fluid.

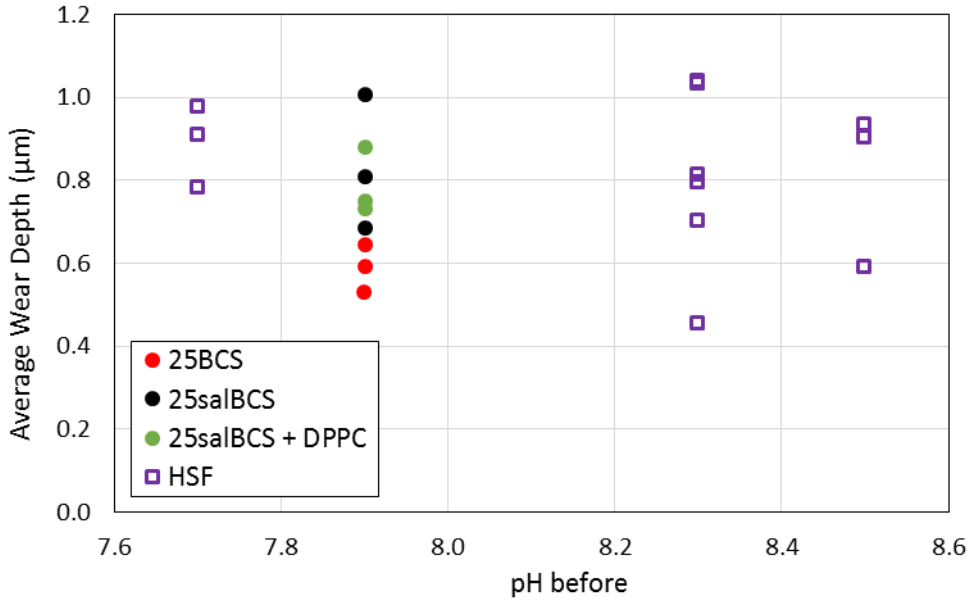


Figure 4.15 - A plot of the AWD vs pH before testing.

Table 4.7 - Pathology and starting pH of HSF fluids.

Sample	Disease	Start pH
041	OA, RA	8.3
077	OA	8.3
110	OA	8.3
113	OA	8.5
135	-	7.7
145	OA, RA	8.5
156	OA	8.5
164	OA	8.3

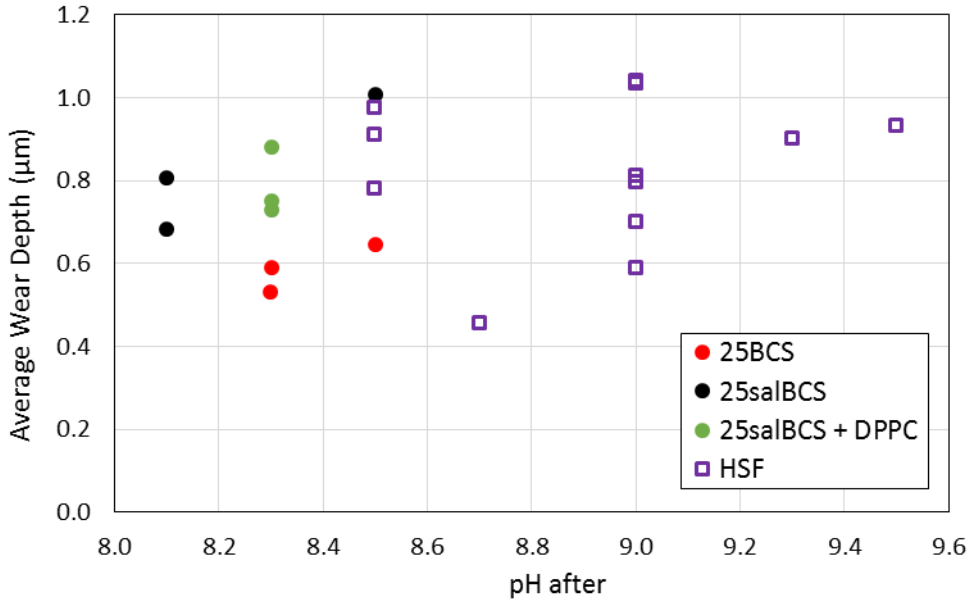


Figure 4.16 - A plot of the AWD vs the pH after testing.

Figure 4.17 shows a positive correlation between the AWD and the change in pH before and after testing. For BCS samples with saline (25salBCS and 25salBCS + DPPC) the wear is marginally higher for corresponding pH differentials compared to samples with no additional saline (25BCS and HSF).

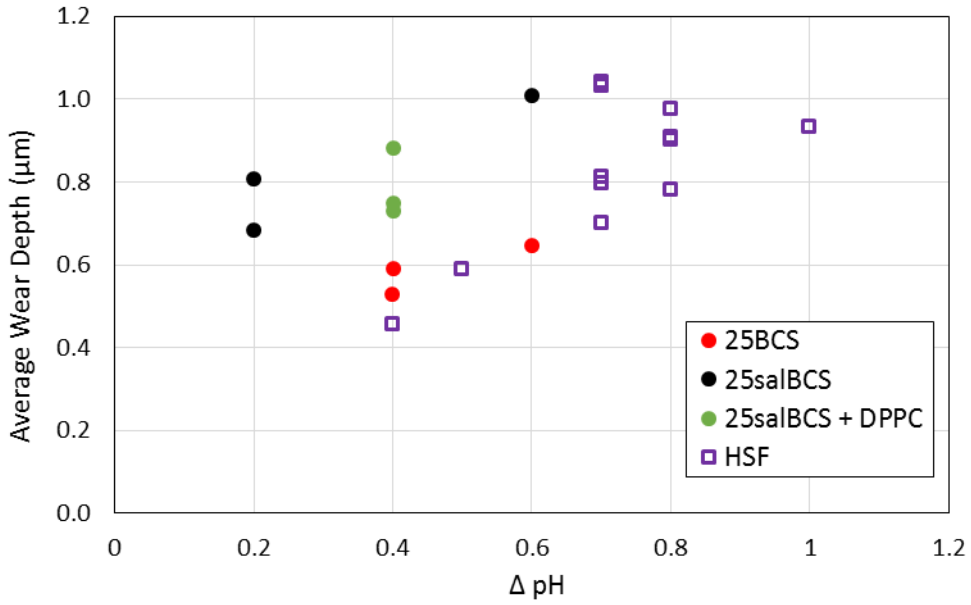


Figure 4.17 - A plot of the AWD vs change in pH before and after testing.

4.5 Discussion

Model and human SF's have been used in order to relate how the chemistry affects the friction and wear of CoCrMo implants. Initially comparisons were made between 25BCS and 25salBCS to understand the effect of saline on the reference fluid (25BCS). Secondly the total and specific protein content was altered to replicate an array of pathologies, the CoF and AWD of these solutions were reported with and without the addition of DPPC. Thirdly the effect of HA was investigated in the solutions saline, mBCS and mBCS + DPPC. Fourthly the effect of HSF on CoF and AWD was investigated, it was important to compare these physiological fluids to the model SF's created. Finally, the effect of pH on AWD was reported.

4.5.1 The Effect of Saline in 25BCS

25BCS is the most commonly used screening fluid used to assess the wear of artificial joints and therefore is used as the reference in this thesis. As model fluids were made using physiological saline the solution 25salBCS was compared to 25BCS, unsurprisingly this increased the friction and wear which can be attributed to tribo-corrosive mechanisms. Corrosion occurs spontaneously with CoCrMo as the free energy is less than zero (249). Metal ions are oxidised and spontaneously released into a solution leaving the electrons behind, creating potential at the metal-solution interface, the size of which is an indicator of the reactivity (249). Corrosion is accelerated in saline because the dislocated ions (Cl^-) increase the conductivity allowing more metal ions to pass into the solution (250). The ions released form an oxide which act to protect the surface from further corrosion, however during articular motion this layer is removed via abrasion allowing further corrosion to occur. This combination of corrosion and abrasion has been reported to form a more severe condition increasing the material loss the contact zone (232, 251, 252), in one study 20 – 30% of the material degradation was attributed to corrosion related damage (238)

4.5.2 The Effect of Total and Specific Protein Concentration

A series of model SF solutions were tested for a range of protein concentrations. Overall both the friction and measured wear decreased with increasing protein concentration (Figure 4.4 and Figure 4.5) which agrees with earlier results from our group (110, 112) and other studies reported in literature (177, 198). The effect of the A/G ratio can be analysed by comparing mBCS and mH as they have the same overall protein content but different A/G ratios. Our evidence is limited however CoF and wear are reduced for increasing A/G ratio, suggesting that γ-G is more effective in reducing wear

of CoCrMo than BSA. γ-G has been reported to dramatically reduce the wear (110, 111) and produce thick deposited films (109, 198).

Walker et al. (196) tested a range of model fluids (BSA, γ-G and HA in DI water and ringers solutions) in a bench top test. The CoF was in the range 0.15 – 0.23; which is slightly lower than the reported results.

4.5.3 The Effect of the Addition DPPC to Proteins

The effect of DPPC with no proteins had little effect on CoF and AWD, giving comparable results to that of saline suggesting that DPPC does not have an effect by itself. The effect of DPPC with proteins was more complex, for low A/G ratio (0.8, 1.5) wear increased but for higher A/G ratio (2.0, 3.0) wear decreased for the same overall protein concentration (Figure 6b), suggesting that DPPC inhibits the wear protection of high γ-G content fluids. Other studies on phospholipids are conflicting, they have been reported as a naturally occurring boundary lubricant (146, 150, 154, 202, 203). It was shown in a joint simulator test PC phospholipids diluted in a gelatine solution gave significantly less wear when compared to 25BCS and that increasing the phospholipid concentration reduced the wear (154) however it could not be concluded whether it acts on the surface itself as a bilayer or in conjunction with all or specific proteins (146, 203). On the other hand Trunfio-Sfarghio et al. (206) reported that lipids increased the CoF for healthy, Steel-on-Steel and Steel-on-Polyethylene joints. Lipids adsorbed onto a steel surface were quickly removed from the contact by tribological stresses. Furthermore, it was shown that the addition of BSA and HA caused the CoF to increase further.

4.5.4 The Effect of the Addition of HA and DPPC to Proteins

The addition of HA to saline solution, mBCS and mBCS + DPPC increased both the friction and wear. Similarly Walker et al. (196) showed that for articulation of CoCrMo alloys, individually HA had a higher CoF than protein solutions and the addition of HA to γ-G increased the CoF. For a CoCrMo pin on UHMWPE disc test Gispert et al. (197) showed that a salt solution containing HA gave a higher CoF than the salt solution alone.

Nečas et al. (198) investigated the effect of SF composition (BSA, γ-G, phospholipids and HA) on film formation. Two model fluids were tested, model 1 had an A/G ratio of 2.5 and had a low phospholipid and HA concentration whilst model 2 had an A/G ratio of 3 with a high phospholipid and HA concentration. It was reported that under loaded but static conditions increasing the concentration of phospholipids and HA reduced the film thickness of deposited films. Behaviour changed under dynamic conditions, model 1 (A/G = 2.5, low HA and DPPC concentrations) the film was thin (~ 50 – 70

nm) and stable whereas model 2 (A/G = 3, high HA and DPPC concentrations) the film thickness increased rapidly to 900 nm. The effect of the A/G ratio was not discussed and is hard to decouple the roles of proteins, phospholipid and HA. Film thickness measurements of only HA were negligible.

Therefore, it can be concluded that in artificial joints HA does not have a lubrication function, this has important consequence as visco-supplement injections for patients who have already undergone joint replacements will be ineffective.

4.5.5 The Effect of HSF on Friction and Wear

The friction and wear of HSF samples varies between μ = 0.241 – 0.268 and AWD 0.590 – 1.04 μm respectively. At the lower end of the scale results are comparable to 25BCS (HSF41 and HSF113) where the corresponding friction and AWD values are μ = 0.240 and 0.589 μm respectively. However, in some cases the AWD could be up to 77% more than predicted by 25BCS and on average 44% larger. For three quarters of the HSF specimens the AWD was over 0.2 μm (37%) greater than 25BCS which has huge implications on tribological testing of artificial joints as it is apparent that 25BCS does not accurately replicate the AWD.

Few studies have previously tested the lubrication properties of HSF, one of which was published by Walker et al. (196) who used a CoCrMo disc on CoCrMo ball. HSF results were compared to DI water, Ringer's, polyox, BSA, γ-G, HA and γ-G + HA solutions. The CoF of HSF was similar to γ-G and lower than that of Ringers solution and BSA, the wear of HSF was superior to that of Ringers solution but not compared to other lubricants (196). Yao et al. (107) reported friction tests with a pin-on-disk tribometer (MoP), the CoF of PP HSF was the lowest compared to DI water, varying concentrations of BCS diluted with DI water and bovine SF.

Although high friction does not usually always result in higher wear, for the case of model fluids there does appear to be a correlation perhaps as the same system with similar species in the lubricant is used. When the HSF samples are overlaid onto this plot they fall close to 25BCS suggesting that this is an appropriate lubricant.

4.5.6 The Effect of pH on Wear

The pH of all fluids increase during testing, the model fluids with and without DPPC changed from 6 before the wear test to 6.5 after the wear test. All BCS containing fluids had a starting pH of 7.9 the same as specified in the certificate of analysis (253). The starting pH for HSF varied somewhat, the lowest value was recorded for HSF135 was 7.7 where the pathology was unknown. All other samples were in the range pH = 8.3 – 8.5, which is slightly higher than previously reported for OA (7.4 – 8.1)

and RA (6.6 – 7.6) pathologies (104). After testing the pH for BCS containing fluids and HSF was between 8.1 – 8.5 and 8.5 – 9.5 respectively. These values are higher than the reported pH of PP SF which in the range 7.5 – 8.5 (104). In *vivo* the PP fluids show an increase in pH from diseased pathologies (104), suggesting that the pH of HSF could increase *in vivo* due to artificial joint articulation.

There was a positive correlation between the change of pH during testing and the AWD (Figure 4.17). The study of tribo-corrosion is very important and the metal ion concentration, pH and the ionic strength all have an effect (254). It is known that corrosion is a major concern between fretting of the at the head neck interface (254-257), however the contribution to wear of the load bearing surfaces is unclear (238). In this study it has been shown that the wear increases for an increased ionic strength (AWD: 25BCS – 0.589 µm, 25salBCS – 0.746 µm). A larger AWD, therefore an increased metal debris/ion concentration, correlated with a large change in pH for the HSF and BCS fluids. In this case the question remains to what the cause is and what is the effect. Corrosion products of CoCrMo in an aqueous environment include Co II hydroxide, Cr III oxide, Cr III hydroxide (258). Co II hydroxide is soluble within the pH range ~5 – 7 whereas Cr III oxide and Cr III hydroxide require strong acid and bases to dissolve (258). There is limited evidence to fully understand this mechanism and is beyond the scope of this study.

4.6 Conclusions

The chapter has explored the effect of model SF composition and HSF on CrCoMo friction and wear in a simple bench test. The conclusions are as follows:

- Measured wear of CoCrMo couples decreases with protein content in model SF.
- HSF samples gave up to 77% higher wear than the accepted screening fluid 25BCS.
- Increasing the A/G ratio increases the wear suggesting γ-G has superior wear-reducing properties
- The effect of phospholipid addition is more complex; wear is reduced for high A/G ratio but increased for low A/G ratios.
- HA itself is not an effective lubricant in artificial joints
- The size of AWD was proportional to an increase in sample pH, before and after the wear test.

Chapter 5: Optical Imaging of Wear Scars

Summary

In this chapter the rubbed surfaces and residual films on the ball and disc were examined by optical, SEM and WLI techniques. A low power microscope was used to obtain an overall image of the wear scar and surrounding deposits. An SEM was used to image deposits in and around the wear scar at a higher magnification. The surface roughness and topography of untested and tested surfaces was investigated using WLI images. The pattern of deposits were similar for all fluids: model, BCS and human SF. They showed amorphous rainbow deposits formed at either side of the wear scar for both the ball and the disc. On the ball black particulate deposits were also observed beyond the rainbow films, whist on the disc they were scattered around the wear scar. Analysis of the WLI images identified abrasion to be the dominate wear mechanism.

5.1 Introduction

Formation of adherent organic deposits on both CoCrMo and UHMWPE implant surfaces has been reported extensively in the literature for tests on hip simulators (198), bench top tests (48, 112, 143, 207-210) and importantly explanted joints (150, 170, 211, 212). They have been observed using both low power microscopes and SEM imaging.

Most commonly these deposits have been attributed to proteins, and are reported to be thick and adherent (48, 112, 207-210). Wimmer et al. (170) suggested they '*…act as solid lubricant and have a beneficial effect on the wear behaviour of the MOM articulation*.' Other studies have identified glycoproteins as the active wear reducing component (143), this was attributed to the presence of hydrophilic carbohydrate chains forming a low-shear strength fluid layer upon adsorption. Additionally phospholipids have also been reported to be present in the adsorbed film and in some cases thought to be the active wear and friction reducing species (150, 202). On the other hand Pourzal et al. (212) suggested the primary lubricating film comprised of a "graphitised" carbon film.

In each of these reports it is suggested that solid, residual layers are formed on the rubbing surfaces and reduce the wear. They act to hinder surface fatigue and prevent adhesion for both metals and UHMWPE (48, 143, 150, 170, 202, 211, 224). *In vivo* these deposited films have been found at the boundary of the articulating contact region as seen in Figure 5.1 (170).

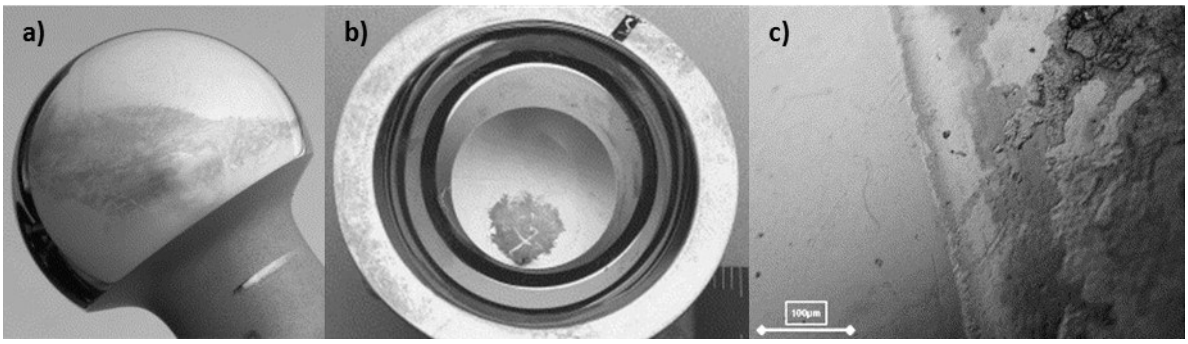


Figure 5.1 - Macroscopic visible deposited films on a explanted prosthesis a) Femoral head b) Acetabular cup c) microscopic image of rainbow interference fringes at transition zone on the femoral head in (a). (170).

SEM imaging is often used to give information about the surface morphology of biological films (259) however it is seldom applied to the study of films on artificial joint surfaces. Büscher et al. (218) identified a globular tribolayer however the analysis was not detailed enough to provide more detailed information. Therefore, this powerful imaging tool could be used to provide information about the morphology and formation of deposited films.

SEM images are also used to examine wear scar surfaces (48, 170, 218) and to distinguish between mechanisms that are purely mechanical and are a combination of chemical and mechanical. Research into implant wear has concentrated on understanding the factors that control wear, such as material properties, bearing design and manufacturing (29, 52, 171, 173, 218, 219, 232) and very few studies have focussed on the fundamental wear mechanisms (48, 170, 211). Further improvements in wear performance will only be possible if the underlying mechanisms and the contribution of SF chemistry are fully understood.

The test described in Chapter 3 uses reciprocating sliding motion and therefore all the major wear mechanisms (adhesion, abrasion, surface fatigue and tribochemical reactions) may act together (48). Grooves and scratches are easily identifiable and therefore abrasion is most commonly reported as the acting mechanism (52, 218, 219), whilst this is correctly attributed to the main form of material loss little research has concentrated on the initiating factors.

Wimmer et al. (48) suggested that the initial wear particle could be produced by one of two ways. The first assumes that an oxide layer is generated via tribochemical reactions which begins to spall off once it reaches a critical thickness. In the second, a wear particle is generated by cyclic contact stresses which is small enough to completely oxidise once torn off the main body. It is assumed that the normal loads are not carried by the fluid and therefore the particles act as the interfacial media. Depending

upon the particles size it may become stuck or dislodged on/in one surface causing abrasion (scratches or grooves) or act as rolling particles resulting in surface fatigue (indentations) (220).

The work in this chapter examines residual film formation and wear scar appearance for the test specimens from Chapters 3 and 4. The following questions were addressed:

1. Do SF organic deposits form on the articulating surfaces? If so, do they contribute to the lubrication process?
2. If surface films are formed are they similar for model, BCS and HSF?
3. Can the morphology of the films be imaged and observed?
4. What wear mechanisms are present/dominant?

5.2 Experimental Programme

There were two aims of this of this chapter, the first was to observe and evaluate the residual films in and around the wear scar for both model, BCS and human SF. The second aim was to examine the wear scar on the disc to identify the acting wear mechanisms. The objectives were as follows:

1. Understand the effect of SF constituents on the residual deposited films using an optical microscope.
    - Proteins (BSA and γ-G)
    - Lipids (DPPC)
    - HA
2. Observe the shape and morphology of residual deposited films using SEM
3. Observe and analyse the wear scar appearance on the disc to identify acting wear mechanisms using a WLI.

5.3 Materials and Methods

5.3.1 Optical Microscopy

After completion of HFRR tests both ball and disc were removed. The ball and disc were rinsed with DI water for 10 s and air dried before observation under an optical microscope. Care was taken to remove excess fluid but not to disturb the residual films. Once fully dried, surfaces were observed using a low power microscope (Axioscope, Zeiss; Germany) connected to an Infinity 2 (Lumenera Corporation; Ottawa).

5.3.1.1 Wear Volume on Ball

The wear volume on the ball was calculated by measuring the approximate diameter of the wear scar from the optical images. Equation 5.1 was used to measure the volume lost, V, where R is the ball radius and h the maximum wear depth which can be calculated using equation 5.2. The radius of the wear scar is r (260).

$$V = \pi h^2 \left(R - \frac{h}{3}\right) \quad (5.1)$$

$$h = R - \sqrt{R^2 - r^2} \quad (5.2)$$

5.3.2 Scanning Electron Microscope (SEM)

Surfaces were observed using a scanning electron microscope (SEM; JCM-6000 NeoScope, JEOL USA Inc.) to achieve high definition detailed images of the surfaces.

To image surface residual films, surfaces were gold coated using a JEOL Smart coater (JEOL USA inc) in order to prevent deposits from charging. Specimens were placed into the sputter chamber at a distance of 20 mm. Once evacuated, specimens are coated for 1 minute achieving a 5 nm thickness.

5.3.3 Wear Scar Analysis

In order to identify wear mechanisms the residual film was removed. Discs were soaked in 2% Decon90 solution in an ultrasonic bath for 10 minutes, before rinsing three times for 10s with distilled water. The specimens were then soaked in distilled water in the ultrasonic bath for a further 10 minutes. Once complete specimens were rinsed with isopropanol and air dried.

White light interferometry was used to image the surface topography. The surface roughness, r_a measurement was taken directly from the imaging programme 'Vision'. Measurements from the surfaces of untested samples were taken as well as areas inside and outside the wear scar outlined by the white boxes in Figure 5.2.

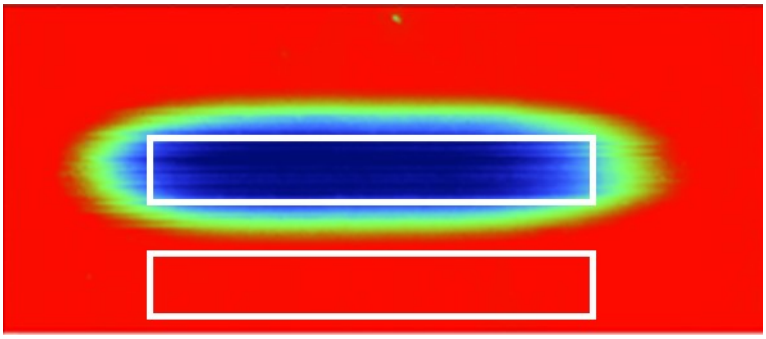


Figure 5.2 - An example wear scar showing the areas inside and outside the wear scar used to measure surface roughness.

5.4 Results: Optical Microscopy

Images of the wear scars and surrounding areas were taken for of the ball and disc specimens for each test performed. The images shown are representative of the wear scar and residual film for each fluid sample.

Figure 5.3 shows the wear scars located at the centre of the images surrounded by surface deposits formed during rubbing. The majority of the deposits occur at either end of the stroke, although a halo is often seen around the whole scar. On the ball there are two distinct regions which have been named the 'rainbow' and 'black' regions. The rainbow regions are at either end of the wear scar where the film appears to be transparent, smooth and amorphous. Interference colours are observed (261) suggesting a thickness of 0.1-1μm, beyond the rainbow films black particulate deposits are observed.

On the disc small rainbow regions are located at the end of the wear scars and dispersed black deposits are scattered across the surface. Residual films are more abundant on the balls and therefore the results will focus on these images. All the deposits were highly adherent once removed from the supernatant fluid and dried. Figure 5.4 shows an expanded region of an mBCS image which illustrates the rainbow and black regions. Deposits are insoluble, appear viscous and are stongly adhered to the surface.

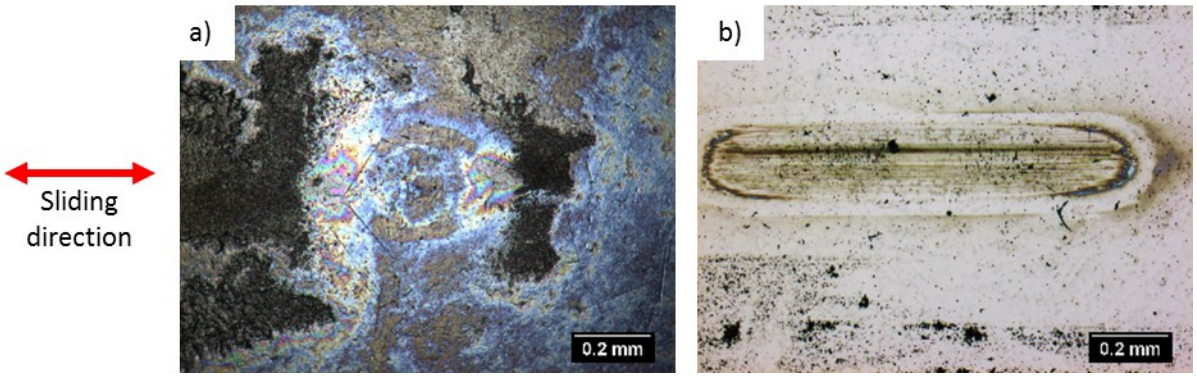


Figure 5.3 – Imaging of wear scars and surface deposits using a low power microscope for 1 ml 25BCS a) ball b) disc.

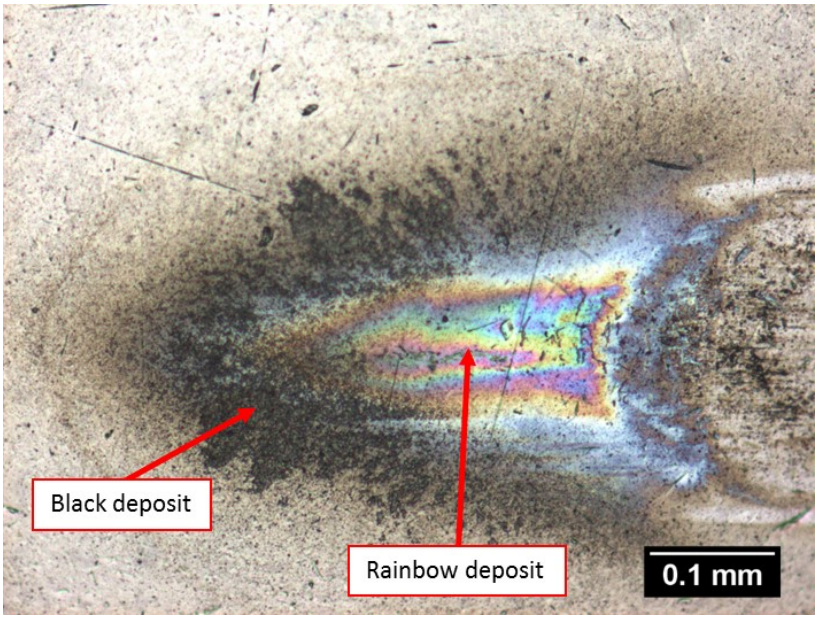


Figure 5.4 – Close up of deposits from mBCS fluid at the end of the stroke.

5.4.1 Effect of Increasing BCS Concentration

Figure 5.5 shows the wear scar and residual films on the balls for increasing BCS concentration, rainbow and black regions are present in all images. Both rainbow and black deposits are least abundant for 10BCS, the rainbow region is predominantly blue suggesting a thin film and the black regions are far from the wear scar. As the BCS concentration increases the rainbow region shows a higher number of interference fringes suggesting a thicker film and the black deposits become larger, for 100BCS the black film extends to fully surround the wear scar.

The calculated wear scar volume from the ball is shown in Figure 5.6. The volume decreases for increasing protein concentration following the same trends as shown in section 3.4.2, therefore these calculations will not be performed for other images in this chapter.

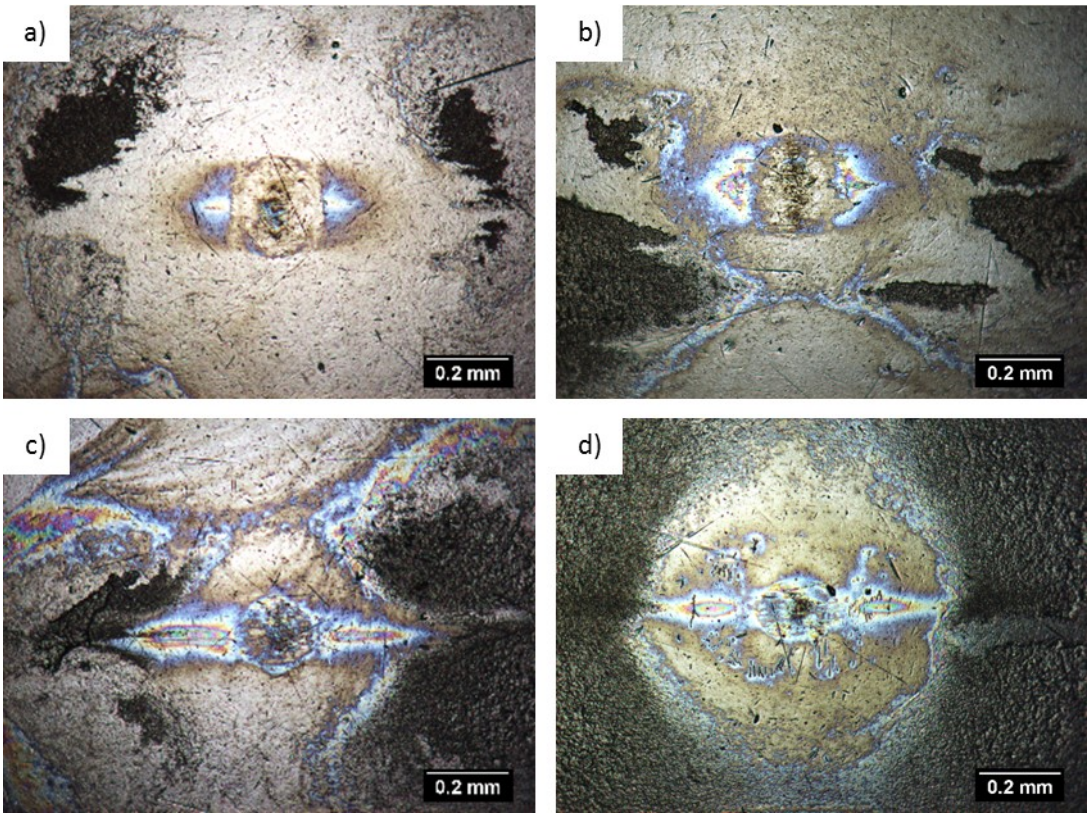


Figure 5.5 – Images of wear scars on balls for 2 ml BCS a) 10BCS b) 25BCS c) 50BCS d) 100BCS.

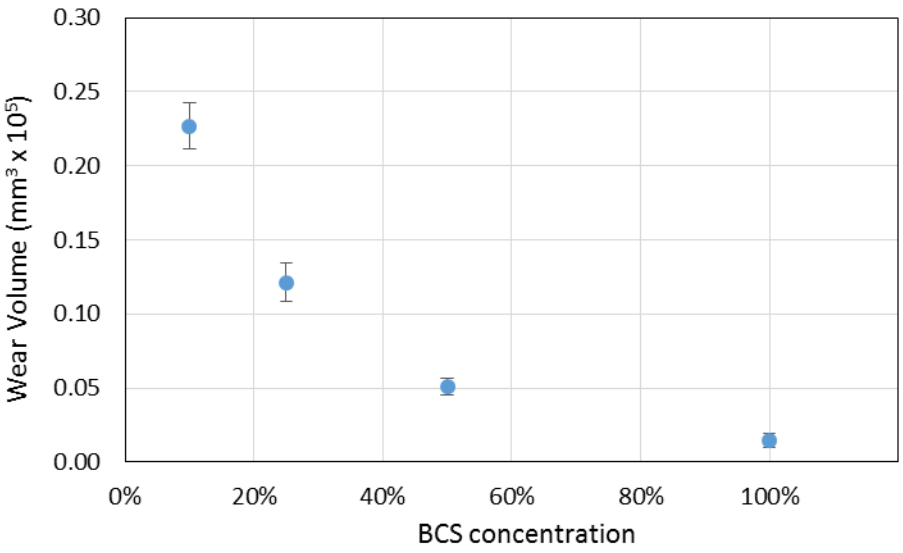


Figure 5.6 – Wear scar volume on ball vs BCS concertation.

5.4.2 Effect of the Addition of Saline

Figure 5.7 compares the wear scars of 25BCS and 25salBCS to see the effect of saline on the formation of the residual film. The most obvious observation is that the black deposit for 25salBCS is smaller and thinner. On the other hand, the rainbow film is smaller on the 25BCS sample than the 25salBCS sample however differences are minimal.

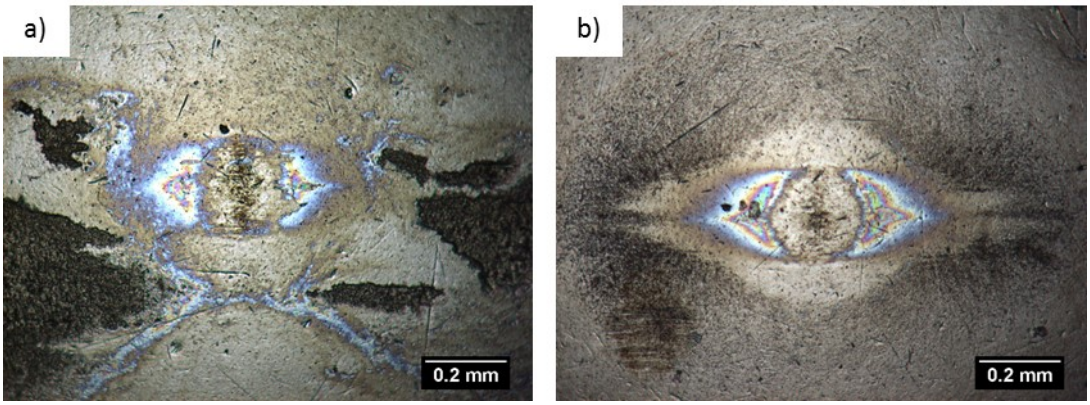


Figure 5.7 – Images of wear scar on balls for a) 2ml 25BCS and b) 2 ml 25salBCS.

5.4.3 Effect of Protein Concentration

Wear scar images from the ball for model fluids; saline, 25salBCS, mBCS, mH, mOA and mPP with and without DPPC are shown in Figure 5.8.

For all solutions containing proteins (Figure 5.8 b-f) distinct rainbow regions at either side of the wear scar were present in similar quantities whilst the black deposits generally appear to increase for increasing protein concentration. The rainbow region is not present for the solutions containing DPPC alone; therefore, it suggests that it is predominately protein based.

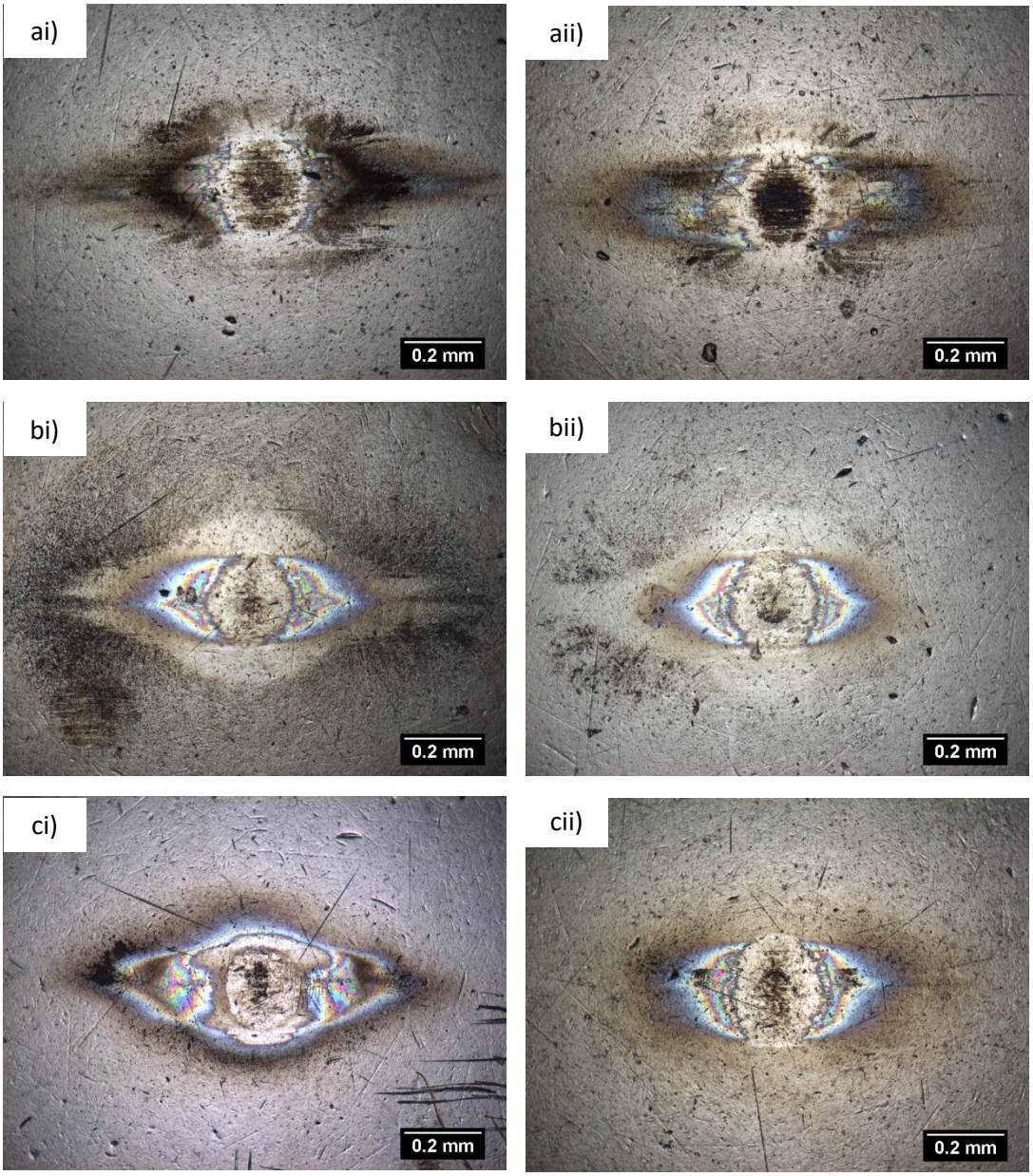
The amount of black deposits appears to be linked to the protein concentration. For example, the lubricants 25salBCS, mBCS and mH, had the lowest total protein concentration (18 mg/ml) and the black deposits in these images (Figure 5.8 bi, ci and di) appear to be the least abundant. The sample mOA had a protein concentration of 30 mg/ml and in these images (Figure 5.8 e i) where the amount of black deposits appears to have increased. The sample with the largest amount of black deposits is mPP (Figure 5.8 fi) with a total protein concentration of 40 mg/ml and have begun to extend around the side of the wear scar.

The fluids mBCS and mH without DPPC (Figure 5.8 c i and d i) have the same total protein concentration however they have an A/G ratio of 0.8 and 2 respectively. A larger amount of black deposits on either side of the wear scar can be observed for mBCS compared to mH, where these deposits are barely visible. Although evidence is limited this suggests the deposits could be due to γ-G rather than BSA.

5.4.4 The Effect DPPC

The images for saline with and without DPPC (Figure 5.8 a ii & ii respectively) show predominately black deposits. The wear scar itself is blackened in comparison to the wear scars of the proteinaceous model fluids. Cobalt oxides are black in appearance and therefore it is possible that the blackened wear scar is due to formation of a thin cobalt oxide layer (249).

By comparing samples with and without the addition of DPPC (Figure 5.8 a-f i (no DPPC) to a-f ii (DPPC)) it is possible to see how DPPC affects the formation of deposits, the behaviour is complex and DPPC appears to inhibit the amount of black deposits formed for 25salBCS, mBCS and mOA. However, the amount of black deposits appears to increase for mH and mPP.


ai)
0.2 mm
aii)
0.2 mm
bi)
0.2 mm
bii)
0.2 mm
ci)
0.2 mm
cii)
0.2 mm

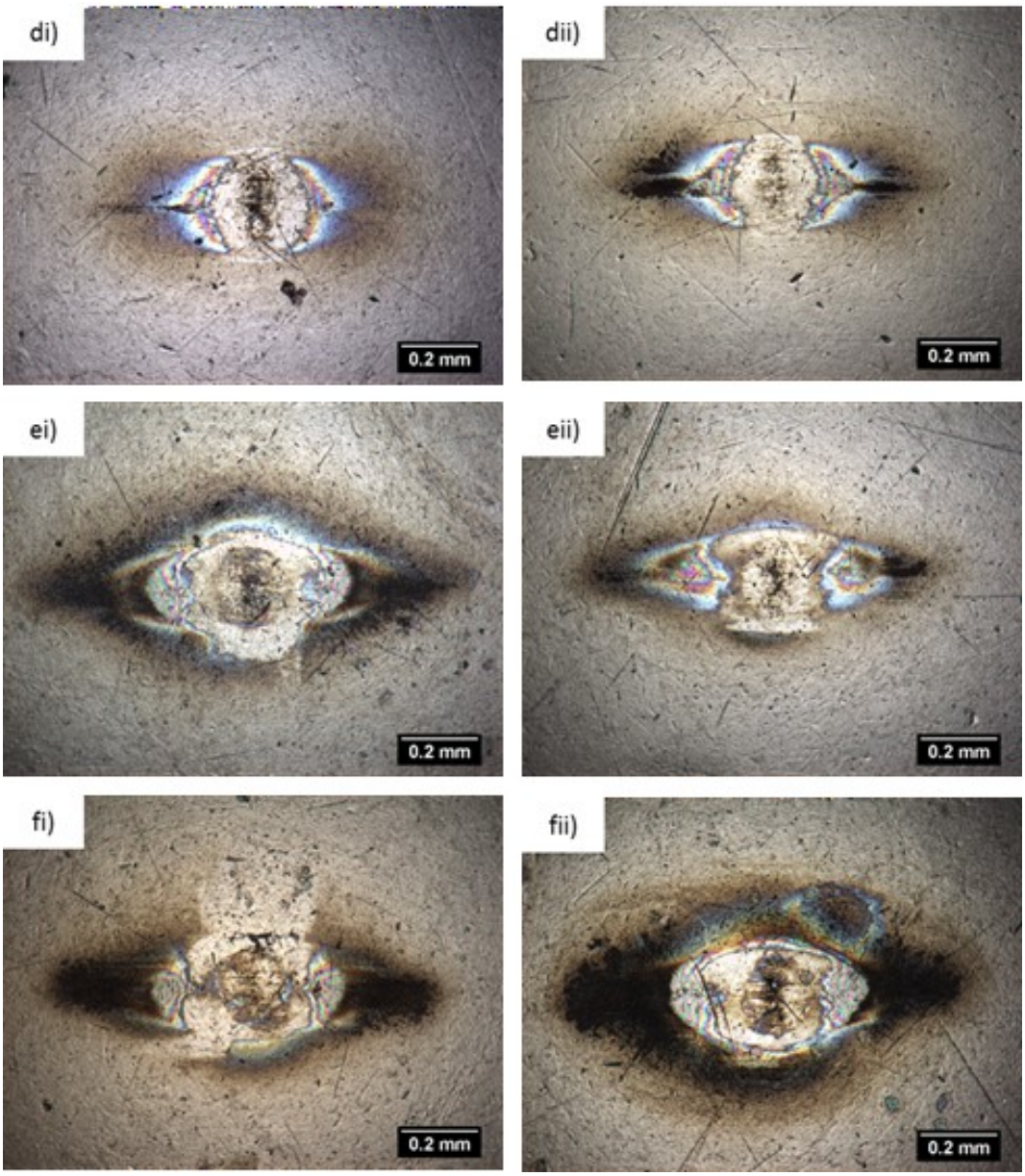


Figure 5.8 - Images of wear scar on balls with and without DPPC present a) i) Saline ii) Saline + DPPC b) i) 25BCS w/saline ii) 25BCS w/saline + DPPC c) i) mBCS ii) mBCS + DPPC d) i) mH ii) mH + DPPC e) i) mOA ii) mOA + DPPC f) I mPP ii) mPP + DPPC.

5.4.5 Effect of HA

Figure 5.9 shows images of the wear scar on ball for HA, mBCS + HA and mBCS + HA + DPPC. For HA only the wear scar is blackened similar to that of saline and only DPPC suggesting that an oxide layer is present and therefore corrosion may be playing a role. No rainbow or black regions are observed however there is darker patches at either end of the wear scar. For mBCS + HA and mBCS + HA + DPPC the deposits have similar rainbow regions either side of the wear scar and reduced black deposits.

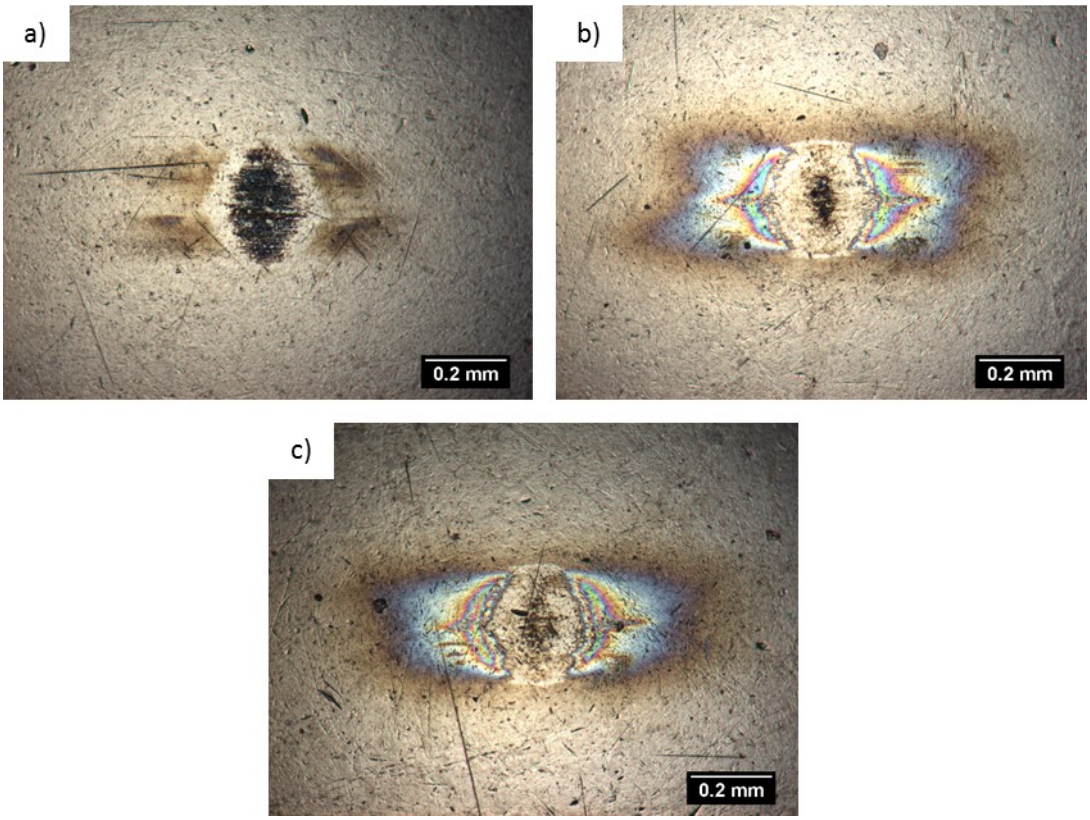


Figure 5.9 a) HA b) mBCS + HA c) mBCS + HA + DPPC.

5.4.6 HSF

Similar rainbow films were observed for the HSF samples; however, the black deposits appeared to differ compared to the model samples. Differences were also observed between tests that gave high and low wear. Figure 5.10 shows the wear scar and residual film for two samples HSF113 (low wear) and HSF156 (high wear). For the low wear sample (Figure 5.10 a) a thin dark film is present at either side of the rainbow film, Figure 5.10 a ii shows the end of the residual film where small amounts of thicker black deposits are located. Figure 5.10 b shows the film deposits from a high wear sample, the residual film either side of the rainbow film covers a smaller area and is in two distinct patches which have interference fringes.

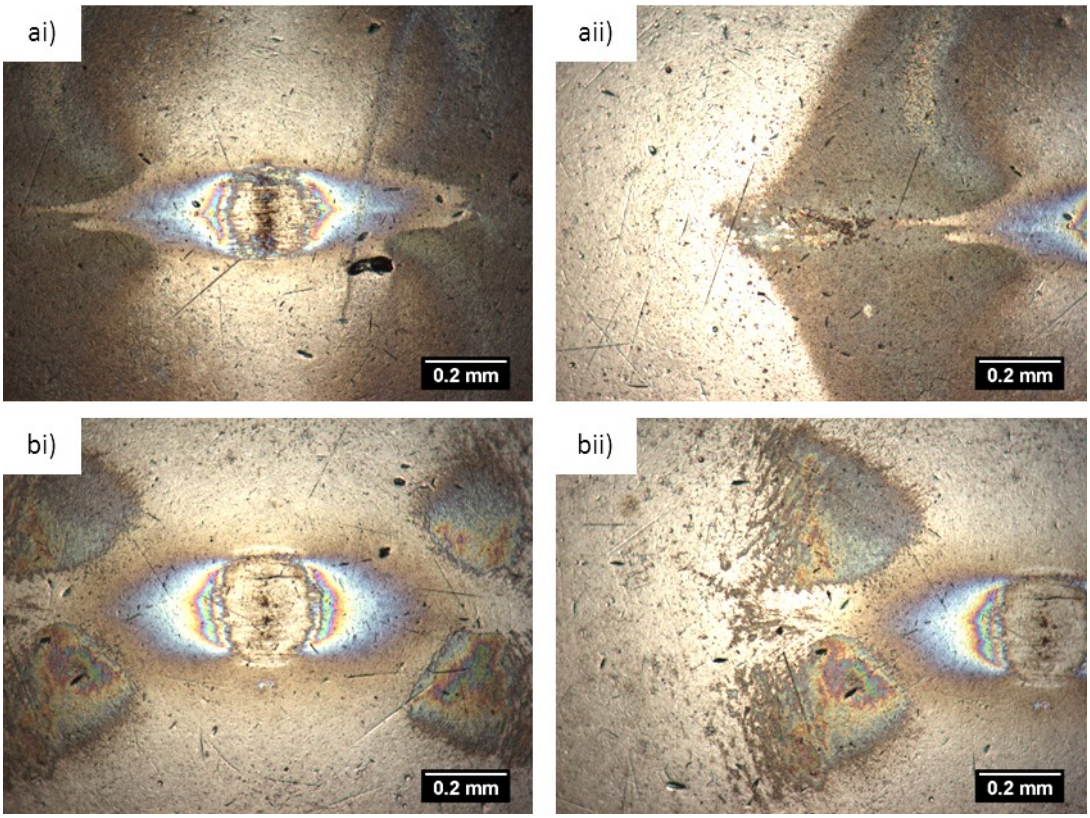


Figure 5.10 – Wear scar and surface deposits on a) HSF 113 (low wear) i) Central ii) Side b) HSF 156 (high wear) i) Central ii) Side.

5.4.7 Roll Formation

The formation of 'rolls' were observed on the ball and inside the wear scar on the disc and is shown in Figure 5.11. These were observed for mBCS, mOA and mPP without DPPC, where the γ-G content was larger than 10 mg/ml. The lengths of the rolls are in the range 5 – 62 µm, measured from the optical images.

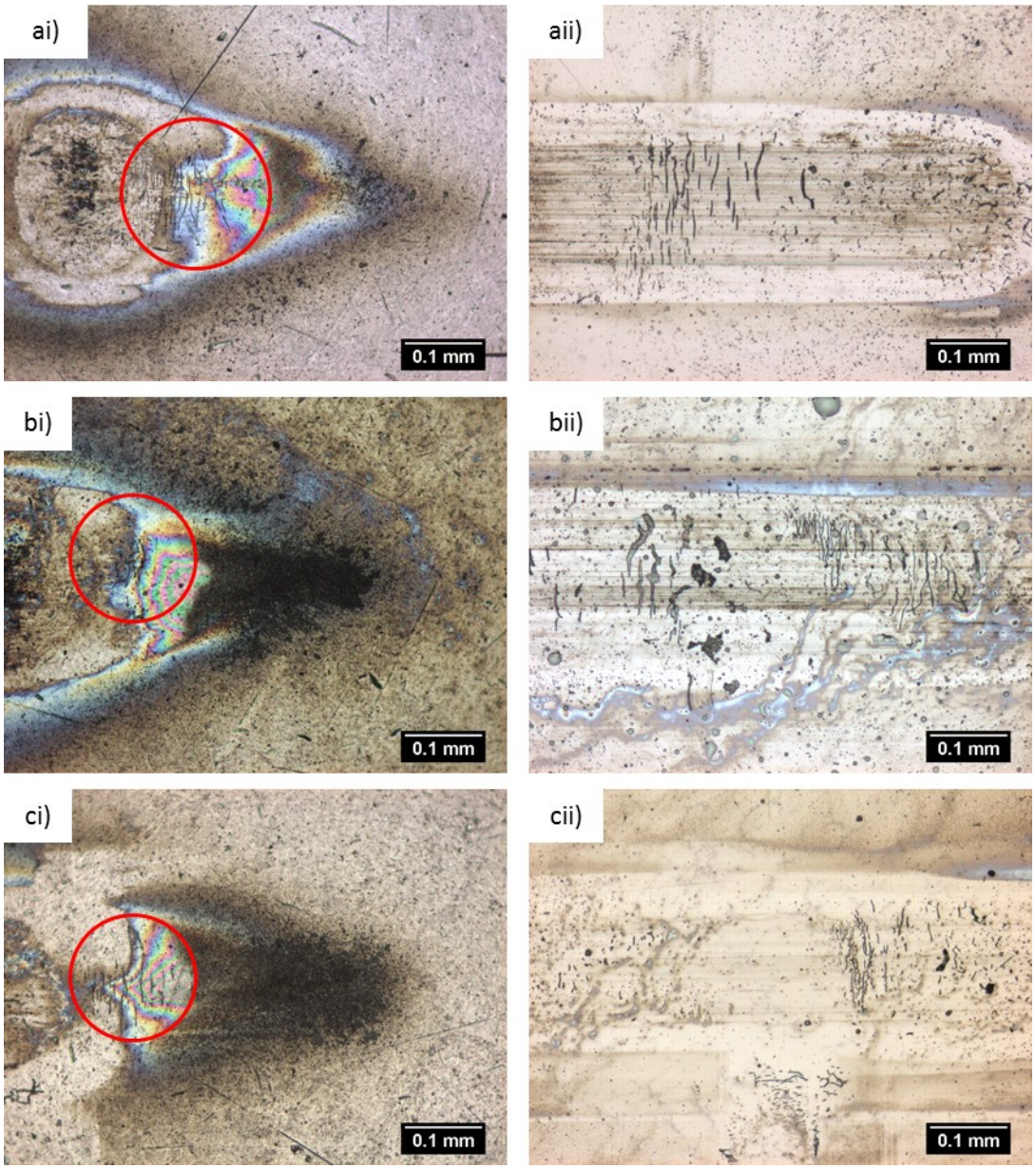


Figure 5.11 –Roll formation inside wear scars a) mBCS i) Ball ii) Disc b) mOA i) Ball ii) Disc c) mPP i) Ball ii) Disc.

Roll like deposits were also observed for HSF041 and HSF113 samples, both of which had similar AWD to 25BCS, Figure 5.12 shows these rolls inside the disc wear scar and are located within the circles. The rolls are much shorter in length and are in the range ~1 – 14 µm and are less abundant than those observed in the model fluids.

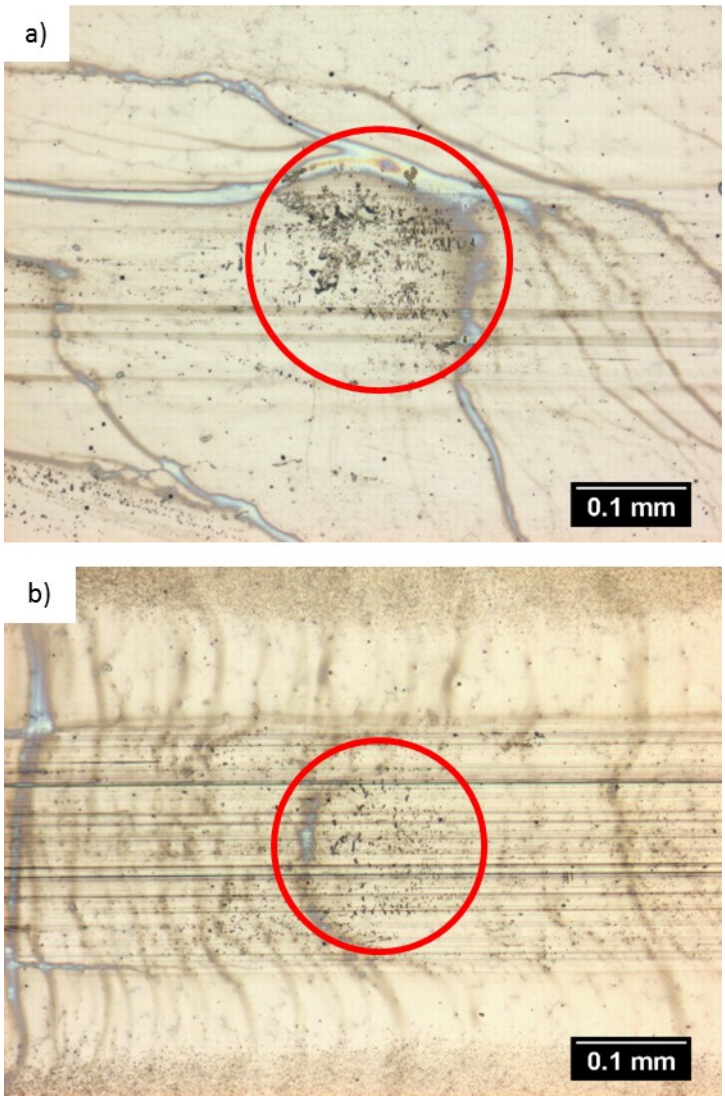


Figure 5.12 - Disc scars with roll formation of low AWD specimens a) HSF041 b) HSF113.

5.5 Results: SEM imaging

5.5.1 Deposited Films

An example of an SEM image of a black deposit from a ball tested with 25BCS is shown in Figure 5.13 and it has a fine fibrous, porous structure. Figure 5.13a is at a lower magnification and shows fibril like structures within the deposit, whereas at a higher magnification (Figure 5.13 b) they are not as easily identifiable. At a higher magnification it can be seen that these deposits have a densely matted structure.

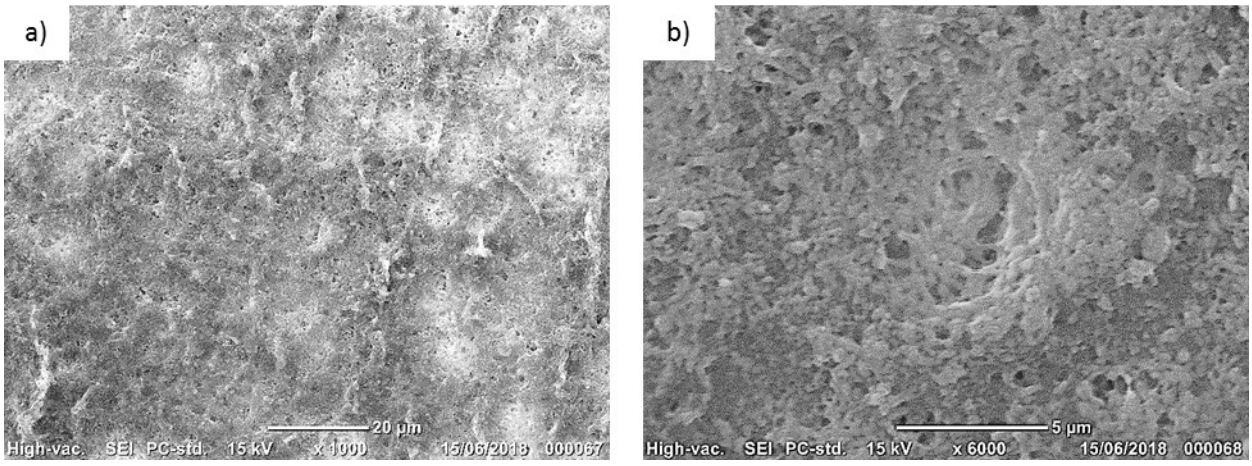


Figure 5.13 – Black deposits on ball from 25BCS a) x1000 b) x6000.

SEM images from black deposits at the end of the disc scar for 25BCS are shown in Figure 5.14 and are shown at a higher magnification (x3000) in Figure 5.15. Some deposits are agglomerated rope-like fibres (Figure 5.15a), whilst others are single fibres and aligned perpendicular to the sliding direction (Figure 5.15b) similar to deposits seen the model fluids in section Roll Formation.

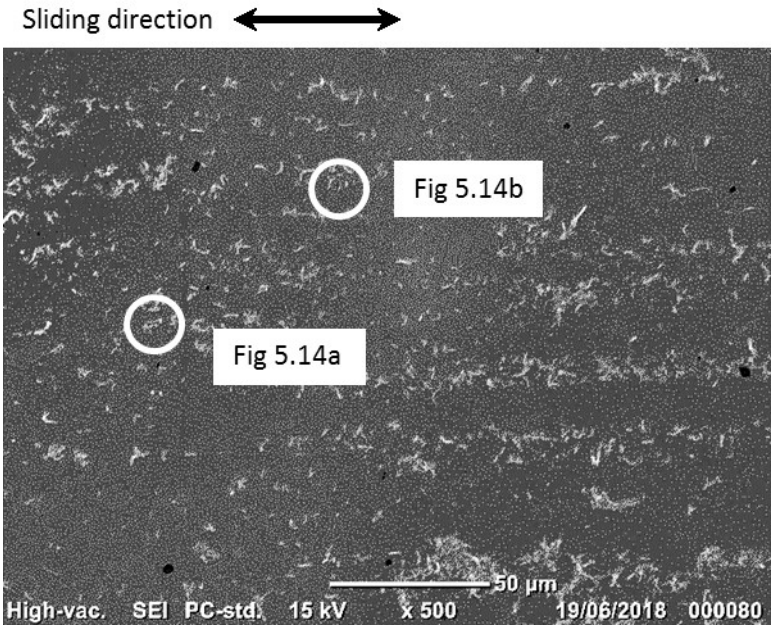


Figure 5.14 – Black deposits on disc at end of wear scars from 25BCS.

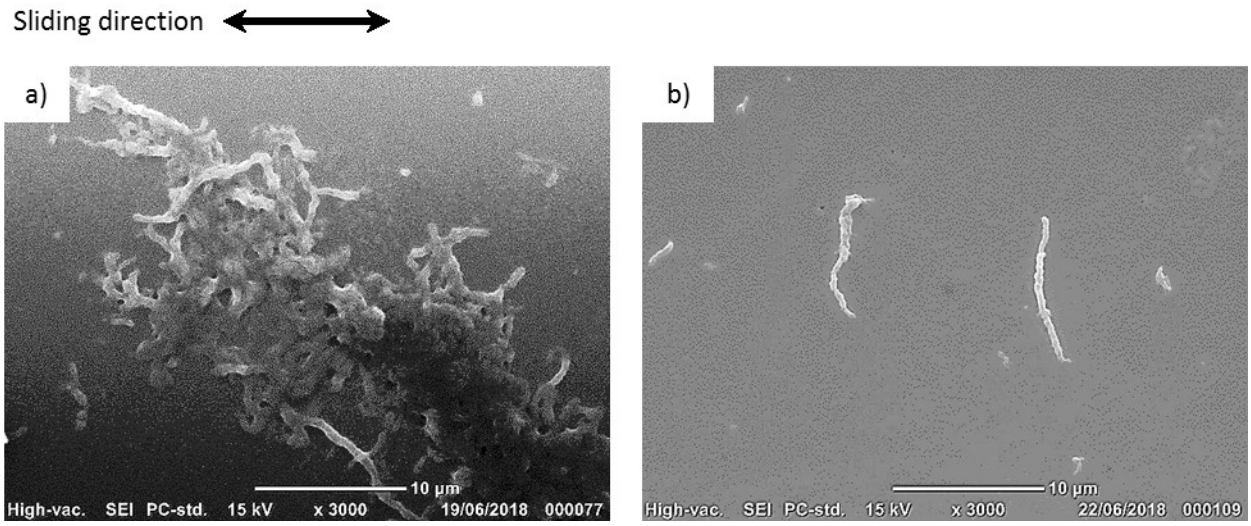


Figure 5.15 – Black deposits at the end of the wear scar for 25BCS a) Agglomerated fibres b) Singular fibres.

Additional evidence in this study shows that the material passes through the contact: Figure 5.16 shows single fibrils 3.9 µm within the wear scar for 25BCS.

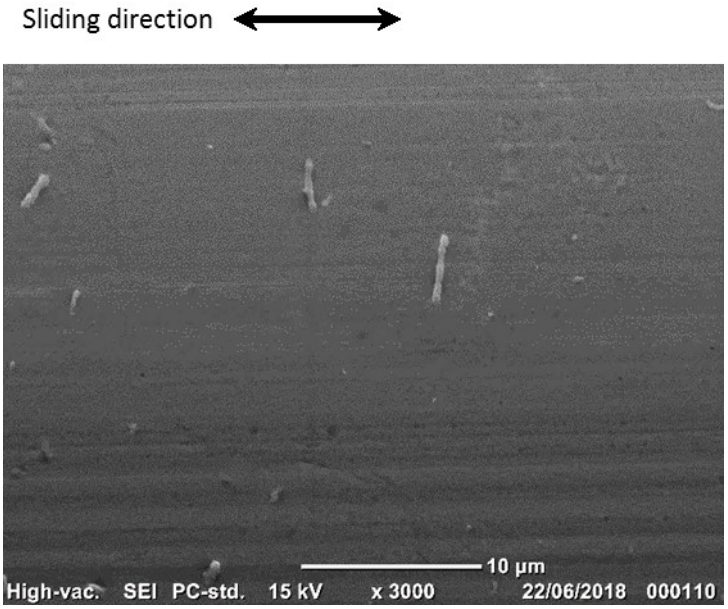


Figure 5.16 – Fibril deposits inside the wear scar for 25BCS.

These rope structures were also observed for HSF samples. Figure 5.17 shows low (x250) and high (x4000) magnification SEM images of remaining deposits in the centre of the wear scar for HSF110.

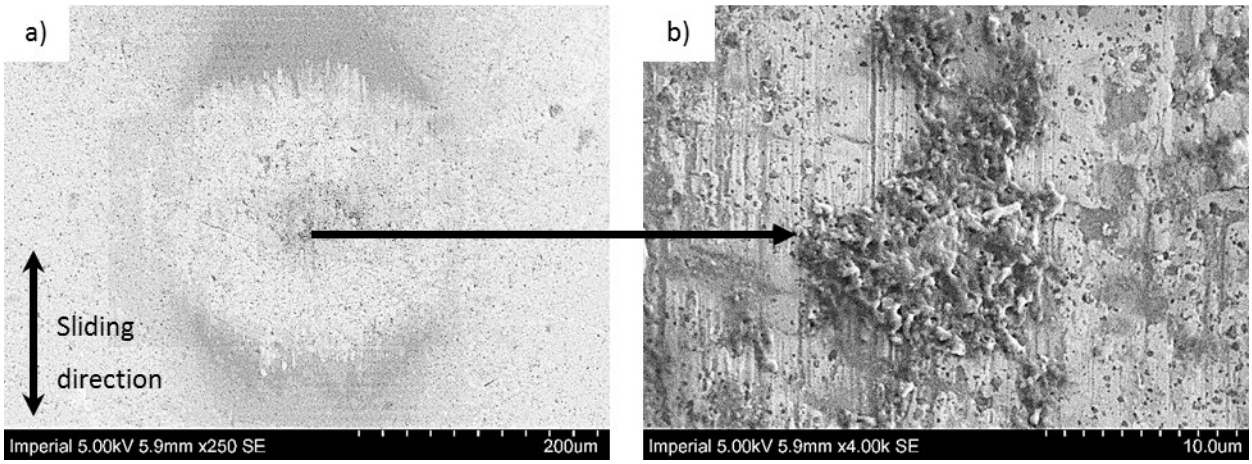


Figure 5.17 – Deposits inside the wear scar on the disc for HSF110 a) x250 b) x4000.

5.6 Results: Wear Scar Analysis

White light interferometry was used to image the surface topography and analyse the roughness of untested discs, unworn areas located outside the wear scar and surface inside the wear scar.

Figure 5.18 shows that the surface of the disc prior to testing is characterised by 'blocky' carbides of ~0.1 µm in height (Figure 5.18a), this is typical of as-cast CoCrMo alloys (49). Figure 5.19 shows the surface topography of the ball which has a rougher appearance. The asperities are between 0.10 – 0.15 µm in height and 5 – 20 µm wide.

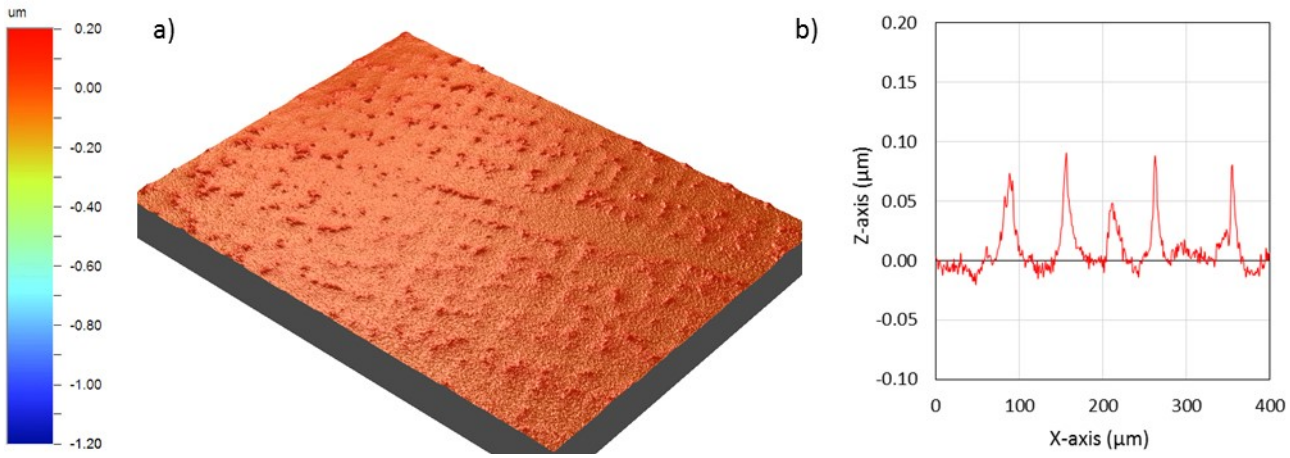


Figure 5.18 – Surface topography of an untested disc a) 3-D image b) Graphical profile.

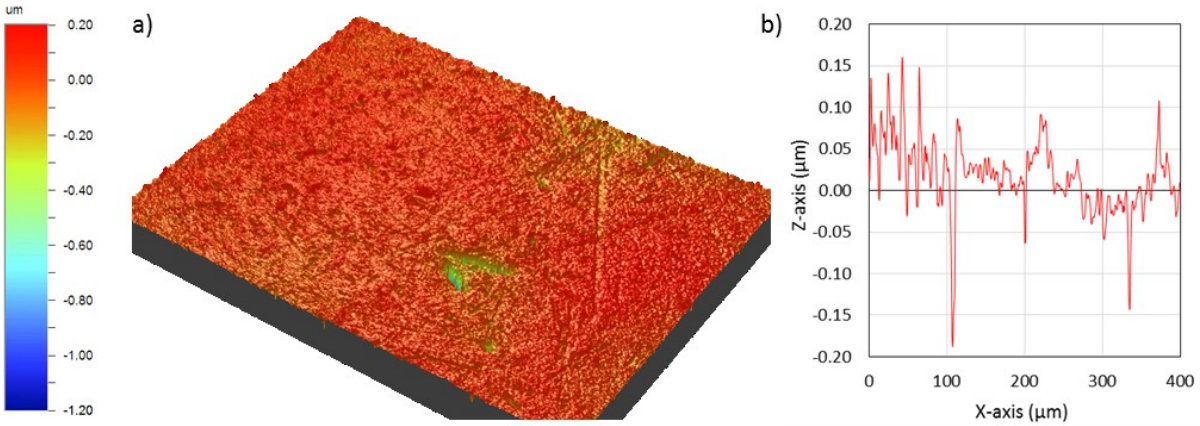


Figure 5.19 - Surface topography of an untested ball a) 3-D image b) Graphical profile.

Figure 5.20 gives examples of the surface topography from the centre of the disc wear scar for 25BCS, saline and HSF164. Figure 5.20 ai - ci give a 3-D visualisation showing that each sample exhibits scratches and grooves parallel the sliding direction, the difference in colour represents the AWD. Figure 5.20 a ii – c ii shows the width and depth of the groves and scratches, which are around 5 - 15 µm wide which is similar in size to the asperities on the ball which are likely to be causing the abrasion.

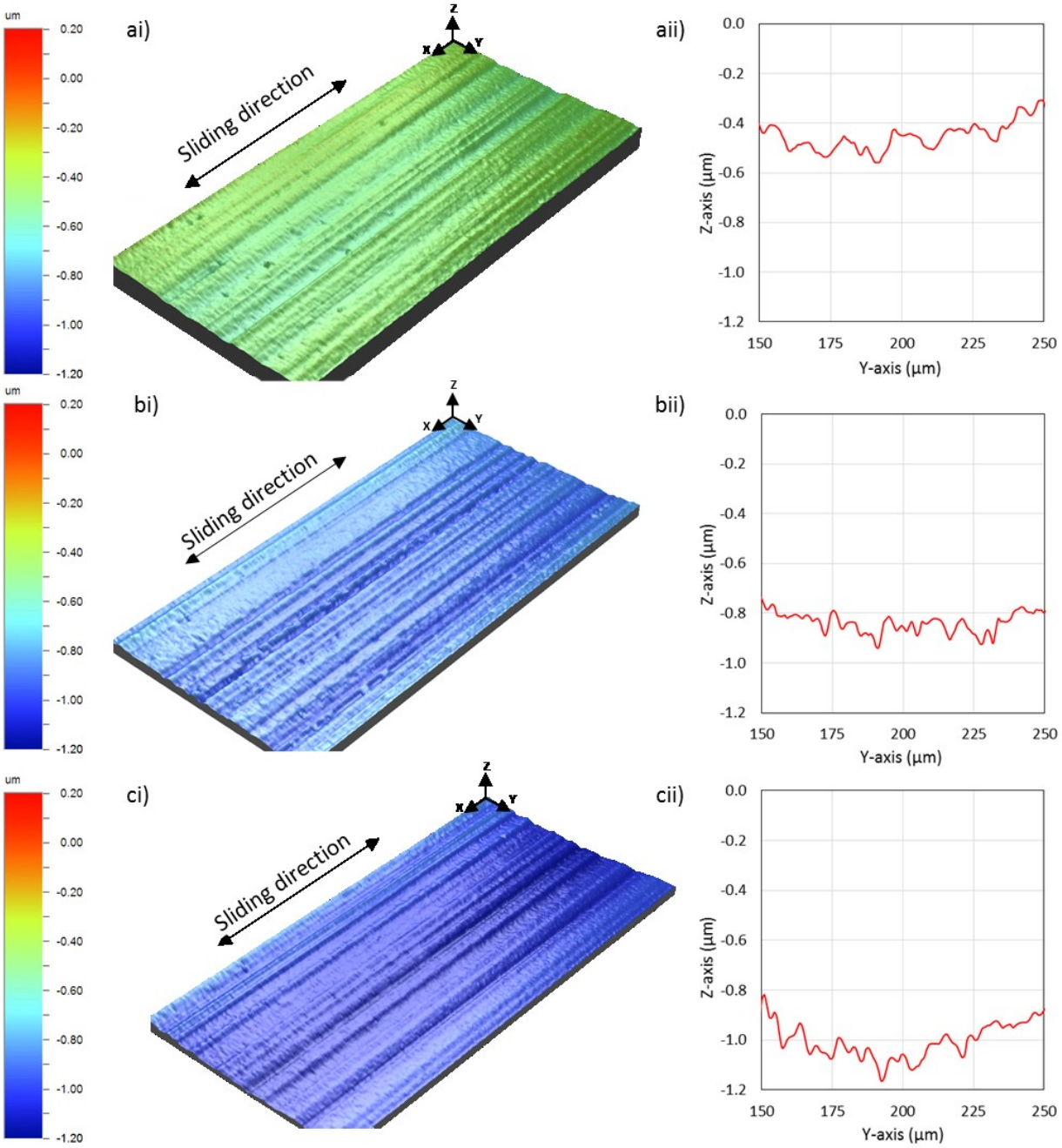


Figure 5.20 –Example of surface topography of the disc wear scar a) 3-D image b) Graphical profile for i) 25BCS ii) Saline iii) HSF164.

Inside the wear scars deep pits were often present as shown in Figure 5.21 which shows examples for 25BCS and HSF110. The depth of the pits are shown in Figure 5.21b and are in the range 0.72 –1.19 µm.

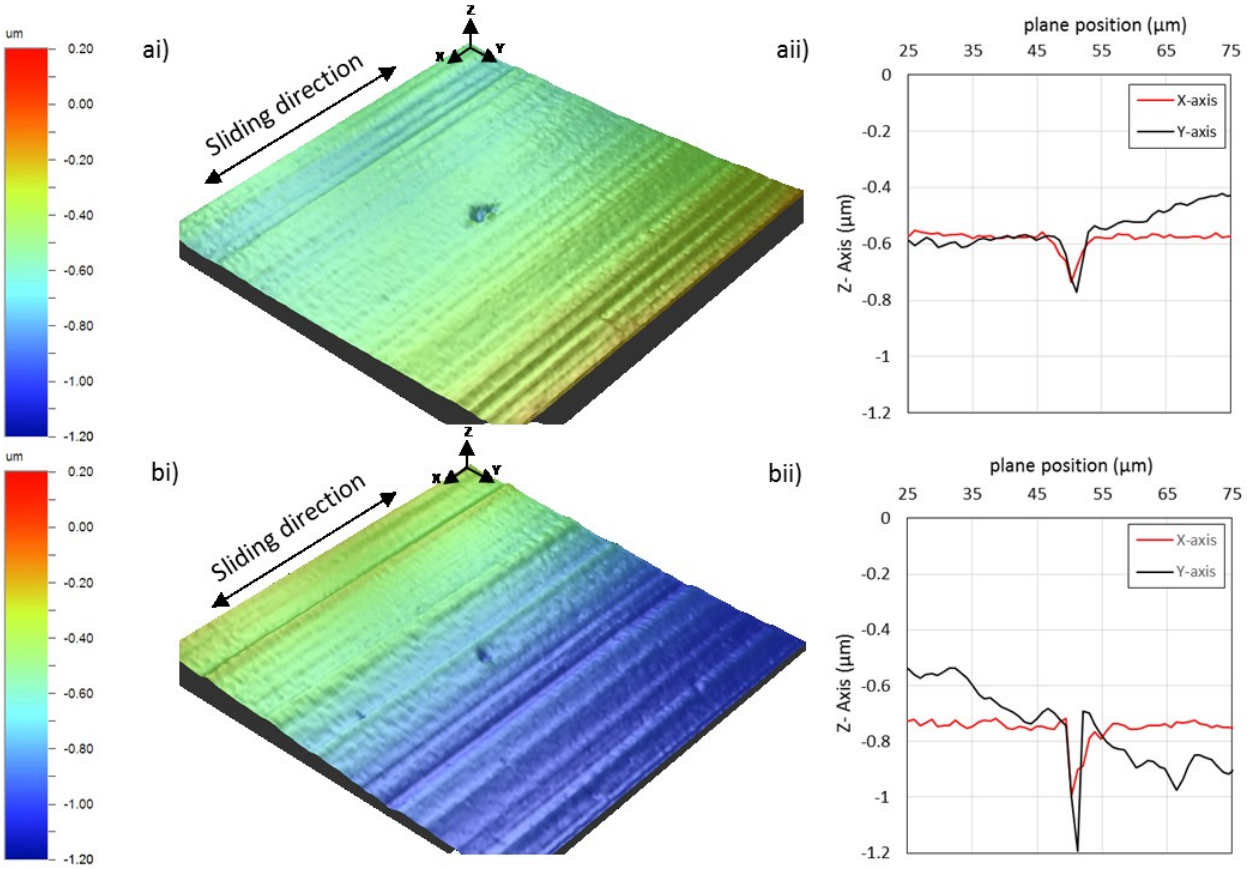


Figure 5.21 - Example of plucked carbide from the disc wear scar a) 3-D image b) Graphical profile for a) 25BCS b) HSF110.

The surface roughness, r_a, of the unworn surface was $r_a = 9.1 \pm 1.9$ nm this is compared to the unworn areas outside the wear scar which would have been in contact with the lubricating fluids for samples 25BCS, saline and HSF samples in Figure 5.22. There is little difference in the surface roughness of the untested sample and the unworn regions for the 25BCS samples. However, there was an increase in the r_a when the surface was in contact with both saline and the HSF samples. This was most pronounced for saline suggesting that surface corrosion had occurred.

The surface roughness from inside the wear scars for all samples analysed exhibited a large increase when compared to the untested surfaces which is illustrated in Figure 5.22. The saline samples have the largest surface roughness at $r_a = 122.2 \pm 23.1$ nm which is unsurprising as tribo-corrosion will play a role (238). On average inside the wear scar the HSF samples have a surface roughness $r_a = 90.1 \pm 24.5$ nm and 25BCS $r_a = 59.1 \pm 10.0$ nm.

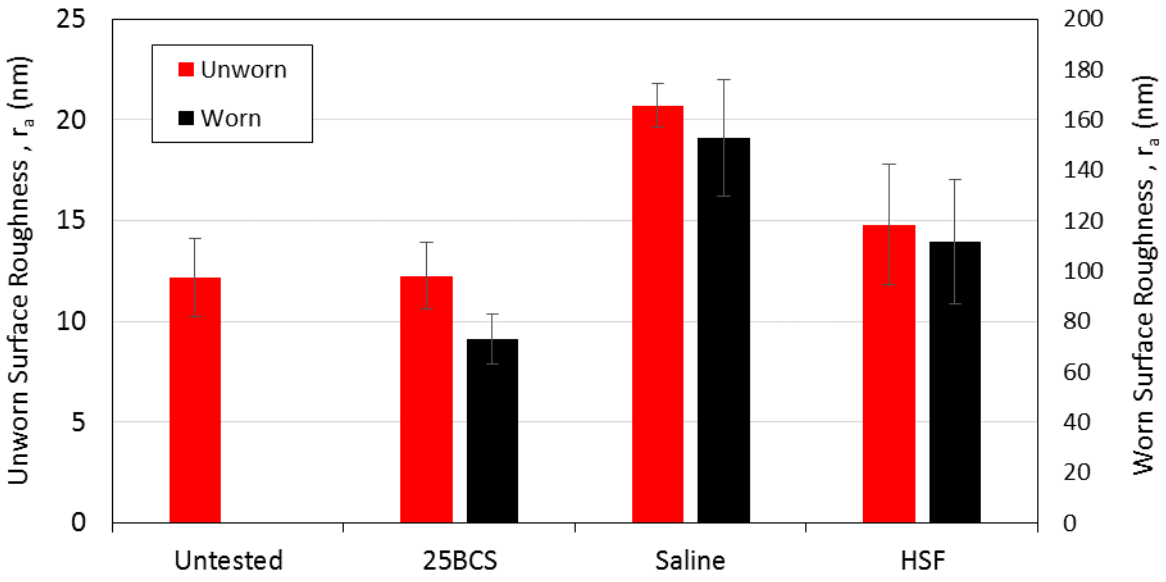


Figure 5.22 – Surface roughness (r_q) of an untested disc, unworn and worn areas of the disc samples 25BCS, Saline and HSF samples.

5.7 Discussion

Optical and SEM imaging methods were used to examine the pattern of lubricant deposits formed during the wear tests. Surface topography both in and outside the rubbed region was analysed by WLI. The aims were to provide relate these observations to SF chemistry and measured wear, and to provide insights into lubrication and wear mechanisms. Firstly, the effect of increasing the BCS concentration was analysed before looking at the effect of the total and specific protein concentration with and without DPPC and HA. Finally, surface film patterns from HSF samples were examined and divided into high and low wear classifications.

5.7.1 Optical and SEM Imaging

At the end of the HFRR test deposited films were observed in and around the wear scar on both the ball and disc specimens. Similar patterns of amorphous rainbow films and black dispersed particles were observed for all protein-containing fluids including BCS, model and, importantly HSF samples. These were insoluble, appeared viscous and strongly adhered to the surface. These films were not observed for the saline, DPPC and HA fluids suggesting they are primarily proteins. High viscosity deposits have been reported to form at the inlet and was attributed to aggregated proteins (112).

The similarity of the model and HSF patterns suggested the fundamental lubrication mechanisms were alike. However, differences were observed in the extent of the deposits depending on the protein content, presence of DPPC and ionic strength of the solution.

Overall the amount of rainbow and black deposits appeared to increase for increasing BCS and total protein concentration. It was shown in Chapter 3 that for increasing BCS/protein concentration the wear decreased which suggests film formation contributes to wear prevention. This observation agrees with previous results from our group (110, 112, 200) and a number of other studies (48, 170, 177, 198, 211).

As well as total protein content the composition (A/G ratio) also affected film pattern and AWD. mBCS and mH have the same total protein content (18 mg/ml) but different specific protein content (A/G = 0.8 and 2 respectively). Limited evidence indicates that the black deposits are greater for mBCS which has a lower A/G ratio and therefore a higher γ-G content and exhibited a lower AWD. These findings indicate that these black deposits are more likely to form when γ-G is present. γ-G has been reported to reduce wear in other studies (110, 111) and at a low A/G ratios (262). In addition γ-G preferentially absorbs onto a chromium surface at a faster rate when compared to BSA (98).

25BCS is the most common reference fluid, however model fluids tested in Chapter 4 were made using saline with a known ionic strength. It is of interest to compare residual films from 25BCS and 25salBCS to understand how saline affects the residual films. Whilst the change of rainbow deposits was negligible the thickness and volume of black deposits decreased, which can be related to the higher wear seen in 25salBCS. The reduction in surface deposits agrees with Parkes et al. (98) where it was shown that an increase in ionic strength decreased the absorption rate of BSA. 25salBCS (Figure 5.8 bi) and mBCS (Figure 5.8 ci) have the same total and specific protein content as well as ionic strength however 25salBCS contains additional constituents such as phospholipids and HA because it is derived from bovine blood (39, 253). The black deposits have a different appearance, 25salBCS is fine and dispersed whilst for mBCS the deposits appear thick and concentrated at the end of the rainbow deposits. The AWD for 25salBCS was larger than mBCS by 32 nm, which indicates that other constituents are playing a role in the formation of the residual film. A comparison of residual films formed with and without DPPC (Figure 5.8) at first glance appears complex. The amount of black deposits visually observed decreases for 25salBCS, mBCS and mOA but increases for mH and mPP with the addition of DPPC. However, when compared to the A/G ratio and AWD the relationship becomes clearer. The model fluids 25salBCS, mBCS and mOA have a low A/G ratio (0.8, 0.8 and 1.5 respectively; high percentage of γ-G) and the AWD increases with the addition of DPPC. Conversely the model fluids

mH and mPP have a high A/G ratio (2 and 3 respectively; low percentage of γ-G) and the AWD decreases with addition of DPPC.

A study by Parkes et al. (98) measured the adsorbed mass of proteins and lipids adsorbed onto a silica surface using a quartz micro balance. Proteins present were BSA and γ-G (A/G = 4.2; low percentage γ-G), the lipid was DPPC. It was reported that the addition of DPPC increased the mass adsorbed by 145% showing the increase in adsorbed film for a protein/lipid mix at low γ-G concentration. It was concluded that both proteins and DPPC was adsorbed on the silica surface. Other studies have shown for static adsorption 14% less BSA and 81% less γ-G adsorbed onto a PC lipid compared to a silica surface (263). Evidence of lipid deposits has also been reported for films on explanted joints (150).

In the context of the results presented this suggests that DPPC inhibited the ability of both BSA and γ-G to absorb onto the rubbing surfaces, however this has a greater effect on γ-G. It is likely that for all fluids the black deposit comprises of both proteins and DPPC however at low A/G ratios the amount is reduced as less γ-G can adsorb. At a high A/G ratio the deposited film increases as DPPC only marginally decreases the amount of proteins that can be adsorbed so the resultant deposit of proteins and DPPC is greater than the protein only deposit.

The rainbow and black deposit patterns were observed for all the HSF samples. For analysis the samples were divided into two categories; high and low wear. The AWD for two of the samples (HSF041 and HSF113) was comparable to 25BCS and therefore defined as low wear. The AWD for the additional six samples was over 37% greater than 25BCS and therefore defined as high wear (HSF077, HSF110, HSF135, HSF145, HSF156 and HSF164), examples for each are given in Figure 5.10. Again, the extent of the black deposits particularly inside the wear scar appear to scale with the measured wear.

As discussed in Chapter 4 for samples with high AWD the change in pH was greater (stronger base). Observations from this chapter suggested that the high AWD is associated with small amounts of black deposits. It is known that a higher pH can alter the charge of amino acids in the proteins, increasing the repulsion between the surface and protein (264-266) which has been reported to cause 40 % less γ-G to be adsorbed onto a silica surface at a pH of 8.1 compared to 7.4 (98).

Further information about the structure of these deposits were investigated using SEM imagining. Roll like deposits were observed on both ball and disc in model fluids mBCS, mOA and mPP all with a γ-G content greater than 10 mg/ml. These rolls were also observed for the low wear human samples HSF041 and HSF113, comparatively they were less abundant and can only be seen on the disc. The length of the rolls were in the range of 5-62 µm and 1-14 µm for the model and human samples respectively. No fibular deposits were observed when DPPC was present.

Murakami et al. (262) reported similar adsorbed fibular films as a result of articulation using a PVA-glass interface. Evidence of fibrils was shown for solutions of single protein solutions of BSA and γ-G and mixtures in A/G ratios of 0.5 and 1. It was stated when the A/G = 0.5 the deposits were more strongly adsorbed, and the fibular aggregates were more abundant compared to the solution with A/G = 1. Additionally, rolling motion of isolated fibular formations was observed at the same speed of articulation.

Fibular like deposits were identified at the end and inside the wear scar, the fibres appear to be aligned perpendicularly to the sliding direction in 25BCS. Other coiled rope-like structures were identified for 25BCS and HSF110. As these deposits were identified in protein only solutions in mBCS, mPP it follows that these are formed of proteins. In the literature denatured proteins are described as having fibril structures some of which twist around each other to form insoluble supercoiled rope-like structures (267-271). SEM images for partially denatured whey protein (mixture of globular proteins) showed a similar fibular structure (272)

5.7.2 WLI Analysis of Test Surfaces

The surface roughness (Ra) of the untested disc and ball surfaces was 9.12 ± 1.9 and 39.6 ± 1.5 nm respectively. WLI images also showed the presence of carbides which are typical of as-cast CoCrMo alloys (49, 112, 169). It is reported that these carbides are hard in nature and have a high chromium, molybdenum and carbon content when compared to the metal matrix phase. The carbides in the unworn sample had a height of ~0.1 μm, the size of carbides from unworn femoral heads are approximately 0.08 – 0.10 μm in height (49, 112) and have upper surface dimensions of approximately 50 x 20 μm (112).

The roughness of the untested surface was r_a = 9.1 ± 1,9 nm which is consistent with the surface finish in most commercial hip replacements (55). This was compared to roughness of regions of the CoCrMo discs which were unworn but were in contact with the test fluid. Little difference was seen for the 25BCS samples however there was an increase in surface roughness of the saline and interestingly the HSF samples. This was most pronounced for the saline solution with a r_a = 16.9 ± 1.1 nm, which is unsurprising as saline will corrode the CoCrMo surface (273). The r_a of the HSF samples increased to 11.7 ± 3.0 nm which could possibly be due to tribo corrosion reactions with proteins (95).

WLI imaging of the wear surfaces showed the average surface roughness (r_a) increased significantly compared to the untested sample. Saline had the roughest wear scar (122.2 ± 23.1 nm) followed by HSF (90.1 ± 24.5 nm) and 25BCS (59.1 ± 10.0 nm), which scales with the result from outside the wear

scar. Haley et al. (59) measured the surface roughness of implants before and after testing in a hip simulator. The roughness of the untested surface was r_a = 6.7 ± 2.3 nm which increased to a maximum at r_a = 27.4 ± 7.2 nm at 1 million walking gait cycles, after which the surfaces began to smooth and at 2 million cycles r_a = 19.8 ± 2.9 nm. Additional tests were run with a 10s dwell between each cycle, this resulted in a higher roughness which is more representative of the wear test performed in this thesis the ball comes to a stop at the end of each stoke on turn around. The roughness after 0.6 million walking cycles with a 10s dwell was r_a = 35.9 ± 16.3 nm in comparison to r_a = 17.5 ± 1.9 nm after 0.5 million cycles with no dwell period.

Deep pits were also present which had a depth in the range 0.72 –1.19 µm this has been attributed to carbides being partially torn out (48). As the articulating surfaces were made of the same materials and thus had identical microstructures, the two equally hard protruding carbides were cyclically loaded against each other which caused cracking, fracture and partial-pull out (112). It is most likely that these hard fractured carbides in the contact are the initiating cause of abrasive wear in the softer, more vulnerable metal matrix (48, 49, 112)

Imaging of the surface topography in the wear scars revealed that the most obvious wear mechanism present is abrasion due to the multiple scratches or grooves in the wear scar (218); due to the sub mechanisms micro-ploughing and micro-cutting.

5.7.3 Lubricating Mechanisms

An important observation is that for the BSC, model and human SF exhibit the same pattern of lubricant deposits, the rainbow deposits are located either end of the wear scar beyond which is black particulate. This further illustrates that these black deposits may inhibit wear which is repeatedly reported in literature (48, 110, 112, 170, 177, 198, 200, 211).

The formation of thick deposits at either end of the wear scar suggests that high viscosity material is formed during sliding, it collects in the inlet region (110-112, 200) and is deposited at the turn-round. The formation of solid (48, 274) or high viscosity (112) deposits has been widely reported and these are thought to contribute to increased surface separation (108) and wear reduction (48). A number of studies also identified these tribochemical reaction layers as an acting wear mechanism to protect the rubbing surfaced (48). These are often attributed to denatured proteins that adhere rigidly to the surfaces preventing adhesion and reducing wear (48) (218).

Fibular like deposits were observed in and around the wear scar in some model and HSF samples. Banquy et al. (147) sheared human, bovine and equine SF between two mica surfaces at a pressure of

20 MPa. Fibular deposits were identified to act as roller bearings to separate rubbing surfaces. It was suggested that above a critical speed (~ 40 nm/s) proteins and biopolymers initially aggregate to form a homogeneous gel. Further shearing causes these gels to break up and form discrete particles, become elongated and provide surface separation. They continually grow as the gel and SF adsorb onto the particle as it rolls.

5.8 Conclusions

In this chapter the wear surfaces were examined by optical microscope, SEM and WLI. The conclusions are as follows:

- Substantial residual films are deposited in and around the wear scar, these are mainly observed on the ball.
- Deposits for both model and human samples were very similar and included two distinct regions; black and rainbow.
- Lower wear was associated with greater rainbow/black deposits suggesting this material is present in the contact zone and contributes to surface protection.
- Fibular like deposits were observed in and around the wear scar for high γ-G model fluids without the presence of DPPC and for low wear HSF samples.
- SEM images verified the presence of fibular deposits and identified intertwined fibrils to form supercoiled rope like structures inside the wear scar on the ball and disc for both 25BCS and HSF.
- Abrasion were identified as the dominant wear mechanisms for material loss.
- There was an increase in surface roughness inside the wear scar.

Chapter 6: Micro IRRAS Examination of Wear Scar Deposits

Summary

In this chapter Micro-IRRAS was implemented to examine the organic chemical composition of surface deposits formed in and around the wear scars as shown in Chapter 5. Analysis of deposits on the ball was carried out for all model and human fluids tested in Chapter 4. FTIR spectra were taken from both 'rainbow' and 'black' regions and compared to untested fluids. The spectra showed these deposits were predominately proteins with an increased native β-sheet (N-β) content compared to the untested fluid. In some cases, lipids were found to be associated with the deposits. The HSF deposits were shown to have broadly similar protein structure, although in most cases the N-β content was less, and lipids were often present.

6.1 Introduction

Identification of the composition and distribution of films formed during *in vitro* and *in vivo* testing could provide insights into the role of SF species in the lubrication and wear process. The model SF fluids used in this study contained various mixtures of proteins and phospholipids as these have been identified as components in anti-wear films formed on implant surfaces for BCS and HSF.

There have been a number of studies reporting film formation on CoCrMo surfaces from hip simulator (198), bench top tests (48, 112, 207-210) and explanted specimens (150, 170, 211, 212). Generally two different types of film have been reported; these are proteins or glycoproteins (48, 112, 143, 198, 207-209) and phospholipids (150, 202, 210). The lipid layers are usually considered to be classical boundary films, typically a few nanometres thick, of molecules adsorbed at the implant surfaces (150, 210).

Proteins and glycoproteins have been reported to form thick and adherent films on implant surfaces in bench-test, hip simulator and explanted joints (48, 110, 112, 170, 200, 207-209). These deposits have been identified as denatured proteins and are considered to act as solid boundary films, which protect the sliding surfaces and reduce wear (48). In earlier work proteins were thought to denature due to the higher temperatures that are generated within the contact zone during rubbing particularly

in MoP joints (275). More recent studies in the Tribology Group have suggested that shear also contributes to protein denaturing and phase separation (112, 200)

In the case of phospholipids several studies have suggested they act as boundary lubricants, forming bi-layer films, for biological and artificial surfaces (150, 202). Hills and co-workers (150) analysed surface material from a series of MoP implants using a specific solvent extraction method to remove the phospholipids. The results showed eight different types of phosphatidylcholines to be present with the unsaturated (DPPC) molecules the most predominant (150).

FTIR is a particularly powerful tool for the identification of organic films as the position and intensity of absorption bands provides information on the chemical composition, molecular structure and bonding interactions (276). The IR molecular fingerprints of proteins (277-280) and lipids (281, 282) have been reported extensively in literature. FTIR can also be used to detect changes in diseased and damaged biological tissue (283-287) and to diagnose diseases, for instance arthritis in SF (288-291).

The aim of this chapter was to identify the organic composition of the surface deposited films formed during wear tests and to examine whether there is significant difference to the untested fluids. Additionally, it will be investigated if any biomarkers are present in HSF IR spectra that indicate high wear for MoM implants.

6.1.1 FTIR Theory

Molecular bonds and groups of atoms naturally vibrate at frequencies that fall within the infrared spectrum. Therefore, functional groups absorb IR at their resonant frequencies which gives rise to characteristic absorption bands. A normal mode of vibration is infrared active if there is a change in the dipole moment of the bond during the course of vibration. Thus, symmetrical vibrations are usually not detectable or have very low absorbance. Strong IR absorptions are observed for groups with permanent dipoles, for example carboxyl groups in polypeptide backbones. The vibrational frequency can be modelled (Equation 6.9) (292) using the harmonic oscillator model where a bond is represented by two-point masses of molecules or functional groups (m1 and m2) connected by a spring of stiffness k. This shows that the vibrational frequency is dependent upon the bond strength (i.e single, double or triple bond) and mass of molecules or functional groups. The frequencies are also sensitive to the group environment, electronegativity of neighbouring atoms or groups and presence of hydrogen bonding (292) (277).

$$v = \frac{1}{2\pi c}\sqrt{\frac{k(m_1 + m_2)}{m_1 m_2}} \qquad (6.9)$$

Micro IRRAS is a sampling technique which allows FTIR analysis from small areas (10-100 μm diameter) of thin films (100-800 nm) supported on a reflective metal surface. An IR beam is focussed onto the film and then reflected at the metal surface before being refocussed onto a detector; effectively the IR radiation is transmitted through the sample twice. The equipment combines a Perkin Elmer Multiscope IR microscope coupled to a Spectrum One FTIR spectrometer.

The Multiscope IR microscope uses Cassegrain collection optics for high performance infrared micro spectroscopy this is combined with a video viewer for optical microscopy. The IR and visual systems use the same Cassegrain system and therefore both focal points are at the remote aperture. The video viewer is used to focus onto the sample and located though a 100 μm aperture, which can then be switched to IR mode to record a spectrum. This means when the sample position is adjusted to focus the visible image the sample is correctly positioned for collecting IR spectra. The system can operate in both reflectance and transmittance, however in this chapter only reflectance is used and therefore only the theory of this will be discussed.

Figure 6.1 shows the path of the visible beam for viewing the sample in reflectance and the infrared beam for collecting spectra. When viewing the sample (Figure 6.1a) relay mirror M1 receives light from an illuminator and directs it down one side of cassegrain C1 to the sample. C1 collects light from the sample and sends it upwards through the remote aperture towards the video viewer. When in this mode the IR are blocked from reaching the sample.

The path of the IR beam (Figure 6.1b) differs slightly when collecting a spectrum. An IR beam is directed to M1 from mirror M2. Similar to the viewing set up the beam is directed down one side of the cassegrain the incident radiation is passed through the thin film which is then reflected off the metallic surface onto the other side of the C1 and through the remote aperture. An additional mirror is now in place to block the beam reaching the optical microscope and onto the Cassegrain C2. The beam travels through the Cassegrain C2 to focus on the MCT detector that collects the radiation.

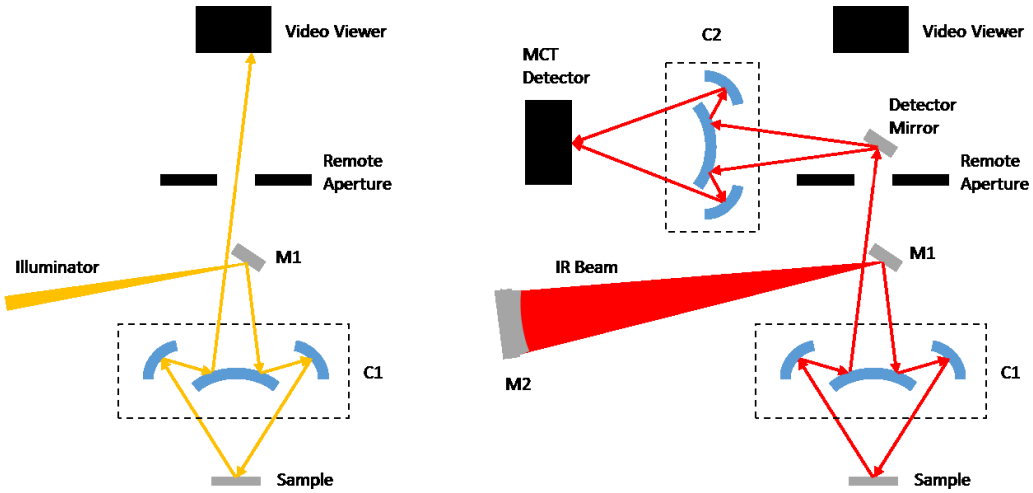


Figure 6.1 – a) Path of visible beam for viewing a sample in reflectance b) Path of infrared beam for collecting spectra in reflectance. Adapted from (293)

When the radiation is passed through the sample, the wavelengths absorbed are dependent upon which molecules are present, and the rest is transmitted. Therefore, at the detector the IR beam no longer contains specific wavelengths of radiation which represents a molecular 'fingerprint' of the sample. The detector output is converted to interpretable spectra using the Fourier Transform. The energy is recorded as a function of frequency (cm^{-1}) or wavelength.

6.1.2 Infrared Spectroscopy of SF's and Components

6.1.2.1 Synovial Fluid

FTIR has been used extensively to study SF composition (288, 289) (290, 291) (284). Attempts to find biomarkers of OA (288, 289, 291) and RA (290, 291) SF have been made over the years. It was concluded that spectra can be used to differentiate between healthy and arthritic SF (288-291).

In the reported literature (288-291) spectra were taken from dried films onto a CaF_2 window to avoid the intense water bands obscuring the organic component peaks (288-291) near 1645 cm^{-1} (277). A similar approach has been adopted in the current work.

6.1.2.2 Proteins

The infrared absorption spectrum of proteins is dominated by bonds on the polypeptide backbone of the amino acid structure. The amide I peak is the most intense peak in the range of 1600 - 1700 cm^{-1} and arises mainly due to the C=O (~80%) stretching vibration (278) with contributions from the out of phase CN stretching vibration (277). The amide II peak is a combination of the NH bending (~60%) and

CN stretching vibration (~40%) absorbing frequencies in the range of 1510 – 1580 cm^{-1} (278, 279) (277).

Amide I and II vibrations are hardly affected by the nature of the side chain however peak position is affected by the secondary structure of the backbone (277-280). Secondary structures present in a protein can be identified by the peak position of the amide bands. It is reported that the Native (N-β) and Fibril β-sheet (F-β) structures can be distinguished by a difference in wavenumber (k) (294). Table 6.1 outlines the frequency ranges for the different assignments.

Table 6.1 - Secondary structures associated with amide I and II peaks combined from (277, 278, 294-303).

Secondary Structure	Wave Number Band Range (cm^{-1})
	Amide I
Turns and bends	1700 - 1660
α – helix/random coil	1660 - 1645
N-β (native, antiparallel)	1700 - 1680 1648 - 1630
F-β (fibril, parallel)	1630 - 1611

Amide A (~3270-3310 cm^{-1}) and B (3030 – 3100 cm^{-1}) represent NH stretching vibrations. The frequency depends upon the strength of the hydrogen bond (277). However, this can be masked by the OH stretch (3700-3100 cm^{-1}) which is a strong and broad peak attributed to residual water (304).

The 3100-2800 cm^{-1} range is the alkyl stretch region which contains four main peaks CH_3 (ν_{asym}), CH_2 (ν_{asym}), CH_3 (ν_{sym}) and CH_2 (ν_{sym}) which are present in proteins (305) and other organic components including lipids. Table 6.2 outlines the approximate band positions of each of these peaks (279).

Table 6.2 - Approximate band assignment for lipids (279).

Assignment	Wavenumber (cm^{-1})
CH_3 (ν_{asym})	2959 - 2951
CH_2 (ν_{asym})	2930 - 2928
CH_3 (ν_{sym})	2874
CH_2 (ν_{sym})	2854 - 2850

6.1.2.3 Lipids

Lipid are a heterogeneous group of organic molecules (114) composed of fatty acids which have a hydrocarbon tail that terminates in a carboxylic acid group (Figure 6.2) (114). Phospholipids are a subcategory of lipids and contain additional phosphate and chlorine groups as shown in Figure 6.3 (279, 306). They are a known constituent of BCS (41) and HSF (39) and therefore DPPC was added to some of the model fluids in Chapter 4.

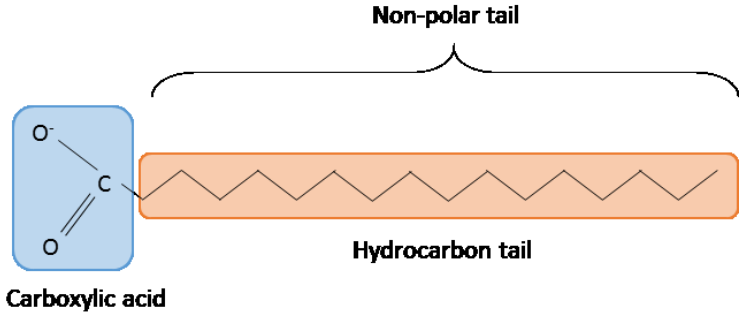


Figure 6.2 – Structure of a fatty acid. Adapted from (114).

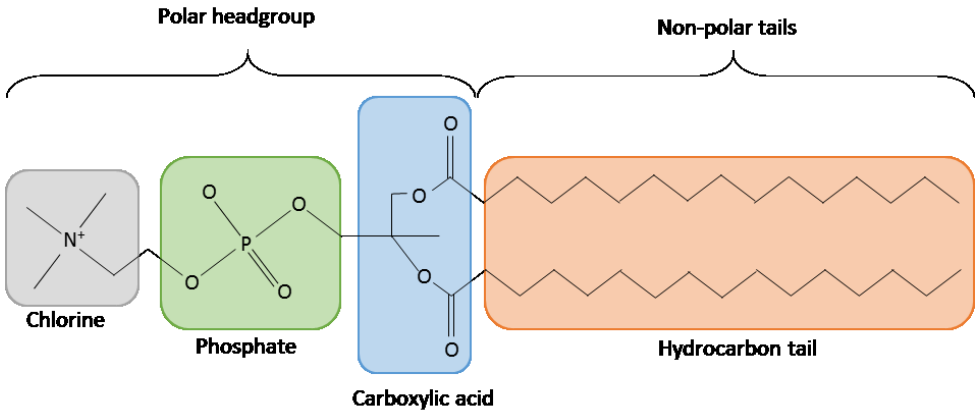


Figure 6.3 - Structure of DPPC. Adapted from (279, 306).

Two distinct regions dominate the FTIR spectra of lipids, the first of which is in the region 3100-2800 cm^{-1} and contains four peaks due to CH_3 (ν_{asym}), CH_2 (ν_{asym}), CH_3 (ν_{sym}) and CH_2 (ν_{sym}) vibration modes from the alkyl chain (282). These provide very similar absorption frequencies to proteins, the only clear difference can be seen in the CH_2 (ν_{asym}) where lipids have a characteristic absorbance at 2916 – 2922 cm^{-1} compared to 2928 – 2930 cm^{-1} (279, 306). The bands are also much narrower which is characteristic of an ordered all-trans alkyl chain (279).

The second spectral region can be found below 1800 cm^{-1} and is a result of vibrations in the polar head group. Within this region the most intense peak is usually due to an ester stretch (C=O) at 1735-1750 cm^{-1} (281). These bonds can be seen in Figure 6.3. The wavenumber ranges for these vibrations are summarised in Table 6.3.

Table 6.3 – Approximate band assignment for lipids (279, 306).

Assignment	Wavenumber (cm^{-1})
CH_3 (ν_{asym})	2959 - 2951
CH_2 (ν_{asym})	2922 - 2916
CH_3 (ν_{sym})	2874
CH_2 (ν_{sym})	2853 - 2850
C=O (stretch)	1733 - 1730

FTIR spectra can provide information on the structure and organisation of bio membranes and lipid assemblies (306). The vibration frequency depends upon the physical state of the chains and therefore measurements of the CH_2 (ν_{asym}) peak position and half band width can be used to probe the structure of the lipid films (279). The ester carbonyl stretching band is also sensitive to hydrogen bonding (279).

6.2 Experimental Programme

The overall aim of this chapter was to examine the composition of untested fluids and deposited films formed as a result of the wear tests using Micro-IRRAS spectroscopy. The objectives were as follows:

1. To study changes in the Micro-IRRAS spectra of untested fluids due to changes in constituents

- Saline
- Proteins (BSA and γ-G)
- Lipids (DPPC)

2. To analyse and compare Micro-IRRAS spectra of the untested samples for BCS, model and human SF's.
3. To analyse and compare Micro-IRRAS spectra of deposited films for the BCS, model and human SF's.

6.3 Materials and Methods

Micro-IRRAS was used to analyse two types of surface films; fresh untested fluid and wear surface deposits. For the untested fluids it was necessary to remove excess water from the samples to avoid the problems of intense bands at 1645 cm^{-1} obscuring the Amide I peak (277). To analyse the fresh fluids (untested 25BCS, model and human fluids) a small amount was retained before testing and 10 μl pipetted onto a clean CoCrMo ball and left to air-dry for 24hrs. The other advantage of this method was it allowed direct comparison with the dried surface deposits formed during the wear tests.

Additional, single constituent solutions of BSA, γ-G and DPPC were made and analysis of these untested fluids was performed in order to understand the characteristics of simple fluids before progressing to the more complicated BCS, model and human SF. BSA and γ-G were tested at a concentration of 12 mg/ml (12Alb) and 6 mg/ml (6Glob) respectively in order to replicate the concentrations in mH. The untested DPPC was used at a concentration of 0.5 mg/ml as this was the concentration used in all model solutions

The untested spectra were compared to those from the wear deposits on the ball. As outlined in Chapter 5 once the ball was removed from the wear test it was lightly rinsed with DI water and allowed to air dry for 24hrs. Spectra from both the black and rainbow regions were obtained from the tested balls.

The Micro-IRRAS sampling method is shown in Figure 6.4. A Perkin Elmer Multiscope Infrared Microscope coupled to a Spectrum One FTIR was used to take Micro-IRRAS spectra from a small area of the films. The sample diameter was 100 μm, 100 scans were taken and the resulting spectrum was baseline corrected, smoothed (13 point) and normalised (to absorbance 0.1 at 1650 cm^{-1}) using the standard Perkin Elmer software. The Amide I band was used as the normalisation standard. Peaks were found via deconvolution (Bessel, γ = 2, smoothed 65%). The background spectrum was 200 scans using a clean gold disc.

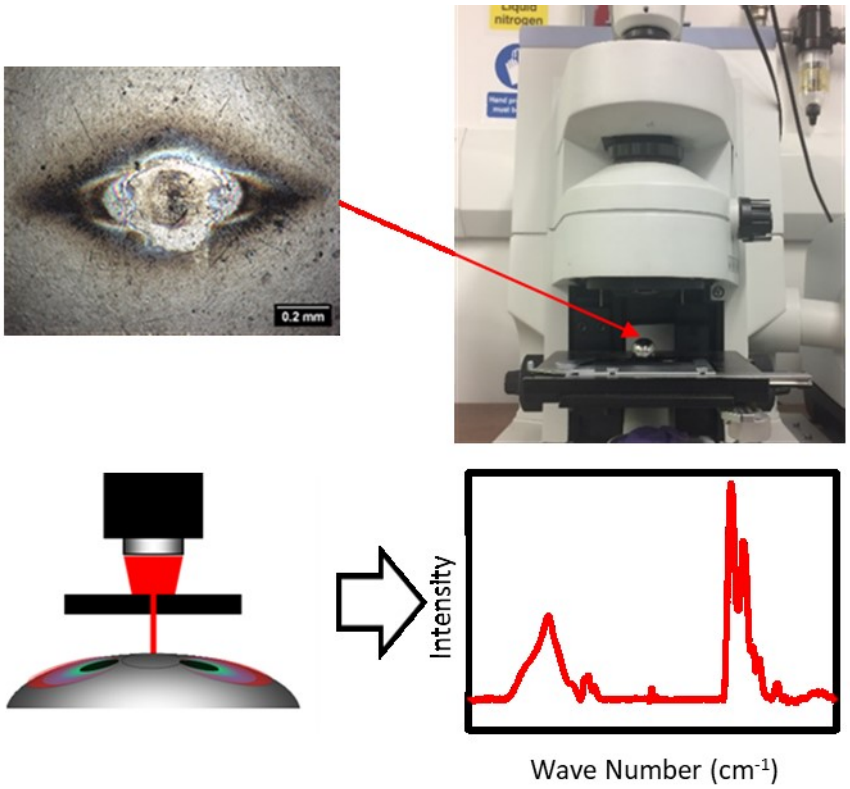


Figure 6.4 - Micro-IRRAS analysis of organics deposits on the ball.

Initially untested fluids were analysed and compared, starting with the single components: BSA, γ-G and DPPC; followed by the screening fluids 25BCS and 25salBCS and finally the model fluids (with and without DPPC). Secondly spectra from tested samples were taken from both the black and rainbow regions, the films within the wear scar were too thin to provide good quality spectra and have not been included. Lastly spectra from both the tested films and untested fluids were compared. The same process was performed for HSF. Residual wear test films of DPPC and HA alone were too thin to obtain spectra and therefore are not reported.

Typical spectra from untested and tested films are shown in Figure 6.5. The two regions of interest are highlighted by the dashed boxes. The region 1450 – 1750/1800 cm^{-1} is the amide I and II band region which provides information on the secondary structure of proteins. The region 2800 – 3000 cm^{-1} represents the CH stretch region which can give information about the alkyl chain structure and the presence of non-protein species. Further analysis in this chapter will only report these two regions.

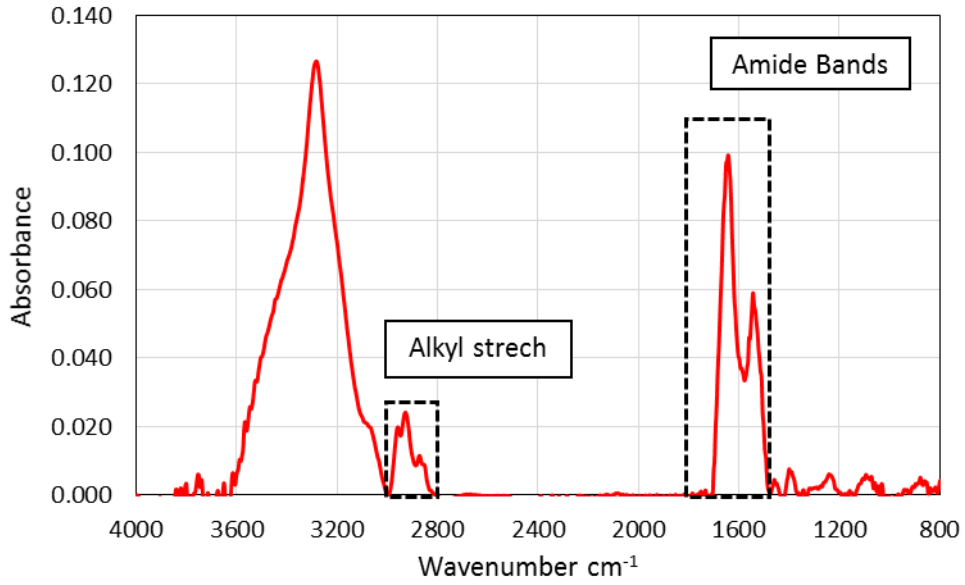


Figure 6.5 – A typical spectra from the residual films with the regions 1750-1450 cm^{-1} and 3000 – 2800 cm^{-1} outlined.

6.4 Results: Untested Fluid Reference Spectra

6.4.1 Model Fluid Components: BSA, γ-G and DPPC

Thin film IR spectra from the untested fluids of 12Alb and 6Glob in the 1750-1450 cm^{-1} wavenumber range are shown in Figure 6.6 where the amide I and II bands are labelled. The deconvolution spectra are also plotted for each sample and the overlapping peaks are labelled. It can be clearly seen that 12Alb and 6Glob have different peak locations, the strongest peak for 12Alb was at 1651 cm^{-1} representing an α-helix/random coil secondary structure (277, 278), shoulder peaks were located at 1666, 1659, 1642 and 1632 cm^{-1}. The strongest peak for 6Glob was at 1642 cm^{-1} representing a N-β secondary structure (277, 278) with shoulder peaks at 1659, 1651 and 1632 cm^{-1}.

Similar to the amide I peak, the amide II peak of 6Glob appeared to be located at a slightly lower wavenumber however deconvolution of these peaks revealed that the strongest peak was located at 1539 cm^{-1} for both 12Alb and 6Glob with overlapping peaks at 1557, 1548, 1530 and 1520 cm^{-1}. Literature relating the amide II peak to secondary structure is limited and a peak at 1539 cm^{-1} did not relate to any structures (277, 278) and therefore no assignments were made for the amide II band. Table 6.4 summarises the amide I and II results. In all further analyses the amide II bands are not reported but will be shown in Appendix 11.3.

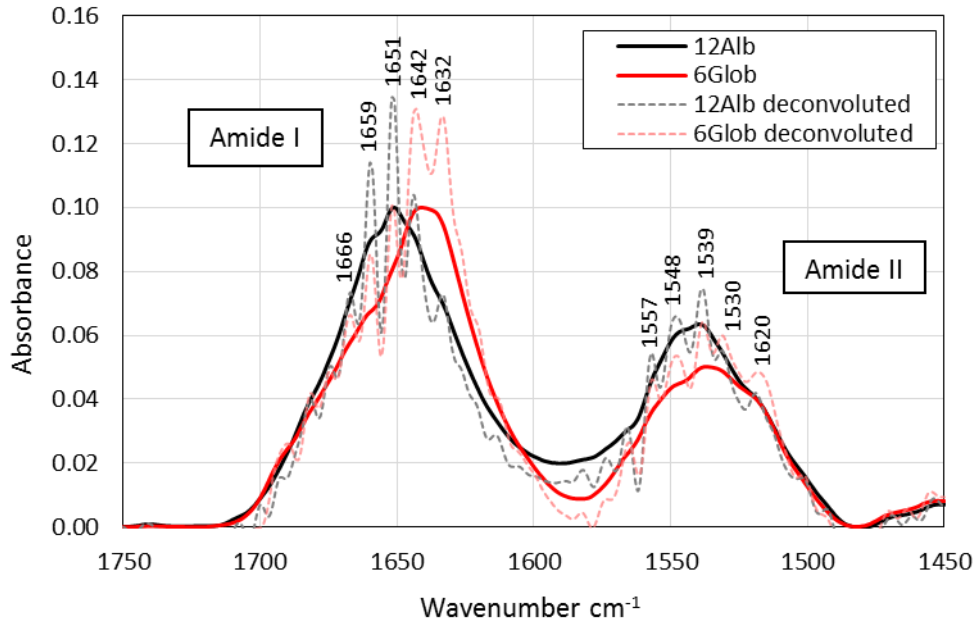


Figure 6.6 - Micro-IRRAS analysis comparing the untested fluids of 12Alb and 6Glob in the range 1750-1450 cm^{-1}.

Table 6.4 - Summary of IR peaks from deconvolution and secondary structure assignment untested fluids of 12Alb and 6Glob in the range 1750 - 1450 cm^{-1}. (Bold type represents most intense peak).

Peaks	Wavenumber (cm^{-1})		Assignment
	12Alb Untested	6Glob Untested	
Amide I	1668		turns and bends
	1660	1659	α-helix/random coil
	1652	1652	α-helix/random coil
	1641	1642	N-β
	1632	1632	N-β
Amide II	1557	1557	
	1548	1549	
	1539	1539	
	1531	1532	
	1520	1520	

Spectra comparing 12Alb and 6Glob in the region 3000 – 2800 cm^{-1} are shown in Figure 6.7. As expected four peaks are observed at 2957, 2933, 2870 and 2854 cm^{-1} representing CH_3 (ν_{asym}), CH_2

(ν_{asym}), CH_3 (ν_{sym}) and CH_2 (ν_{sym}) respectively. Both CH_3 (ν_{asym}) and CH_3 (ν_{sym}) have a higher intensity compared to CH_2 (ν_{asym}) and CH_2 (ν_{sym}) and the CH_2 (ν_{sym}) peak is barely visible for the sample 12Alb. Overall 12Alb has a higher intensity than 6Glob, which could be due to the fact that the molarity of 12Alb (180 µM) is 450% greater than 6Glob (40 µM). Peak positions are shown in Table 6.5.

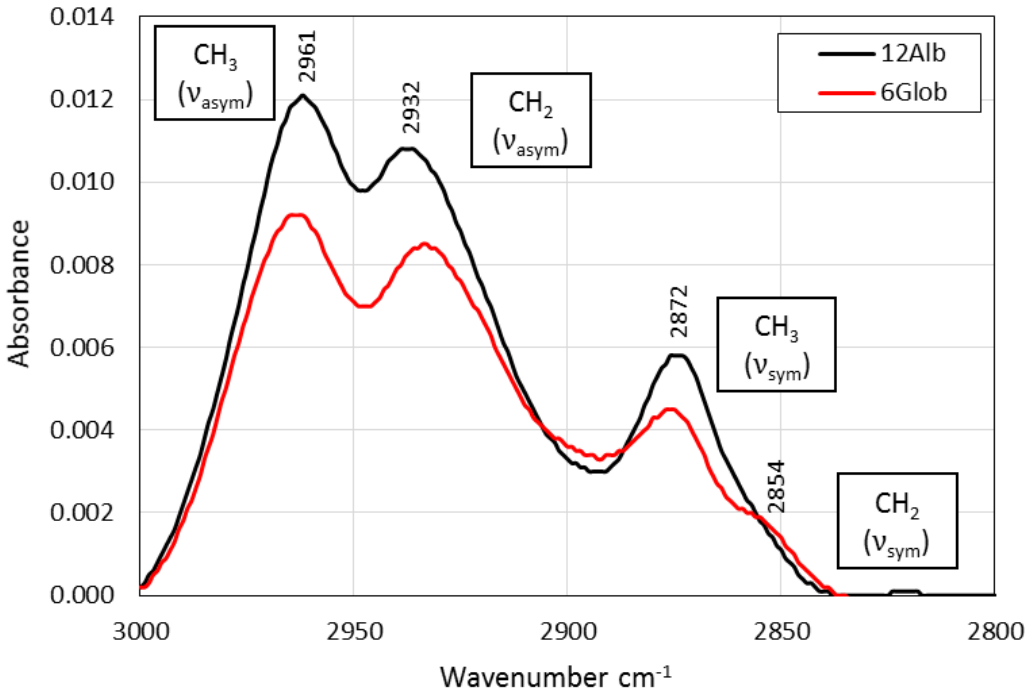


Figure 6.7 - Micro-IRRAS analysis comparing the untested fluids of 12Alb and 6Glob in the range 3000-2800 cm^{-1}.

Table 6.5 - Summary of IR peaks from deconvolution for untested 12Alb and 6Glob for 3000 - 2800 cm^{-1}. (Bold type represents the most intense CH_2/CH_3 peak).

Peaks	Wavenumber (cm^{-1})	
	12Alb	6Glob
CH_3 (ν_{asym})	2961	2962
CH_2 (ν_{asym})	2932	2931
CH_3 (ν_{sym})	2872	2874
CH_2 (ν_{sym})		2854

An untested sample of DPPC was analysed to identify absorbance peaks in the C=O stretch and alkyl stretch region Figure 6.8 shows a spectrum in the 1800-1450 cm^{-1} range, the C=O stretch is clearly identifiable at 1733cm^{-1} (the spectral range was increased to 1800 cm^{-1} to include this peak).

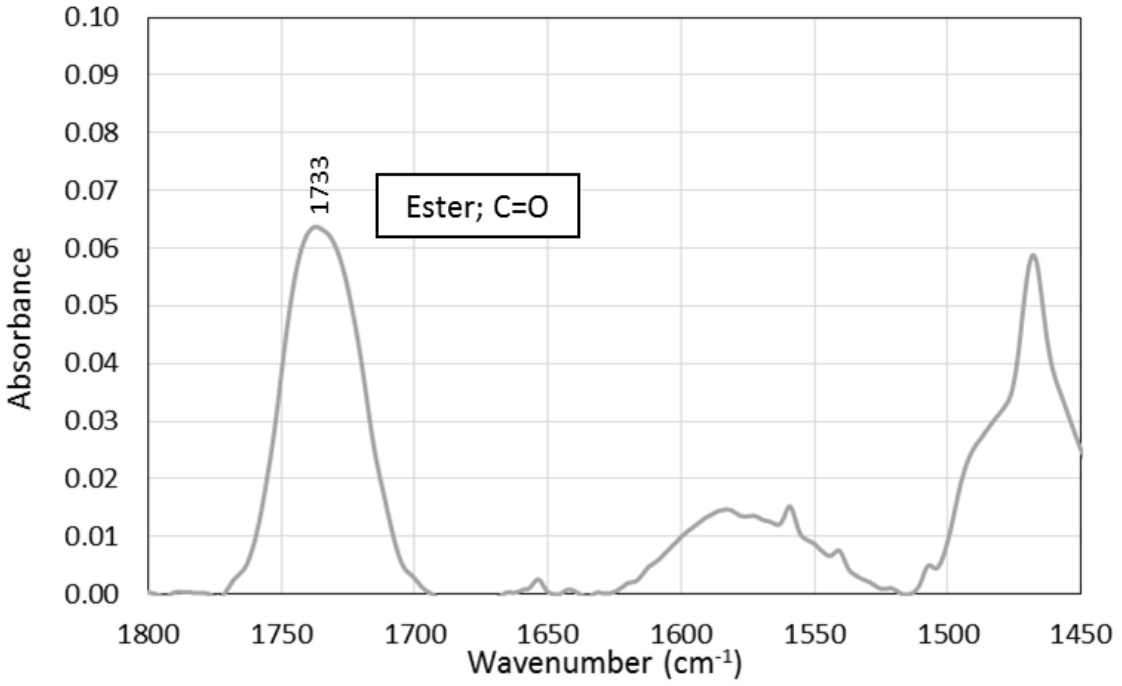


Figure 6.8 - Micro-IRRAS analysis of the untested film 0.5 mg/ml DPPC in the range 1800-1450 cm^{-1}.

Figure 6.9 shows the alkyl stretch region, it is interesting to compare this to 12Alb and 6Glob. There are two distinct differences, the most obvious change is the relative intensity of peaks. For the protein only solutions both of the CH_3 (ν_{asym}) and CH_3 (ν_{sym}) have the highest intensity, however for the DPPC solution CH_2 (ν_{asym}) and CH_2 (ν_{sym}) have the highest intensity.

The second difference is a shift in the wavenumber of the CH_2 (ν_{asym}) peak from ~2932 cm^{-1} to ~2916 cm^{-1} and CH_2 (ν_{sym}) from ~2854 cm^{-1} to ~2849 cm^{-1}. In addition, the DPPC bands in the 3000-2800 region C-H stretch are relatively narrow, both of these changes indicate a highly ordered all-trans alkyl chain (307). Table 6.6 summarises the peak positions in the alkyl stretch region.

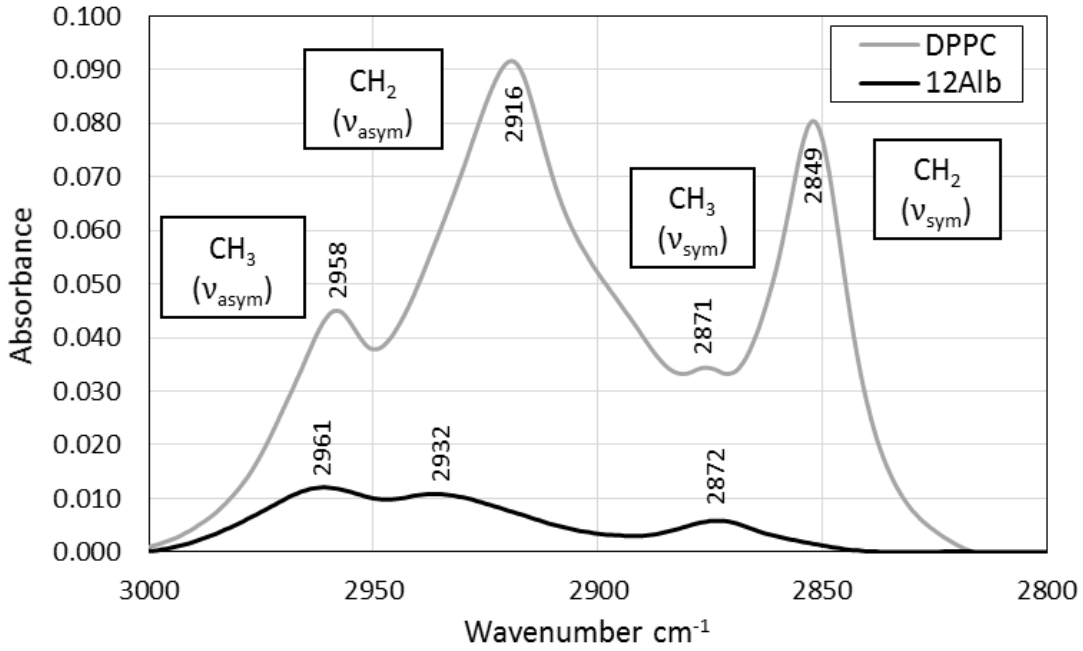


Figure 6.9 - Micro-IRRAS analysis of the untested film 0.5 mg/ml DPPC in the range 3000-2800 cm^{-1}.

Table 6.6 - Summary of IR peaks from deconvolution for untested 0.5 mg/ml DPPC. (Bold type represents the most intense CH_2/CH_3 peak).

Peaks	Wavenumber (cm^{-1})
	25salBCS
C=O	1733
CH_3 (ν_{asym})	2958
CH_2 (ν_{asym})	2916
CH_3 (ν_{sym})	2871
CH_2 (ν_{sym})	2849

6.4.2 25BCS and 25salBCS

Spectra from untested films of 25BCS and 25salBCS in the region of 1750-1450 cm^{-1} are shown in Figure 6.10 where the amide I and II bands are almost identical, which is expected as they have the same specific and total protein content.

Deconvolution of these bands reveal that amide I band comprises of overlapping peaks with the strongest peak at 1641 cm^{-1}, indicative of a N-β secondary structure. Shoulders are present at 1659,

1651 and 1632 cm^{-1} which can be assigned to the secondary structures α-helix/random coil and N-β respectively. Table 6.7 summarises these results.

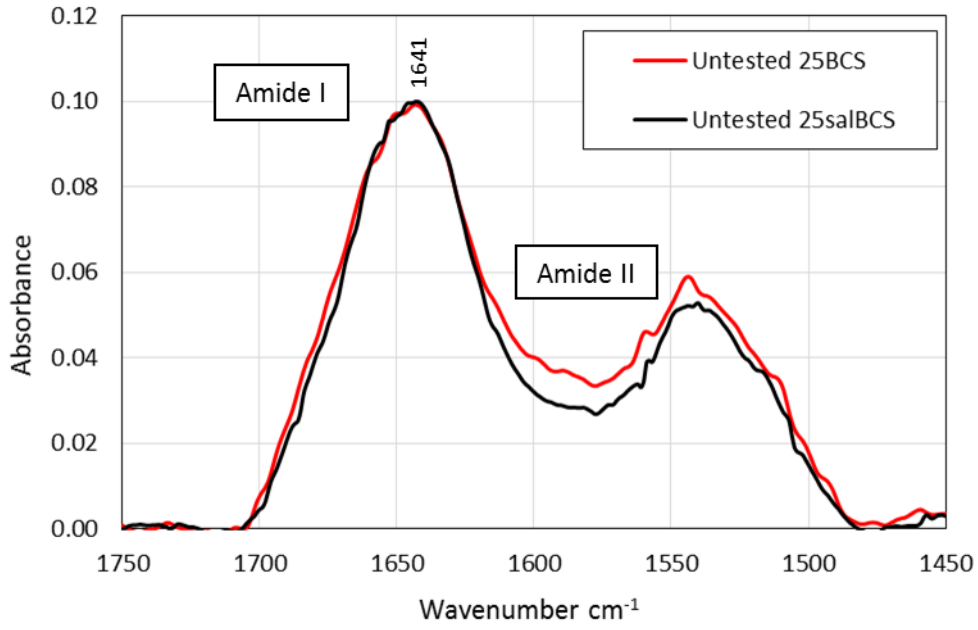


Figure 6.10 - Micro-IRRAS analysis of untested films comparing 25BCS and 25salBCS in the range 1750-1450 cm^{-1}.

Table 6.7 - Summary of IR peaks for untested 25BCS and 25salBCS for 1750-1450 cm^{-1}. (Bold type represents most intense peak).

Peaks	Wavenumber (cm^{-1})		Assignment
	25BCS	25salBCS	
Amide I	1659	1659	α-helix/random coil
	1651	1651	α-helix/random coil
	1641	1641	N-β
	1632	1632	N-β

Figure 6.11 compares 25BCS and 25salBCS spectra in the region 3000 – 2800 cm^{-1}, four distinct peaks are present at 2957, 2933, 2870 and 2851 cm^{-1} representing CH_3 (ν_{asym}), CH_2 (ν_{asym}), CH_3 (ν_{sym}) and CH_3 (ν_{sym}). Spectral deconvolution reveals an additional peak which appears as a shoulder at 2917 cm^{-1} in the CH_2 (ν_{asym}) region which indicative of a highly ordered all-trans alkyl chain (307). This is possibly due to fatty acids which is unsurprising as they are present in BCS (308); however, the concentration is unknown. Peak positions for 25salBCS are very similar to 25BCS and are within ± 1 cm^{-1} when compared to 25BCS, these are summarised in Table 6.8.

It is apparent that the CH_3 (ν_{asym}) and CH_2 (ν_{asym}) peaks for 25salBCS are more intense than 25BCS, which could be due to 25salBCS having a higher ionic strength than 25BCS. However, the peak intensities for CH_3 and CH_2 (ν_{sym}) are relatively similar for 25BCS and 25salBCS.

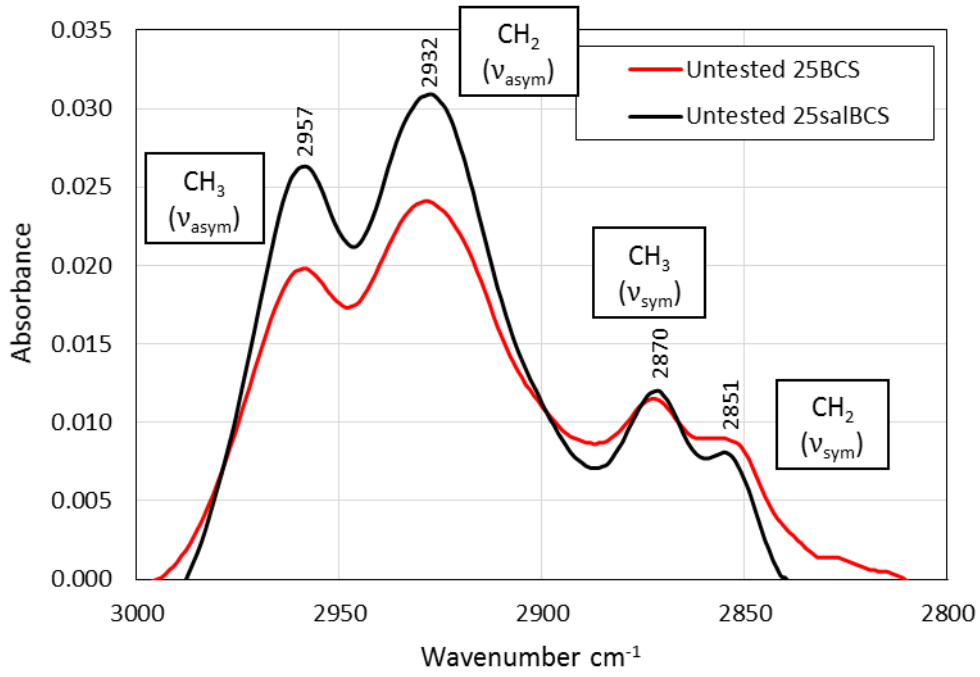


Figure 6.11 - Micro-IRRAS analysis of untested films comparing 25BCS and 25salBCS in the range 3000 - 2800 cm^{-1}.

Table 6.8 - Summary of IR peaks from deconvolution for untested 25BCS and 25salBCS for 3000 - 2800 cm^{-1}. (Bold type represents the most intense CH_2/CH_3 peak).

Peaks	Wavenumber (cm^{-1})	
	25 BCS	25salBCS
CH_3 (ν_{asym})	2957	2957
CH_2 (ν_{asym})	2932 2917	2931 2917
CH_3 (ν_{sym})	2870	2870
CH_2 (ν_{sym})	2851	2851

6.4.3 Model Fluids without DPPC

Spectra from untested films for model fluids mBCS, mH, mOA and mPP are compared in Figure 6.12, peak positions are not marked as they are too close together. Deconvolution shows the same four

overlapping peaks in these model fluids that were found in 12Alb, 6Glob and the BCS solutions (25BCS and 25salBCS). The deconvoluted peak positions of the amide I band for mBCS, mH, mOA and mPP are summarised in Table 6.9, 25salBCS is shown for comparison.

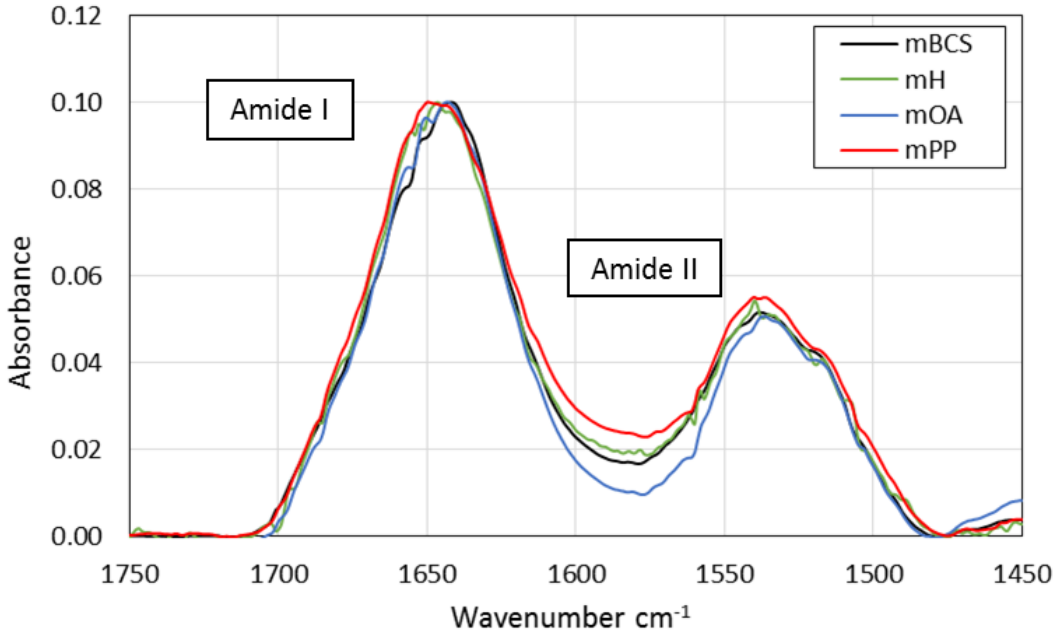


Figure 6.12 - Micro-IRRAS analysis of untested films comparing mBCS, mH, mOA and mPP in the range 1750-1450 cm^{-1}.

Table 6.9 - Summary of IR peaks from deconvolution and secondary structure assignment for untested 25salBCS, mBCS, mH, mOA and mPP for 1750 - 1450 cm^{-1}. (Bold type represents most intense peak).

Peaks	Wavenumber (cm^{-1})					Assignment
	25salBCS	mBCS	mH	mOA	mPP	
Amide I	1659	1659	1655	1659	1659	α-helix/random coil
	1651	1651	1647	1650	1651	α-helix/random coil
	1641	1641	1640	1643	1642	N-β
	1632	1632	1631	1632	1632	N-β
A/G	0.8	0.8	2	1.5	3	

The peak position for the amide I band for the different fluids varies over the wavenumber range 1640-1651 cm^{-1} and appears to scale with A/G ratio as shown in Figure 6.13. For fluids with a high γ-G content (25salBCS, mBCS and mOA) the peaks with the highest intensity were assigned a N-β secondary structure at ~1640 cm^{-1} (277, 278). Whereas the fluids with a high BSA percentage (mH and

mPP) had peaks with the highest intensity, assigned to an α-helix/ random coil configuration at ~1650 cm^{-1} (277, 278).

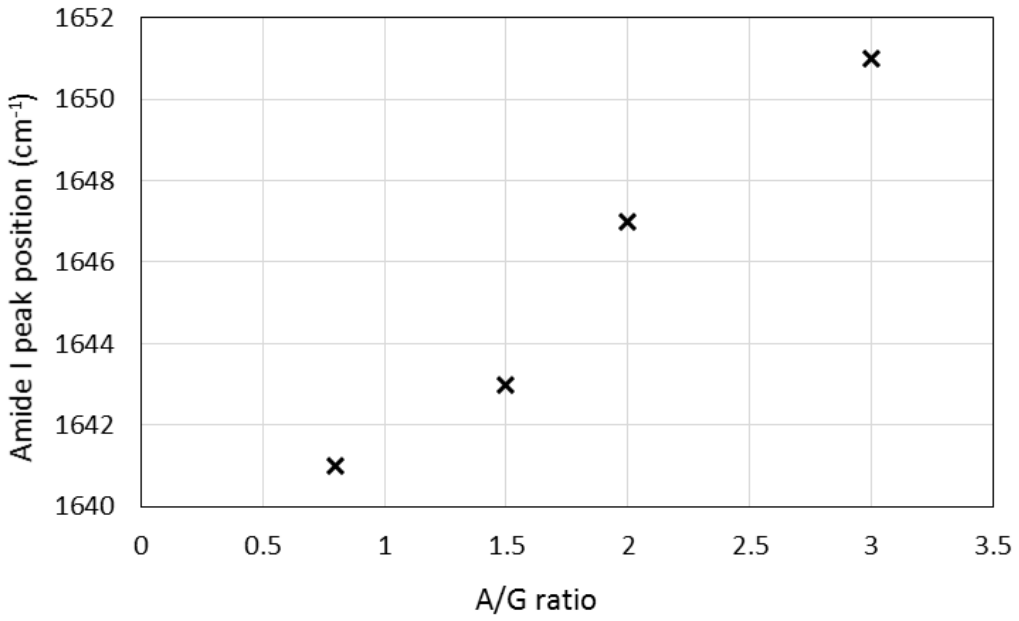


Figure 6.13 - Amide I peak position vs A/G ratio.

It is interesting to compare the most intense peak position of 25salBCS and mBCS as they have the same specific and total protein concentration. This was identical for the amide I band.

Figure 6.14 shows the spectra for the alkyl stretch region comparing model fluids mBCS, mH, mOA and mPP. The peak positions for mBCS were 2961, 2934, 2874 cm^{-1} for CH_3 (ν_{asym}), CH_2 (ν_{asym}) and CH_3 (ν_{sym}) respectively. A shoulder in the CH_2 (ν_{asym}) peak at 2917 cm^{-1} was observed for the sample mPP suggesting that some highly ordered trans alkyl chains are present. This sample has the highest BSA content and it has been reported that sometimes fatty acids can be detected in BSA, but are only present in low quantities (309). No obvious peak was present for the CH_2 (ν_{sym}), it is probable that it was too small to detect. The peak positions for each model fluid are very similar; however, when compared to 25salBCS are slightly elevated, this is summarised in Table 6.10.

There is a drop in the total intensity of the fluids mBCS and mOA in the alkyl stretch region. For all fluids the CH_3 peaks have a higher relative absorbance than the CH_2 peaks.

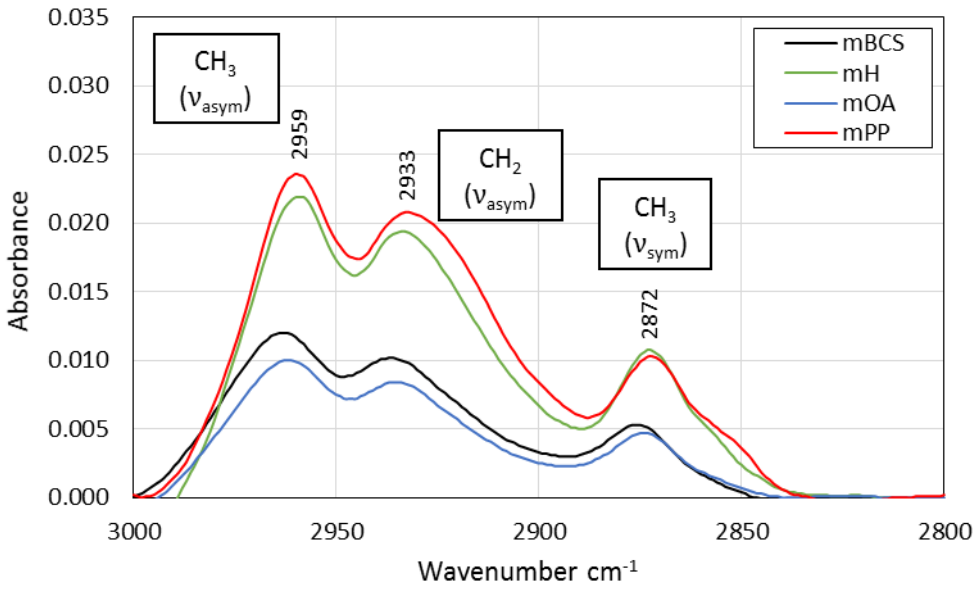


Figure 6.14 - Micro-IRRAS analysis of untested fluids comparing mBCS, mH, mOA and mPP in the range 3000 - 2800 cm^{-1}.

Table 6.10 - Summary of IR peaks positions from deconvolution for untested 25salBCS, mBCS, mH, mOA and mPP for 3000 - 2800 cm^{-1}. (Bold type represents the most intense CH_2/CH_3 peak).

Peaks	Wavenumber (cm^{-1})				
	25salBCS	mBCS	mH	mOA	mPP
CH_3 (ν_{asym})	2957	2961	2959	2961	2959
CH_2 (ν_{asym})	2931 2917	2934	2933	2934	2932 2917
CH_3 (ν_{sym})	2870	2874	2872	2872	2871
CH_2 (ν_{sym})	2852				
A/G	0.8	0.8	2	1.5	3

6.4.4 Model Fluids with DPPC

Spectra for 25salBCS and model fluids with DPPC show two distinct differences from spectra of these fluids without the addition of DPPC, an example is shown in Figure 6.15 for mBCS with and without DPPC. Table 6.11 summarises the peaks positions of C=O stretch and deconvoluted amide I band for 25salBCS and all model fluids with DPPC. The first difference is the presence of an additional peak at ~1735 cm^{-1} due to the C=O stretch from the DPPC ester group (279). The second difference is a shift

in both amide I and II bands to higher wavenumbers. For the amide I band deconvolution revealed the same four overlapping peaks identified in the solutions without DPPC were present, however the most intense peak was at ~1659 cm^{-1}, an α-helix/random coil conformation (277, 278). This compared to the model fluids without DPPC which were in the range 1641-1651 cm^{-1} an N-β/α-helix/random coil conformation (277, 278).

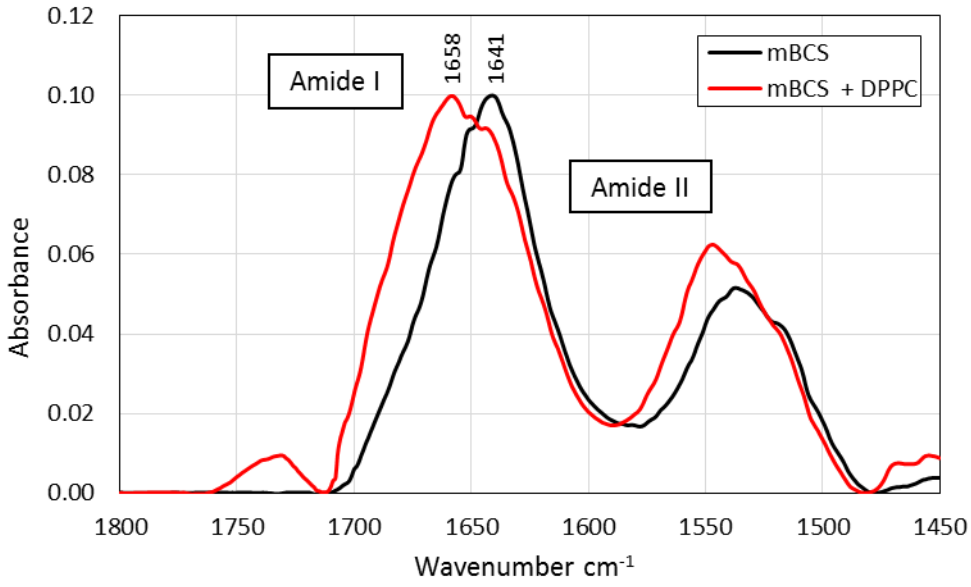


Figure 6.15 - Micro-IRRAS analysis of untested films comparing mBCS and mBCS + DPPC in the range 1750-1450 cm^{-1}.

Table 6.11 - Summary of IR peaks from deconvolution and secondary structure assignment for untested 25salBCS + DPPC, mBCS + DPPC, mH + DPPC, mOA + DPPC and mPP + DPPC for 1750 - 1450 cm^{-1}. (Bold type represents most intense peak).

Peaks	Wavenumber (cm^{-1})					Assignment
	25salBCS + DPPC	mBCS + DPPC	mH + DPPC	mOA + DPPC	mPP + DPPC	
Ester	1735	1735	1735	1737	1737	C=O
Amide I	1659	1658	1658	1658	1659	α-helix/random coil
	1650	1649	1649	1649	1651	α-helix/random coil
	1641	1641	1640	1642	1642	N-β
	1632	1631	1632	1632	1632	N-β
A/G	0.8	0.8	2	1.5	3	

The alkyl stretch region for the untested fluid mOA + DPPC is compared to mOA in Figure 6.16. The positions of each CH peak for all model fluids with DPPC are summarised in .

Table 6.12 and compared to the DPPC-only spectra and mOA. The graph shows the usual wavenumbers, common in both the DPPC and model fluids, at 2958, 2872 and 2849 cm^{-1} representing CH_3 (ν_{asym}), CH_3 (ν_{sym}) and CH_2 (ν_{sym}) respectively plus a doublet peak for CH_2 (ν_{asym}) at 2932 and 2916 cm^{-1}.

The model fluids with DPPC have increased CH peak intensities compared to model fluids without DPPC this is unsurprising as the presence of DPPC contributes additional alkyl chains and the spectra are normalised to the amide I peak, therefore relative to the fluids without DPPC more alkyl chains will be present. Additionally, the appearance peaks at 2916 and 2849 cm^{-1} provides further evidence of the highly ordered all-trans alkyl chains that are characteristic of lipids (307).

There were also relative peak height changes for model fluids with and without DPPC. For fluids with DPPC the CH_3 and CH_2 bonds have peaks of similar height for both the asymmetric and symmetric stretch whereas in fluids without DPPC the CH_3 bonds are dominant. This is a particularly noticeable change for the CH_2 (ν_{sym}) peak which cannot be seen in the model fluids without DPPC. This relative change in peak height provides additional evidence of the presence of DPPC.

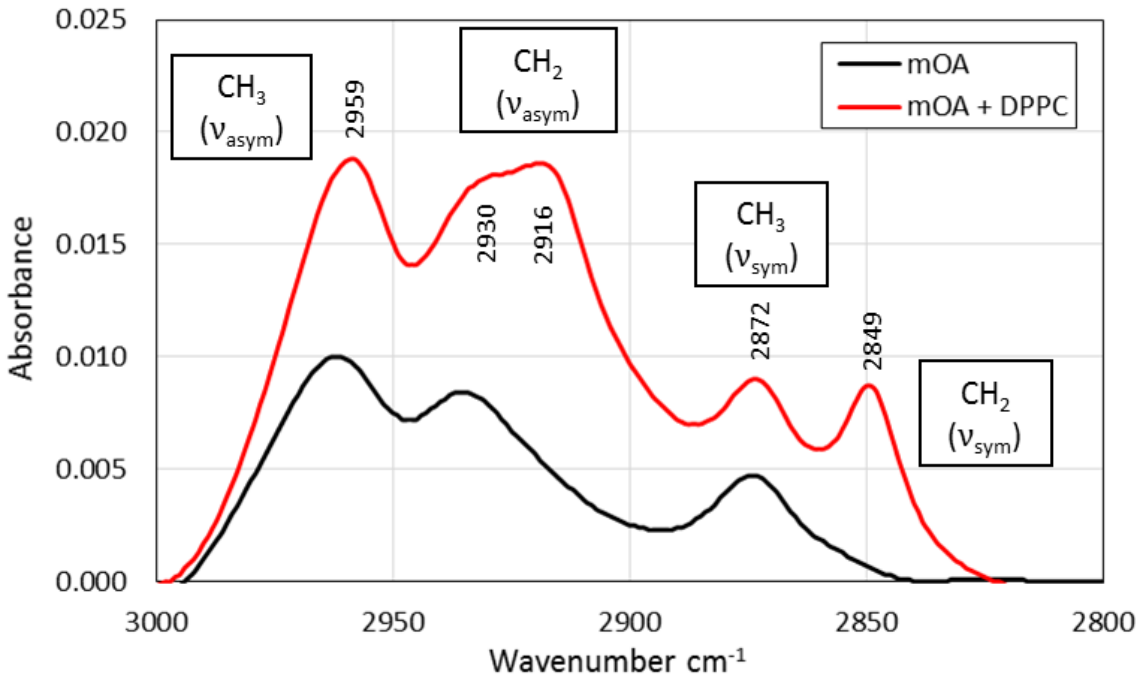


Figure 6.16 - Micro-IRRAS analysis of untested films comparing mBCS and mBCS + DPPC in the range 3000 - 2800 cm^{-1}.

Table 6.12 - Summary of IR peaks from deconvolution for untested 25salBCS, mBCS and mBCS + DPPC for 3000 - 2800 cm^{-1}. (Bold type represents the most intense CH_2/CH_3 peak).

Peaks	Wavenumber (cm^{-1})						
	DPPC	mOA	25salBCS + DPPC	mBCS + DPPC	mH + DPPC	mOA + DPPC	mPP + DPPC
CH_3 (ν_{asym})	2956	2961	2960	2959	2958	2958	2958
CH_2 (ν_{asym})	**2916**	2934	2932 **2916**	2928 **2916**	2930 **2917**	2930 **2916**	2932 **2917**
CH_3 (ν_{sym})	2872	2872	2873*	2872	2872	2872	2871
CH_2 (ν_{sym})	2850		2848	2849	2849	2849	2849

6.5 Results: Spectra from Wear Scar Deposits

In this section Micro-IRRAS analysis of the surface deposits formed in the wear tests is compared to the untested fluid reference spectra.

6.5.1 25BCS and 25BCSsal

Figure 6.17 compares spectra of both the black and rainbow deposited films to the untested fluid for 25BCS, the deconvoluted spectra is also shown for the black deposit. It can clearly be seen that both the rainbow and black films are almost identical. The most intense peak has shifted to 1632 cm^{-1} representing an N-β structure from 1641 cm^{-1} (α-helix/random coil). For the untested samples shoulder peaks are located at 1659, 1650, 1643 and 1612 cm^{-1} which represent α-helix/random coil, N-β and F-β structures respectively and can be seen in the deconvoluted spectra. Wavenumbers of the overlapping peaks for both 25BCS and 25salBCS are shown in Table 6.13.

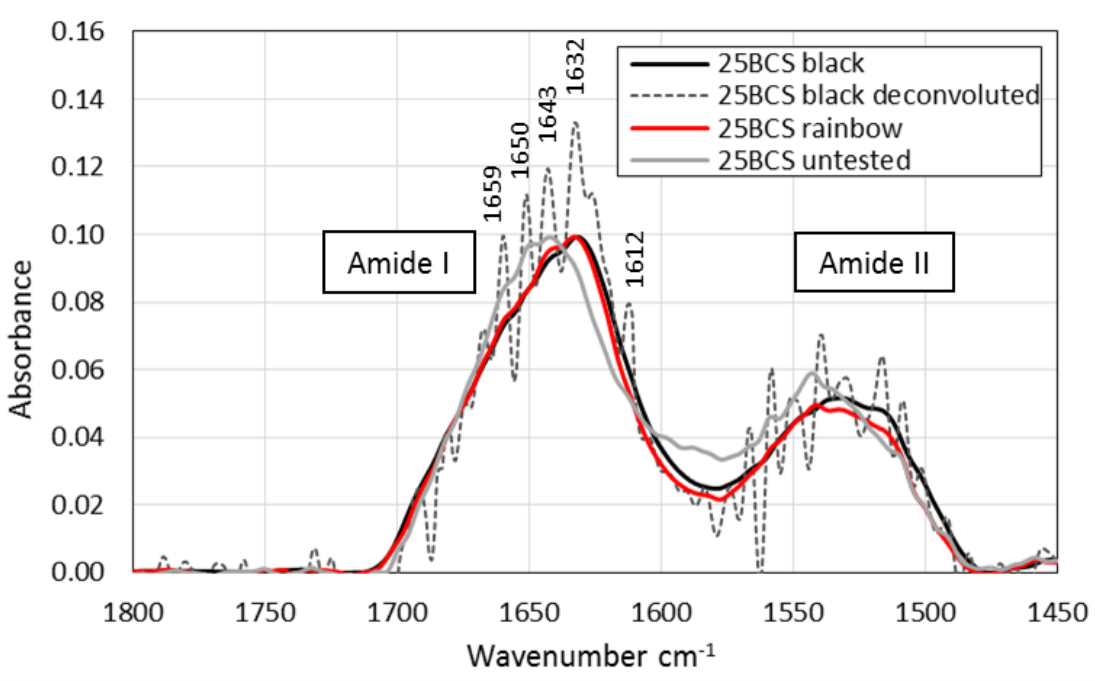


Figure 6.17 - Micro-IRRAS analysis of tested films comparing 25BCS black &rainbow deposits in the range 1800-1450 cm^{-1}.

Table 6.13 - Summary of IR peaks from deconvolution and secondary structure assignment for tested black and rainbow deposits for BCS fluids in the region 1800 - 1450 cm^{-1}. (Bold type represents most intense peak, ^{w} denotes a weak peak).

Peaks	Wavenumber (cm^{-1})		Assignment
	25BCS	25salBCS	
Amide I			
Black	1659	1658	α-helix/random coil
	1650	1650	α-helix/random coil
	1643	1642	N-β
	1632	1632	N-β
	1612 ^{w}	1612 ^{w}	F-β
Rainbow	1659	1658	α-helix/random coil
	1651	1650	α-helix/random coil
	1643	1643	N-β
	1632	1633	N-β
	1613 ^{w}	1612 ^{w}	F-β
A/G	0.8	0.8	

Figure 6.18 compares spectra in the alkyl stretch region for 25BCS, spectra for both the black and rainbow deposits are shown with spectra from the untested fluid. The peak positions for both the black and rainbow deposits were almost identical to the untested fluid and are summarised in Table 6.14 for the black and rainbow deposits (both 25BCS and 25salBCS). Peak positions of the rainbow and black films are identical, in the amide and CH stretch region, and therefore tables detailing this will not be included in this chapter but can be found in Appendix 11.3.

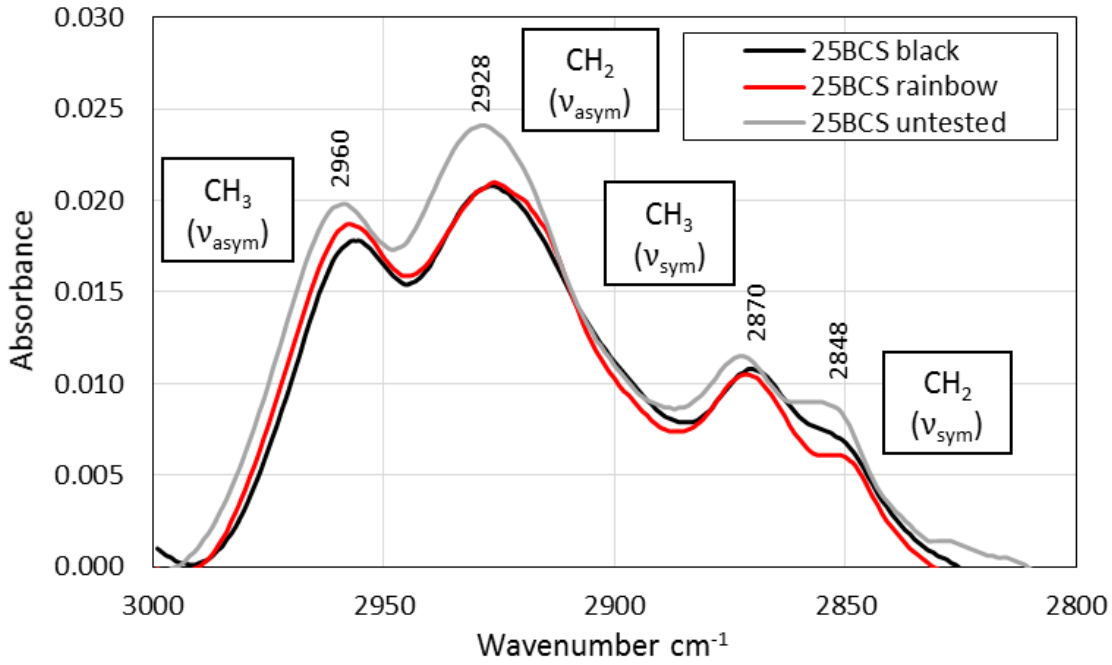


Figure 6.18 - Micro-IRRAS analysis comparing spectra from untested fluids to both black and rainbow tested deposits for 25BCS in the range 3000 - 2800 cm^{-1}.

Table 6.14 - Summary of IR peaks from deconvolution of spectra for black and rainbow deposits from the BCS samples for 3000 - 2800 cm^{-1}. (Bold type represents the most intense CH_2/CH_3 peak, no bold indicates similar peak heights).

Peaks	Wavenumber (cm^{-1})	
	25 BCS	25salBCS
CH_3 (ν_{asym})		
Black	2960	
Rainbow	2961	2960
CH_2 (ν_{asym})		
Black	2928	
Rainbow	2928	2929
CH_3 (ν_{sym})		
Black	2870	
Rainbow	2871	2870
CH_2 (ν_{sym})		
Black	2848	
Rainbow	2847	2849

6.5.2 Model Fluids without DPPC

Figure 6.19 compares IR spectra from the untested fluid and to both the black and rainbow residual deposits for mOA in the range 1800 -1450 cm^{-1}. The deposit spectra show that the amide I and II bands had noticeably broadened shifted to lower wavenumbers compared to the untested fluid reference spectrum. Each of the model fluids shifted from a higher wavenumber (range: 1641 – 1651 cm^{-1}) to ~1632 cm^{-1} (N-β). Deconvolution reveals that the same four over-lapping peaks were present (untested 25BCSsal: 1659, 1651, 1641, 1632) as identified in the untested fluids. However, an additional peak was identified at 1612 cm^{-1} which is representative of F-β (277, 278), this was present in all deposit spectra however was weak for both of the BCS fluids. The wavenumbers of the overlapping peaks within the amide I band are summarised in Table 6.15 for the black and rainbow deposited films. The peak positions of the rainbow spectra and amide II band are shown in Appendix 11.3.

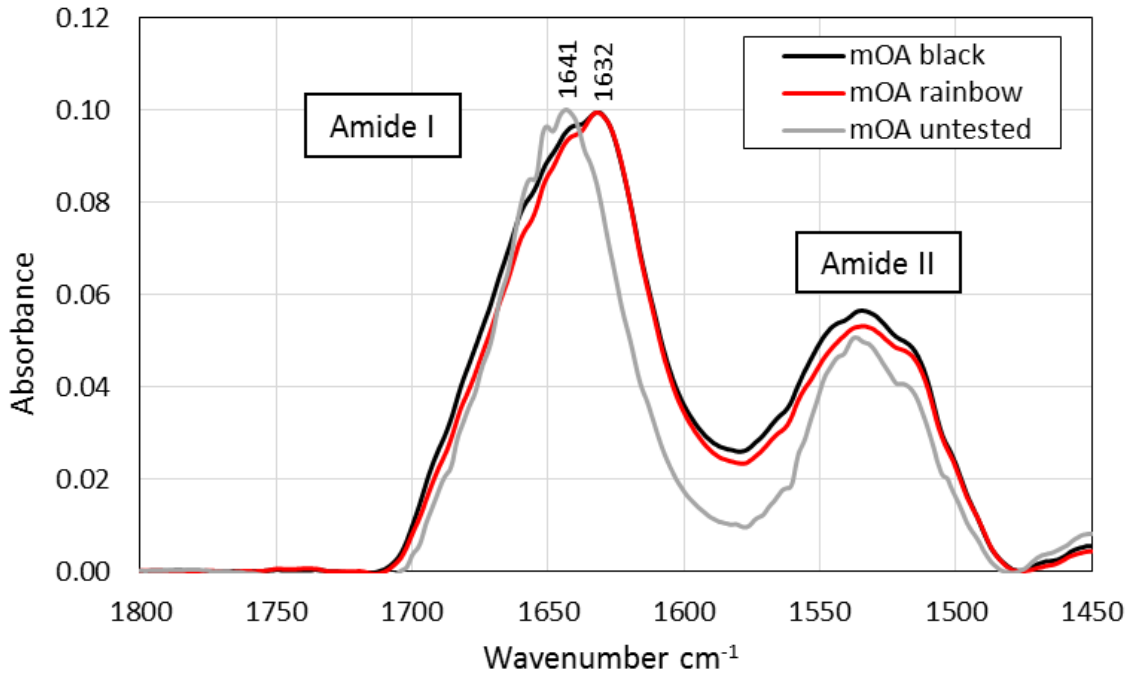


Figure 6.19 - Micro-IRRAS analysis comparing spectra from untested fluids to both black and rainbow deposits for mOA in the range 1800-1450 cm^{-1}.

Table 6.15 - Summary of IR peaks from deconvolution and secondary structure assignment for tested black deposits for model fluids in the region 1800 - 1450 cm^{-1}.

Peaks	Wavenumber (cm^{-1})					Assignment
	25BCS	mBCS	mH	mOA	mPP	
Amide I						
Black	1659	1659	1659	1659	1659	α-helix/random coil
	1650	1651	1650	1650	1650[w]	α-helix/random coil
	1643	1641	1642	1642	1643	N-β
	1632	1632	1632	1632	1633	N-β
	1612 [w]	1613	1612	1613	1613	F-β
A/G	0.8	0.8	2	1.5	3	

Figure 6.20 compares spectra in the alkyl stretch region for the wear test deposits (black and rainbow films) and untested fluids for the model fluid mOA. The positions of the CH peaks for all the model fluids (without DPPC) are summarised Table 6.16 for the black deposits. The remainder of this chapter

will not show the peak positions of the rainbow deposits in the tables as they are identical the black deposits but are reported in Appendix 11.3.

The peak positions were very similar to that of the untested fluid at ~2960, ~2930, ~2870 and ~2850 cm^{-1} representing CH_3 (ν_{asym}), CH_2 (ν_{asym}), CH_3 (ν_{sym}) and CH_2 (ν_{sym}) respectively.

Differences are observed in the CH stretch peak intensities: rainbow deposits > black deposits > untested. The relative peak height between the CH_3 and CH_2 peaks is unchanged.

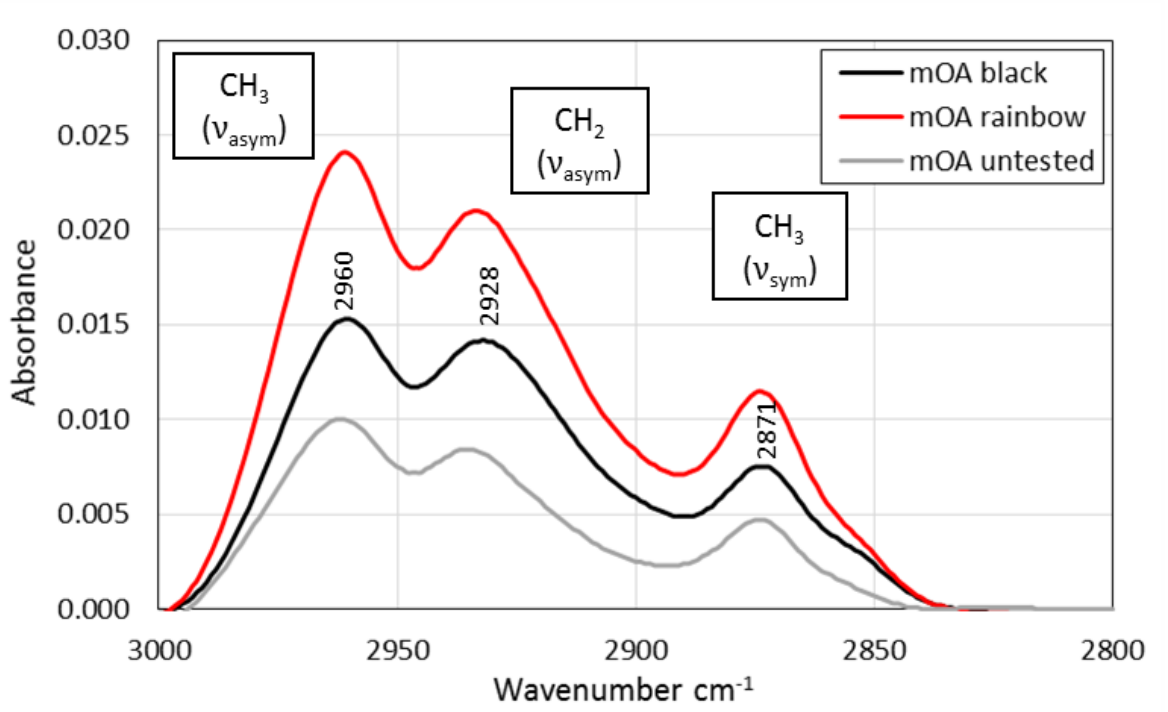


Figure 6.20- Micro-IRRAS analysis comparing spectra from untested fluids to both black and rainbow tested deposits for mOA in the range 3000 - 2800 cm^{-1}.

Table 6.16 - Summary of IR peaks from deconvolution of spectra for black deposits from the model samples for 3000 - 2800 cm^{-1}. (Bold type represents the most intense CH_2/CH_3 peak, no bold indicates similar peak heights).

Peaks	Wavenumber (cm^{-1})				
	25 BCS	mBCS	mH	mOA	mPP
CH_3 (ν_{asym})	2959	2959	2959	2960	2960
CH_2 (ν_{asym}	2930	2928	2929	2928	2929
CH_3 (ν_{sym}	2872	2870	2871	2871	2872
CH_2 (ν_{sym}	2851	2850	2850	2850	2850

6.5.3 Model Fluids with DPPC

The shape and position of the amide I and II bands were almost identical for all the BCS and model fluids with DPPC, however the lipid peak at ~1735 cm^{-1} was present only in the black deposits. Figure 6.21 shows an example of the spectra from the rainbow and black deposits for mBCS + DPPC.

Figure 6.22 compares spectra from the black deposits to the untested films for mBCS + DPPC and mPP + DPPC. It is apparent that similarly to the fluids without DPPC there was a shift in the Amide I peak position to a lower wavenumber. However, across the samples the position of the most intense peak varied: for fluids with a low A/G ratio (25BCS, 25salBCS, mBCS and mOA) 1641 cm^{-1} was dominant. A peak at 1612 cm^{-1}, which is characteristic of F-β was weak (277, 278). Whereas for fluids with a high A/G ratio (mH and mOA) the most intense band was at 1632 cm^{-1} and the peak at 1612 cm^{-1} was relatively larger. This suggests that the presence of DPPC is impeding the formation of N-β and F-β (277, 278). This slight difference in peak position can be observed in Figure 6.22.

Deconvolution of these spectra also reveals that five overlapping peaks were present in the deposits (~1659, ~1648, ~1640, ~1632 and ~1612 cm^{-1}) as for the model fluids (no DPPC) as summarised in Table 6.17 for the amide I black deposits.

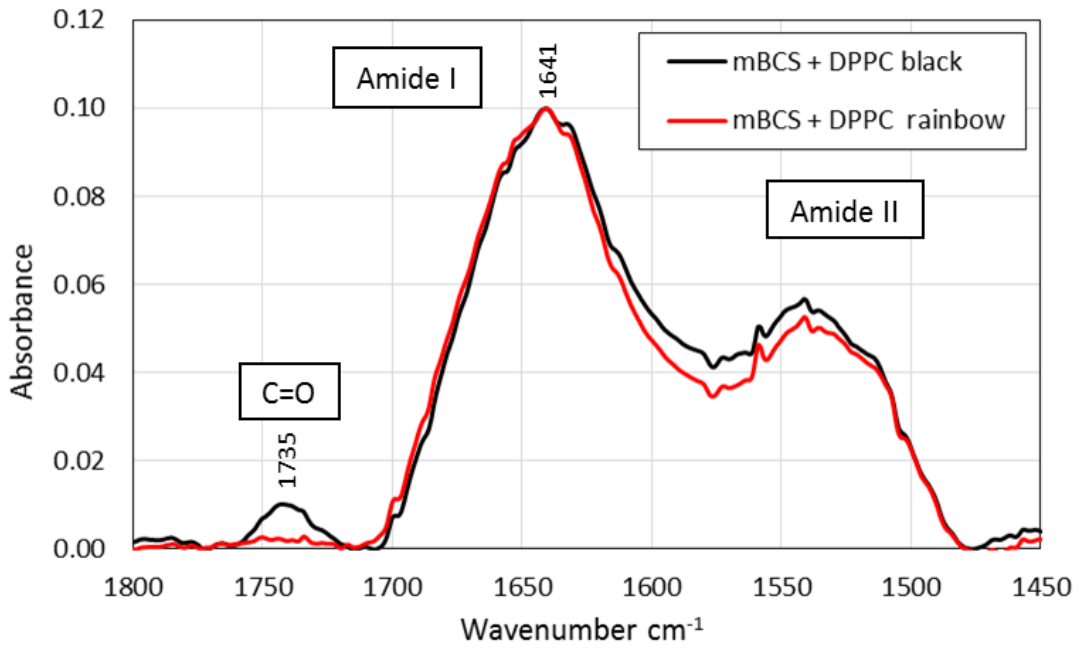


Figure 6.21 - Micro-IRRAS analysis of wear deposits comparing mBCS + DPPC black and rainbow deposits in the range 1800 - 1450 cm^{-1}.

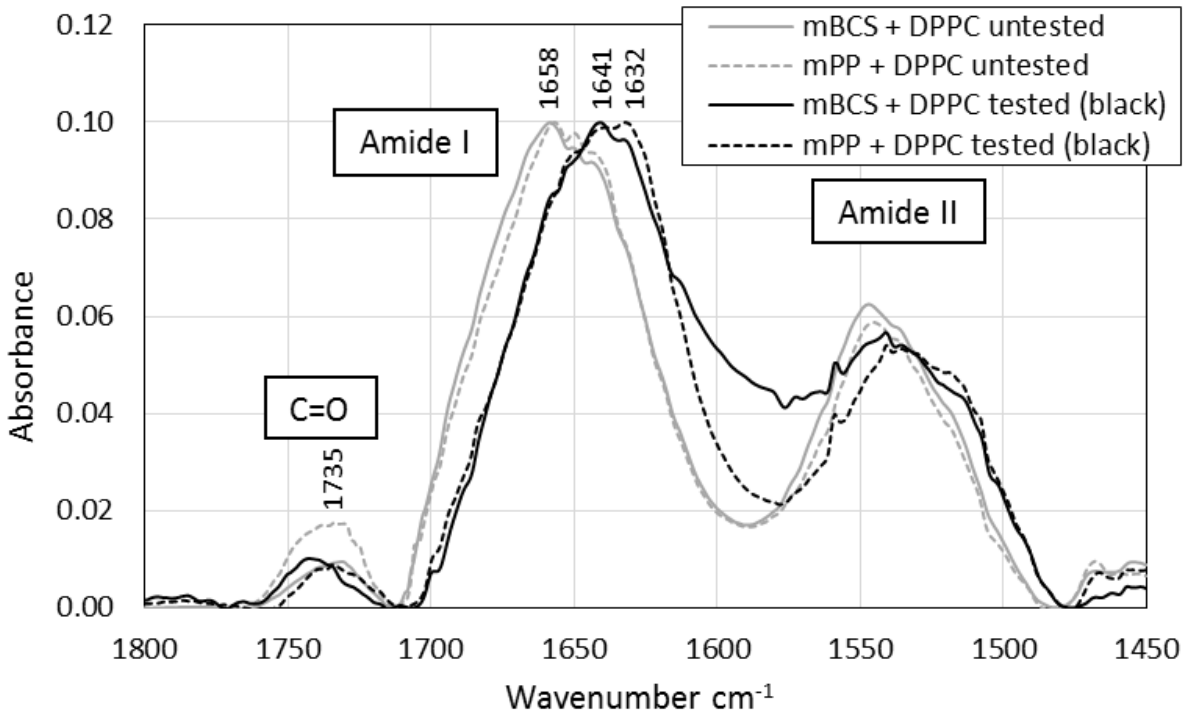


Figure 6.22 - Micro-IRRAS analysis comparing tested films and untested fluids of mBCS + DPPC and mPP + DPPC of 1800-1450 cm^{-1}.

Table 6.17 - Summary of IR peaks from deconvolution and secondary structure assignment for model fluids + DPPC for the black deposits in the range 1800 - 1450 cm^{-1}.(Bold type represents most intense peak, ^{w} denotes a weak peak).

Peaks	Wavenumber (cm^{-1})					Assignment
	25salBCS + DPPC	mBCS + DPPC	mH + DPPC	mOA + DPPC	mPP + DPPC	
Ester						
Black	1735	1735	1734	1735	1735	C=O
Amide I						
Black	1659	1659	1658	1657	1658	α-helix/random coil
	1651	1651	1648	1648	1651	α-helix/random coil
	1641	1641	1640	1640	1642	N-β
	1632	1631	1630	1631	1632	N-β
	1612^{w}	1611^{w}	1612	1612^{w}	1611	F-β
A/G	0.8	0.8	2	1.5	3	

Figure 6.23 compares the CH stretch spectra for the untested fluid mBCS + DPPC and black/rainbow wear deposits. Deconvolution confirms that the peak positions are at ~2960, ~2870 and ~2850 cm^{-1} for the peaks CH_3 (ν_{asym}), CH_3 (ν_{sym}) and CH_2 (ν_{sym}) respectively. Whilst for CH_2 (ν_{asym}) a doublet peak at ~2930 and ~2916 cm^{-1} representing both proteins and lipids was present. A summary of peak positions of the black deposits are shown in Table 6.18 for each of the model fluids and 25salBCS with additional DPPC.

Differences were seen when comparing relative peak intensities in this region. Spectra for untested and rainbow very similar with a slight increase in ~ 2920 cm^{-1} CH_2 (ν_{asym}) peak for the rainbow deposits. Large differences were seen for the black deposits with an overall increase in peak intensities relative to the amide I and a dramatic increase in ~ 2920 cm^{-1} CH_2 (ν_{asym}) and ~ 2850 cm^{-1} CH_2 (ν_{sym}). This was observed for all model and BCS fluids tested with additional DPPC, the A/G ratio did not appear to affect this region of the spectra. This confirms the observations from the Amide I region analysis that the lipids are associated with the black dispersed deposits rather than the rainbow films.

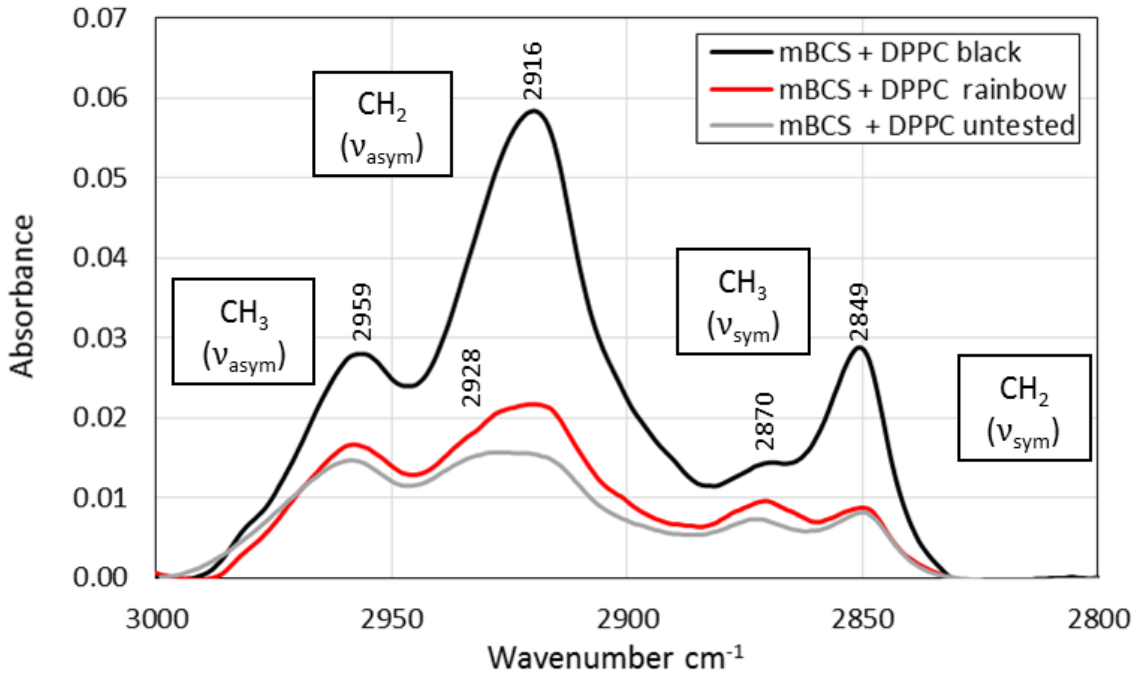


Figure 6.23- Micro-IRRAS analysis comparing spectra from untested fluids to black and rainbow deposits for mBCS + DPPC in the range 3000 - 2800 cm^{-1}.

Table 6.18 - Summary of IR peaks from deconvolution for tested model fluids with DPPC for the black deposits in the range 3000 - 2800 cm^{-1}. (Bold type represents the most intense CH_2/CH_3 peak, no bold indicates similar peak heights).

Peaks	Wavenumber (cm^{-1})					
	DPPC	25salBCS + DPPC	mBCS + DPPC	mH + DPPC	mOA + DPPC	mPP + DPPC
CH_3 (ν_{asym})	2958	2957	2959	2960	2959	2958
CH_2 (ν_{asym})	2918	2928 2917	2927 2916	2928 2917	2929 2917	2930 2916
CH_3 (ν_{sym})	2871	2871	2870	2870	2870	2872
CH_2 (ν_{sym})	2850	2850	2849	2851	2852	2850

6.6 Results: HSF Samples

6.6.1 HSF: Untested Samples

Spectra of the amide I and II band region for example HSF samples are compared to 25BCS in Figure 6.24. HSF110 is representative of all other samples not shown on the graph and shows a clear difference in peak position compared to 25BCS. Deconvolution of the amide I band indicates five overlapping peaks at 1666, 1658, 1649, 1641 and 1631cm^{-1} representing the secondary protein structures turns and bends, α-helix/random coil, α-helix/random coil, N-β and N-β respectively (277, 278). For all of these cases the most intense peak was at 1659 cm^{-1}, which is assigned to the α-helix/random coil configuration. In addition, the peak at 1666 cm^{-1} was not present in 25BCS. Turns and bends are associated with the N-β, which has an anti-parallel structure, the bends and turns reverse the direction of the polypeptide chain so that intra-molecular bonds are formed (277, 294).

The spectra from two samples HSF77 and HSF113 shown in Figure 6.24 deviated from the norm (HSF110). For HSF77 a large shoulder was observed containing overlapping peaks 1650 and 1641 cm^{-1} indicating the sample contained a slightly different protein composition. The spectra for sample HSF113 had a very similar peak position compared to 25BCS. Deconvolution of this data showed that the amide I peak contained only four overlapping peaks at 1658, 1650, 1642 and 1632 cm^{-1} representing the secondary structures α-helix/random coil, α-helix/random coil, N-β and N-β respectively (277, 278). With the most intense peak is at 1642 cm^{-1}, N-β, the same as 25BCS.

Table 6.19 summarises the location of all overlapping peaks in the amide I band found from deconvolution for all the human samples, 25BCS is shown for comparison.

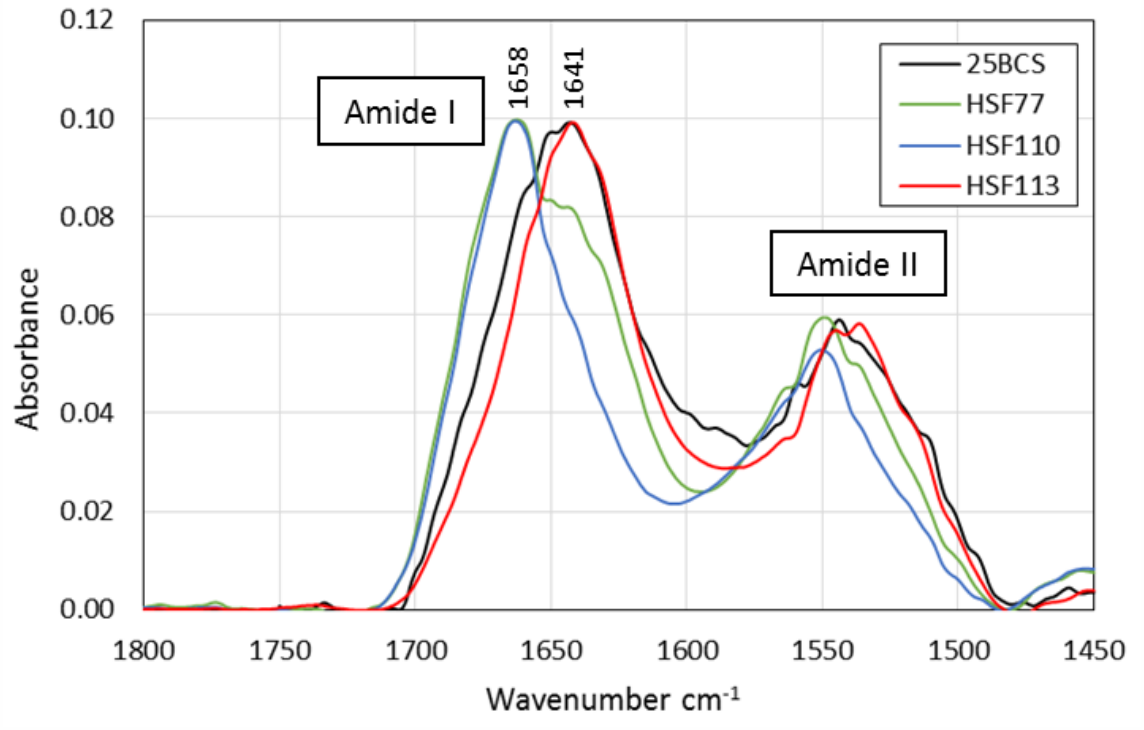


Figure 6.24 - Micro-IRRAS analysis of untested fluids 25BCS, HSF77, HSF110 and HSF113 in the range 1800-1450 cm^{-1}.

Table 6.19 - Summary of IR peaks from deconvolution and secondary structure assignment for all untested HSF fluids and 25BCS in the range 1800 - 1450 cm^{-1}. (Bold type represents most intense peak, ^{w} denotes a weak peak).

Peaks	Wavenumber (cm^{-1})									Assignment
	25BCS	HSF 041	HSF 077	HSF 110	HSF 113	HSF 135	HSF 145	HSF 156	HSF 164	
Amide I		1667	1666	1666		1666	1666	1666	1667^{w}	turns and bends
	1659	1659	1659	1658	1658	1659	1661	1658	1658	α-helix/random coil
	1651	1650	1650	1649	1650	1650	1649	1649	1650	α-helix/random coil
	1641	1642	1642	1641	1642	1642	1642	1642	1643	N-β
	1632	1633	1632	1631	1632	1632	1632^{w}	1632^{w}	1632	N-β

Figure 6.25 compares the spectra of the alkyl stretch region for the fluids HSF77, HSF110, HSF113 and 25BCS. The peak positions of the HSF fluids are at ~2960, ~2930, ~2870 and ~2850 cm^{-1} representing CH_3 (ν_{asym}), CH_2 (ν_{asym}), CH_3 (ν_{sym}) and CH_2 (ν_{sym}) respectively. A shoulder at ~2916 cm^{-1} was not observed

in any of the HSF samples indicating lipids were not present in detectable concentrations in the bulk fluid. Table 6.20 summarises peak positions in the alkyl stretch region for all HSF samples, 25BCS is shown for reference.

The overall CH peak intensities for 25BCS were significantly larger than the HSF samples.

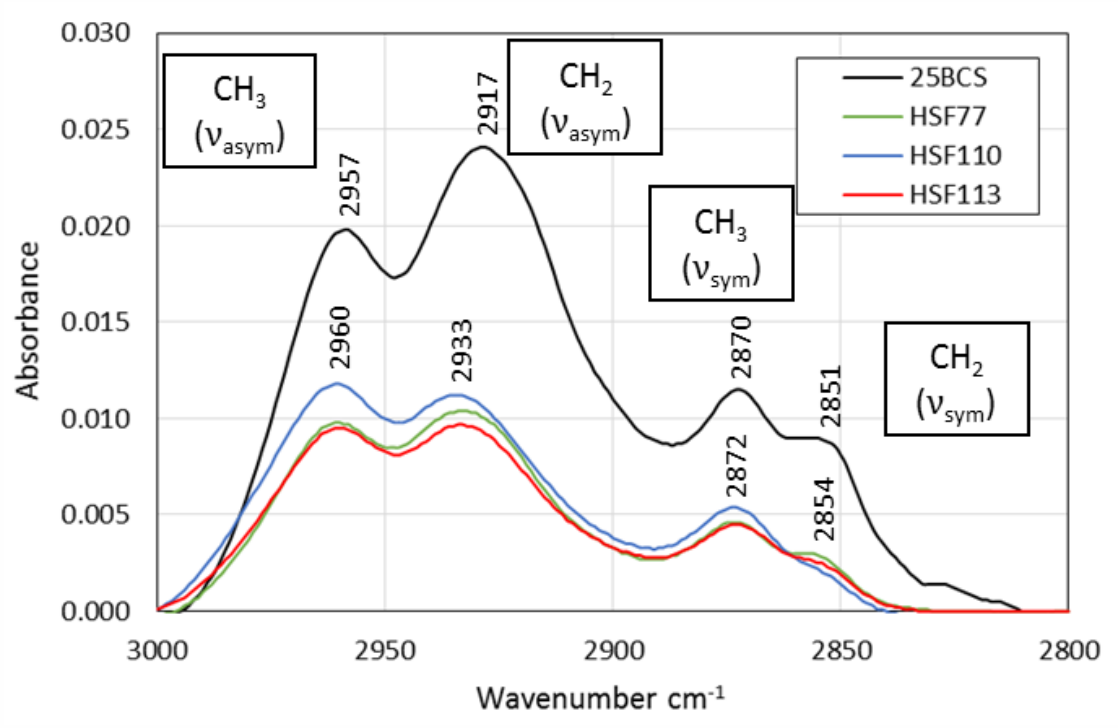


Figure 6.25 - Micro-IRRAS analysis comparing untested fluids 25BCS, HSF 77, HSF110 and HSF 113 in the range 3000 - 2800 cm^{-1}.

Table 6.20 - Summary of IR peaks from deconvolution for all untested HSF fluids in the range 3000 - 2800 cm^{-1}. (Bold type represents the strongest peak).

Peaks	Wavenumber (cm^{-1})								
	25BCS	041	077	110	113	135	145	156	164
CH_3 (ν_{asym})	2957	2963	2961	2961	2961	2961	2960	2960	2960
CH_2 (ν_{asym})	2932 2917	2930	2933	2935	2933	2930	2933	2935	1930
CH_3 (ν_{sym})	2870	2873	2873	2873	2873	2872	2872	2872	2873
CH_2 (ν_{sym})	2851	2854	2854	2854	2854	2854	2854	2854	2853

6.6.2 HSF: Wear Test Deposits

Figure 6.26 and Figure 6.27 show example IR spectra from black and rainbow wear deposits for HSF41 and HSF164. In all the HSF samples examined the amide I and II bands shifted to a lower wavenumber compared to the untested fluid spectra. Typical amide I main peak changes were from 1660 to < 1650 cm^{-1}.

For HSF41 a C=O peak at 1735 cm^{-1} is also present in both the black and rainbow deposits whereas this is only present in the black deposits for HSF110, HSF156 and HSF164 and not observed for all other HSF samples. The peaks at ~ 1730 cm^{-1} were not observed in the untested fluid spectra. A summary of the positions of the overlapping peaks in the amide I band obtained from deconvolution of the spectra from the black deposits is given in Table 6.21.

Analysis of these HSF wear-test deposits was more complex than for the model fluids. For the black deposits the most intense peaks were at 1632 cm^{-1} (N-β) for HSF113, 1643 cm^{-1} (N-β) for HSF41 and HSF77, ~1650 cm^{-1} (α-helix / random coil) for HSF110, HSF135, HSF156 and HSF164 and lastly 1659 cm^{-1} (α-helix/random coil) for HSF 145. For comparison the strongest peak for 25BCS was located at 1632 cm^{-1} similar to HSF113 (277, 278). The rainbow deposits differed only for HSF 41 as seen in Figure 6.26 where the strongest peak was located at 1631 cm^{-1} (N-β) (277, 278).

For some samples, HSF41, HSF113, HSF 156 and HSF164 five overlapping peaks were identified at ~1659, ~1651, ~1643, ~1631 and ~1612 cm^{-1} assigned to α-helix/random coil, α-helix/random coil, N-β, N-β and F-β structures respectively (277, 278). For all other samples the N-β peak at ~1612 cm^{-1} was not present.

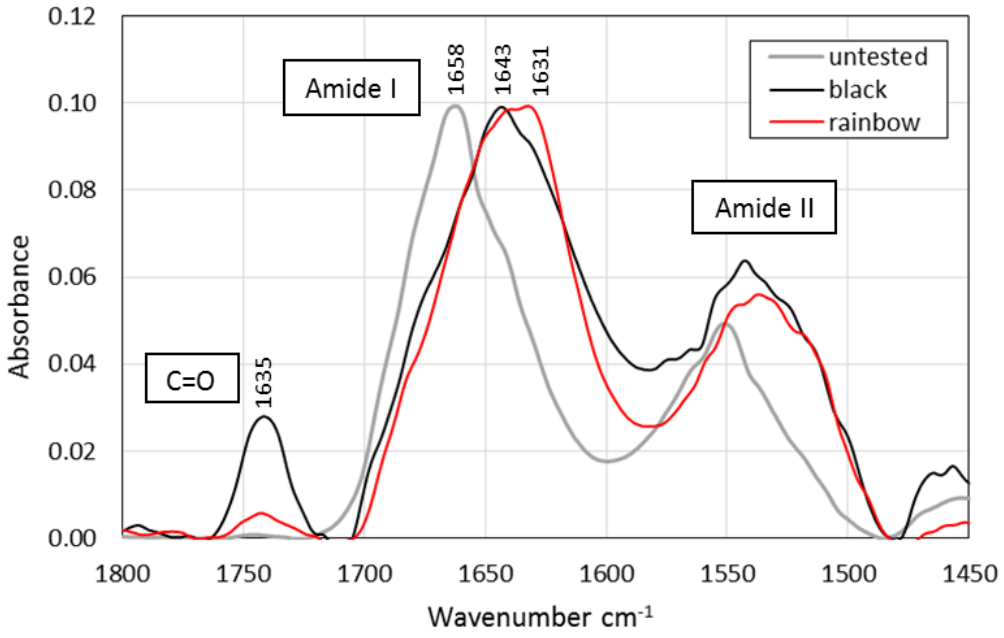


Figure 6.26 - Micro-IRRAS analysis comparing the untested fluid, black and rainbow deposits from HSF041 in the range 1800-1450 cm^{-1}.

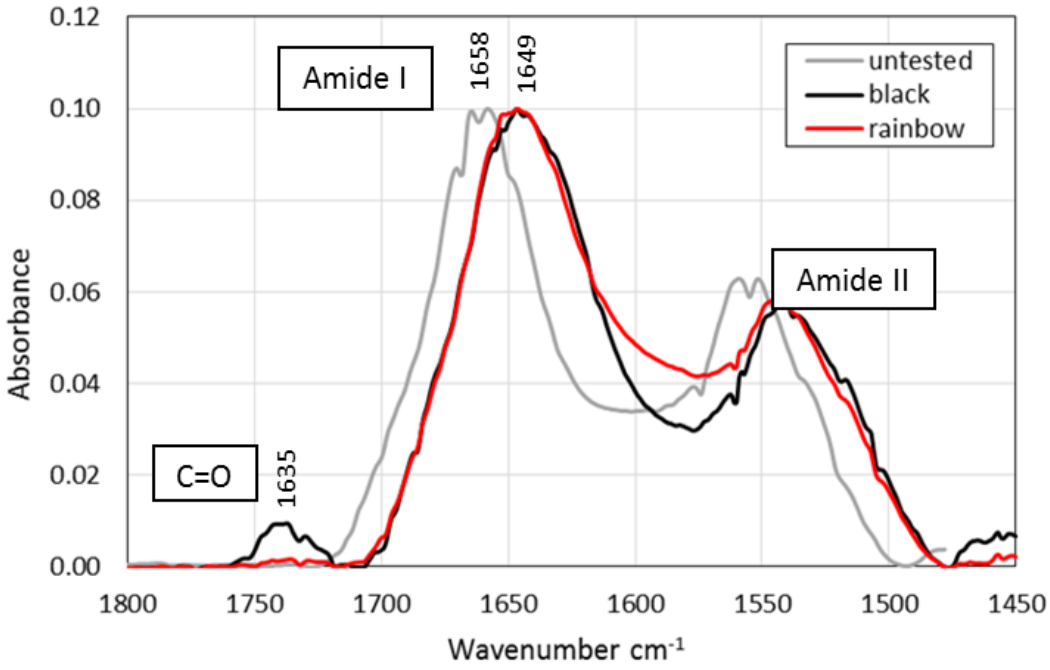


Figure 6.27 - Micro-IRRAS analysis comparing the untested fluid, black and rainbow deposits from HSF164 in the range 1800-1450 cm^{-1}.

Table 6.21 - Summary of IR peaks from deconvolution and secondary structure assignment for all tested HSF samples in the range 1800 - 1450 cm^{-1}. (Bold type represents most intense peak, ^{w} denotes a weak peak).

Peaks	Wavenumber (cm^{-1})									Assignment
	25BS	041	077	110	113	135	145	156	164	
Ester		1735		1735				1735	1737	C=O
Amide I	1659	1659	1660	1657	1660	1658	1659	1659	1658	α-helix/random coil
	1650	1651	1651	1649	1651	1650	1651^{w}	1651	1649	α-helix/random coil
	1643	1643	1643	1641	1642	1639	1642	1642	1642	N-β
	1632	1631	1632	1631^{w}	1632	1630	1630	1632	1633	N-β
	1612^{w}	1612^{w}			1612			1612^{w}	1612^{w}	F-β

The alkyl stretch region is for HSF41 shown in Figure 6.28. The peak positions for of the rainbow deposits are similar to that of the untested fluid at ~2960, ~2930, ~2870 and ~2850 cm^{-1} representing CH_3 (ν_{asym}), CH_2 (ν_{asym}), CH_3 (ν_{sym}) and CH_2 (ν_{sym}) respectively. However, for the black deposits the CH_2 (ν_{asym}) was at ~2916 cm^{-1}. Table 6.22 summarises the exact position for each of the four peaks of all HSF black deposits.

The overall peak intensity is higher for the tested fluids when normalised to the amide I band. The relative peak heights of CH_2 (ν_{asym}) and CH_2 (ν_{sym}) were increased for the black deposits.

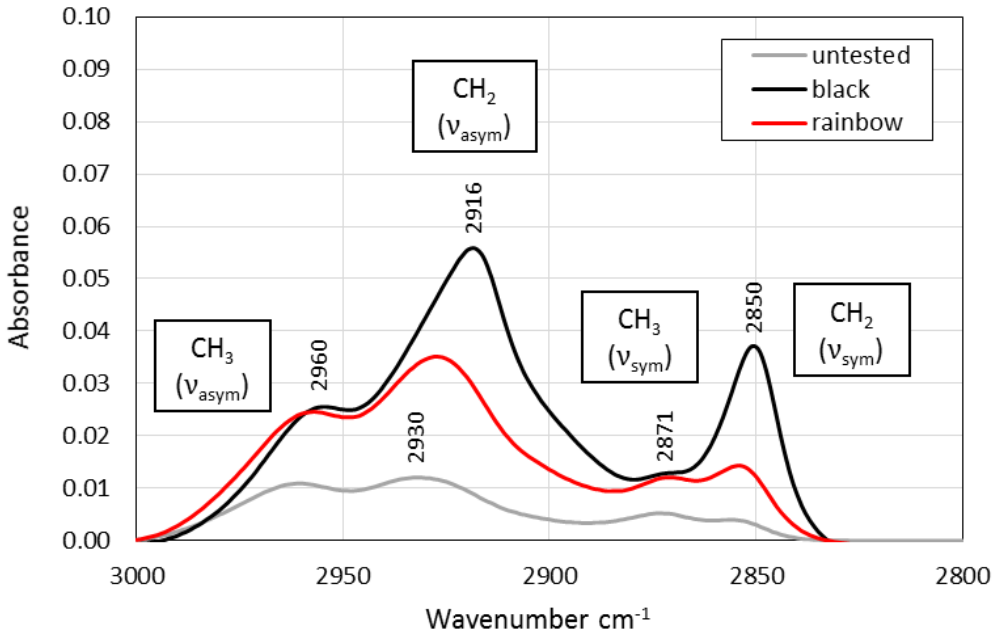


Figure 6.28 - Micro-IRRAS analysis comparing spectra from untested fluids to both black and rainbow tested deposits for HSF41 in the range 3000 - 2800 cm^{-1}.

Table 6.22 - Summary of IR peaks from deconvolution for all tested HSF samples for the black deposits in the range 3000 - 2800 cm^{-1}. (Bold type represents the most intense CH_2/CH_3 peak, no bold indicates similar peak heights).

Peaks	Wavenumber (cm^{-1})								
	25BS	041	077	110	113	135	145	156	164
CH_3 (ν_{asym})	2959	2960	2961	2960	2960	2959	2960	2959	2958
CH_2 (ν_{asym})	2932 2917	2916	2917	2916	2917	2920	2916	2918	2919
CH_3 (ν_{sym})	2872	2871	2870	2870	2870	2871	2870	2871	2870
CH_2 (ν_{sym})	2851	2850	2850	2851	2850	2851	2850	2851	2851

6.7 Discussion

6.7.1 Summary of Results

In this chapter dried untested fluids and residual deposits formed in the wear tests were examined by Micro-IRRAS. Two spectral regions were analysed corresponding to the amide I and II bands (1800 – 1450 cm^{-1}) and alkyl (CH) stretch (3000 – 2800 cm^{-1}). Initially spectra of untested single constituent solutions 12Alb, 6Glob and 0.5 mg/ml DPPC were examined to understand characteristics of each. This was followed by analysis of the untested fluids for BCS solutions and model solutions with and without DPPC. Surface deposits formed during the wear tests were analysed and compared to the untested fluids for BCS, model and HSF samples. The results are summarised below:

1. Untested fluids:
    - Distinct difference in band position between 12Alb (α-helix/random coil; 1652 cm^{-1}) and 6Glob (N-β; 1642 cm^{-1}).
    - DPPC can be identified by peaks at ~ 1735 cm^{-1} (C=O), 2916 cm^{-1} (CH_2 (ν_{asym})) and ~ 2872 cm^{-1} (CH_2 (ν_{sym})).
    - Addition of saline did not alter the band position.
    - Addition of DPPC shifted the amide I band position to a higher wavenumber (without DPPC: range 1641-1651 cm^{-1}, N-β/ α-helix/random coil; with DPPC ~1658 cm^{-1}, α-helix/random coil).
    - HSF fluids generally have a higher amide I peak position (~1659 cm^{-1}, α-helix/random coil).
2. Deposited films:

- The amide I band position shifted to a lower wavenumber when compared to the untested samples.
- Addition of saline did not alter the amide I band position.
- No difference was seen in the amide I band position of the black and rainbow deposits.
- DPPC was only present in the black deposits. Occasionally characteristic lipid peaks were seen in samples where DPPC had not been added, this was attributed to the fatty acids present in BSA.
- Presence of DPPC in high γ-G content fluids hinders ability to form N-β and F-β.

6.7.2 Amide I Peak Position and Protein Secondary Structure

One of the key outcomes of the micro-IRRAS analysis is the identification of protein secondary structures from the amide I peak positions. It is worthwhile at this point to examine this aspect in more detail.

The amide I band position can be used to identify the protein secondary structure. Each secondary structure has a different geometry (turns and bends, α-helix/random coil, N-β, F-β) which dictates the length, direction and hence strength of hydrogen bonds involving amide C=O and NH groups (278). This gives characteristic electron densities resulting in distinctive absorption frequencies. The stronger the hydrogen bonding the lower the electron density and the lower the frequency of the absorption bands (277). Hydrogen bonds in the turns and bends followed by the α-helix/random coil structure are the longest and weakest and therefore these amide I bands absorb at the highest frequency (~1650 cm^{-1}). N-β have a conformation which allows shorter and stronger bonds and hence have a characteristic absorption at lower wavenumber (~ 1640 cm^{-1}) compared to the α-helix/random coil structure. F-β consist of long extended chains where intramolecular bonding is not possible however strong bonds between neighbouring chains (intermolecular) are formed due to their close alignment thus giving rise to a low IR absorption frequency (<1630 cm^{-1}) (278).

6.7.3 Comparison of Untested BCS, Model and HSF Fluids

The peak position of the amide I band of the untested single protein solutions 12Alb and 6Glob varied. These bands were deconvoluted and revealed a number of overlapping peaks in the Amide I region. The most intense peak for 12Alb and 6Glob was at 1651 cm^{-1} (α-helix/random coil) and 1642 cm^{-1} (N-β) respectively. A study by Kaiden et al. (310) reported absorption bands from dried films of BSA at 1658 cm^{-1} representing an α-helix/random coil structure. A study by Sharma et al. (311) reported an absorption band at 1640 cm^{-1} for γ-G from bovine which was assigned to an N-β structure. Literature

reports that roughly 50% of globular proteins such as BSA and γ-G are unordered (114), of the ordered structure 50% of BSA is an α-helix and 40% of γ-G is a N-β (310) which is in agreement with results.

The position of the most intense peak in the amide I band envelope varies for the untested model fluids mBCS, mH, mOA and mPP which appears to scale the A/G ratio as shown in Figure 6.13. When considering the peak positions of the single protein solutions, 12Alb and 6Glob, the results agree. The sample mBCS has the highest proportion of γ-G and the lowest peak position of model samples tested at 1641 cm^{-1} (N-β) followed by mOA at 1643 cm^{-1} (N-β) and mH at 1647 (α-helix/random coil) cm^{-1}. The sample (mPP) with the highest proportion of BSA had the main amide I peak at 1651 cm^{-1} (α-helix/random coil) which was closest to the 12Alb solution. The proteins γ-G and BSA have a molecular weight of 150kDa (116) and 66.5 kDa (115) respectively and it is therefore it follows that γ-G has more of an effect on the position of the amide I band compared to BSA.

Addition of DPPC to the BCS and model solutions shifted the amide I and II bands towards a higher wavenumber. The most intense overlapping peak in the amide I band for each case was at ~ 1658 cm^{-1}, an α-helix/random coil conformation. Lipid-protein interactions occur in plasma fluids and can result in an increase in the helical component which is supported by the current FTIR results (312).

The amide I band for the HSF untested samples was usually located at 1659 cm^{-1} representing an α-helix/random coil secondary structure (277, 278), which is similar to the model fluids with DPPC and therefore this higher wavenumber could correlate with the presence of lipids (312).

Each peak had the same shape excluding HSF77 which had a large shoulder containing over lapping peaks 1650 and 1641 cm^{-1} indicating the sample contained a slightly different protein composition. The only exception was sample HSF113 where the most intense peak was located at 1642 cm^{-1} representing a N-β secondary structure and was similar in shape to the spectra of 25BCS, the reference fluid (277, 278). It is interesting to note that this sample, HSF113, exhibited low wear which was also comparable to 25BCS. The higher frequency recorded for almost all the HSF samples was probably due to the effect of lipids on protein structure noted for the model fluids.

6.7.4 Wear Test Deposits

Micro-IRRAS analysis was carried out for all test deposits and where possible spectra were taken from both black and rainbow regions and compared to spectra from the untested fluids. These films were described in Chapter 5 and appeared to have different structures; as dispersed particulates/fibrils (black) and insoluble amorphous films (rainbow).

For all fluids the deposited spectra displayed a shift in the main amide I band (compared to the untested fluid) to a lower wavenumber, representing a change from a predominately α-helical/random coil to an N–β structure with an additional peak representing an F-β structure. For the untested model and BCS fluids the most intense peak was in the range 1641 - 1651 cm^{-1} this shifted to ~1632 cm^{-1} (277, 278) for samples without DPPC. For post-test films an additional peak at ~1612 cm^{-1} was present which is often attributed to a F-β structure (277, 278).

For the BCS and model fluids with DPPC the shape and position of the amide I and II bands of spectra from the black and rainbow deposits were almost identical, however the lipid peak at ~1735 cm^{-1} was present only in the black deposits. The peak was more intense (relative to amide I absorbance) than in the untested fluid spectra and suggests that lipids are involved in the denaturing/aggregation process. The resulting β structure proteins have effectively scavenged this molecule.

The position of the amide I band of the BCS and model fluids with DPPC was related to the A/G ratio. For samples with a low A/G ratio (high γ-G content; 25salBCS, mBCS and mOA) the peak was located at ~1641 cm^{-1} (N-β) whilst for samples with a high A/G ratio (low γ-G content; mH and mPP) the peak was located at ~1631 cm^{-1} N-β (277, 278). Additionally peaks at 1612 cm^{-1} (F-β) were present in all deposited films however these were weak for the low A/G ratio samples (277, 278). Therefore, this suggested that lipids have a greater effect of preserving the α-helix/random coil structure of γ-G. This can be related to wear, for a low A/G ratio (high γ-G content) α-helix/random coil structure is preserved by the lipids, inhibiting the formation of N-β and F-β, which is related to an increase in wear. These results are summarised in Figure 6.22.

Table 6.23 – Model fluids, A/G ration, major amide I peak position with and without DPPC and ΔAWD.

Model Fluids	A/G ratio	Major Amide I Peak Position (cm^{-1})		Δ AWD (nm) $\left[\begin{matrix}\text{No}\\ \text{DPPC}\end{matrix}-\begin{matrix}\text{With}\\ \text{DPPC}\end{matrix}\right]$
		No DPPC	With DPPC	
25salBCS	0.8	1632	1641	-41
mBCS	0.8	1632	1641	-168
mOA	1.5	1632	1640	-119
mH	2	1632	1630	130
mPP	3	1633	1632	35

The main differences observed in the alkyl stretch region for the BCS and model samples with additional DPPC was the increase in intensity of the CH_2 (ν_{asym}) and CH_2 (ν_{sym}) peaks at 2916 and 2850cm^{-1} respectively. Additionally these peaks had a reduced Full Width Half Maxima (FWHM) suggesting that the lipids present formed highly ordered all-trans alkyl chains in the deposited films at increased concentration in the black deposits (307). This increase in peak intensity was only observed in the black deposits and little change was seen for the rainbow deposits when compared to the untested fluid. This can be related to the amide band region where the spectra only showed the presence of lipids in the black deposits, providing further evidence that these regions may be scavenging lipids.

Analysis of the wear deposits for the HSF samples was more complex. The main conclusion is that, similarly to BCS and model fluids, the position of the most intense amide I peak of the deposits shifted to a lower wavenumber.

The most intense overlapping peak in sample HSF135 was located at the highest wavenumber, 1659 cm^{-1} an α-helix/random coil structure, samples HSF110, HSF135, HSF156 and HSF164 were assigned the same secondary structure although the most intense peak was located at a lower wavenumber (~1649 cm^{-1}) (277, 278). The most intense peak for two of the samples, HSF041 and HSF077, was located at 1643 cm^{-1} representing a N-β secondary structure. The only sample to show the same characteristics as 25BCS with the most intense peak located at 1632 cm^{-1}, a N-β, was sample HSF113 (277, 278). A peak at ~1612 cm^{-1} showing the presence of F-β was only present in samples HSF041, HSF113, HSF156 and HSF164.

The peak at ~1733 cm^{-1} assigned to the C=O /lipid which was not detected in the untested fluids was apparent in both black and rainbow deposits for HSF41, in only the black deposits for HSF110, HSF156 and HSF164 and not observed for all other samples. There did not appear to be a correlation with the presence of the C=O peak with the position of the amide I band.

In the alkyl chain region, the bands from the black deposit narrowed, intensified and shifted from ~2930 cm^{-1} to 2917 cm^{-1} for the CH_2 (ν_{asym}) peak and from 2854 to 2850 cm^{-1} for the CH_2 (ν_{sym}) peak indicating that highly ordered all-trans alkyl chains and hence lipids are present to some extent in the deposited films.

6.7.4.1 F-β secondary structure

The F-β structure is of particular interest as it has a parallel β-sheet structure which are characteristic of aggregated proteins (277, 278, 294-303). The most common aggregate is the amyloid fibre which

appear to be highly ordered and rope like (313), this analysis does not explicitly provide evidence of its presence and therefore further experimental work will be reported in Chapter 7.

6.7.4.2 Summary of Wear Deposit Analysis

The main changes that are observed between the untested and tested fluids is the shift of the amide I band to a lower wavenumber suggesting the formation of N-β with the presence of F-β. This occurs for high γ-G content fluids without DPPC, however the presence of DPPC appears to inhibit N-β formation with high γ-G content fluids. The development of N-β with the presence of F-β is less common for HSF samples.

The alkyl stretch region, which is often ignored, has provided important information in the analysis of these deposited films. The shift of the CH_2 (ν_{asym}) from 2930 cm^{-1} to 2916 cm^{-1} and the presence of the CH_2 (ν_{sym}) at 2850cm^{-1} indicated the presence of lipids. The intensity of these peaks increased and HBW decreased indicating that they were highly ordered all-trans alkyl chain (279). Lipids were also be identified using the ester peak (C=O) at ~1735 cm^{-1}. These where characteristic of both the model fluids with DPPC and the HSF fluids in the black deposits only, suggesting that this region scavenges lipids.

6.7.5 Effect of Amide I Position on AWD

For all wear deposits the wavenumber of the major peak amide I peak decreased compared to the untested fluids. It is therefore interesting to see if the wear deposit amide I position can be related to the AWD. The AWD is plotted against the major amide I peak position for BCS (no DPPC) and model fluids (no DPPC) in Figure 6.29 where no correlation is seen. The same is done for model fluids (+ DPPC) and HSF (contain lipids) in Figure 6.30 where the AWD increases for increasing peak wavenumber. Therefore, the presence of N-β and F-β in the deposited films is associated with low wear for fluids containing DPPC or lipids.

The HSF fluids tested have OA pathologies therefore should theoretically have an A/G ratio of ~1.5. Analysis from the model fluids suggested that DPPC/lipids inhibited the formation of N- β and F-β in high γ-G fluids which could also fit with results from the HSF fluids. However, the chemical composition of the HSF fluids is unknown and therefore further analysis should be performed to better understand this correlation. Unfortunately, this outside the scope of this thesis.

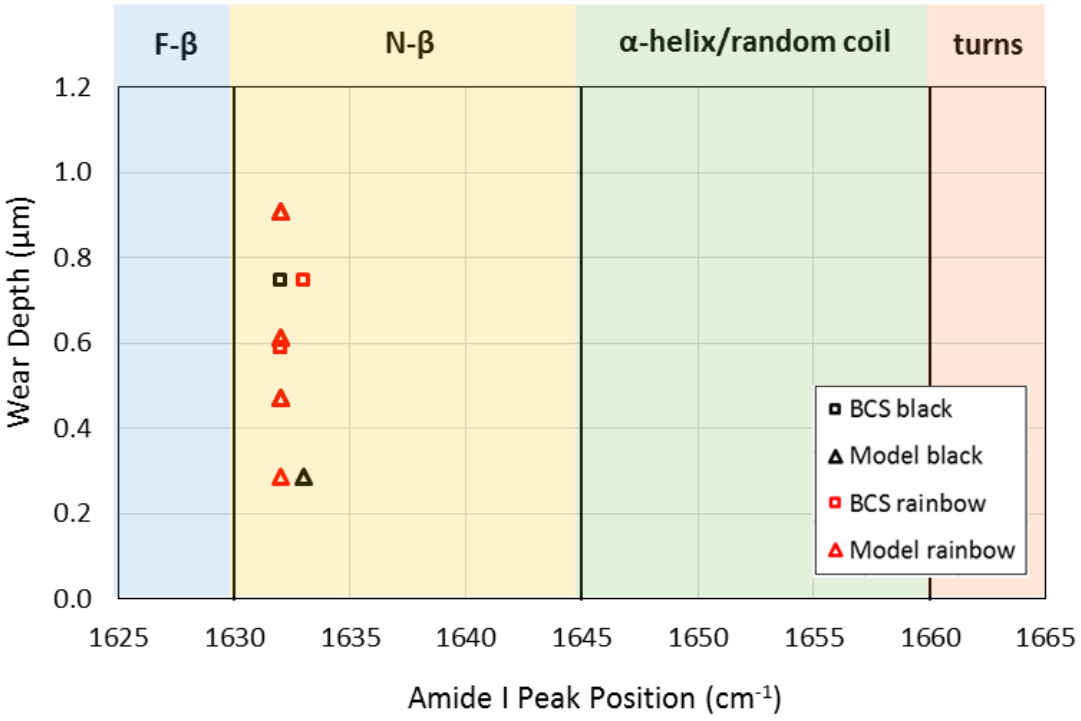


Figure 6.29 – AWD Vs amide I major peak position for BCS and Model fluids.

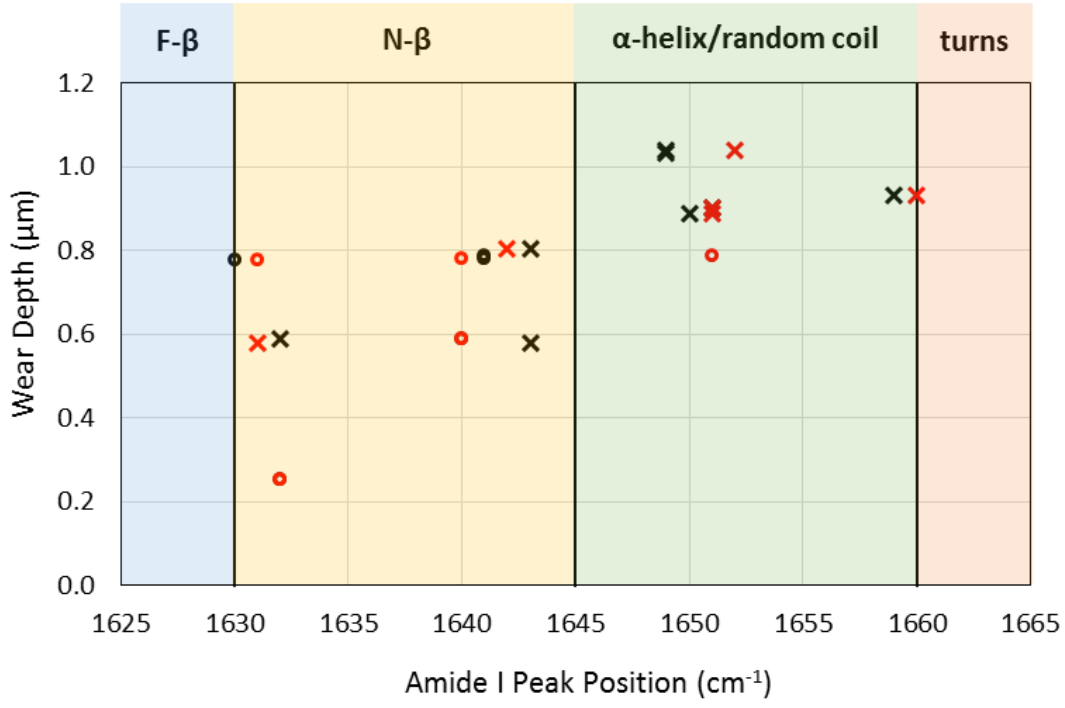


Figure 6.30 - AWD Vs amide I major peak position for model fluids + DPPC and HSF fluids.

6.8 Conclusions

Untested fluids:

- Proteins secondary structure can be classified using the amide I and II bands, however it is only the amide I band that is useful.
- The alkyl stretch region and the appearance of a carbonyl (ester) peak was used together to identify the presence of lipids.
- The position of the amide I band, and hence secondary structure depended upon the specific protein content
- The secondary structure of all model fluids shifted towards an α-helix/random coil conformation in the presence of a lipid.
- The HSF secondary protein structure was usually mainly α-helix/random coil compared to N-β for 25BCS indicating a fundamentally different protein composition.

Wear deposits:

- Both rainbow and black residual deposits were predominately proteins
- The amide I band of residual deposits shifted towards a N-β / F-β strand conformation for all samples tested.
- In model fluids DPPC appeared to inhibit the formation of N-β / F-β in model fluids.
- In HSF lipids were found in some of the films and possibly inhibited N-β/F-β formation, therefore lipids could play an important role in the denaturing process.
- F –β and therefore potentially amyloids fibrils were present in the deposited films for all model fluids and some HSF samples
- A low wavenumber amide I peak position was associated with lower wear.

Chapter 7: Fluorescence Imaging

Summary

In this chapter the protein structure of the wear deposits was investigated further using fluorescent dye (Thioflavin-T (ThT)) specific to aggregated F-β. Model and human SF samples were doped with ThT and wear tests were performed using the protocol devised in Chapter 3. The wear scars were imaged optically using visible light as in Chapter 5, however fluorescence microscopy imaging was also carried out. Finally, as in Chapter 6 Micro-IRRAS was performed to analyse the chemical composition of untested fluids and residual deposited films.

7.1 Introduction

Thick, organic deposits on implant surfaces have been reported for simulator and explant hip joints (143, 170, 212, 224). These deposits have been identified as denatured proteins (170, 224) and are considered to act as solid boundary films which act to protect the sliding surfaces and reduce wear.

A number of causes of protein-denaturing in tribology have been suggested including thermal effects (224, 275), high pressure (275) and shearing (213, 314). In our optical interferometry work (112) we have observed protein aggregation occurs very rapidly at the onset of sliding and suggest that shear alone can induce denaturing and the formation of insoluble structures.

In Chapter 6 Micro-IRRAS identified that the deposits formed on the rubbing surfaces during wear tests had a higher N-β content compared to the native untested fluids and contained denatured aggregated proteins F-β. The α-helix/unordered protein secondary structures of the untested fluids appeared to transform to an increased N-β/F-β composition. However, further supporting evidence is required to define the nature of these denatured/aggregated (F-β) protein films.

Aggregation of proteins is a common occurrence in nature and can be due to thermal, chemical or shear effects caused by changes in the non-covalent bond interactions. There are three main types of protein aggregate: amorphous, oligomers and amyloid fibrils. Amyloid fibres are highly ordered, rope-like structures (269) and are the most thermodynamically stable (313). Amorphous aggregates are disordered (315) and are the most commonly occurring aggregate (313), both form insoluble deposits (315). On the other hand oligomers are soluble and are formed of two or more polypeptide chains

connected by non-covalent bonds (316) they often precede amyloid fibrils (313). A schematic of the three types of aggregate is shown in Figure 7.1 (313).

Protein deposits reported in Chapter 6 appeared to have a have high N-β content with the presence of F-β structure which is associated with amyloid fibrils. Aggregates of protein monomers assemble to form fibrils with a high content of β-sheet of defined dimensions, which are called amyloids (317). Amyloids have been known to form from many different proteins, but most commonly originate from an N-β secondary structure in a characteristic cross-β conformation (318). A Cross-β sheet structure is where a β-sheet polypeptide chain arranged parallel to the fibril axis with their consistent β-stands perpendicular to the fibril axis (319).

Amyloid plaques (aggregates) are primarily comprised of the amyloid β-peptide (Aβ) ~ 38-42 residues long (296). Aβ can exist as a soluble small monomer or larger oligomers and insoluble fibres as shown in Figure 7.1 (296). It is now widely considered that Aβ oligomers are more toxic than Aβ fibres and therefore play a direct role in the amyloid pathogenesis (320). Cerf et al. (296) used ATR-FTIR to distinguish between Aβ oligomers and fibrils. It was found that Aβ oligomers had an anti-parallel β-sheet structure and therefore had two distinct peaks at 1695 and 1630 cm^{-1} whereas the fibrils have a highly stable parallel β-sheet structure with a strong peak at 1630 cm^{-1}.

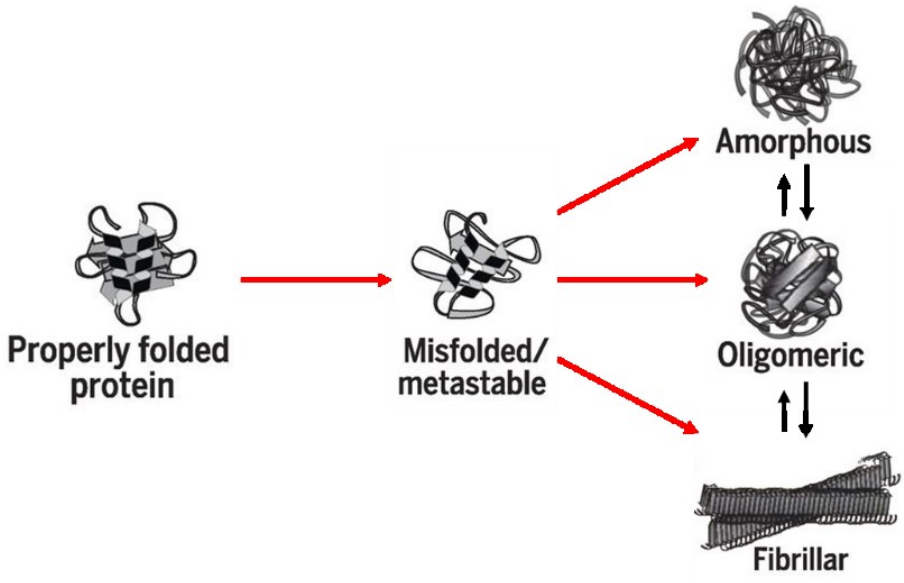


Figure 7.1 - Schematic illustration of protein aggregation. Adapted from (313).

Alongside FTIR analysis a standard way of identifying fibrils is the use of Thioflavin-T (ThT), which is a fluorescent dye reported to be specific to β-sheet rich structures such as amyloid (321). ThT has the ability to distinguish Aβ structures from the precursor protein, monomer and non-amyloid fibril amorphous aggregates (317). Visualisation of β-sheet rich/amyloid aggregates has been extensively reported in the literature, both *in vivo* and *in vitro*, to detect these structures in a wide range of research areas from Alzheimer's (322) to barnacle glue (298).

The aim of this chapter is to further investigate the nature of the deposited film, whether this consists of amyloid fibrils and if their production can be related to the wear and patient SF chemistry. To do this the untested fluids must be first doped with ThT and bench top wear tests performed. Wear surface deposits can then be imaged to determine whether amyloid/β-sheet rich structures are present, their secondary structures also investigated using Micro-IRRAS.

7.2 Fluorescence Imaging of Amyloids

7.2.1 Theory

A fluorescence method which is specific to amyloid fibrils will be used. A fluorophore is a molecule that absorbs energy, a photon, at a specific wavelength of light and re-emits at a different, but specific, wavelength. The amount of energy and wavelength of the emitted light is dependent upon the fluorophore and its chemical environment (323). It is a fast, simple and inexpensive method to identify and measure chemical constituents in a solution.

Fluorescence can be broken down into three steps, absorption, internal conversion and emission which are outlined below and depicted schematically in Figure 7.2, a simplified Jablonski diagram (323, 324).

Absorption: Photons are absorbed by the fluorophore molecules causing electrons to move from their ground state, S_0, to an excited state S_n (n>1)

Internal Conversion: The electrons return from their excited state S_n to the lowest excited state S_1 by dissipating part of its energy to the surrounding environment. This state lasts for a finite period of time, typically nanoseconds.

Emission: Electrons will return form their excited stare S_1 to return to its ground state S_0 via emission of a photon on energy generating florescence. The energy of emitted photon is less than the absorbed photon due to energy lost during internal conversion, energy dissipated in the medium as heat and transfer of energy to neighbouring molecules.

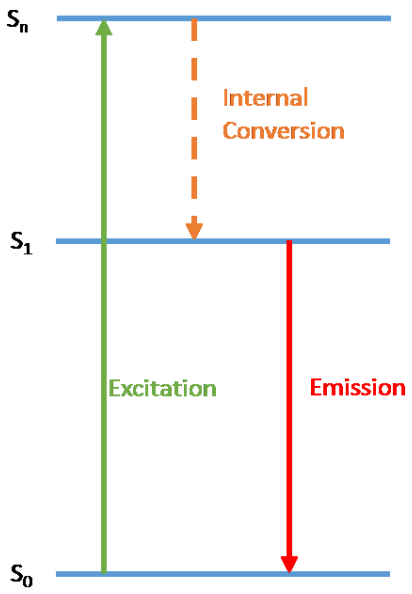


Figure 7.2 - Joblonski diagram showing three stages of fluorescence. Adapted from (98).

The energy of a photon is related to the wavelength using Plank's equation (Eq 7.10) (324) where E is the energy, c is the speed of light ($3x10^8$ m/s), h is the Planck's constant ($6.63x10^{-34}$ kg/s) and λ is the wavelength. The difference between the absorbed and emitted wavelength is known as the Stokes shift, emission will always be at a lower energy therefore higher wavelength (323).

$$E = h\nu = \frac{hc}{\lambda} \qquad (7.10)$$

This change in wavelength allows the light generated from emission to be separated from the light required to excite the molecule. In the current system the fluorophore Thioflavin-T is used; it brightly fluoresces at the excitation and emission maxima 450 and 482 nm respectively (325). A royal blue LED illuminator is passed through the excitation filter which transmits light in the wavelength range 425-448 nm. A dichromatic mirror, placed at 45^0 to the light path, reflects shorter wavelengths of excitation to the specimen and passes longer the wavelengths from the emission towards the barrier filter. The barrier filter only transmits light in the range 455-500 nm to the camera, wavelengths from the illuminator are blocked. A schematic of the filter cube is shown in Figure 7.3 and the transmission wavelengths of the excitation and barrier filters and the dichroic mirror used are shown in Figure 7.3b.

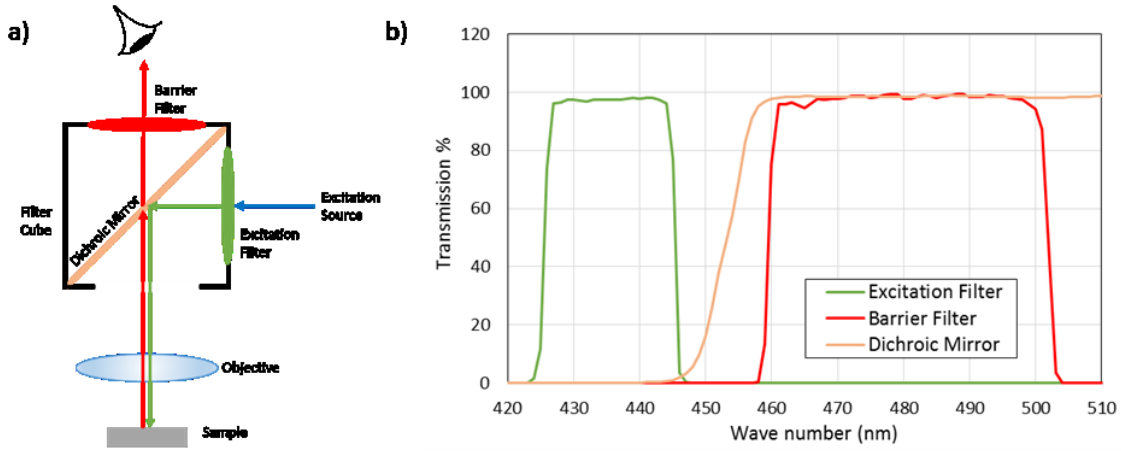


Figure 7.3 – a) A Schematic of a filter cube b) Transmission wavelengths of the excitation and barrier filters used. Adapted from (326)

7.2.2 ThT Fluorescence

Thioflavin-T is widely reported in literature to exhibit enhanced fluorescence when bound to cross β-sheet and amyloid fibrils (321, 327). It displays a dramatic shift of excitation maximum (385 to 450 nm) and the emission (445 to 482 nm) (325) resulting in ~120% increase in energy emitted. The increase in fluorescence is due to the protein binding to the dye. The exact mechanism of ThT binding is unclear, however experimental data and quantum mechanical predictions suggest that ThT behaves as a 'molecular rotator' and the increase in fluorescence arises from the selective immobilisation of a subset of ThT conformers (328). For free ThT, when in solution, a low energy barrier allows free rotation of the shared carbon bond between the two aromatic rings of the molecule (329). The molecular structure of ThT is shown in Figure 7.4a and the planes of rotation about the shared carbon bond is shown in Figure 7.4b. Minimal fluorescence is observed when the molecule is free to rotate in a solution as the energy from the photon is dissipated by the molecule in rotation, the excited state is preserved when rotation is immobilised. It is thought that amyloid fibres and potentially N-β present a ThT-binding site that sterically "locks" the molecules resulting to a large increase in ThT fluorescence. Cross β-sheet structures are common in amyloid fibres, and it is therefore accepted that these surfaces provide the binding site (329).The binding of ThT to the aggregated amyloid peptides occurs within seconds (321).

Despite its wide spread use as an amyloid stain, it is the cross β- sheet structures, which can also be present in some non- amyloid β-sheets, that act as a binding site (329) it was stated by LeVine (321) that '*It is likely that both the β-sheet and the aggregated state provide the environment to stabilize the long wavelengths of the ThT fluorescent complex, regardless of the identity of the participating*

peptides.' Meaning that ThT is likely to bind to both amyloid fibres and high N-β content proteins. Additionally ThT fluorescence increases with increasing viscosity (330).

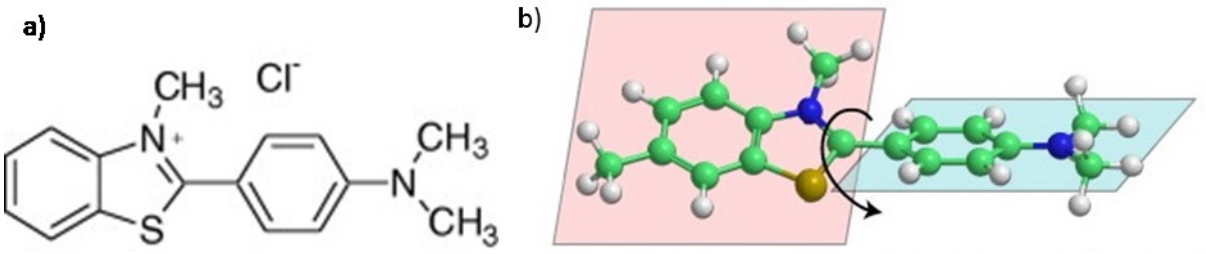


Figure 7.4 – a) Molecular structure of ThT (327) b) The two planes of rotation about the shared carbon bond (329).

7.3 Experimental Programme

The overall aim of this chapter was to investigate the possibility of amyloid fibrils occurring in the residual deposits and if they are beneficial or detrimental to wear. More specifically to investigate if particular SF chemistries are more prone to the formation of aggregated strands/amyloid fibres and if these can be identified in untested HSF samples. The objectives were as following:

1. To perform wear tests with ThT doped model and HSF samples.
    - Ensure the presence of ThT does not affect the wear.
    - Further understand the roles of albumin, γ-G and DPPC.
2. Optically observe residual deposited films
    - Visible light microscope
    - Using a fluorescent microscope specific to ThT
3. Use Micro-IRRAS analysis to identify the secondary structure of proteins.
    - Observe differences in the amide I band between different untested fluids.
    - Analyse differences in the amide I band between untested fluids and deposited films.

7.4 Materials and Methods

The following test procedures were implemented in this chapter to investigate the aggregation of proteins which are outlined in the following sections. In this Chapter each test fluid is ThT-doped in order to fluorescently image high N-β content proteins/amyloid fibril.

7.4.1 HFRR Bench Top Wear Test

The adapted HFRR and 'final' protocol developed in Chapter 3 was implemented. WLI was used to image the wear scar and to analyse the depth at 30%, 50% and 70% of its length and friction was recorded throughout the test.

7.4.2 Optical and Fluorescent Imaging

As in Chapter 5, post-test the ball was lightly rinsed with DI with water for 10 s in order to remove excess fluid and air dried. Care was taken to remove excess fluid but not to disturb the residual film. Once dried, surfaces were observed using a low power microscope (Axioscope, Zeiss; Germany) connected to an Infinity 2 (Lumenera Corporation; Ottawa). In addition, fluorescent imaging was carried out. A Navitar fluorescent microscope with an Olympus filter cube set (Chroma (435/480nm) 49001 - ET – ECFP) and mid-blue LED (all supplied by Close Ups Ltd, UK) was used with a CCD camera (Grasshopper3, Pointgrey, Canada). For each sample images were taken using both optical setups so that comparisons could be made and high N-β content/amyloids residual films could be identified.

Prior to each wear test each of 10 µl of the untested sample was pipetted onto a glass slide and a cover slip placed on top to ensure it did not dry. The untested samples were imaged under the fluorescence microscope to investigate if high N-β content/amyloid fibrils were present.

7.4.3 Micro-IRRAS Analysis

Micro-IRRAS analysis was performed to obtain information on the chemical composition of both the untested fluids and tested samples using the same methods as outlined in Chapter 6.

7.4.4 Test Fluids

Four model solutions were tested using BCS (Sigma Aldrich, 12133C), BSA (Sigma Aldrich, A7906) and γ-G (Sigma Aldrich, G7516) and 1,2-Dipalmitoyl-sn-glycero-3-phosphocholine (DPPC; Sigma Aldrich, P4329). ThT (Sigma Aldrich, T3516) was used as obtained. The test solutions are summarised in Table 1.

Table 7.1 - Model fluids with ThT.

	Solution	Constituents
A	ThT	375 μM ThT
B	25BCS + ThT	25BCS 375 μM ThT
C	25salBCS + DPPC + ThT	25BCS 154 mM NaCl 0.5 mg/ml DPPC 375 μM ThT
D	12Alb + ThT	12 mg/ml BSA 375 μM ThT
E	6Glob + ThT	6 mg/ml γ-G 375 μM ThT

For solution A ThT (375 μM) was dissolved in DI water by weight and gently stirred at room temperature. For solution B; an initial solution of 500 μM ThT was prepared, this was then combined with 100BCS in a 3:1 ratio to achieve 25BCS with ThT at a concentration of 375 μM. Solution C was made by dissolving NaCl by weight in DI water at a physiological concentration of 154 mM. DPPC saline solution was then prepared by the method outlined in Chapter 4. Once at room temperature ThT was dissolved into the solution to a concentration of 500 μM, which was then combined with 100BCS in a 3:1 ratio. For the single protein solutions (D and E) 9 mg/ml saline was dissolved into a 375 μM ThT saline solution before the addition of the proteins by weight.

Human samples tested are listed in Table 7.2, in Chapter 4 samples were grouped based on age and disease for sample volumes ≥ 2 ml. The age group 70-79 with only OA had four available samples (105, 108, 128 and 163) and therefore chosen for testing as this was the closest category to the samples used in Chapter 4.

Table 7.2 - Gender, age and disease and volume of human samples.

	Sample	Gender	Age	Disease	Volume (ml)	# of tests
F	105	M	88	OA	2	1
G	108	F	76	OA	2	1
H	128	F	76	OA	2	1
J	163	M	78	OA	2	1

Human samples were doped with ThT to achieve a concentration of 375 µM. To do this ThT was initially dissolved in DI water by weight to achieve a concentration of 3750 µM. The HSF samples were then combined in a 9:1 ratio with the ThT solution to achieve the same ThT concentration that was used in the model samples.

7.5 Results

7.5.1 Wear

The AWD of each of the model and human fluids tested is shown in Figure 7.5. The ThT solution gave an AWD of 0.73 µm which is less than what was measured for the other non-protein/lipid/HA solutions and saline. However, this is unsurprising as tribo-corrosion will increase wear for the saline solutions (232, 251, 252).

The addition of ThT to 25BCS and 25salBCS causes a 7% and 3% increase in the AWD of respectively, giving values of 0.63 and 0.77 µm. Showing that the effect on the wear from the addition of ThT is minimal.

The AWD of 12Alb was 1.10 µm whereas the AWD for 6Glob was 20% lower at 0.89 µm despite 12Alb having double the protein concentration of 6Glob and 450% greater molarity (6Glob 40 µM and 12Alb 180 µM) providing further evidence that γ-G is more effective at reducing the wear than BSA.

The HSF samples doped with ThT are compared to HSF164 which gave AWD of 1.04 µm, the largest of all previous HSF wear tests. Two of the HSF doped samples, HSF128 and HSF163, exhibited an AWD

slightly greater than this at 1.08 and 1.06 µm. The AWD of the third sample, HSF108, was reduced at 0.24 µm. This is a 62% reduction in AWD compared to 25BCS + ThT and 78% compared to HSF128.

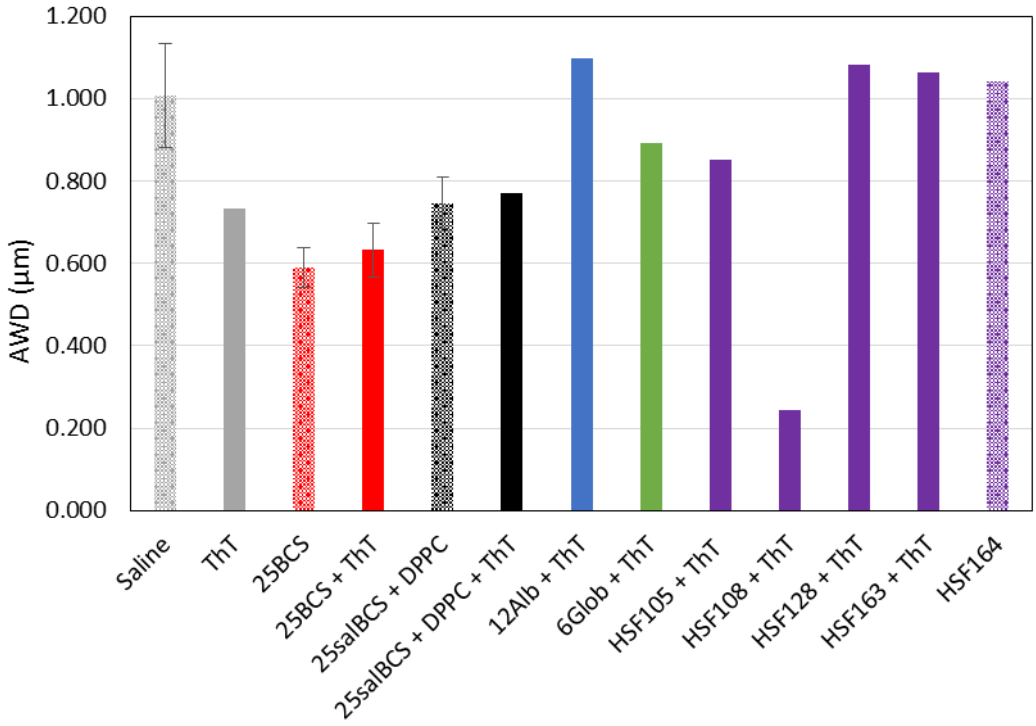


Figure 7.5 – AWD for the model and HSF samples.

7.5.2 Optical and Fluorescent Imaging of Wear Scar Deposits

All untested samples showed similar images and therefore only 25BCS and HSF128 are shown as an example in Figure 7.6. Both images are black with no obvious fluorescent particles indicating that amyloids/high N-β aggregates are not present in the untested fluid. The HSF samples have a dull blue background in comparison to the black of the model fluids. This was attributed to the high viscosity of HSF samples (330).

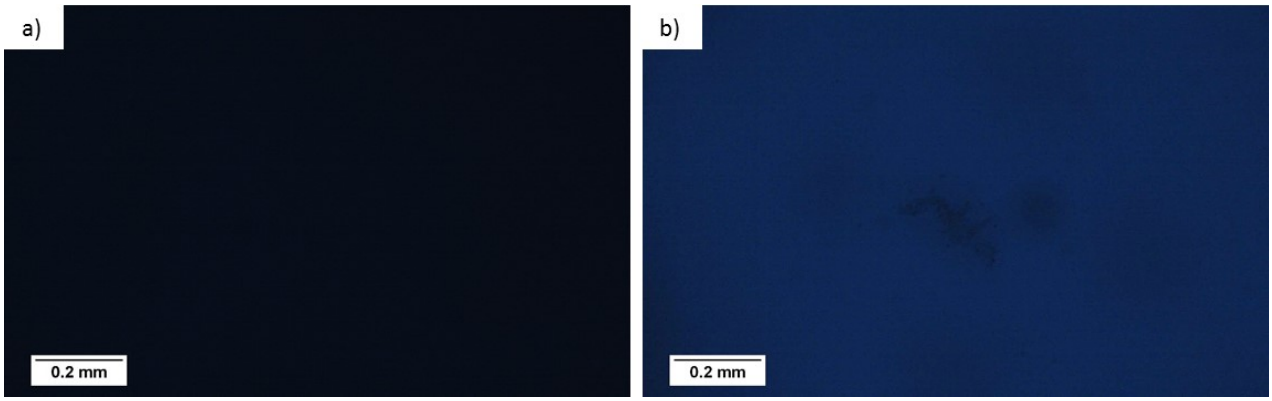


Figure 7.6 - Optical Images taken with fluorescence set up of untested fluids a) 25BCS and b) HSF128.

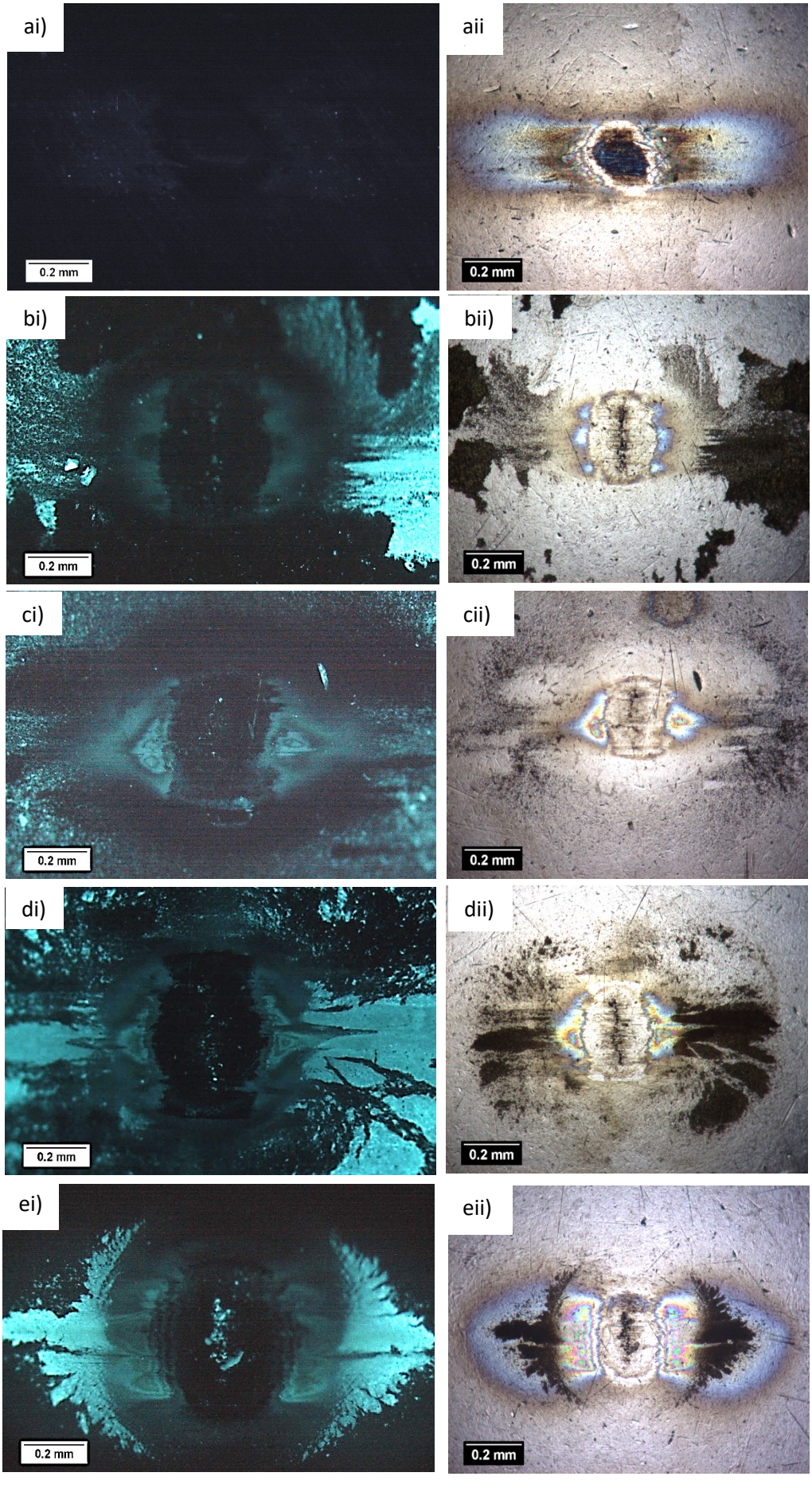
Figure 7.7 shows the optical images of the wear scars and residual deposits formed on the balls under the visible and fluorescence microscopes.

Figure 7.7 ai and ii show the wear scar as a result of a ThT only solution. It can be seen that there are thin films deposited either side of the wear scar however the corresponding fluorescence image is very faint. This shows that residual films or the wear debris as a result of the ThT does not fluoresce by itself.

It can be seen that the bright blue regions around the wear scar in the fluorescent images (b-j i) correspond to the black deposits and are indicative of high N-β content proteins/ amyloid fibres. This is particularly noticeable for 25BCS, 25salBCS, 12Alb and 6Glob, the only HSF sample that these bright blue deposits are visible for is HSF108 which exhibited the lowest wear of all samples tested. For the HSF samples 128 and 163 the thin dark films appear to fluoresce to a lesser extent, with some possible bright fibular structures within the films which are circled in Figure 7.7 hi and ji.

Bright blue fibular deposits can also be seen inside the wear scar for 25BCS, 25salBCS, 12Alb, 6Globand HSF163, providing further evidence that these aggregated proteins pass through the contact.

The rainbow deposits close to the wear scar are clearly visible in the samples with a larger number of interference fringes, this is unsurprising as this indicates a larger film thickness. These films fluoresce bright blue indicating N-β rich proteins or amyloid fibres, these were brightest for 25salBCS, 12Alb, 6Glob and HSF108. The samples 25BCS HSF128 and HSF163 fluoresce faintly however this corresponds to a thin film as seen by the small number of interference fringes in the optical images.


ai)
aii
bi)
bii)
ci)
cii)
di)
dii)
ei)
eii)
0.2 mm

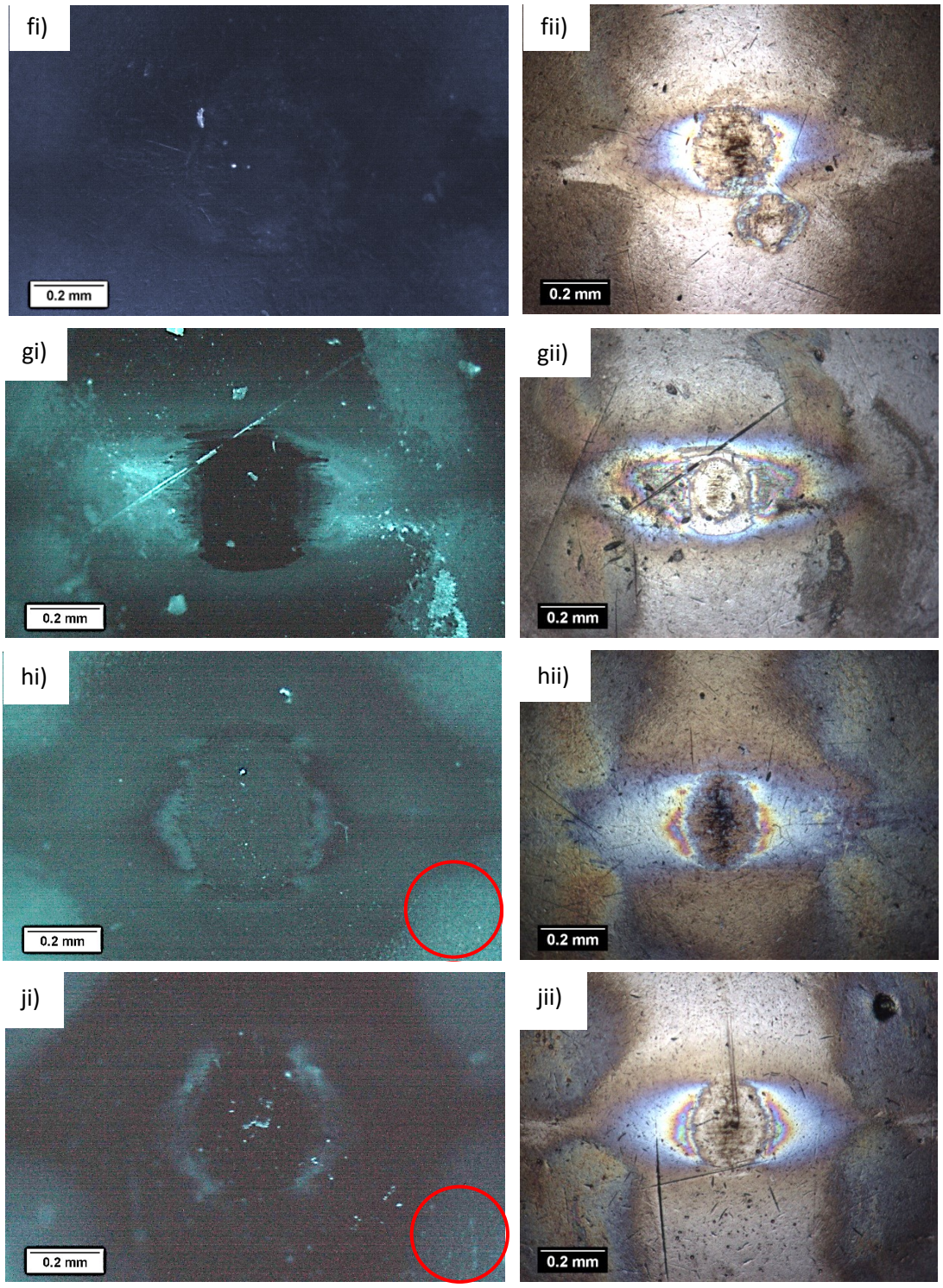


Figure 7.7 - Optical Images taken with i) Navitar set up ii) Zeiss Axioscope for a)ThT b) 25BCS, c) 25salBCS + DPPC d) 12Alb e) 6Glob f) HSF105 g) HSF108 h) HSF128 j) HSF163.

For the HSF samples thick black deposits were only observed for samples HSF105 and HSF108 and are shown in Figure 7.8. For sample HSF105 the thick black deposit is brighter than the surrounding

residual film however it does not fluoresce as brightly as the model fluids. On the other hand, for HSF108 the thick black deposit is bright blue, suggesting a high N-β content/amyloid fibres.

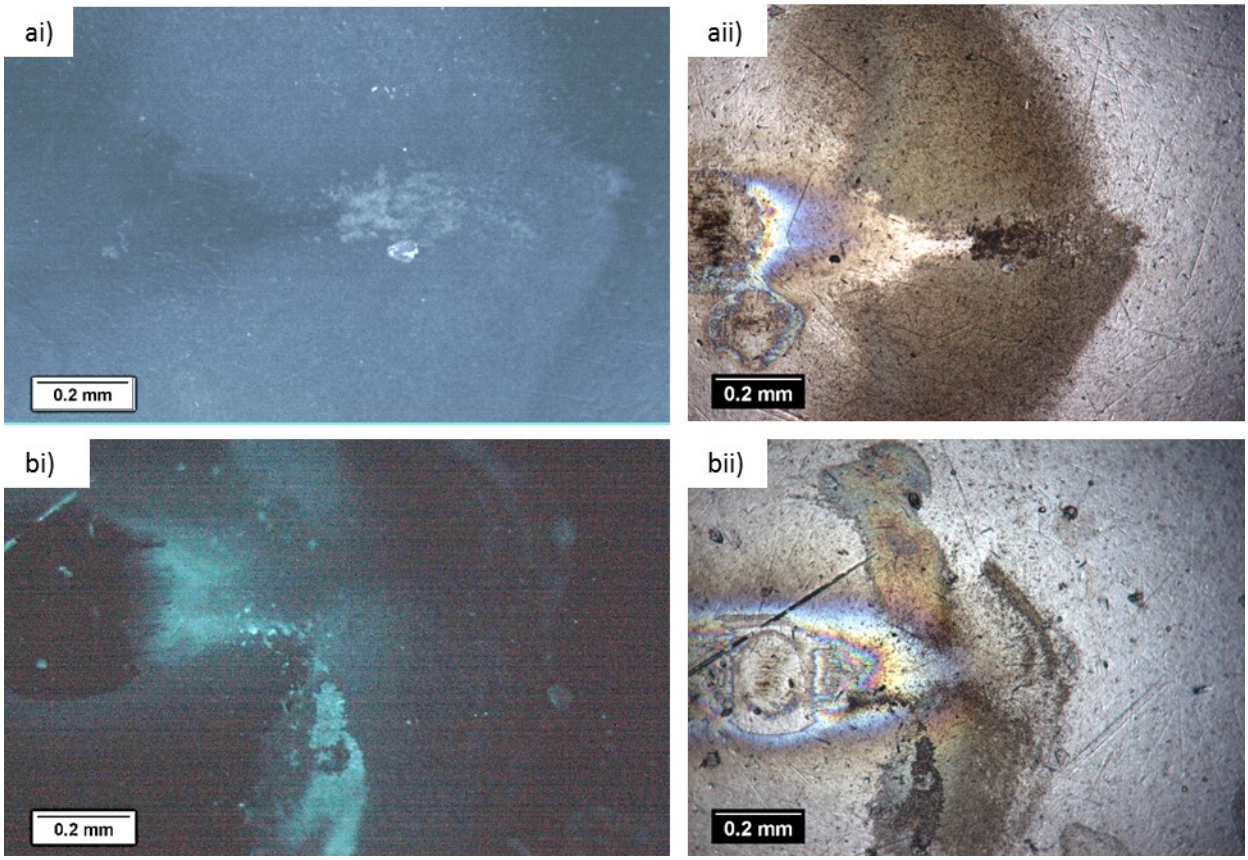


Figure 7.8 - Optical Images of black deposits taken with i) Navitar set up ii) Zeiss Axioscope for a) HSF105 b) HSF108.

7.5.3 Micro-IRRAS Analysis

Spectra in the range 1800-1450 cm^{-1} and 3000-2800 cm^{-1} showing the amide I and II bands and the alkyl chain region are shown in Figure 7.9. These compare the untested fluids and tested films of 25BCS and 25BCS + ThT. It was shown in Chapter 6 that the difference in the black and rainbow deposits was minimal and therefore only the spectra from the black deposits are shown. It can be seen that the addition of ThT does not change the position of the amide I or II band for the untested films or the tested deposits. Table 7.3 summarises the overlapping peaks from spectral deconvolution of the amide I band only as it is this peak which is used to identify the secondary structure.

For the untested fluids the same four overlapping peaks were present in 25BCS + ThT compared to 25BCS at 1659, 1651, 1641, 1632 cm^{-1} representing the secondary structures α-helix/random coil, α-

helix/random coil, N-β and N-β respectively, the strongest peak for both samples was located at 1641 cm^{-1}. For the tested black deposits, main peak had shifted to 1632 cm^{-1}. The same five overlapping peaks were present in 25BCS + ThT compared to 25BCS. This comprised of the four in the untested fluids with the addition of a peak at 1612 cm^{-1} which represented F-β. For both samples the amide II peak becomes broader.

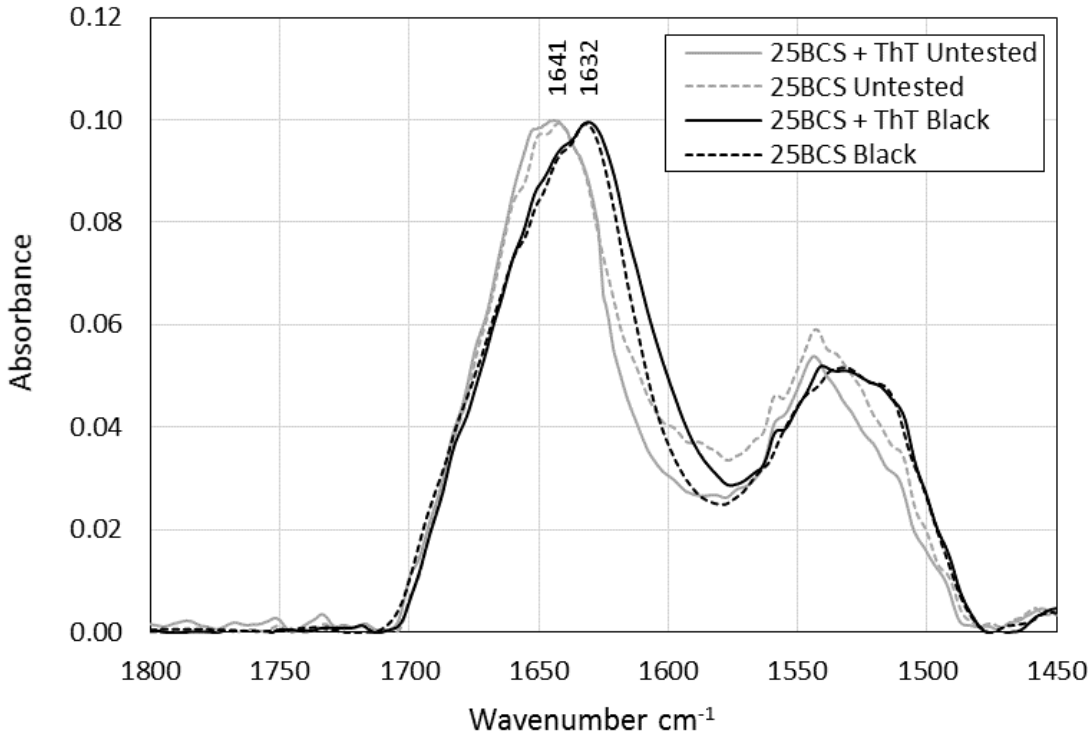


Figure 7.9 - Micro-IRRAS analysis comparing the untested fluids and tested films of 25BCS and 25BCS + ThT in the range 1800-1450 cm^{-1}.

Table 7.3 - Summary of IR peaks from deconvolution and secondary structure assignment for untested fluids and tested black deposits of 25BCS and 25BCS + ThT in the range 1800 - 1450 cm^{-1}. (bold most intense peak, ^{w} denotes a weak peak).

Peaks	Wavenumber (cm^{-1})				Secondary Structure
	25BCS Untested	25BCS + ThT Untested	25BCS Black	25BCS + ThT Black	
Amide I	1659	1659	1659	1659	α-helix/random coil
	1651	1651	1650	1652	α-helix/random coil
	1641	1641	1643	1643	N-β
	1632	1632	1632	1632	N-β
			1612 ^{w}	1612	F-β

From Figure 7.10 it can clearly be seen that there is a difference in the peak position of the untested fluids of 12Alb and 6Glob. Table 7.4 summarises the overlapping peaks at 1659, 1651, 1641, 1632 cm^{-1} found in all untested fluids and tested films. The strongest overlapping peak in the untested samples for 12Alb + ThT and 6Glob + ThT were at 1652 cm^{-1} (α-helix/random coil) and 1643 cm^{-1} (N-β) respectively.

For the wear test deposits, the main Amide I band shifted to a lower wavenumber and the five common overlapping peaks were present at ~1660, 1652, ~1642, ~1631 and 1612 cm^{-1}. The most intense peak for 12Alb + ThT shifted from 1652 cm^{-1} (untested) to 1642 cm^{-1} for the black deposits (N-β). For 6Glob + ThT the main Amide I band shifted from 1643 cm^{-1} (untested; N-β) to 1632 cm^{-1} (N-β) for the black deposits. The peak at 1612 cm^{-1} representing F-β was present for 6Glob + ThT but weak for 12Alb + ThT.

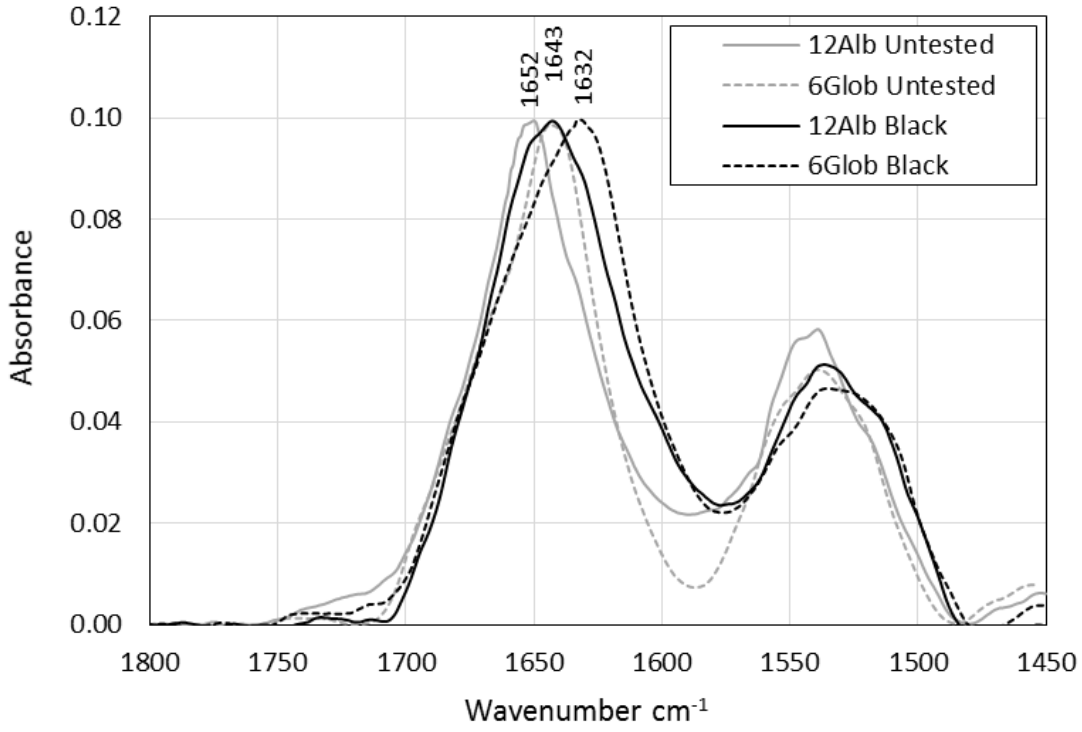


Figure 7.10 - Micro-IRRAS analysis comparing the untested fluids and tested films of 12Alb + ThT and 6Glob + ThT in the range 1800-1450 cm^{-1}.

Table 7.4 - Summary of IR peaks from deconvolution and secondary structure assignment untested fluids and tested black deposits of 25BCS and 25BCS + ThT in the range 1800 - 1450 cm^{-1}. (bold represents strongest peak, ^{w} denotes a weak peak).

Peaks	Wavenumber (cm^{-1})				Secondary Structure
	12Alb Untested	6Glob Untested	12Alb Black	6Glob Black	
Amide I	1668				Turns and bends
	1660	1659	1660	1659	α-helix/random coil
	1652	1652	1652	1652	α-helix/random coil
	1641	1642	1642	1641	N-β
	1632	1632	1631	1632	N-β
			1612^{w}	1612	F-β

Spectra from the untested HSF + ThT fluids are shown in Figure 7.11, 25BCS + ThT is shown for comparison. It can be seen that the peak positions of the amide I band for HSF105 + ThT, HSF128 + ThT and HSF163 + ThT are very similar at ~ 1660 cm^{-1}. The Amide I peak position of HSF108 + ThT and 25BCS + ThT are similar but at a lower wavenumber ~ 1642 cm^{-1}.

A summary of the deconvoluted peak positions is shown in Table 7.5. HSF105 + ThT, HSF128 + ThT and HSF163 + ThT have peaks at 1666, ~1660, 1650, ~1642, 1632 cm^{-1} with the strongest at 1660 cm^{-1} (α-helix/random coil). 25BCS + ThT and HSF 108 + ThT have peaks ~1660, 1650, ~1642, 1632 cm^{-1} with the strongest at ~1642 cm^{-1} (N-β). The strongest peaks are indicated in bold. The shift to a lower wavenumber of these two samples is also evident in the amide II band.

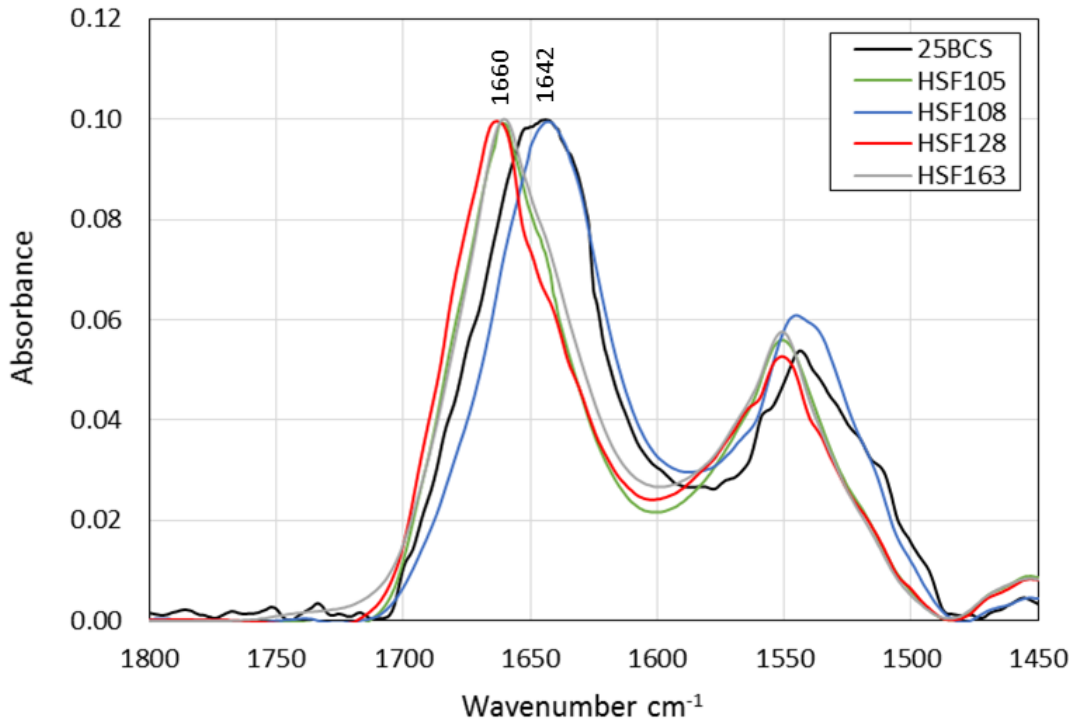


Figure 7.11 - Micro-IRRAS analysis comparing the untested fluids of 25BCS, HSF105, HSF108, HSF128 and HSF 163 with ThT the range 1800-1450 cm^{-1}.

Table 7.5 - Summary of IR peaks and secondary structure assignment untested fluids of 25BCS + ThT, HSF105 + ThT, HSF108 + ThT, HSF128 + ThT and HSF163 + ThT in the range 1800 - 1450 cm^{-1}. (bold strongest peak).

Peaks	Wavenumber (cm^{-1})					Assignment
	25BCS + ThT	HSF 105 + ThT	HSF108 + ThT	HSF128 + ThT	HSF163 + ThT	
Amide I		1666		1666	1666	Turns and bends
	1659	1660	1660	1659	1658	α-helix/random coil
	1651	1650	1651	1650	1650	α-helix/random coil
	1641	1642	1642	1641	1643	N-β
	1632	1632	1632	1632	1632	N-β
						F-β

Figures 12-14 compare spectra of the untested fluids and black test deposits for HSF105 + ThT, HSF108 + ThT and HSF 163 + ThT respectively, a summary of the positions of the deconvoluted peaks and secondary structure assignment is given in Table 7.6.

As for previous results all spectra from the test deposits exhibit a shift in the Amide I peak position to a lower wavenumber when compared to their untested counterpart. The position of the strongest peak varied for HSF105 + ThT, HSF128 + ThT and HSF163 + ThT the peak was located at 1641 cm^{-1} whilst for HSF108 + ThT it was at 1632 cm^{-1}, which is comparable to 25BCS + ThT.

The peaks common in all four HSF and BCS samples for black test-deposits are present at 1660, 1651, 1642, 1632 cm^{-1} representing the secondary structures α-helix/random coil, α-helix/random coil, N-β and N-β. For 25BCS + ThT and HSF108 + ThT an additional peak is present at 1612 cm^{-1} representing F-β. In each case, the FWHM of the HSF samples broadened. The shift to a lower wavenumber and increase in FWHM is also exhibited in the amide II band. In Figure 7.14 a strong lipid C=O peak can be seen at 1740 cm^{-1} for HSF163 in the spectra from the black deposit only, this was not observed in the untested fluid.

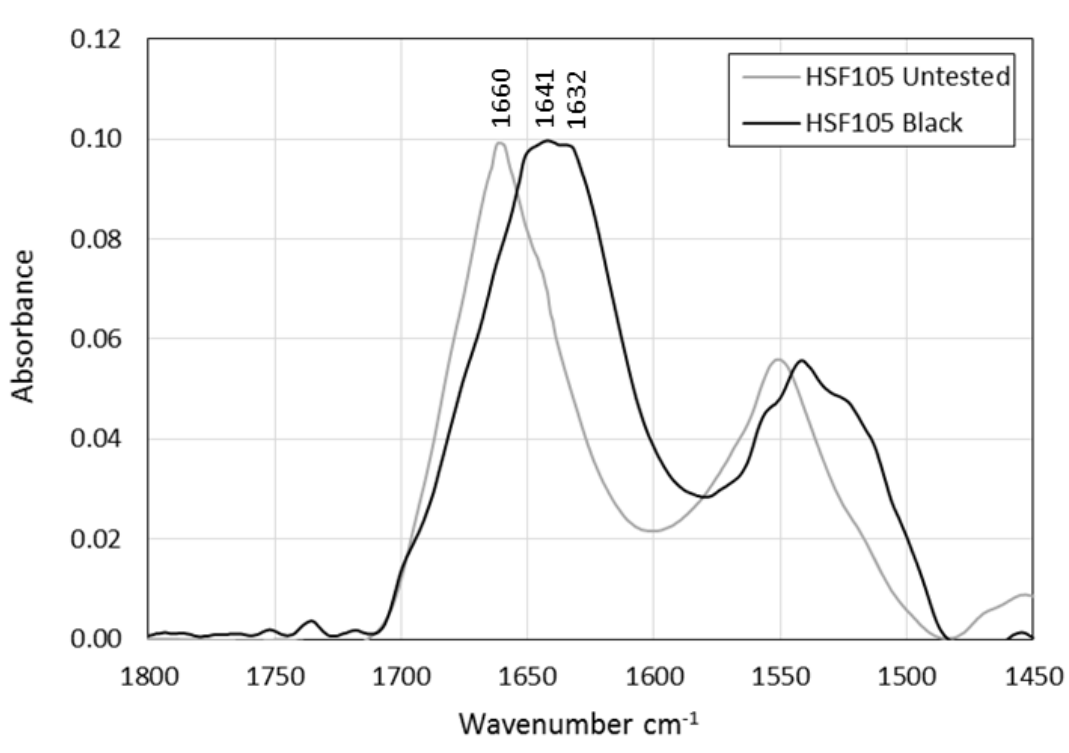


Figure 7.12 - Micro-IRRAS comparing untested fluids and tested films of HSF105 with ThT the range 1800-1450 cm^{-1}.

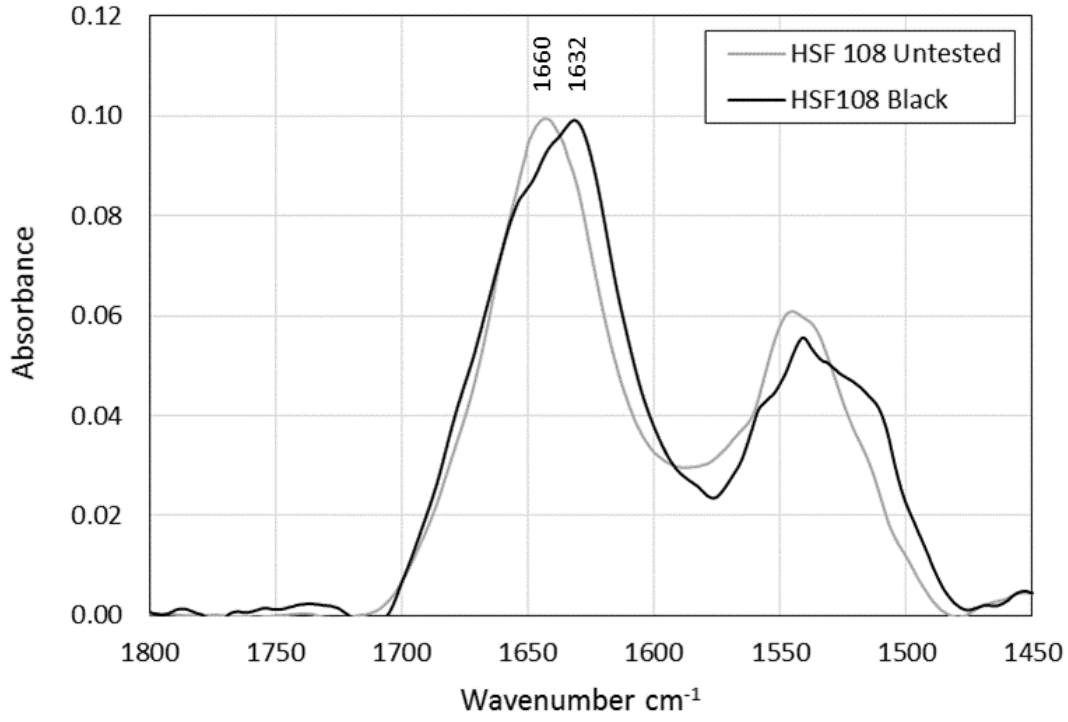


Figure 7.13 - Micro-IRRAS comparing the untested fluids and tested films of HSF108 with ThT the range 1800-1450 cm^{-1}.

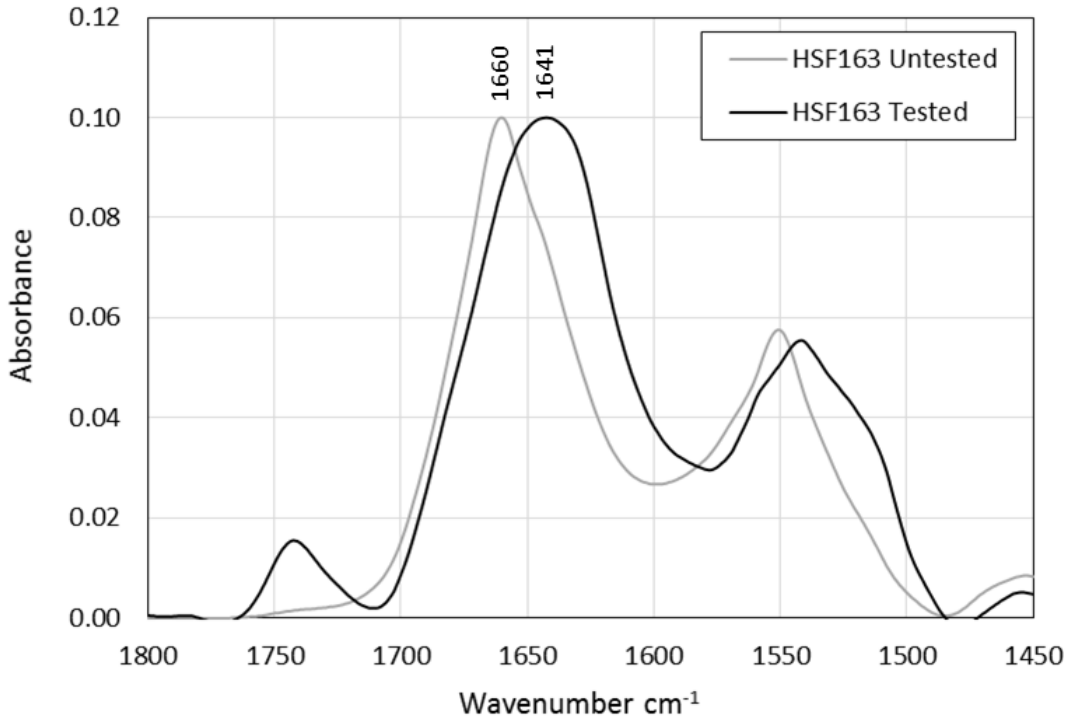


Figure 7.14 -Micro-IRRAS comparing the untested fluids and tested films of HSF163 with ThT the range 1800-1450 cm^{-1}.

Table 7.6 - Summary of IR peaks and secondary structure assignment for untested fluids of 25BCS + ThT, HSF105 + ThT, HSF108 + ThT, HSF128 + ThT and HSF163 + ThT in the range 1800 - 1450 cm^{-1}. (bold: strongest peaks, ^{w} denotes a weak peak).

Peaks	Wavenumber (cm^{-1})					Assignment
	25BCS + ThT	HSF 105 + ThT	HSF108 + ThT	HSF128 + ThT	HSF163 + ThT	
Amide I	1659	1660	1659	1660	1660	α-helix/random coil
	1650	1651	1639	1650	1652	α-helix/random coil
	1643	1642	1640	1641	1642	N-β
	1632	1632	1632	1632	1632	N-β
	1612 ^{w}		1612			F-β

7.6 Discussion

Model and human SF's have been doped with ThT and used in the bench top wear test developed in Chapter 3. Initially the AWD of all model and human SF's tested were compared, 25BCS and 25salBCS + DPPC was shown as references and to see the effect of the addition of ThT. The next phase of this chapter included optical imaging of the ball wear scars as performed in Chapter 5, however the addition of ThT allowed fluorescent imaging of N-β rich/ amyloid deposits. Finally, Micro-IRRAS analysis was performed on the untested fluids and deposited films, to investigate the secondary structure of the proteins present.

7.6.1 AWD Measurements

A series of selected model SF were tested and compared to HSF samples from patients in the age range 76 – 88 all with OA. These samples were doped with ThT and the results compared to the ThT solution alone.

AWD of the ThT only sample was 0.73 µm which was less than measured for saline at 1.01 µm, suggesting ThT does not contribute to excessive wear of the CoCrMo surfaces. This is unsurprising as tribo-corrosion will be expected to contribute to wear for the saline solution (251).

Comparing the AWD of 25BCS + ThT to 25BCS was of interest as 25BCS is used as the reference in this thesis. It can be seen that the addition of ThT had minimal effect on the AWD increasing by 7% from 0.59 to 0.63 µm. This result is echoed by the 3% increase in AWD as a result of the addition of ThT to 25salBCS + DPPC. It can therefore be concluded that the addition of ThT to the test fluids does not

have a significant impact on the AWD. This is unsurprising as it is known that ThT does not alter the structure and therefore the function of a protein (331).

The model fluids 12Alb and 6Glob were tested to see if either single protein increased AWD, the concentration of each fluid was based upon the concentrations used in mH. The fluid 12Alb gave an AWD of 1.10 µm compared to 0.89 µm for 6Glob. This is of interest as the AWD of a BSA only solution gave 23% more wear despite having double the total protein concentration and 4.5 times the molar concentration indicating that γ-G is more effective in reducing wear of CoCrMo than BSA. This is consistent with results reported in Chapter 4 and literature which reported dramatically reduced wear of CoCrMo samples (110, 111, 177, 262) and produce thick films (109, 198, 332)

Four HSF samples were tested HSF105, HSF108, HSF128 and HSF163; two of these (HSF128 and HSF163) gave a very high AWD of 1.08 and 1.06 µm respectively. The AWD of sample HSF105 was 0.85 µm although this is less than HSF128 and HSF163 it is still represents a 31% increase on 25BCS and is within the high wear range 0.80 – 1.04 µm reported in Chapter 4.

The AWD of sample HSF108 was significantly smaller than all HSF samples at 0.243 µm, this represented a 58% decrease in AWD from 25BCS. The model solution mPP an mPP + DPPC with a total protein concentration of 40 mg/ml gave an AWD in a similar range 0.25 – 0.29 µm.

7.6.2 Optical Imaging

The ThT images of untested fluids were dark with no bright fluorescence indicating that no amyloid fibrils were present. The HSF images appeared to be dark blue, whilst the model fluids appeared black suggesting that the HSF bulk fluids increased overall fluorescence, this was thought to be due to the effect of increased viscosity (330).

Figure 7.7 and Figure 7.8 compare images from the visible light and fluorescent microscopes for model and human SF fluids, showing the deposited films in and around the wear scar. The visible light image for ThT gave a similar wear scar for as saline, there was no evidence of rainbow deposits however black deposits either side of the wear scar, possibly wear debris, was present at either side. The images taken under the fluorescent microscope did not show significant amounts of ThT fluorescence and are representative of a 'background' reference image.

Fluorescent images were obtained for surface deposits with both model and human SF samples. For the model samples the background fluorescence was particularly intense, and potentially masked the details of individual fibular formation. The increase in background fluorescence is likely due to the

increase in viscosity of the fluid (330) whilst the bright fibrils indicate the presence of high N-β/ amyloid deposits (329).

In samples HSF128 and HSF163 the background fluorescence is less intense and fibular structures can be seen (which are circled in Figure 7.7 hi and ji). In the case of HSF105 the fluorescence is weak in and around the wear scar, and the bright blue area which corresponds to a black deposit can be seen further away from the wear scar. In some cases bright fluorescent "coil" deposits are seen in the wear scar possibly indicating entangled fibres forming a rope structure as shown in the SEM images in Chapter 5.

ThT fluorescence is reported to be specific to cross β–sheet fibrils and insensitive to N-β domains (331, 333). LeVine in an early paper (333) showed for a range of native proteins (β, αβ) including serum albumin did not induce fluorescence and concluded "*only the multimeric fibrillary forms of the β-sheet polymers, not β-sheet monomers or oligomers, fluoresce with ThT*". He also suggested the requirement was for "*stacked cross β-pleated sheet structures*" which was why the β–sheet domains in native proteins did not fluoresce. Similarly Malmos et al. (331) stated that *"ThT with amyloid fibrils is highly specific. Neither amorphous aggregates nor soluble proteins in folded, unfolded, or partially folded states enhance ThT fluorescence"*.

Although it is widely accepted that ThT binds specifically to high N-β content deposits/amyloid fibrils caution has to be taken as this dye also used to indicate high viscosity solvents (330). Thus two interpretations of the fluorescence response are possible, and complimentary, the rubbing proteins denature and form, high viscosity (112), N-β/F-β aggregates. A key question is whether the associated fluorescence is due to amyloid fibrils or high viscosity effects. Evidence of amyloid fibrils is examined using Micro-IRRAS analysis in the next section.

7.6.3 Micro-IRRAS Analysis

In this chapter only the amide region, 1800-1450 cm^{-1} is presented as it is the amide I peak that has been extensively reported in literature to provide information about the secondary structure of the proteins present. When comparing the untested fluids and tested films of the amide II band, it shifts to a lower wavenumber and becomes broader as was observed in Chapter 6.

Spectra in the region 1800-1450 cm^{-1} was presented comparing the samples 25BCS and 25BCS + ThT. Spectra of untested fluids were very similar for both 25BCS and 25BCS + ThT, which was also true for the tested films; the amide I peaks contained the same overlapping peaks for each fluid. The Amide I primary peaks were at 1641 cm^{-1} (N-β) for both of the untested fluids and 1632 cm^{-1} (N-β) for the

tested films, indicating that the addition of ThT did not impact the secondary structure of the proteins. It is accepted in literature that ThT does not alter the structure of a protein (331).

Analysis of the untested fluids 12Alb and 6Glob showed that the strongest peaks were at 1652 cm^{-1} and 1643 cm^{-1} which is assigned to α-helix/random coil and N-β structures respectively. These results are in agreement with literature which report that the main component of the ordered structure of BSA was 50% α-helix (310). For globular proteins, such as γ-G, roughly 50% are unordered (114); 40% of the ordered structure of γ-G is a N-β (310).

The spectra of the tested films exhibited a shift in amide I peak position to a lower wavenumber for both 12Alb and 6Glob. The strongest peak for 12Alb (1642 cm^{-1}) now represented a N-β structure whilst 6Glob (1632 cm^{-1}) represented a N-β structure.

Untested fluid spectra of HSF108 was very similar to that of 25BCS with the strongest peaks at 1642 cm^{-1} (γ-G) representative of an N-β structure whilst for HSF105, HSF128 and HSF163 the strongest peak was located at 1660 cm^{-1} indicative of an α-helix/random coil structure. As for all other model and human samples the tested films exhibited a shift to a lower wavenumber compared to their untested counterparts. For HSF105 and HSF163 a broad peak indicated that three strong peaks for α-helix/random coil and N-β secondary structures. For HSF105, HSF128 and HSF163 the strongest peak indicated a N-β structure whist for 25BCS and HSF108 the strongest peak was located at 1632 cm^{-1} indicating a N-β. Peaks at 1612 cm^{-1} were present in 25BCS and HSF108 representing F-β (β-aggregated strands).

It is clear that during rubbing the proteins denature to form N-β/F-β secondary structures for both model and human SF. By doping these samples with ThT it was possible to visualise N-β rich and possible amyloid deposits. The question remains to whether these deposits are N-β or amyloid fibril deposits.

Several studies (294, 296, 297, 302) have reported using Amide I IR bands to distinguish between N-β proteins and the aggregated oligomer and insoluble fibril structures. Zandomeneghi et al. (294) in their review of the literature reported broad spectral ranges for the Amide I band of 1643-1630 cm^{-1} for the N-β proteins and 1630-1611 cm^{-1} for amyloid fibrils.

Cerf et al. (296) reported amyloid fibrils had a parallel β-sheet conformation which was associated with a strong band at 1630 cm^{-1}. The soluble oligomeric form with an antiparallel β-sheet structure had IR bands in the Amide I region at ~ 1630 cm^{-1} (strong) and a much weaker component at 1695 cm^{-1}. Ami et al. Ami, (297) reported similar results in their study of amyloid fibrils in tissue of patients

affected by systemic light chain (LC) amyloidosis. In initial tests *in vitro* fibrils were prepared and the FTIR spectra compared to purified LC protein obtained from patient tissue. They assigned Amide I peaks at ~1691 and ~ 1636 cm^{-1} in the purified sample to N-β protein. In addition, minor peaks at 1652 cm^{-1} where assigned to α-helix/random coil structures. For the *in vitro* amyloid F-β fibril the main Amide I peak shifted to a lower wavenumber, typically at 1629 cm^{-1}. Analysis of *ex vivo* amyloid fibres from heart tissue also showed the main Amide I peak at ~ 1630 cm^{-1}. They concluded "the ~ 1630 cm^{-1} band can be considered a marker of amyloid aggregates in tissues" (296). Other studies (298, 300) have shown fibril Amide I bands absorbing at lower wavenumber ~ 1620-1612 cm^{-1}. Zou et al. (300) in their study of hen egg white lysosome aggregation suggested anti-parallel β-sheet oligomers had two characteristic peaks at ~1614 cm^{-1} and 1686 cm^{-1}. The parallel β-sheet fibril structure had peaks at ~1618 cm^{-1}. A second peak at 1660-1670 cm^{-1} normally associated with this structure was not observed because of the sampling method.

In summary for the deposits from the tested samples 6Glob, 25BCS and HSF108 shifted to a lower wavenumber at ~1632 cm^{-1}. In comparison 12Alb, HSF105, HSF128 and HSF163 shifted to ~1641 cm^{-1}, however deconvolution of this data showed shoulder peaks at ~1632 cm^{-1}. Amide I peak shoulders at ~1612 cm^{-1} were present in samples 12Alb, 6Glob, 25BCS and HSF108. For all spectra no peak at ~1690 cm^{-1} is observed although it is not often found (296, 297).

These results suggest that the BCS solutions (with a known high γ-G content) and γ-G forms deposits with a greater parallel β-sheet content. Most of the HSF samples (excluding HSF108) form films with some parallel β-sheet content but the main component is N-β protein. The ThT results support this conclusion and also indicate amyloid fibril content. However due to some of the uncertainties of assigning amyloid structures in literature (321) this remains a tentative conclusion.

The presence of parallel β-sheet deposits can be related to the wear value. For example, 6Glob had half the total protein content with nearly 20% of the molarity of 12Alb however the AWD for this sample was 19% less than for 12Alb. Both the ThT fluorescent imaging and associated IR spectra indicate far greater parallel β-sheet deposit formation for 6Glob compared to 12Alb. HSF108 also formed significant amounts of parallel β-sheet wear deposits; the AWD for this sample was 78% less than HSF128 which had arguably the lowest deposited film N-β/F-β content.

7.7 Conclusions

- Wear increased by small but insignificant increments with the addition of ThT

- A solution containing only γ-G proteins had superior wear properties compared to BSA despite having a lower total protein content.
- Imaging using ThT showed that the wear deposits were brightly fluorescent for the model fluids, but this reduced somewhat for the HSF samples. Confirming the deposits were N-β rich and contained amyloid fibres.
- The ThT also confirmed the high viscosity of the deposits with an increase in background fluorescence.
- Micro-FTIR analysis showed that a parallel β-sheet structure corresponded to the brighter deposited films 25BCS, 6Glob and HSF108. All other films contained predominately N-β-sheet with some parallel β-sheet (F-β) structure.
- The presence of parallel β-sheet structure (F-β) indicates a reduction in wear and is possible related to the γ-G content.

Chapter 8: General Discussion, Future Work and Conclusions

Summary

In this chapter the main findings of the research are reviewed and the implications for implant tribology and SF chemistry are discussed. Areas of research for the future are outlined. Firstly, the wear test is critically looked at and potential changes to improve the simulation of physiological conditions are considered. The possibility of using other material combinations is also discussed. SF lubrication mechanisms reported in this work are reviewed and the clinical implications discussed. Further experimental work to look more closely at the β–sheet lubrication mechanism in natural joints and with model fluids is also considered. The clinical implications of the results and further research to link wear and HSF chemistry through the collaboration with the Musculoskeletal Group is discussed. Finally, conclusions are drawn on this thesis

8.1 CoCrMo Wear Test

8.1.1 Matching Physiological Conditions

Initial work was done to match test conditions as closely as possible to that of a MoM hip joint. The articulation velocity is reported to be transient and in the region 2 – 49 mm/s (72, 73). The test profile used a frequency of 1 Hz and a stroke length of 1 mm which meant the sliding speed varied from 0 - 40 mm/s within the range of *in vivo* conditions. Tests were run for 1 hr which meant the sliding distance on the ball was 144 m much lower than that for typical bench top tests which are usually in the region 25 – 1500 km (15, 168, 227).

Due to the Teflon fluid bath a thermal lag was induced in the set up meaning the temperature was unstable and fluctuated by roughly 3^0C, therefore tests were run a little below body temperature at 35^0C to ensure the proteins in the fluid did not thermally denature (15, 168, 334)

The mean contact pressures were reduced from 467 to 216 MPa by increasing the diameter of the ball from 6 to 19.05 mm. This is still somewhat larger than calculated in *vivo* pressures in a MoM bearing couple, 20 – 50 MPa (74-80), however is comparable to pressures caused by edge loading (237). Initial wear will decrease the contact pressure very rapidly. The final contact pressure can be calculated by

measuring the diameter of the wear scar, for 25BCS the average value was calculated to be p_{mean} = 23.7 ± 2.3 MPa which is in the physiological range.

The partial pressure of oxygen in SF is much lower than atmospheric conditions (239, 241), therefore this was reduced to in *vivo* conditions, however this was found not to have an effect on the AWD. The extended test time and continuous flow of nitrogen increased the possibility of fluid evaporation and therefore this condition was not used.

8.1.2 Test Repeatability

It was important that tests were robust as in many cases < 3 ml of HSF was available and therefore repeats were not possible. Often hip simulator (54, 59, 171-174) and pin-on-disk (166-168, 225, 245) tests have very poor repeatability.

The repeatability of the current test protocol was determined using the CoV which is a measure of the dispersion of data points about the mean (244). It was shown that tests were more repeatable for higher volumes of fluid, but this was not affected by the protein concentration. For tests using 2 ml of BCS the CoV of the AWD ranged from 2 – 12 %. It was concluded that these tests had acceptable repeatability and therefore can be used to obtain meaningful results from single samples.

8.1.3 Future Work

Future work should initially concentrate on reducing the contact pressure as presently this is larger than the *in vivo* operating conditions. There are two ways in which this could be done. One option could be to further increase the size of the ball, all though this may sound simple, calculations show that to reduce the contact pressure to 50 MPa the ball diameter must be increased to 170.7 mm which would not be feasible in this set up. The second option would be to reduce the load, calculations show that reducing this to 0.25 N using a ball diameter of 19.05 mm would reduce the contact pressure to 136 MPa which is still too large. Therefore, both of these methods should be done in tandem, Figure 8.1 plots the mean contact pressures against the ball diameter for a range of loads. The maximum in *vivo* contact pressure, 50 MPa, is shown for reference. The ball diameter for when each load curve reaches 50 MPa is marked, which shows if the load is reduced to 0.1 N a ball diameter of 54 mm is required which could be implemented if a hemisphere was used.

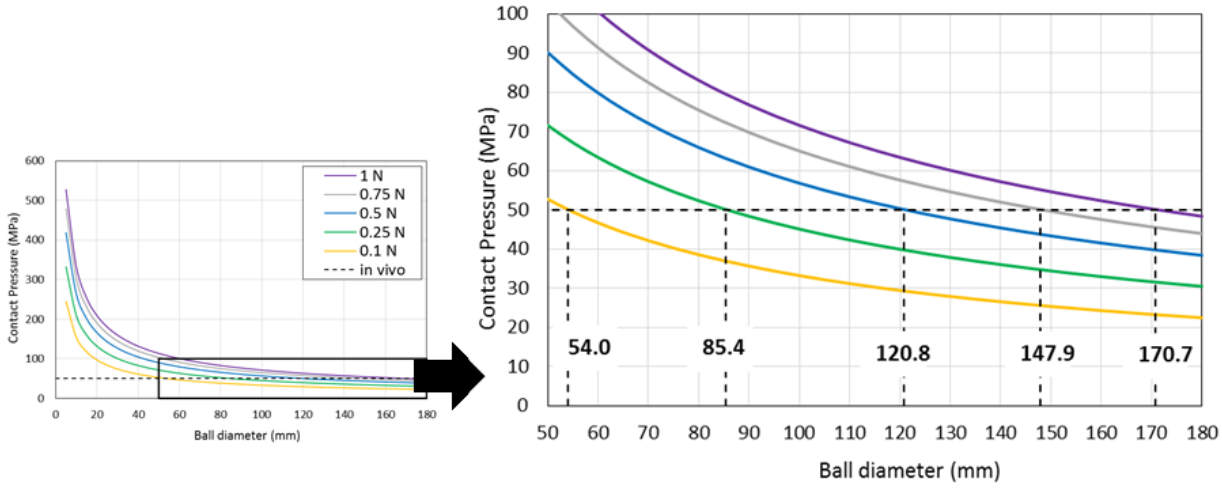


Figure 8.1 - Mean contact pressure vs ball diameter for a range of loads.

There is little room to increase significantly the sliding distance to match that used in other wear tests (25 – 1500 km (15, 168, 227)). Using the current conditions (1 mm stroke length at 20Hz) the test would have to be run for 173 hours to reach a distance of 25 km which would be impossible due to fluid evaporation.

Further testing could be performed to investigate the wear of different implant material combinations such as CoC, MoP and MoP. The most obvious selection would be MoP or CoP as these are the most commonly implanted bearing couple in the UK (1). However, historically cross-shear has been important in determining the wear of UHMWPE which is not possible in the current test. Under linear motion the molecules orientate along the direction of sliding leading to significant strain hardening resulting in an increased wear resistance (229). Advances in the production and manufacturing of HXLPE mean that it has become the gold standard in MoP and CoP arthroplasty. Studies have shown that cross-shear of HXLPE does not significantly increase the wear (335) and therefore could be used in this test set-up. There are no obvious problems with a testing a CoC couple in this rig. Additionally, tests could be performed using surgical grade CoCrMo and compared to the results reported in this thesis using Stellite®21.

Preliminary tests were performed using a MoC bearing couple, which has been considered for hip arthroplasty (336), with 25BCS. Initial tests performed showed that a slight increase in the CoF and significant increase in the AWD as shown in Figure 8.2 and providing evidence that this would be a high risk replacement for MoM arthroplasty.

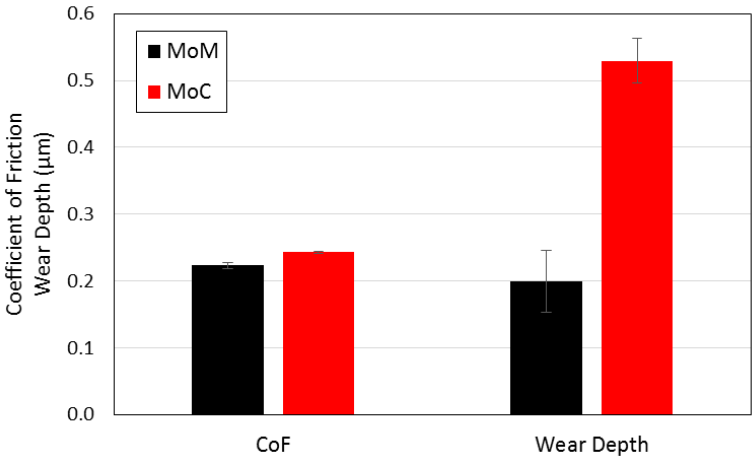


Figure 8.2 - CoF and AWD of MoM and MoC bearing couples for 25BCS.

8.2 Clinical Implications

It was shown that the AWD is larger when the contact is lubricated with HSF compared to 25BCS, which is the most commonly used screening fluid. The evidence from this research suggests that the formation of β-sheet deposits is linked to lower wear and this can be related to the chemical composition of the fluid, which includes the protein profile (concentration and A/G ratio) and the presence of phospholipids. BCS has an A/G ratio of 0.8 whereas OA HSF (corresponding to samples used in this work) is reported to have an A/G ratio of 1.5, due to a lower γ-G content (37). It is also reported that phospho/lipids are present at a higher concentration in OA HSF (41) compared to 25BCS (35). From this work it is suggested that lipids are important in the lubrication mechanism as they inhibit the formation of intermolecular bonded parallel β-sheets and possibly amyloid fibrils.

SF is a filtration of blood plasma which permeates through the synovial membrane into the synovial capsule (99). In a human knee it has been reported that the pore size of the capsule is 8.6 and 20 nm for healthy and 8.5 and 36 nm OA for large and small pore respectively (337). Whereas BCS is produced by centrifuging bovine blood to remove blood cells before filtration with a pore size of 200 nm (308). Therefore, BCS fluids have much larger molecules present which could a key factor in contributing to β-sheet formation and the low wear produced by BCS fluids.

8.2.1 Development of SF Implant Risk Analysis

One of the objectives identified in the research collaboration with the Musculoskeletal Group was to investigate chemical composition and the effect on CoCrMo wear. The original intention was to

analyse the chemical composition (proteins and phospho/lipids) of each patient fluid so that it could be related to the wear tests. The ultimate aim was to identify an implant risk biomarker for patient SF. Unfortunately, it was not possible to achieve this before submission of the thesis however it is hoped this will be possible in the near future.

However, some information can be gained on the chemical composition from the FTIR spectra of the untested fluids, which gives evidence on the secondary structure of proteins and the presence of phospho/lipids, although these are usually below the detection threshold. Accordingly, phospho/lipids were not detected in the untested HSF samples, however in some cases they were associated with the wear deposits.

The relationship between protein secondary structure in the untested fluid and wear is explored in Figure 8.3, the AWD is plotted against amide I band position where no clear correlation is seen.

There is a distinction between samples without phospho/lipids (BCS and model) and with phospho/lipids (+ DPPC and HSF). The amide I peak position for the untested model and BCS samples vary between 1641 – 1652 cm^{-1}, by simply adding DPPC to model fluids the amide I band shifts too chemical composition ~1659 cm^{-1} (α-helix/random coil) which is in line with the majority of HSF samples, suggesting that 25BCS + DPPC may be a better screening fluid substitute.

Even though the amide I peak of the model and BCS fluid with additional DPPC matches with HSF the AWD is still underestimated on average by 44% and in the worst case by 77%. This result should be considered when measuring the wear rate in hip simulators and bench top tests.

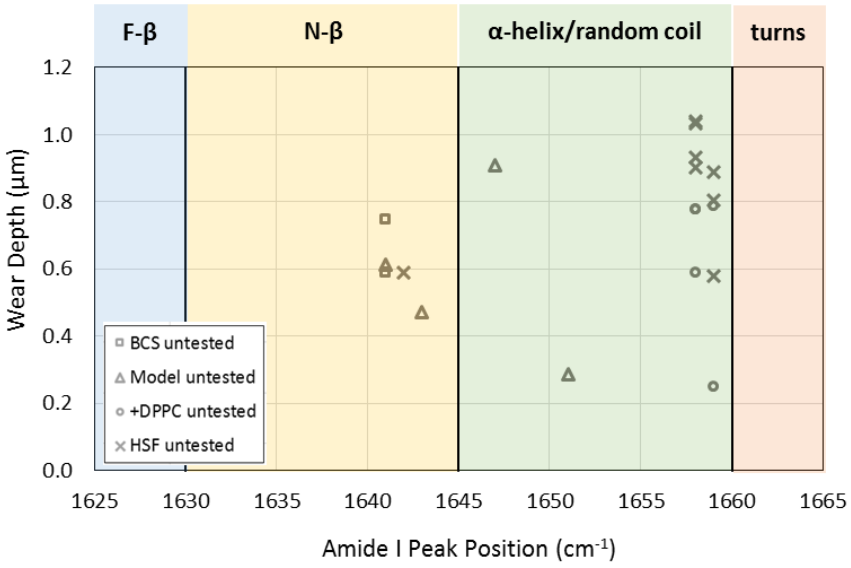


Figure 8.3 - Amide I peak position of untested samples vs AWD for HSF samples.

8.2.2 Future Work

Future work will be carried out in collaboration with the Musculoskeletal Group at St Mary's Hospital to develop the SF analysis and wear profiling. More information on patient SF chemistry is needed to fully interpret the results presented in this thesis. Two different methods are required to identify both proteins and smaller molecules such as phospho/lipids. Polyacrylamide gel Electrophoresis (PAGE) analysis is an analytical method used to identify the total and specific protein concentration within a solution by separation in a gel. This method has been used numerous times in literature on HSF samples (338, 339). NMR analysis can be used to identify small molecules such as phospho/lipids and this has been carried out by the Musculoskeletal Group. The molecules can be identified using information from literature and databases such as the Human Metabolite Database (340). The ultimate aim would be to identify patients at risk of increased wear, for this a large cohort of patients with similar pathologies would be required. It is hoped that funding for this study will be obtained in the near future.

8.3 Lubrication and Wear Mechanisms

Similar and distinct patterns of insoluble deposits were found on the rubbing surfaces for all protein containing fluids, suggesting that the same fundamental lubrication mechanism prevails. The abundance of the deposit was dependent upon the lubricant chemistry. Additionally, evidence of deposits remaining inside the rubbed region was obtained via optical and SEM imaging suggesting they play a role in lubricating film formation. The formation of N-β/F-β rich films was associated with low wear.

Micro-IRRAS analysis of the deposited films revealed that they were mainly proteins, although under some conditions lipids also appeared to be present. The analysis focussed on the amide I band which provides information on the secondary structure of the proteins. For all SF (model, BCS, HSF) samples the wear test deposits showed an increase in N-β proteins compared to the untested fluids. This was shown by a decrease in the wavenumber of the major amide I peak from ~ 1650cm^{-1} (α-helical) to ~<1630 cm^{-1} (N-β).

The peak position is related to the strength of hydrogen bonding which is specific to secondary structure (278). The bonds in a α-helix are long and weak due to the helical structure (278, 341, 342)

whereas the geometric shape N-β structure is flatter and therefore allows intramolecular hydrogen bonding to occur (278, 341, 342). Denatured proteins are misfolded and consist of long extended chains allowing strong hydrogen bonding to occur between neighbouring chains (278).

8.3.1 Evidence on Explanted Joints

Prior to work performed in this thesis, two explanted modular hip joints (FH1 and FH2) were provided by Ian Clarke and Michelle Burgette from the DARF Loma Linda Centre. The femoral heads were analysed under visible light microscopy and Micro-IRRAS analysis by Dr Philippa Cann.

Images showed evidence of gelatinous, rainbow and black deposits and are shown in Figure 8.4 alongside their location on the femoral head. The whole femoral head shown was not an explanted prosthesis, but from a hip simulator study at DARF, it exhibited identical deposit patterns and is therefore used as an example. The red circle represents the area Micro-IRRAS were taken.

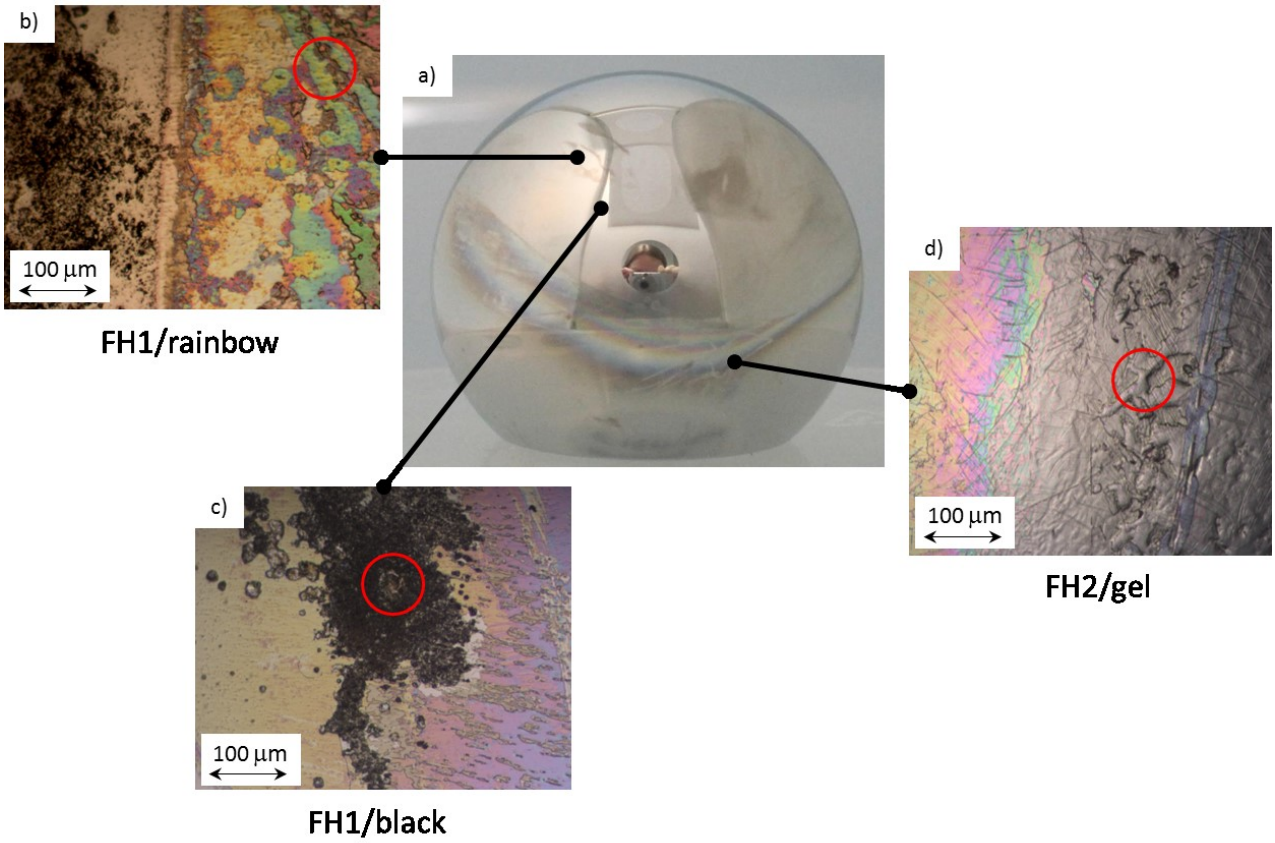


Figure 8.4 – a) Photograph of femoral head from DARF simulator study with rain bow films and black particulate b) zoomed in rainbow deposit from FH1 c) Zoomed in black deposit from FH1 d) Zoomed in gel deposit from FH2.

Micro-IRRAS analysis was performed on these three regions and spectra of the amide and CH stretch region are shown in Figure 8.5 and Figure 8.6 respectively. Deconvolution was performed on each spectra as described in Chapter 6. Results showed for each spectra that the major overlapping peak in each case was located at ~1651 cm^{-1} (α-helix/random coil) with overlapping peaks at 1658 cm^{-1} (α-helix/random coil), 1641 cm^{-1} (N-β), 1633 cm^{-1} (N-β) and 1613 cm^{-1} (F-β). There is little definition between the amide bands in spectra of samples from the FH1 head suggesting that other chemical species may be present. Additionally for prosthesis FH1 it could be argued, from a peak at 1735 cm^{-1}, that a lipid is present in the black and rainbow films (277, 278, 294-303).

Analysis of the CH stretch shows that the film FH2/gel is predominately proteinaceous as the peaks are located at 2960, 2934 and 2873 cm^{-1} representing the peaks CH_3 (ν_{asym}), CH_2 (ν_{asym}) and CH_3 (ν_{sym}) respectively. For the FH1/rainbow and FH1/black deposits the CH_2 (ν_{asym}) peak shifted to ~2916 cm^{-1} and a peak at 2850 cm^{-1} representing CH_2 (ν_{sym}) became more intense (279). The deposit FH1/rainbow had a shoulder at 2931 cm^{-1} indicating that lipids were present in a lower concentration compared to FH1/black.

These results are is comparable to the deposits formed in the HFRR wear test with HSF samples. The main amide I peak was located at ~1651 cm^{-1} and N-β and F-β was present. The black film in the CH stretch showed characteristics of a lipid.

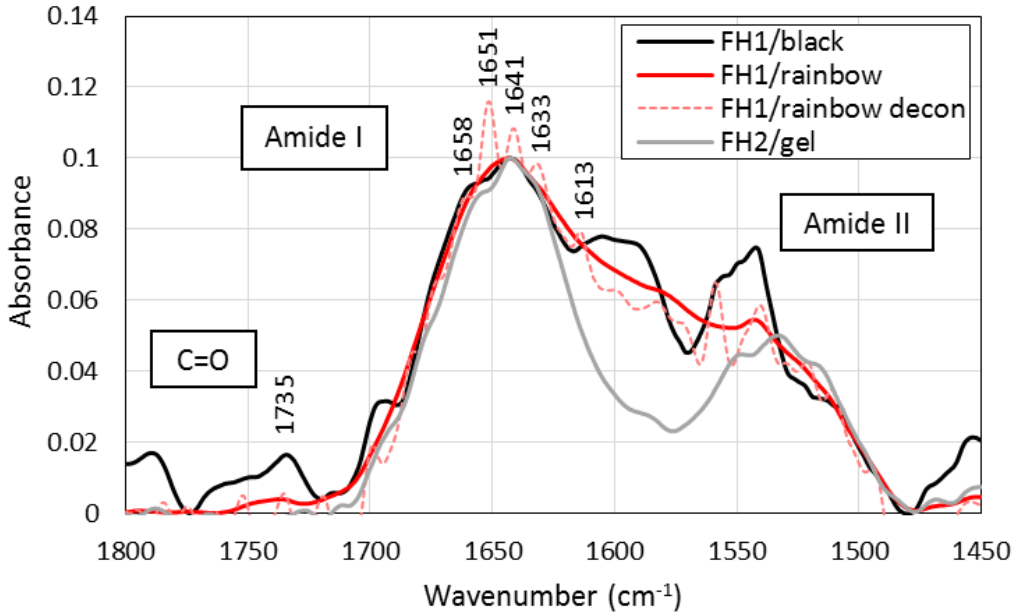


Figure 8.5 – Spectra from micro-IRRAS analysis in the region 1450 – 1800 cm^{-1} black, rainbow and gel films.

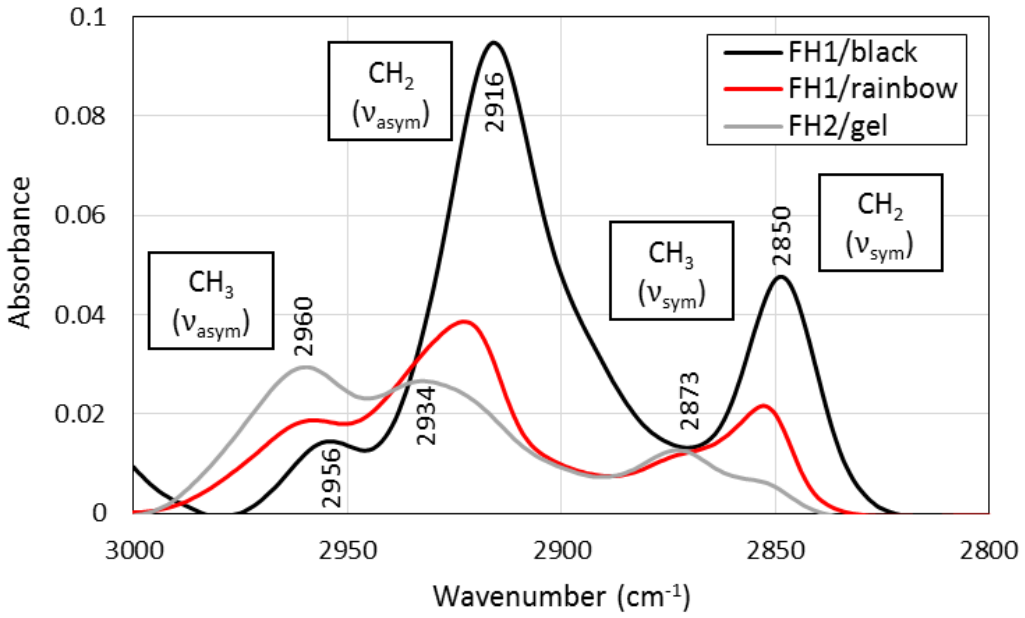


Figure 8.6 - Spectra from micro-IRRAS analysis in the region 2800 – 3000 cm^{-1} black, rainbow and gel films.

8.3.2 Amyloid Fibres?

In some cases deposits had a fibular structure, and these were observed inside and outside the wear scar. SEM imaging revealed that thicker deposits found inside the wear scar appeared to be entangled fibrils. Deposits with this type of structure are often linked to amyloid fibres which have been described to *'…twist around each other to form a supercoiled rope-like structure.'* (269).

Micro-IRRAS analysis of the deposits provided supporting evidence, from a peak at ~1612 cm^{-1} (294), that the films contained F-β structures. The term F-β can be used to describe three main types of denatured protein; amorphous, oligomers and amyloid fibres. Oligomers are soluble and therefore unlikely to be the F-β present in the insoluble film (316). Amyloid fibres are highly ordered, rope-like (269) and the most thermodynamically stable (313) whilst amorphous deposits are disordered (315). Therefore, further analysis was required to investigate if amyloids were present in the deposits.

Fluorescence of ThT-doped sample deposits reinforced the evidence for the presence of amyloid fibres. ThT fluorescence is widely reported in the literature as a method to detect amyloid fibres (321, 327). Results showed that both black and rainbow films fluoresced, however this was more pronounced for the black deposits. In addition, the BCS and model fluid deposits appeared to be more abundant and fluoresce more intensely than the HSF samples. This suggests that HSF does not form amyloid deposits as readily as the screening fluid which could be due to the presence of phospholipids in the native fluid.

Clearly the identification of amyloid fibrils in the wear deposits is surprising and must be considered with care. Despite its widespread use as an amyloid stain, it is the cross β-sheet structure that provides the ThT binding site (321, 329) and this is not unique to amyloid fibrils. The cross β-sheet structure is characteristic of amyloid fibres but can also be present in non-N-β although this is not as common (329). It follows that ThT will also fluoresce brightly when exposed to high N-β content proteins, therefore it cannot be explicitly stated that the deposits contain amyloid fibres.

Amyloids are associated with over 50 serious diseases such as Alzheimer's and type II diabetes, not including OA (318). The presence of amyloids in and about the joint is generally considered a rare occurrence, however in the 1970 and 80's multiple studies reported their presence (343-346). Egan et al. (343) identified amyloid deposits in surgically removed articular cartilage in 10 out of 18 elderly patients undergoing arthroplasty with OA. It was concluded that the presence of amyloid deposits were age related. Ladefoged et al. (344) identified amyloid deposits from surgically removed synovial membrane and the fibrous capsule in 23% of 116 consecutive primary hip replacements due to OA.

The frequency of amyloids appears to increase with age and have been reported in 10-56 % of various organs examined at autopsy in elderly subjects (347-349). The presence of amyloids is generally considered to have no pathological significance however they could play a role in the lubrication and wear mechanisms of artificial joints.

Although amyloids are often associated with disease, as long as their environment can alleviate their toxicity (298), they have also been reported to have functional roles in a wide range of biological applications from bacteria and fungi to insects, invertebrates and humans (350). More recent reports have stated that amyloids are a '*…low-energy quaternary structure..'* rather than a *'…'misfolded' toxic protein…'* (350).

If these functional amyloid fibres are formed then it is important to understand their properties and if they make good anti-wear films. It is reported in literature that they are among the stiffest biological molecules presently known (351) with a yield strength similar to silk (3 - 20 GPa) (352) and a high fracture strength and ultimate tensile strength similar to steel (352). They are resistant to degradation under high temperatures, high concentrations of detergents and denaturants and extensive physical loads (351). Other studies have identified them as natural bio-adhesives and to form in protective membranes (298, 350, 353-355).

The high yield and tensile strength, and robust nature reported in other studies (351) (352) indicates F-β can sustain high loads and severe gait cycles. We believe proteins are shear denatured in the

converging gap and are entrained into the contact to provide a protective layer separating the surfaces and preventing damage. On reversal at the end of a stroke, the inlet reservoir is deposited in what becomes the exit region. Previous work in this group has shown that the apparent high viscosity fluid inlet is self-replenishing (110-112, 200, 213).

8.3.3 What Initiates Fibril Formation?

One of the key questions of this study is what causes denaturing and amyloid formation? Denatured deposited films have been reported to reduce the wear in several studies (48, 110-112, 170, 200, 204, 213, 224, 356, 357) and their formation has been attributed to thermal effects (204, 224, 357), the presence of metal ions (356) and as a result of shear (110-112, 200, 213, 357). To partly answer these questions additional preliminary tests were performed to provide an insight into the initiation of protein denaturing and fibril formation. The observation from earlier work in rolling and sliding contacts (110-112, 200, 213) was that the insoluble protein phase formed very rapidly as soon as motion was initiated indicating it was due to shear rather than thermal effects. The insoluble phase was also seen in the inlet region suggesting it formed at low pressures but under shear in a confined geometry. To explore this idea two simple tests were performed in the absence of metal ions:

1. Effect of heating protein solutions observed as thin films between glass microscope slides.
2. Low pressure rubbing of protein solutions held between glass microscope slides.

Thermal denaturing was investigated by heating ThT doped 25BCS and HSF samples to > 60^0C for 10 minutes. To observe the sample, before and after heating, 10 µL of fluid was pipetted from the bulk fluid onto a glass slide, a cover slip was placed on top to stop evaporation. The initial state was black, with no amyloid proteins. After heating no bright blue amyloids, and importantly fibrils were formed under these conditions.

Shear denaturing was investigated by manually shearing (10-50 strokes) two samples which were doped with ThT as described in Chapter 7; 25BCS and HSF106 (pathology: OA, age: 46, gender: female). A small volume (10 µL) of the fluid was pipetted onto a glass microscope slide and covered by a second glass slide which was then slid gently back and forth. Images were taken of the initial state were black, with no fluorescent structures present, suggesting no agglomerates were present for either fluid, an example (25BCS + ThT) is shown in Figure 8.7. On shearing distinct fibrils formed rapidly in the 25BCS (Figure 8.8a) solution but were not as abundant for the HSF106 samples (Figure 8.8b). In all cases the initial fibril orientation is perpendicular to the direction of shear, which was also observed in the HFRR tests Figure 5.12.



Figure 8.7 – Fluorescence image of initial state for 25BCS + ThT.

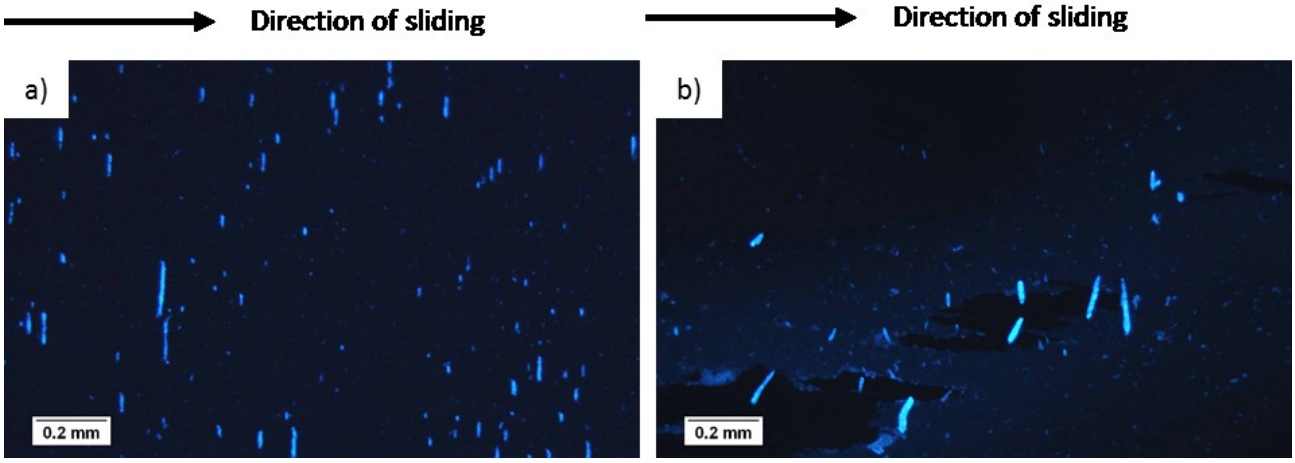


Figure 8.8 - Fluorescence image of sheared state for a) 25BCS + ThT b) HSF106 + ThT.

The fibrils were also observed under a Differential Interference Contrast (DIC) polarised light microscope as shown in Figure 8.9 for 25BCS + ThT, in this case cross shear is applied after linear shear. The initial state shows few agglomerates (Figure 8.9a), once sheared fibrils are rapidly formed perpendicular to the direction of sliding (Figure 8.9b), cross shearing caused the fibrils to coalesce (Figure 8.9c). It is important that these fibrils can be observed by visible light, as it shows that these are insoluble in aqueous conditions providing further evidence that these are F-β amyloids.

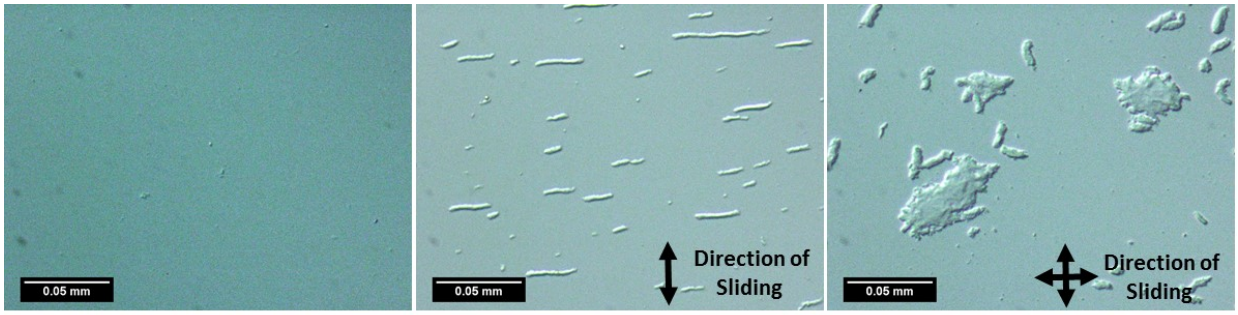


Figure 8.9 – DIC image of 25BCS a) Initial state b) Unidirectional sliding c) Cross shear sliding.

No preliminary tests were performed to investigate denaturing due to metal ions.

8.3.4 Possible Lubrication Mechanisms

Micro-FTIR and ThT fluorescence showed that both the rainbow and black deposits comprised of F-β proteins however the films had a significantly different appearance. The rainbow deposit was close to the wear scar and had a smooth amorphous appearance whilst the black deposits have a coiled rope structure. Therefore, we suggest that shear aggregation is the main driver of the denatured and F-β proteins which are represent the black regions. However thermal effects might additionally transform shear-denatured proteins that pass through the contact that form the amorphous, rainbow films. It has been shown by Zou et al. that amyloids form high viscosity gels when heated (300). The gels form in the inlet region and are deposited at the turn-round point. This has implications on the design of wear rigs, as the reciprocating motion maybe required for these aggregates to be deposited. The *in vivo* gait cycle exhibits reciprocating motion alike the HFRR test rig and therefore in a uni-directional sliding test, these protective aggregates may not be deposited.

The lack of fibril formation due to thermal effects and the very rapid formation under thin film sliding conditions suggests very strongly that denaturing and fibril formation is shear-driven. Fibril formation was also associated with high γ-G content fluids, such as BCS. Low wear was associated with fibril formation. We suggest that the fibrils are most likely to form under the following conditions:

- Narrowing gap
- Hydrophobic surfaces
- Mechanical shear
- High γ-G (N-β) environment

The narrowing gap is required to trap the proteins, this can be related to literature where a study by Nečas et al. (198) reported that a decrease in Cl resulted in a decrease in the wear in a pendulum test with CoCrMo, BIOLOX®forte and BIOLOX®delta couples articulating against glass. This is corroborated Smith et al. (358) who reported that a decrease in Cl resulted in an increase in film thickness using 25BCS in a hip simulator.

The influence of the rubbing surfaces and hydrophobicity/hydrophilicity on shear-denaturing is unclear. Other papers that have reported this protein 'roll' phenomena under shear action have used mica/mica which is hydrophilic (147) and PVA/glass with a hydrophobic DPPC film (262). Native articular cartilage has a hydrophobic surface (359) therefore it is plausible that this mechanism occurs in natural joints.

It is suggested that the larger proteins are trapped in the convergent gap and possibly adhere to the surfaces. Banquy *et al.* (147) reported a gel layer adsorbed in the contact zone where the pressures and shear rates are highest. The attached proteins are now susceptible to being pulled apart, breaking the intermolecular hydrogen bonding, by the shear forces exposing the hydrophobic core (114), and deforming them to form long fibrils where intramolecular hydrogen bonds are formed. This thesis has shown that fibrils are more likely to form in a high γ-G (N-β) environment, which was associated with low wear. Other studies by our group and elsewhere have shown that γ-G helps reduce the wear (110, 111, 262) and produces thick deposited films (109, 198). Murakami et al. reported γ-G has a strong hydrophobic binding strength that is able to adsorb onto the solid surface (262).

When lipids were present the number of fibrils decreased and the wear increased. The major class of phospholipids present in SF are the zwitterionic phosphatidylcholines, such as DPPC, and have a positively charged polar head (98). We suggested that lipids play an active role in the lubrication mechanism by forcing the secondary structure to have a high α-helix conformation (312) and shielding the γ-G preventing it from adsorbing onto the surface, it is therefore less susceptible to shear and the formation of insoluble F-β is inhibited.

A schematic of the proposed lubrication mechanism is shown in Figure 8.10 whilst Figure 8.11 summarises the observed deposit morphology alongside possible chemical interactions. The semi contact width, a, was calculated to be 0.038 mm giving a contact area, A, of 4.63×10^{-3} mm^2. The indentation height, δ, was calculated at 0.155 µm. Assuming that the system is operating in boundary lubrication the thickness of the rainbow deposits can be estimated to be in the range $h_{rainbow} = 0.5 – 5.2$ µm whilst he black deposits are forming at a gap height in the range 4 – 32 µm.

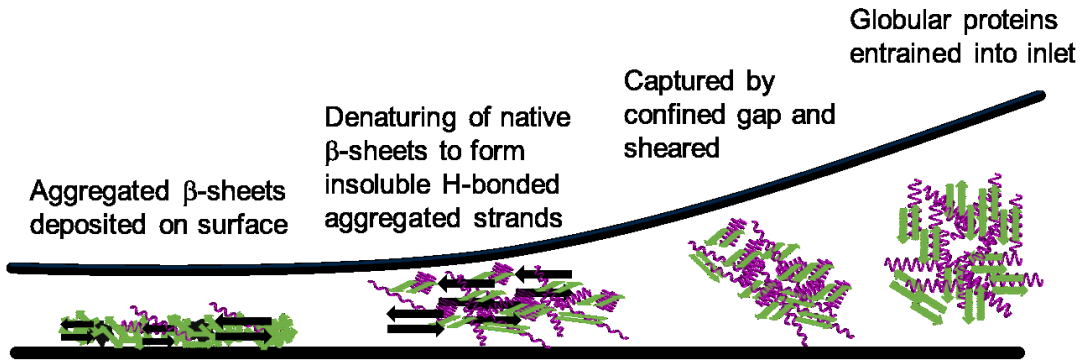


Figure 8.10 – Proposed mechanism of globular proteins captured and entrained into contact.

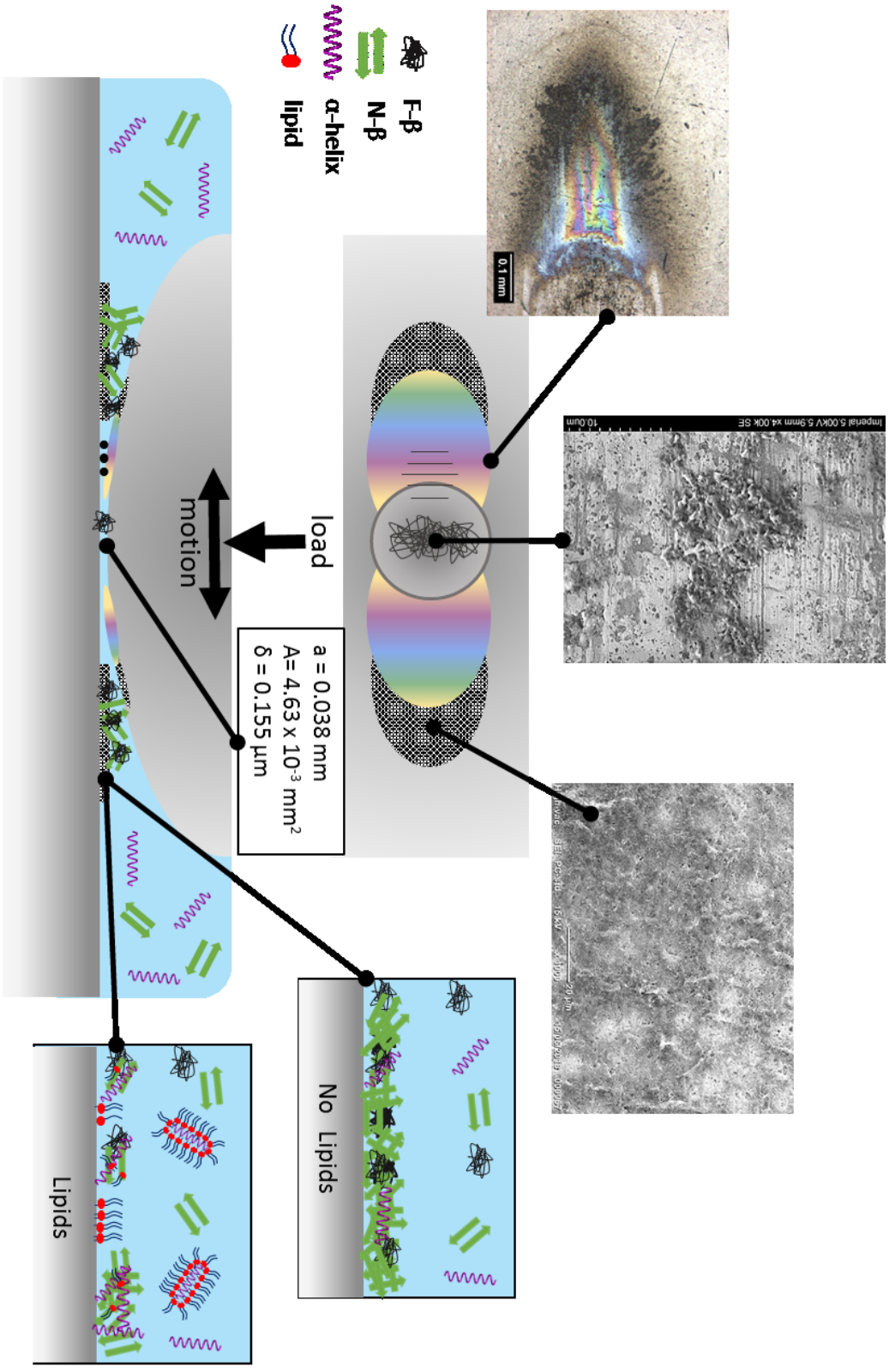


Figure 8.11 – Proposed lubrication mechanism showing the deposit morphology observed from tests and possible chemical interactions

8.3.5 Future Work

Further research needs to be carried out to provide more supporting evidence of fibril formation. Literature states the presence of amyloid fibrils, *in vitro* or *in vivo,* is verified by three methods; identification of a fibular morphology (Transmission Electron Microscopy (TEM)), a β-sheet structure (FTIR or X-Ray) and birefringence upon staining with Congo Red (360). Staining with ThT is not a 'defining' criteria for amyloid fibrils however it is widely accepted to brightly fluoresce present (361).

To further investigate the effect of fluid chemistry (protein type, lipids etc), substrate properties (hydrophilic/hydrophobic) and shearing conditions on fibril formation. It would be preferable if fibril formation could be observed in real-time and a simple sliding device mounted under the fluorescence microscope would provide this.

No work as thus far been performed investigating the effect on ions on protein aggregation, and therefore this avenue could also be looked into. Powdered forms of cobalt, chromium and molybdenum are readily available and therefore addition of these to an untested sample could be investigated. Additionally, the size and concentration of wear debris found in the bulk fluid after the wear test could be characterised.

This potential new lubrication mechanism that considers the biological interactions of the molecules could have an impact on the design of the implant. For example, bearing surfaces could be re-designed in order to promote the formation and adherence of the deposited films in order to protect them from wear. Therefore, future studies could concentrate on investigations of the interactions between the deposits and current/new bearing materials and further determining the physical and mechanical properties of the deposits.

Finally, the impact of tribocorrosion on the wear should be investigated using electrochemical techniques to measure the conductivity of the fluid.

8.4 Conclusions

8.4.1 HFRR Wear Test

A simple, repeatable, CoCrMo wear test for use with small fluid volumes was successfully developed. The friction was measured throughout the test whilst the AWD and AWV were analysed post-test using WLI. The AWD was shown to have a higher repeatability than the AWV. The testing was confined CoCrMo couples, however this could be extended to CoC/MoC as well as MoP/CoP if crosslinked UHMWPE was used. The minimum useable fluid volume is 2 ml.

8.4.2 Effect of Chemical Composition

A range of model fluids with different specific and total protein, phospholipid and HA concentrations was tested and compared to HSF fluids with OA pathologies. It was shown that varying concentrations of proteins and phospho/lipids effected the wear and risk of revision of a prosthesis. The AWD decreased for increasing protein concentration however this levelled of above ~28 mg/ml (50BCS). Increasing the A/G ratio also increased the wear suggesting that γ-G has superior wear reducing properties. The effect of phospholipids on the friction and wear was complex; at a high A/G ratio the CoF and AWD was reduced, at a low A/G ratio the CoF and AWD was elevated. The constituent HA was not found to be an effective lubricant in artificial joints.

The most important result was that the AWD of HSF was on average 44% and in the severest case 77% larger than measured with 25BCS. This was attributed to the fact 25BCS is more likely to form N-β/ F-β deposits, due to the lower A/G ratio and absence of phospho/lipids, which were related with low wear. It is therefore suggested that the screening fluid should be modified to include DPPC. However, this composition still underestimated the AWD, therefore care should be taken with the clinical interpretation of studies using 25BCS as a screening fluid.

The solution 25BCS should be modified to better replicate the specific and total protein content and lipid concentration of OA or PP fluids. For example:

OA – 25% w/w BCS + 10 mg/ml BSA + 0.5 mg/ml DPPC

PP – 25 w/w BCS + 20 mg/ml BSA + 0.5 mg/ml DPPC

Finally, it was found that the AWD was proportional to an increase in pH.

8.4.3 Lubrication and Wear Mechanisms

Similar patterns of deposited films were found in and around the wear scar on both the ball and disc for all protein-containing fluids. This included an amorphous rainbow films close to the wear scar surrounded by black particulates. The amount of deposits increased with increasing protein concentration and low A/G ratio. This observation correlated with reduced wear suggesting that this material acts to protect the surfaces from damage.

Fibril/roll deposits were observed inside and outside the wear scar for high γ-G content fluids (without additional DPPC). Similar, but smaller formations, were also observed located inside the wear scar for low-wear HSF samples. SEM imaging revealed these deposits to be intertwined fibrils forming a rope-

like coil. Importantly these were observed inside the contact region suggesting they are involved in the lubrication process.

The chemical composition of untested fluids and their deposits were analysed using Micro-IRRAS analysis and compared to investigate protein secondary structure. The addition of lipids to the model untested fluid shifted the secondary structure to an α-helix/random coil conformation which was representative of the HSF fluids in contrast to the non-lipid BCS and model fluids with an N-β conformation.

It was found that both the black and rainbow deposits comprised predominantly of proteins however the secondary structure had shifted towards an N-β / F-β strand conformation, which was indicated by a shift in the amide I peak to <1640 cm^{-1}. Lower wear was associated with a lower amide I wavenumber peak and the appearance of minor peaks at ~1612 cm^{-1} indicating F-β formation. The presence of a phospho/lipid appeared to inhibit this formation therefore it was concluded that these macromolecules played an important role in the lubrication mechanism. The occurrence of F-β was intriguing as it potentially indicates the presence of amyloid fibres. This was present in all of the model and BCS and some of the HSF's wear deposit spectra.

The presence of amyloid fibres was further investigated by doping model and human SF with ThT and performing wear tests. Wear deposits were imaged using ThT optics. The deposits brightly fluoresced showing aggregated fibril structures, however this was somewhat reduced for the HSF samples. In many cases low-level background fluorescence was also observed which is attributed to the increased viscosity of the deposits.

Micro-IRRAS of the deposits showed that a parallel β-sheet structure related to brightly fluorescing deposited films. This was particularly apparent in 25BCS, 6Glob and HSF108. The combination of fluorescence and Micro-IRRAS analysis confirms that the deposits were N-β rich and/or contained amyloid fibres which was related to a reduction in wear. It was possible that high γ-G concentrations were indicative of F-β formation however more tests are required to confirm this.

The surface topography was analysed using WLI, the wear scar had an increased surface roughness and consisted of scratches and groove and therefore abrasion was identified as the dominate wear mechanisms for material loss.

9 References

1. 14th Annual Report 2017 national Joint Registry for England, Wales and Northern Ireland. 2016.

2. Chen A, Gupte C, Akhtar K, Smith P, Cobb J. The global economic cost of osteoarthritis: how the UK compares. Arthritis. 2012;2012.

3. Knight SR, Aujla R, Biswas SP. Total Hip Arthroplasty-over 100 years of operative history. Orthop Rev (Pavia). 2011;3(2).

4. Learmonth ID, Young C, Rorabeck C. The operation of the century: total hip replacement. The Lancet. 2007;370(9597):1508-19.

5. Fisher J, Dowson D. Tribology of Total Artificial Joints. Proceedings of the Institution of Mechanical Engineers, Part H: Journal of Engineering in Medicine. 1991;205(2):73-9.

6. Willert H-G, Bertram H, Buchhorn GH. Osteolysis in alloarthroplasty of the hip. The role of ultra-high molecular weight polyethylene wear particles. Clin Orthop Relat Res. 1990(258):95-107.

7. Kumar N, Arora N, Datta B. Bearing surfaces in hip replacement–evolution and likely future. Medical Journal Armed Forces India. 2014;70(4):371-6.

8. Hedlundh U, Ahnfelt L, Hybbinette C-H, Wallinder L, Weckström J, Fredin H. Dislocations and the femoral head size in primary total hip arthroplasty. Clin Orthop Relat Res. 1996(333):226-33.

9. Dowson D, Jin ZM. Metal-on-metal hip joint tribology. Proceedings of the Institution of Mechanical Engineers Part H, Journal of Engineering in Medicine. 2006;220(2):107-18.

10. Drummond J, Tran P, Fary C. Metal-on-Metal Hip Arthroplasty: A Review of Adverse Reactions and Patient Management. Journal of Functional Biomaterials. 2015;6(3):486-99.

11. Cuckler JM. The rationale for metal-on-metal total hip arthroplasty. Clin Orthop Relat Res. 2005;441:132-6.

12. Amarasekera H, Griffin D. Surface Replacement of Hip Joint. Recent Advances in Hip and Knee Arthroplasty: InTech; 2012.

13. Doorn PF, Campbell PA, Worrall J, Benya PD, McKellop HA, Amstutz HC. Metal wear particle characterization from metal on metal total hip replacements: transmission electron microscopy study of periprosthetic tissues and isolated particles. Journal of Biomedical Materials Research: An Official Journal of The Society for Biomaterials, The Japanese Society for Biomaterials, and the Australian Society for Biomaterials. 1998;42(1):103-11.

14. Doorn PF, Campbell PA, Amstutz HC. Metal Versus Polyethylene Wear Particles in Total Hip Replacements: A Review. Clin Orthop Relat Res. 1996;329:S206-S16.

15. Tipper J, Firkins P, Ingham E, Fisher J, Stone M, Farrar R. Quantitative analysis of the wear and wear debris from low and high carbon content cobalt chrome alloys used in metal on metal total hip replacements. J Mater Sci Mater Med. 1999;10(6):353-62.

16. Haddad F, Thakrar R, Hart A, Skinner J, Nargol A, Nolan J, et al. Metal-on-metal bearings: the evidence so far. JBJS. 2011;93(5):572-9.

17. Elkins C. https://www.drugwatch.com/hip-replacement/recalls/ [cited 2018 28/08/2018].

18. Turner T. Hip Replacement Lawsuits, Verdicts and Settlements 2018 [cited 2018 01/09/2018].

19. D'Antonio JA, Manley MT, Capello WN, Bierbaum BE, Ramakrishnan R, Naughton M, et al. Five-year Experience with Crossfire (R) Highly Cross-linked Polyethylene. Clin Orthop Relat Res. 2005;441:143-50.

20. Atienza JC, Maloney WJ. Highly cross-linked polyethylene bearing surfaces in total hip arthroplasty. J Surg Orthop Adv. 2008;17(1):27-33.

21. Digas G, Kärrholm J, Thanner J, Herberts P. 5-year experience of highly cross-linked polyethylene in cemented and uncemented sockets: two randomized studies using radiostereometric analysis. Acta Orthop. 2007;78(6):746-54.

22. Dumbleton JH, D'antonio JA, Manley MT, Capello WN, Wang A. The basis for a second-generation highly cross-linked UHMWPE. Clin Orthop Relat Res. 2006;453:265-71.

23. Kurtz SM, Manley M, Wang A, Taylor S, Dumbleton J. Comparison of the Properties of Annealed Crosslinked (Crossfire™) and Conventional Polyethylene as Hip Bearing Materials. Bulletin-Hospital for Joint Diseases. 2002;61(1-2):17-26.

24. Schwartsmann CR, Boschin LC, Gonçalves RZ, Yépez AK, de Freitas Spinelli L. New bearing surfaces in total hip replacement. Revista Brasileira de Ortopedia (English Edition). 2012;47(2):154-9.

25. Christel P. Biocompatibility of surgical-grade dense polycrystalline alumina. Clin Orthop Relat Res. 1992;282:10-8.

26. Carnes KJ, Odum SM, Troyer JL, Fehring TK. Cost analysis of ceramic heads in primary total hip arthroplasty. JBJS. 2016;98(21):1794-800.

27. Rahaman MN, Yao A, Bal BS, Garino JP, Ries MD. Ceramics for prosthetic hip and knee joint replacement. J Am Ceram Soc. 2007;90(7):1965-88.

28. Sandhu HS, Middleton RG. Controversial topics in orthopaedics: ceramic-on-ceramic. Ann R Coll Surg Engl. 2005;87(6):415.

29. Clarke IC, Gustafson A. Clinical and hip simulator comparisons of ceramic-on-polyethylene and metal-on-polyethylene wear. Clin Orthop Relat Res. 2000;379:34-40.

30. Urban JA, Garvin KL, Boese CK, Bryson L, Pedersen DR, Callaghan JJ, et al. Ceramic-on-polyethylene bearing surfaces in total hip arthroplasty: seventeen to twenty-one-year results. JBJS. 2001;83(11):1688-94.

31. D'antonio JA, Capello WN, Naughton M. Ceramic bearings for total hip arthroplasty have high survivorship at 10 years. Clin Orthop Relat Res. 2012;470(2):373-81.

32. Fisher J. Bioengineering reasons for the failure of metal-on-metal hip prostheses: an engineer's perspective. JBJS. 2011;93(8):1001-4.

33. Bellon T. Johnson & Johnson hit with $247 million verdict in hip implant trial 26/11/2017 [cited 2018 28/08/2018].

34. De Smet KA, Van Der Straeten C, Van Orsouw M, Doubi R, Backers K, Grammatopoulos G. Revisions of metal-on-metal hip resurfacing: lessons learned and improved outcome. Orthopedic Clinics. 2011;42(2):259-69.

35. Sigma Aldrich, Certifivate of Analysis, Catalog Number 12133C, Lot Number 11N238. In: SAFC, editor.

36. Oates KMN, Krause WE, Jones RL, Colby RH. Rheopexy of synovial fluid and protein aggregation. Journal of the Royal Society Interface. 2006;3(6):167-74.

37. Mavraki A, Cann PM. Friction and lubricant film thickness measurements on simulated synovial fluids. Proceedings of the Institution of Mechanical Engineers, Part J: Journal of Engineering Tribology. 2009;223(3):325-35.

38. Ghosh S, Choudhury D, Das NS, Pingguan-Murphy B. Tribological role of synovial fluid compositions on artificial joints — a systematic review of the last 10 years. Lubrication Science. 2014;26(6):387-410.

39. Fam H, Bryant JT, Kontopoulou M. Rheological properties of synovial fluids. Biorheology. 2007;44(2):59-74.

40. Perlmann GE, Ropes MW, Kaufman D, Bauer W. The Electrophoretic Patterns of Proteins in Synovial Fluid and Serum in Rheumatoid Arthritis. The Journal of Clinical Investigation. 1954;33(3):319-25.

41. Mazzucco D, Scott R, Spector M. Composition of joint fluid in patients undergoing total knee replacement and revision arthroplasty: correlation with flow properties. Biomaterials. 2004;25(18):4433-45.

42. Publication BS. Implants for surgery - Metalic materials. BS ISO 5832-4:20142014.

43. Standard B. Implants for surgery — Metallic materials Part 12: Wrought cobalt-chromium-molybdenum alloy. BS ISO 5832-12:20072007.

44. Smith AJ, Dieppe P, Vernon K, Porter M, Blom AW. Failure rates of stemmed metal-on-metal hip replacements: analysis of data from the National Joint Registry of England and Wales. The Lancet. 2012;379(9822):1199-204.

45. Santavirta S, Konttinen Y, Lappalainen R, Anttila A, Goodman S, Lind M, et al. Materials in total joint replacement. Curr Orthop. 1998;12(1):51-7.

46. Di Puccio F, Mattei L. Biotribology of artificial hip joints. World Journal of Orthopedics. 2015;6(1):77-94.

47. Schwartsmann CR, Boschin LC, Gonçalves RZ, Yépez AK, de Freitas Spinelli L. New bearing surfaces in total hip replacement Revista Brasileira de Ortopedia (English Edition). 2012;47(2):154-9.

48. Wimmer M, Loos J, Nassutt R, Heitkemper M, Fischer A. The acting wear mechanisms on metal-on-metal hip joint bearings: in vitro results. Wear. 2001;250(1):129-39.

49. McMinn DJ. Modern hip resurfacing: Springer Science & Business Media; 2009.

50. Cawley J, Metcalf J, Jones AH, Band T, Skupien D. A tribological study of cobalt chromium molybdenum alloys used in metal-on-metal resurfacing hip arthroplasty. Wear. 2003;255(7-12):999-1006.

51. McMinn D. Development of metal/metal hip resurfacing. Hip Int. 2003;13(2_suppl):41-53.

52. Chan FW, Bobyn JD, Medley JB, Krygier JJ, Tanzer M. Wear and lubrication of metal-on-metal hip implants. Clin Orthop Relat Res. 1999;369:10-24.

53. Bowsher J, Nevelos J, Pickard J, Shelton J. Do heat treatments influence the wear of large diameter metal-on-metal hip joints? An in vitro study under normal and adverse gait conditions. Trans 49th Orthop Res Soc. 2003;28:1398.

54. Dowson D, Hardaker C, Flett M, Isaac GH. A hip joint simulator study of the performance of metal-on-metal joints: Part I: The role of materials. The Journal of Arthroplasty. 2004;19(8, Supplement):118-23.

55. Yan Y, Neville A, Dowson D. Biotribocorrosion of CoCrMo orthopaedic implant materials—assessing the formation and effect of the biofilm. Tribology International. 2007;40(10):1492-9.

56. Matsushita A, Nakashima Y, Jingushi S, Yamamoto T, Kuraoka A, Iwamoto Y. Effects of the femoral offset and the head size on the safe range of motion in total hip arthroplasty. The Journal of Arthroplasty. 2009;24(4):646-51.

57. Wang F, Jin Z, editors. Lubrication modelling of artificial hip joints. IUTAM Symposium on Elastohydrodynamics and Micro-elastohydrodynamics; 2006: Springer.

58. Jin Z, Stone M, Ingham E, Fisher J. (v) Biotribology. Curr Orthop. 2006;20(1):32-40.

59. Hadley MJF. Thesis: Long Term Functional Simualtion of Large Diameter Metal on Metal Hip Implants: The University of Leeds; 2012.

60. Bergmann G, Deuretzbacher G, Heller M, Graichen F, Rohlmann A, Strauss J, et al. Hip contact forces and gait patterns from routine activities. J Biomech. 2001;34(7):859-71.

61. Bergmann G, Graichen F, Rohlmann A. Hip joint loading during walking and running, measured in two patients. J Biomech. 1993;26(8):969-90.

62. Bergmann G, Graichen F, Rohlmann A, Bender A, Heinlein B, Duda G, et al. Realistic loads for testing hip implants. Bio-Med Mater Eng. 2010;20(2):65-75.

63. Brand RA, Pedersen DR, Davy DT, Kotzar GM, Heiple KG, Goldberg VM. Comparison of hip force calculations and measurements in the same patient. The Journal of Arthroplasty. 1994;9(1):45-51.

64. Stansfield B, Nicol A, Paul J, Kelly I, Graichen F, Bergmann G. Direct comparison of calculated hip joint contact forces with those measured using instrumented implants. An evaluation of a three-dimensional mathematical model of the lower limb. J Biomech. 2003;36(7):929-36.

65. Paul J. Biomechanics. SAGE Publications; 1966.

66. Crowinshield RD, Brand RA, Johnston R. The effects of walking velocity and age on hip kinematics and kinetics. Clin Orthop Relat Res. 1978(132):140-4.

67. Paul J. Approaches to design-Force actions transmitted by joints in the human body. Proc R Soc Lond B. 1976;192(1107):163-72.

68. Read L, Nigg B. An analysis of hip joint loading during walking, running, and skiing. Med Sci Sports Exerc. 1999;31(1):131-42.

69. ISO. Implants for surgery - wear of total hip-joint prostheses Part 1: Loading and Displacement Parameters for Wear-Testing Machines and Corresponding Enviromental Conditions for Tests2014.

70. Moody A. Adult anthropometric measures, overweight and obesity. Health Survey for England–2012. 2013;1.

71. Cole TJ, Freeman JV, Preece MA. Body mass index reference curves for the UK, 1990. Arch Dis Child. 1995;73(1):25-9.

72. Jalali-Vahid D, Jin Z, Dowson D. Effect of start-up conditions on elastohydrodynamic lubrication of metal-on-metal hip implants. Proceedings of the Institution of Mechanical Engineers, Part J: Journal of Engineering Tribology. 2006;220(3):143-50.

73. Calonius O, Saikko V. Analysis of relative motion between femoral head and acetabular cup and advances in computation of the wear factor for the prosthetic hip joint. Acta Polytechnica. 2003;43(4).

74. Liu F, Udofia I, Jin Z, Hirt F, Rieker C, Roberts P, et al. Comparison of contact mechanics between a total hip replacement and a hip resurfacing with a metal-on-metal articulation. Proceedings

of the Institution of Mechanical Engineers, Part C: Journal of Mechanical Engineering Science. 2005;219(7):727-32.

75. Besong A, Lee R, Farrar R, Jin Z. Contact mechanics of a novel metal-on-metal total hip replacement. Proceedings of the Institution of Mechanical Engineers, Part H: Journal of Engineering in Medicine. 2001;215(6):543-8.

76. Yew A, Jagatia M, Ensaff H, Jin Z. Analysis of contact mechanics in McKee-Farrar metal-on-metal hip implants. Proceedings of the institution of mechanical engineers, Part H: Journal of Engineering in Medicine. 2003;217(5):333-40.

77. Liu F, Jin Z, Grigoris P, Hirt F, Rieker C. Contact mechanics of metal-on-metal hip implants employing a metallic cup with a UHMWPE backing. Proceedings of the Institution of Mechanical Engineers, Part H: Journal of Engineering in Medicine. 2003;217(3):207-13.

78. Liu F, Leslie I, Williams S, Fisher J, Jin Z. Development of computational wear simulation of metal-on-metal hip resurfacing replacements. J Biomech. 2008;41(3):686-94.

79. Wang W, Jin Z, Dowson D, Hu Y. A study of the effect of model geometry and lubricant rheology upon the elastohydrodynamic lubrication performance of metal-on-metal hip joints. Proceedings of the Institution of Mechanical Engineers, Part J: Journal of Engineering Tribology. 2008;222(3):493-501.

80. Mattei L, Piccigallo B, Stadler K, Ciulli E, Di Puccio F. EHL modeling of hip implants based on a ball-on-plane configuration. Ancona, Italy: AIMETA. 2009:161-73.

81. Dept ICLT. 9. Mixed and Boundary Lubrication. Imperial College London.

82. Ziemer DJ. Basics of Wear: STLE; [cited 2015 31st July]. Available from: http://www.stle.org/resources/lubelearn/wear/#summary.

83. Hamrock BJ, Schmid SR, Jacobson BO. Fundamentals of fluid film lubrication: CRC press; 2004.

84. Dowson D. Tribological principles in metal-on-metal hip joint design. Proceedings of the Institution of Mechanical Engineers, Part H: Journal of Engineering in Medicine. 2006;220(2):161-71.

85. Spikes H. Mixed lubrication—an overview. Lubrication Science. 1997;9(3):221-53.

86. Friedrich K. Friction and wear of polymer composites: Elsevier; 2012.

87. Hutchings I, Shipway P. Tribology: friction and wear of engineering materials: Butterworth-Heinemann; 2017.

88. Masen M. Abrasive Tool Wear in Metal Forming Processes: Twente; 1975.

89. Williams J. Engineering tribology: Cambridge University Press; 2005.

90. Langton D, Jameson S, Joyce T, Hallab N, Natu S, Nargol A. Early failure of metal-on-metal bearings in hip resurfacing and large-diameter total hip replacement: a consequence of excess wear. The Journal of Bone and Joint Surgery British Volume. 2010;92(1):38-46.

91. Isaac G, Thompson J, Williams S, Fisher J. Metal-on-metal bearings surfaces: materials, manufacture, design, optimization, and alternatives. Proceedings of the Institution of Mechanical Engineers, Part H: Journal of Engineering in Medicine. 2006;220(2):119-33.

92. Evans EM, Freeman M, Miller A, Vernon-Roberts B. Metal sensitivity as a cause of bone necrosis and loosening of the prosthesis in total joint replacement. Bone & Joint Journal. 1974;56(4):626-42.

93. Vidal CV, Juan AO, Muñoz AI. Adsorption of bovine serum albumin on CoCrMo surface: effect of temperature and protein concentration. Colloids Surf B Biointerfaces. 2010;80(1):1-11.

94. Vidal CV, Muñoz AI. Effect of physico-chemical properties of simulated body fluids on the electrochemical behaviour of CoCrMo alloy. Electrochimica Acta. 2011;56(24):8239-48.

95. Yan Y, Neville A, Dowson D. Biotribocorrosion—an appraisal of the time dependence of wear and corrosion interactions: II. Surface analysis. Journal of Physics D: applied physics. 2006;39(15):3206.

96. Muñoz AI, Mischler S. Effect of the environment on wear ranking and corrosion of biomedical CoCrMo alloys. J Mater Sci Mater Med. 2011;22(3):437-50.

97. Lewis AC, Kilburn M, Papageorgiou I, Allen G, Case C. Effect of synovial fluid, phosphate-buffered saline solution, and water on the dissolution and corrosion properties of CoCrMo alloys as used in orthopedic implants. Journal of Biomedical Materials Research Part A: An Official Journal of The Society for Biomaterials, The Japanese Society for Biomaterials, and The Australian Society for Biomaterials and the Korean Society for Biomaterials. 2005;73(4):456-67.

98. Parkes M. Thesis: Lubrication Mechanisms of Lipids and Proteins in Model Synovial Fluids: Imperial College London; March 2014.

99. Murakami T, Higaki H, Sawae Y, Ohtsuki N, Moriyama S, Nakanishi Y. Adaptive multimode lubrication in natural synovial joints and artificial joints. Proceedings of the Institution of Mechanical Engineers, Part H: Journal of Engineering in Medicine. 1998;212(1):23-35.

100. Hui AY, McCarty WJ, Masuda K, Firestein GS, Sah RL. A Systems Biology Approach to Synovial Joint Lubrication in Health, Injury, and Disease. Wiley interdisciplinary reviews Systems biology and medicine. 2012;4(1):15-37.

101. Swann DA, Radin EL. The molecular basis of articular lubrication. I. Purification and properties of a lubricating fraction from bovine synovial fluid. J Biol Chem. 1972;247(24):8069-73.

102. J.R. Levick FMPaRMM. Synovial matrix-synovial fluid system of joints, in: Extracellular Matrix, Tissue Function. Harwood Academic Publishers. 1996;2:348–54.

103. Delecrin J, Oka M, Takahashi S, Yamamuro T, Nakamura T. Changes in Joint Fluid After Total Arthroplasty: A Quantitative Study on the Rabbit Knee Joint. Clin Orthop Relat Res. 1994;307:240-9.

104. Kitano T, Ateshian GA, Mow VC, Kadoya Y, Yamano Y. Constituents and pH changes in protein rich hyaluronan solution affect the biotribological properties of artificial articular joints. J Biomech. 2001;34(8):1031-7.

105. Cooke A, Dowson D, Wright V. The rheology of synovial fluid and some potential synthetic lubricants for degenerate synovial joints. Eng Med. 1978;7(2):66-72.

106. Schurz J, Ribitsch V. Rheology of synovial fluid. Biorheology. 1986;24(4):385-99.

107. Yao J, Laurent M, Johnson T, Blanchard C, Crowninshield R. The influences of lubricant and material on polymer/CoCr sliding friction. Wear. 2003;255(1):780-4.

108. Mavraki A, Cann PM. Lubricating film thickness measurements with bovine serum. Tribology International. 2011;44(5):550-6.

109. Parkes M, Myant C, Cann PM, Wong JS. Synovial fluid lubrication: The effect of protein interactions on adsorbed and lubricating films. Biotribology. 2015;1:51-60.

110. Fan J, Myant C, Underwood R, Cann P. Synovial fluid lubrication of artificial joints: protein film formation and composition. Faraday Discuss. 2012;156(0):69-85.

111. Myant C, Underwood R, Fan J, Cann PM. Lubrication of metal-on-metal hip joints: The effect of protein content and load on film formation and wear. Journal of the Mechanical Behavior of Biomedical Materials. 2012;6(0):30-40.

112. Fan J, Myant CW, Underwood R, Cann PM, Hart A. Inlet protein aggregation: a new mechanism for lubricating film formation with model synovial fluids. Proceedings of the Institution of Mechanical Engineers, Part H: Journal of Engineering in Medicine. 2011;225(7):696-709.

113. Mazzucco D, McKinley G, Scott RD, Spector M. Rheology of joint fluid in total knee arthroplasty patients. J Orth Res. 2002;20(6):1157-63.

114. Harvey R, & Ferrier, Denise R. Biochemistry (5th ed., International ed., Lippincott's illustrated reviews). Philadelphia, Pa: London: Wolters Kluwer Health/Lippincott Williams & Wilkins; 2011.

115. Sigma Aldrich, Product infomation - Albumin form bowine serum.

116. Pease LF, Elliott JT, Tsai D-H, Zachariah MR, Tarlov MJ. Determination of protein aggregation with differential mobility analysis: Application to IgG antibody. Biotechnol Bioeng. 2008;101(6):1214-22.

117. Sigma Aldridh, Product Infomation - Fibrogen from human plasma (Catalouge Number F3879). 2015.

118. Davies DV. Paper 7: Properties of Synovial Fluid. Proceedings of the Institution of Mechanical Engineers, Conference Proceedings. 1966;181(10):25-9.

119. Sugio S, Kashima A, Mochizuki S, Noda M, Kobayashi K. Crystal structure of human serum albumin at 2.5 Å resolution. Protein Eng. 1999;12(6):439-46.

120. Peters Jr T. All about albumin: biochemistry, genetics, and medical applications: Academic press; 1995.

121. Fanali G, di Masi A, Trezza V, Marino M, Fasano M, Ascenzi P. Human serum albumin: From bench to bedside. Mol Aspects Med. 2012;33(3):209-90.

122. Larsen MT, Kuhlmann M, Hvam ML, Howard KA. Albumin-based drug delivery: harnessing nature to cure disease. Molecular and cellular therapies. 2016;4(1):3.

123. Whitford D. Proteins: structure and function: John Wiley & Sons; 2013.

124. Pauling L, Corey RB, Branson HR. The structure of proteins: two hydrogen-bonded helical configurations of the polypeptide chain. Proceedings of the National Academy of Sciences. 1951;37(4):205-11.

125. Griffiths. Alph Helix: a right handed helical structure 2009 [02/12/2016]. Available from: https://www.mun.ca/biology/scarr/Gr09-05.html.

126. Pauling L, Corey RB. The pleated sheet, a new layer configuration of polypeptide chains. Proceedings of the National Academy of Sciences. 1951;37(5):251-6.

127. Griffiths. Secondary protein structure: the Beta-pleasted sheet. 2000.

128. Kabir MM. Bioprocessing of Recalcitrant Substrates for Biogas Production: Högskolan i Borås; 2015.

129. Maréchal Y. 2 - Geometrical Properties of H-Bonds and H-Bonded Organized Supramolecular Structures. In: Maréchal Y, editor. The Hydrogen Bond and the Water Molecule. Amsterdam: Elsevier; 2007. p. 25-47.

130. Branden CI. Introduction to protein structure: Garland Science; 1999.

131. Meredith SC. Protein denaturation and aggregation: Cellular responses to denatured and aggregated proteins. Ann N Y Acad Sci. 2005;1066:181-221.

132. Neurath H, Greenstein JP, Putnam FW, Erickson JA. The chemistry of protein denaturation. Chem Rev. 1944;34(2):157-265.

133. Kopito RR. Aggresomes, inclusion bodies and protein aggregation. Trends Cell Biol. 2000;10(12):524-30.

134. Lepock JR, Ritchie KP, Kolios MC, Rodahl AM, Heinz KA, Kruuv J. Influence of transition rates and scan rate on kinetic simulations of differential scanning calorimetry profiles of reversible and irreversible protein denaturation. Biochemistry. 1992;31(50):12706-12.

135. Fang H-W, Hsieh M-C, Huang H-T, Tsai C-Y, Chang M-H. Conformational and adsorptive characteristics of albumin affect interfacial protein boundary lubrication: From experimental to molecular dynamics simulation approaches. Colloids Surf B Biointerfaces. 2009;68(2):171-7.

136. Balazs E. The physical properties of synovial fluid and the special role of hyaluronic acid. Disorders of the Knee. 1974;2:61-74.

137. Morris HR, Thompson MR, Osuga DT, Ahmed AI, Chan SM, Vandenheede JR, et al. Antifreeze glycoproteins from the blood of an antarctic fish. The structure of the proline-containing glycopeptides. J Biol Chem. 1978;253(14):5155-62.

138. Swann DA, Slayter HS, Silver FH. The molecular structure of lubricating glycoprotein-I, the boundary lubricant for articular cartilage. J Biol Chem. 1981;256(11):5921-5.

139. Zappone B, Greene GW, Oroudjev E, Jay GD, Israelachvili JN. Molecular Aspects of Boundary Lubrication by Human Lubricin: Effect of Disulfide Bonds and Enzymatic Digestion†. Langmuir. 2008;24(4):1495-508.

140. Rhee DK, Marcelino J, Baker M, Gong Y, Smits P, Lefebvre V, et al. The secreted glycoprotein lubricin protects cartilage surfaces and inhibits synovial cell overgrowth. The Journal of Clinical Investigation. 2005;115(115 (3)):622-31.

141. Swann DA, Sotman S, Dixon M, Brooks C. The isolation and partial characterization of the major glycoprotein (LGP-I) from the articular lubricating fraction from bovine synovial fluid. Biochem J. 1977;161(3):473-85.

142. Schwarz IM, Hills BA. Surface-active phospholipid as the lubricating component of lubricin. Br J Rheumatol. 1998;37(1):21-6.

143. Roba M, Naka M, Gautier E, Spencer ND, Crockett R. The adsorption and lubrication behavior of synovial fluid proteins and glycoproteins on the bearing-surface materials of hip replacements. Biomaterials. 2009;30(11):2072-8.

144. Bole GG. Synovial fluid lipids in normal individuals and patients with rheumatoid arthritis. Arthritis & Rheumatology. 1962;5:589-601.

145. Prete PE, Gurakar-Osborne A, Kashyap ML. Synovial fluid lipoproteins: Review of current concepts and new directions. Semin Arthritis Rheum. 1993;23(2):79-89.

146. Hills BA, Butler BD. Surfactants identified in synovial fluid and their ability to act as boundary lubricants. Ann Rheum Dis. 1984;43(4):641-8.

147. Banquy X, Lee DW, Das S, Hogan J, Israelachvili JN. Shear-Induced Aggregation of Mammalian Synovial Fluid Components under Boundary Lubrication Conditions. Advanced Functional Materials. 2014;24(21):3152-61.

148. Hills BA. The biology of surfactant: Cambridge University Press; 1988.

149. Hills BA. Oligolamellar lubrication of joints by surface active phospholipid. The Journal of Rheumatology. 1989;16(1):82-91.

150. R Gale L, Chen Y, A Hills B, Crawford R. Boundary lubrication of joints: Characterization of surface-active phospholipids found on retrieved implants. Acta Orthop. 2007;78(3):309-14.

151. Chen Y, Crawford RW, Oloyede A. Unsaturated phosphatidylcholines lining on the surface of cartilage and its possible physiological roles. J Orthop Surg Res. 2007;2:14-.

152. Sarma AV, Powell GL, LaBerge M. Phospholipid composition of articular cartilage boundary lubricant. J Orth Res. 2001;19(4):671-6.

153. Sorkin R, Kampf N, Dror Y, Shimoni E, Klein J. Origins of extreme boundary lubrication by phosphatidylcholine liposomes. Biomaterials. 2013;34(22):5465-75.

154. Bell J, Tipper JL, Ingham E, Stone MH, Fisher J. The influence of phospholipid concentration in protein-containing lubricants on the wear of ultra-high molecular weight polyethylene in artificial hip joints. Proceedings of the Institution of Mechanical Engineers Part H, Journal of Engineering in Medicine. 2001;215(2):259-63.

155. Seifert U. Configurations of fluid membranes and vesicles. Advances in Physics. 1997;46(1):13-137.

156. Dekkiche F, Corneci M, Trunfio-Sfarghiu A-M, Munteanu B, Berthier Y, Kaabar W, et al. Stability and tribological performances of fluid phospholipid bilayers: Effect of buffer and ions. Colloids Surf B Biointerfaces. 2010;80(2):232-9.

157. Keegan G, Learmonth I, Case C. Orthopaedic metals and their potential toxicity in the arthroplasty patient: a review of current knowledge and future strategies. The Journal of Bone and Joint Surgery British Volume. 2007;89(5):567-73.

158. Anissian HL, Stark A, Gustafson A, Good V, Clarke IC. Metal-on-metal bearing in hip prosthesis generates 100-fold less wear debris than metal-on-polyethylene. Acta Orthop Scand. 1999;70(6):578-82.

159. Amstutz HC, Grigoris P. Metal on metal bearings in hip arthroplasty. Clin Orthop Relat Res. 1996;329:S11-S34.

160. Firkins P, Tipper J, Saadatzadeh M, Ingham E, Stone M, Farrar R, et al. Quantitative analysis of wear and wear debris from metal-on-metal hip prostheses tested in a physiological hip joint simulator. Bio-Med Mater Eng. 2001;11(2):143-57.

161. Case C, Langkamer V, James C, Palmer M, Kemp A, Heap P, et al. Widespread dissemination of metal debris from implants. The Journal of Bone and Joint Surgery British Volume. 1994;76(5):701-12.

162. Urban RM, Jacobs JJ, Tomlinson MJ, Gavrilovic J, Black J, Peoc'h M. Dissemination of wear particles to the liver, spleen, and abdominal lymph nodes of patients with hip or knee replacement. JBJS. 2000;82(4):457-77.

163. Olmedo DG, Tasat D, Guglielmotti MB, Cabrini RL. Titanium transport through the blood stream. An experimental study on rats. J Mater Sci Mater Med. 2003;14(12):1099-103.

164. Engh CA, Moore KD, Vinh TN, Engh GA. Titanium prosthetic wear debris in remote bone marrow: a report of two cases. JBJS. 1997;79(11):1721-5.

165. Langton D, Joyce T, Jameson S, Lord J, Van Orsouw M, Holland J, et al. Adverse reaction to metal debris following hip resurfacing: the influence of component type, orientation and volumetric wear. The Journal of Bone and Joint Surgery British Volume. 2011;93(2):164-71.

166. Heuberger M, Widmer M, Zobeley E, Glockshuber R, Spencer N. Protein-mediated boundary lubrication in arthroplasty. Biomaterials. 2005;26(10):1165-73.

167. Saikko V. A multidirectional motion pin-on-disk wear test method for prosthetic joint materials. J Biomed Mater Res. 1998;41(1):58-64.

168. Cooper J, Dowson D, Fisher J. Macroscopic and microscopic wear mechanisms in ultra-high molecular weight polyethylene. Wear. 1993;162:378-84.

169. Varano R, Bobyn J, Medley J, Yue S. The effect of microstructure on the wear of cobalt-based alloys used in metal-on-metal hip implants. Proceedings of the Institution of Mechanical Engineers, Part H: Journal of Engineering in Medicine. 2006;220(2):145-59.

170. Wimmer MA, Sprecher C, Hauert R, Täger G, Fischer A. Tribochemical reaction on metal-on-metal hip joint bearings: A comparison between in-vitro and in-vivo results. Wear. 2003;255(7–12):1007-14.

171. Smith SL, Dowson D, Goldsmith AA. The effect of femoral head diameter upon lubrication and wear of metal-on-metal total hip replacements. Proceedings of the Institution of Mechanical Engineers Part H, Journal of Engineering in Medicine. 2001;215(2):161-70.

172. Dowson D, Hardaker C, Flett M, Isaac GH. A hip joint simulator study of the performance of metal-on-metal joints: Part II: design. The Journal of Arthroplasty. 2004;19(8):124-30.

173. Medley J, Krygier J, Bobyn J, Chan F, Lippincott A, Tanzer M. Kinematics of the MATCO™ hip simulator and issues related to wear testing of metal-metal implants. Proceedings of the Institution of Mechanical Engineers, Part H: Journal of Engineering in Medicine. 1997;211(1):89-99.

174. Bowsher J, Hussain A, Williams P, Shelton J. Metal-on-metal hip simulator study of increased wear particle surface area due to 'severe'patient activity. Proceedings of the Institution of Mechanical Engineers, Part H: Journal of Engineering in Medicine. 2006;220(2):279-87.

175. Yan Y, Neville A, Dowson D, Williams S. Tribocorrosion in implants—assessing high carbon and low carbon Co–Cr–Mo alloys by in situ electrochemical measurements. Tribology International. 2006;39(12):1509-17.

176. Brown SS, Clarke IC. A Review of Lubrication Conditions for Wear Simulation in Artificial Hip Replacements. Tribology Transactions. 2006;49(1):72-8.

177. Wang A, Essner A, Schmidig G. The effects of lubricant composition on in vitro wear testing of polymeric acetabular components. Journal of Biomedical Materials Research Part B: Applied Biomaterials. 2004;68(1):45-52.

178. Unsworth A. Tribology of human and artificial joints. Proceedings of the Institution of Mechanical Engineers Part H, Journal of Engineering in Medicine. 1991;205(3):163-72.

179. Harsha AP, Joyce TJ. Challenges associated with using bovine serum in wear testing orthopaedic biopolymers. Proceedings of the Institution of Mechanical Engineers Part H, Journal of Engineering in Medicine. 2011;225(10):948-58.

180. Murakami T, Yarimitsu S, Nakashima K, Sawae Y, Sakai N. Influence of synovia constituents on tribological behaviors of articular cartilage. Friction. 2013;1(2):150-62.

181. Verberne G, Schroeder A, Halperin G, Barenholz Y, Etsion I. Liposomes as potential biolubricant additives for wear reduction in human synovial joints. Wear. 2010;268(7):1037-42.

182. Karuppiah KK, Sundararajan S, Xu Z-H, Li X. The effect of protein adsorption on the friction behavior of ultra-high molecular weight polyethylene. Tribology Letters. 2006;22(2):181-8.

183. Benz M, Chen N, Israelachvili J. Lubrication and wear properties of grafted polyelectrolytes, hyaluronan and hylan, measured in the surface forces apparatus. Journal of Biomedical Materials Research Part A. 2004;71(1):6-15.

184. Tadmor R, Chen N, Israelachvili JN. Thin film rheology and lubricity of hyaluronic acid solutions at a normal physiological concentration. J Biomed Mater Res. 2002;61(4):514-23.

185. Parkes M, Myant C, Cann PM, Wong JS. The effect of buffer solution choice on protein adsorption and lubrication. Tribology International. 2014;72:108-17.

186. Perez-Jimenez R, Godoy-Ruiz R, Ibarra-Molero B, Sanchez-Ruiz JM. The efficiency of different salts to screen charge interactions in proteins: a Hofmeister effect? Biophys J. 2004;86(4):2414-29.

187. Israelachvili JN. Intermolecular and surface forces: Academic press; 2011.

188. Beynon RJ EJ. Buffer Solutions. First ed: Taylor and Francis; 2003.

189. Manivasagam G, Dhinasekaran D, Rajamanickam A. Biomedical implants: corrosion and its prevention-a review. Recent Patents on Corrosion Science. 2010.

190. Jin ZM, Dowson D, Fisher J. Analysis of fluid film lubrication in artificial hip joint replacements with surfaces of high elastic modulus. Proceedings of the Institution of Mechanical Engineers Part H, Journal of Engineering in Medicine. 1997;211(3):247-56.

191. Vassiliou K, D Elfick A, Scholes S, Unsworth A. The effect of 'running-in'on the tribology and surface morphology of metal-on-metal Birmingham hip resurfacing device in simulator studies.

Proceedings of the Institution of Mechanical Engineers, Part H: Journal of Engineering in Medicine. 2006;220(2):269-77.

192. Dowson D, McNie C, Goldsmith A. Direct experimental evidence of lubrication in a metal-on-metal total hip replacement tested in a joint simulator. Proceedings of the Institution of Mechanical Engineers, Part C: Journal of Mechanical Engineering Science. 2000;214(1):75-86.

193. Scholes S, Unsworth A, Hall R, Scott R. The effects of material combination and lubricant on the friction of total hip prostheses. Wear. 2000;241(2):209-13.

194. Scholes S, Unsworth A. Comparison of friction and lubrication of different hip prostheses. Proceedings of the Institution of Mechanical Engineers, Part H: Journal of Engineering in Medicine. 2000;214(1):49-57.

195. Sharma V, Jaishankar A, Wang Y-C, McKinley GH. Rheology of globular proteins: apparent yield stress, high shear rate viscosity and interfacial viscoelasticity of bovine serum albumin solutions. Soft Matter. 2011;7(11):5150-60.

196. Walker P, Erkman M. Metal-on-metal lubrication in artificial human joints. Wear. 1972;21(2):377-92.

197. Gispert M, Serro A, Colaco R, Saramago B. Friction and wear mechanisms in hip prosthesis: Comparison of joint materials behaviour in several lubricants. Wear. 2006;260(1):149-58.

198. Nečas D, Vrbka M, Rebenda D, Gallo J, Galandáková A, Wolfová L, et al. In situ observation of lubricant film formation in THR considering real conformity: The effect of model synovial fluid composition. Tribology International. 2018;117:206-16.

199. Jalali-Vahid D, Jagatia M, Jin Z, Dowson D. Prediction of lubricating film thickness in UHMWPE hip joint replacements. J Biomech. 2001;34(2):261-6.

200. Myant C, Cann P. In contact observation of model synovial fluid lubricating mechanisms. Tribology International. 2013;63(0):97-104.

201. Brandt J-M, Mahmoud K, Koval S, MacDonald S, Medley J. Antimicrobial agents and low-molecular weight polypeptides affect polyethylene wear in knee simulator testing. Tribology International. 2013;65:97-104.

202. Purbach B, Hills BA, Wroblewski BM. Surface-active phospholipid in total hip arthroplasty. Clin Orthop Relat Res. 2002;396:115-8.

203. Hills BA. Boundary lubrication in vivo. Proceedings of the Institution of Mechanical Engineers, Part H: Journal of Engineering in Medicine. 2000;214(1):83-94.

204. Liao YS, Benya PD, McKellop HA. Effect of protein lubrication on the wear properties of materials for prosthetic joints. Journal of Biomedical Materials Research Part A. 1999;48(4):465-73.

205. Brandt J-M, Charron K, Zhao L, MacDonald SJ, Medley JB. Calf serum constituent fractions influence polyethylene wear and microbial growth in knee simulator testing. Proceedings of the Institution of Mechanical Engineers, Part H: Journal of Engineering in Medicine. 2012;226(6):427-40.

206. Trunfio-Sfarghiu AM, Berthier Y, Meurisse MH, Rieu JP. Multiscale analysis of the tribological role of the molecular assemblies of synovial fluid. Case of a healthy joint and implants. Tribology International. 2007;40(10–12):1500-15.

207. Stevenson H, Parkes M, Austin L, Jaggard M, Akhbari P, Vaghela U, et al. The development of a small-scale wear test for CoCrMo specimens with human synovial fluid. Biotribology. 2018;14:1-10.

208. Nečas D, Sawae Y, Fujisawa T, Nakashima K, Morita T, Yamaguchi T, et al. The Influence of Proteins and Speed on Friction and Adsorption of Metal/UHMWPE Contact Pair. Biotribology. 2017;11:51-9.

209. Nečas D, Vrbka M, Urban F, Křupka I, Hartl M. The effect of lubricant constituents on lubrication mechanisms in hip joint replacements. Journal of the Mechanical Behavior of Biomedical Materials. 2016;55:295-307.

210. Saikko V, Ahlroos T. Phospholipids as boundary lubricants in wear tests of prosthetic joint materials. Wear. 1997;207(1):86-91.

211. Wimmer M, Mathew M, Laurent M, Nagelli C, Liao Y, Marks L, et al. Tribochemical reactions in metal-on-metal hip joints influence wear and corrosion. Metal-On-Metal Total Hip Replacement Devices: ASTM International; 2013.

212. Pourzal R, Theissmann R, Morlock M, Fischer A. Micro-structural alterations within different areas of articulating surfaces of a metal-on-metal hip resurfacing system. Wear. 2009;267(5-8):689-94.

213. Myant C, Cann P. On the matter of synovial fluid lubrication: Implications for Metal-on-Metal hip tribology. journal of the mechanical behavior of biomedical materials. 2014;34:338-48.

214. Vrbka M, Nečas D, Hartl M, Křupka I, Urban F, Gallo J. Visualization of lubricating films between artificial head and cup with respect to real geometry. Biotribology. 2015;1:61-5.

215. Vrbka M, Návrat T, Křupka I, Hartl M, Šperka P, Gallo J. Study of film formation in bovine serum lubricated contacts under rolling/sliding conditions. Proceedings of the Institution of Mechanical Engineers, Part J: Journal of Engineering Tribology. 2013;227(5):459-75.

216. Vrbka M, Křupka I, Hartl M, Návrat T, Gallo J, Galandáková A. In situ measurements of thin films in bovine serum lubricated contacts using optical interferometry. Proceedings of the Institution of Mechanical Engineers, Part H: Journal of Engineering in Medicine. 2014;228(2):149-58.

217. Nečas D, Vrbka M, Křupka I, Hartl M, Galandáková A. Lubrication within hip replacements–Implication for ceramic-on-hard bearing couples. Journal of the Mechanical Behavior of Biomedical Materials. 2016;61:371-83.

218. Büscher R, Täger G, Dudzinski W, Gleising B, Wimmer M, Fischer A. Subsurface microstructure of metal-on-metal hip joints and its relationship to wear particle generation. Journal of Biomedical Materials Research Part B: Applied Biomaterials: An Official Journal of The Society for Biomaterials, The Japanese Society for Biomaterials, and The Australian Society for Biomaterials and the Korean Society for Biomaterials. 2005;72(1):206-14.

219. McKellop H, Park S-H, Chiesa R, Doorn P, Lu B, Normand P, et al. In Vivo Wear of 3 Types of Metal on Metal Hip Prostheses During 2 Decades of Use. Clin Orthop Relat Res. 1996;329:S128-S40.

220. Fischer A. Well-founded selection of materials for improved wear resistance. Wear. 1996;194(1-2):238-45.

221. Quinn TFJ. NASA interdisciplinary collaboration in tribology. A review of oxidational wear. 1983.

222. Lee R, Eliezer Z. On the critical thickness of protective films at sliding interfaces. Wear. 1984;95(2):165-75.

223. Tipper J, Ingham E, Jin Z, Fisher J. (iv) The science of metal-on-metal articulation. Curr Orthop. 2005;19(4):280-7.

224. Wang A, Essner A, Polineni VK, Stark C, Dumbleton JH. Lubrication and wear of ultra-high molecular weight polyethylene in total joint replacements. Tribology International. 1998;31(1–3):17-33.

225. Besong A, Jin Z, Fisher J. Importance of pin geometry on pin-on-plate wear testing of hard-on-hard bearing materials for artificial hip joints. Proceedings of the Institution of Mechanical Engineers, Part H: Journal of Engineering in Medicine. 2001;215(6):605-10.

226. McKellop H, Clarke I, Markolf K, Amstutz H. Friction and wear properties of polymer, metal, and ceramic prosthetic joint materials evaluated on a multichannel screening device. Journal of Biomedical Materials Research Part A. 1981;15(5):619-53.

227. Sawae Y, Murakami T, Chen J. Effect of synovia constituents on friction and wear of ultra-high molecular weight polyethylene sliding against prosthetic joint materials. Wear. 1998;216(2):213-9.

228. Ramamurti BS, Bragdon CR, O'Connor DO, Lowenstein JD, Jasty M, Estok DM, et al. Loci of movement of selected points on the femoral head during normal gait: three-dimensional computer simulation. The Journal of Arthroplasty. 1996;11(7):845-52.

229. Kang L, Galvin AL, Brown TD, Jin Z, Fisher J. Quantification of the effect of cross-shear on the wear of conventional and highly cross-linked UHMWPE. J Biomech. 2008;41(2):340-6.

230. Hutchison JS, Ward RE, Lacroix J, Hébert PC, Barnes MA, Bohn DJ, et al. Hypothermia therapy after traumatic brain injury in children. New Engl J Med. 2008;358(23):2447-56.

231. Bowsher J, Shelton J. A hip simulator study of the influence of patient activity level on the wear of crosslinked polyethylene under smooth and roughened femoral conditions. Wear. 2001;250(1-12):167-79.

232. Mischler S, Munoz AI. Wear of CoCrMo alloys used in metal-on-metal hip joints: a tribocorrosion appraisal. Wear. 2013;297(1-2):1081-94.

233. Mattei L, Di Puccio F, Piccigallo B, Ciulli E. Lubrication and wear modelling of artificial hip joints: A review. Tribology International. 2011;44(5):532-49.

234. Wang F, Jin Z. Effect of non-spherical bearing geometry on transient elastohydrodynamic lubrication in metal-on-metal hip joint implants. Proceedings of the Institution of Mechanical Engineers, Part J: Journal of Engineering Tribology. 2007;221(3):379-89.

235. international A. Standard Specification for Cobalt-28 Chromium-6 Molybdenum Alloy Castings and Casting Alloy for Surgical Implants (UNS R30075). 2012.

236. Stellite D. Stellite 21 Alloy Technical Data.

237. Underwood RJ, Zografos A, Sayles RS, Hart A, Cann P. Edge loading in metal-on-metal hips: low clearance is a new risk factor. Proceedings of the Institution of Mechanical Engineers, Part H: Journal of Engineering in Medicine. 2012;226(3):217-26.

238. Yan Y, Neville A, Dowson D. Biotribocorrosion—an appraisal of the time dependence of wear and corrosion interactions: I. The role of corrosion. Journal of Physics D: applied physics. 2006;39(15):3200.

239. Treuhaft PS, McCarty DJ. Synovial fluid pH, lactate, oxygen and carbon dioxide partial pressure in various joint diseases. Arthritis & Rheumatology. 1971;14(4):475-84.

240. Falchuk K, Goetzl E, Kulka J. Respiratory gases of synovial fluids: an approach to synovial tissue circulatory-metabolic imbalance in rheumatoid arthritis. The American Journal of Medicine. 1970;49(2):223-31.

241. Richman AI, Su EY, Ho G. Reciprocal relationship of synovial fluid volume and oxygen tension. Arthritis & Rheumatology. 1981;24(5):701-5.

242. Tang S, Kwon O-J, Lu N, Choi H-S. Surface characteristics of AISI 304L stainless steel after an atmospheric pressure plasma treatment. Surf Coat Technol. 2005;195(2):298-306.

243. Bauer W, Weber M, Chanbai S. White Light Interferometry. Encyclopedia of Tribology: Springer; 2013. p. 4115-27.

244. Abdi H. Coefficient of variation. Encyclopedia of Research Design. 2010;1:169-71.

245. Saikko V. Wear and friction properties of prosthetic joint materials evaluated on a reciprocating pin-on-flat apparatus. Wear. 1993;166(2):169-78.

246. Galandáková A, Ulrichová J, Langová K, Hanáková A, Vrbka M, Hartl M, et al. Characteristics of synovial fluid required for optimization of lubrication fluid for biotribological experiments. Journal of Biomedical Materials Research Part B: Applied Biomaterials. 2017;105(6):1422-31.

247. Nečas D, Vrbka M, Křupka I, Hartl M. The Effect of Kinematic Conditions and Synovial Fluid Composition on the Frictional Behaviour of Materials for Artificial Joints. Materials. 2018;11(5):767.

248. Jiang J, Stack M, Neville A. Modelling the tribo-corrosion interaction in aqueous sliding conditions. Tribology International. 2002;35(10):669-79.

249. Jacobs JJ, Gilbert JL, Urban RM. Corrosion of metal orthopaedic implants. JBJS. 1998;80(2):268-82.

250. North NA, MacLeod ID. Corrosion of metals. Conservation of Marine Archaeological Objects: Elsevier; 1988. p. 68-98.

251. Wood RJ. Tribo-corrosion of coatings: a review. Journal of Physics D: Applied Physics. 2007;40(18):5502.

252. Sinnett-Jones P, Wharton J, Wood R. Micro-abrasion–corrosion of a CoCrMo alloy in simulated artificial hip joint environments. Wear. 2005;259(7-12):898-909.

253. Sigma Aldrich, Certificate of Analysis, Cataloge number 12133C, Lot number 13J360.

254. Mathew M, Srinivasa Pai P, Pourzal R, Fischer A, Wimmer M. Significance of tribocorrosion in biomedical applications: overview and current status. Advances in Tribology. 2009;2009.

255. Cook RB, Bolland BJ, Wharton JA, Tilley S, Latham JM, Wood RJ. Pseudotumour formation due to tribocorrosion at the taper interface of large diameter metal on polymer modular total hip replacements. The Journal of Arthroplasty. 2013;28(8):1430-6.

256. Dyrkacz RM, Brandt J-M, Ojo OA, Turgeon TR, Wyss UP. The influence of head size on corrosion and fretting behaviour at the head-neck interface of artificial hip joints. The Journal of Arthroplasty. 2013;28(6):1036-40.

257. Bryant M, Ward M, Farrar R, Freeman R, Brummitt K, Nolan J, et al. Characterisation of the surface topography, tomography and chemistry of fretting corrosion product found on retrieved polished femoral stems. Journal of the mechanical behavior of biomedical materials. 2014;32:321-34.

258. Willert HG, Buchhorn GHH, Göbel D, Köster G, Schaffner S, Schenk R, et al. Wear behavior and histopathology of classic cemented metal on metal hip endoprostheses. Clin Orthop Relat Res. 1996;329:S160-S86.

259. Zeng M, Huang Y, Lu L, Fan L, Mangavel C, Lourdin D. Mechanical properties of thermo-moulded biofilms in relation to proteins/starch interactions. Food Biophysics. 2011;6(1):49-57.

260. McCarron R, Stewart D, Shipway P, Dini D. Sliding wear analysis of cobalt based alloys in nuclear reactor conditions. Wear. 2017;376:1489-501.

261. Cann PM, Spikes HA, Hutchinson J. The Development of a Spacer Layer Imaging Method (SLIM) for Mapping Elastohydrodynamic Contacts. Tribology Transactions. 1996;39(4):915-21.

262. Murakami T, Sawae Y, Nakashima K, Yarimitsu S, Sato T. Micro-and nanoscopic biotribological behaviours in natural synovial joints and artificial joints. Proceedings of the Institution of Mechanical Engineers, Part J: Journal of Engineering Tribology. 2007;221(3):237-45.

263. Malmsten M, Lassen B. Competitive protein adsorption at phospholipid surfaces. Colloids Surf B Biointerfaces. 1995;4(3):173-84.

264. Meechai N, Jamieson AM, Blackwell J. Translational diffusion coefficients of bovine serum albumin in aqueous solution at high ionic strength. J Colloid Interface Sci. 1999;218(1):167-75.

265. Su T, Lu J, Thomas R, Cui Z. Effect of pH on the adsorption of bovine serum albumin at the silica/water interface studied by neutron reflection. The Journal of Physical Chemistry B. 1999;103(18):3727-36.

266. Kurrat R, Prenosil J, Ramsden J. Kinetics of human and bovine serum albumin adsorption at silica–titania surfaces. J Colloid Interface Sci. 1997;185(1):1-8.

267. Serpell LC, Sunde M, Benson MD, Tennent GA, Pepys MB, Fraser PE. The protofilament substructure of amyloid fibrils1. J Mol Biol. 2000;300(5):1033-9.

268. Serpell LC. Alzheimer's amyloid fibrils: structure and assembly. Biochimica et Biophysica Acta (BBA)-Molecular Basis of Disease. 2000;1502(1):16-30.

269. Bolognesi B, Tartaglia GG. Physicochemical principles of protein aggregation. Prog Mol Biol Transl Sci. 117: Elsevier; 2013. p. 53-72.

270. Langton M, Hermansson A-M. Image analysis of particulate whey protein gels. Food Hydrocolloids. 1996;10(2):179-91.

271. Gosal WS, Ross-Murphy SB. Globular protein gelation. Current Opinion in Colloid & Interface Science. 2000;5(3-4):188-94.

272. Zhang Z, Arrighi V, Campbell L, Lonchamp J, Euston SR. Properties of partially denatured whey protein products: Formation and characterisation of structure. Food Hydrocolloids. 2016;52:95-105.

273. Toloei A, Stoilov V, Northwood D, editors. The relationship between surface roughness and corrosion. ASME 2013 International Mechanical Engineering Congress and Exposition; 2013: American Society of Mechanical Engineers.

274. Widmer MR, Heuberger M, Vörös J, Spencer ND. Influence of polymer surface chemistry on frictional properties under protein-lubrication conditions: implications for hip-implant design. Tribology Letters. 2001;10(1-2):111-6.

275. Lu Z, McKellop H. Frictional heating of bearing materials tested in a hip joint wear simulator. Proceedings of the Institution of Mechanical Engineers, Part H: Journal of Engineering in Medicine. 1997;211(1):101-8.

276. Dubois J, Shaw RA. Peer Reviewed: IR Spectroscopy in Clinical and Diagnostic Applications. ACS Publications; 2004.

277. Barth A. Infrared spectroscopy of proteins. Biochimica et Biophysica Acta (BBA)-Bioenergetics. 2007;1767(9):1073-101.

278. Jackson M, Mantsch HH. The use and misuse of FTIR spectroscopy in the determination of protein structure. Crit Rev Biochem Mol Biol. 1995;30(2):95-120.

279. Tamm LK, Tatulian SA. Infrared spectroscopy of proteins and peptides in lipid bilayers. Q Rev Biophys. 1997;30(04):365-429.

280. Kong J, Yu S. Fourier transform infrared spectroscopic analysis of protein secondary structures. Acta Biochimica et Biophysica Sinica. 2007;39(8):549-59.

281. Derenne A, Vandersleyen O, Goormaghtigh E. Lipid quantification method using FTIR spectroscopy applied on cancer cell extracts. Biochimica et Biophysica Acta (BBA)-Molecular and Cell Biology of Lipids. 2014;1841(8):1200-9.

282. Chapman D. Infrared spectroscopy of lipids. J Am Oil Chem Soc. 1965;42(5):353-71.

283. Naumann D. FT-infrared and FT-Raman spectroscopy in biomedical research. Applied Spectroscopy Reviews. 2001;36(2-3):239-98.

284. Ellis DI, Goodacre R. Metabolic fingerprinting in disease diagnosis: biomedical applications of infrared and Raman spectroscopy. Analyst. 2006;131(8):875-85.

285. Cohenford MA, Godwin TA, Cahn F, Bhandare P, Caputo TA, Rigas B. Infrared spectroscopy of normal and abnormal cervical smears: evaluation by principal component analysis. Gynecol Oncol. 1997;66(1):59-65.

286. Fernandez DC, Bhargava R, Hewitt SM, Levin IW. Infrared spectroscopic imaging for histopathologic recognition. Nat Biotechnol. 2005;23(4):469.

287. Kneipp J, Beekes M, Lasch P, Naumann D. Molecular changes of preclinical scrapie can be detected by infrared spectroscopy. J Neurosci. 2002;22(8):2989-97.

288. Eysel H, Jackson M, Nikulin A, Somorjai R, Thomson G, Mantsch H. A novel diagnostic test for arthritis: multivariate analysis of infrared spectra of synovial fluid. Biospectroscopy. 1997;3(2):161-7.

289. Shaw R, Kotowich S, Eysel H, Jackson M, Thomson G, Mantsch H. Arthritis diagnosis based upon the near-infrared spectrum of synovial fluid. Rheumatol Int. 1995;15(4):159-65.

290. Staib A, Dolenko B, Fink D, Früh J, Nikulin A, Otto M, et al. Disease pattern recognition testing for rheumatoid arthritis using infrared spectra of human serum. Clin Chim Acta. 2001;308(1-2):79-89.

291. Ziegler CM, Kircher P, Hassfeld S. Analysis of temporomandibular joint synovial fluid using Fourier transform/infrared spectroscopy. J Oral Maxillofac Surg. 2002;60(11):1302-6.

292. Berthomieu C, Hienerwadel R. Fourier transform infrared (FTIR) spectroscopy. Photosynthesis Res. 2009;101(2):157-70.

293. Elmer P. MultiScope System Microscope User's Referance. 1999.

294. Zandomeneghi G, Krebs MR, McCammon MG, Fändrich M. FTIR reveals structural differences between native β-sheet proteins and amyloid fibrils. Protein Sci. 2004;13(12):3314-21.

295. Byler DM, Susi H. Examination of the secondary structure of proteins by deconvolved FTIR spectra. Biopolymers: Original Research on Biomolecules. 1986;25(3):469-87.

296. Cerf E, Sarroukh R, Tamamizu-Kato S, Breydo L, Derclaye S, Dufrêne YF, et al. Antiparallel β-sheet: a signature structure of the oligomeric amyloid β-peptide. Biochem J. 2009;421(3):415-23.

297. Ami D, Lavatelli F, Rognoni P, Palladini G, Raimondi S, Giorgetti S, et al. In situ characterization of protein aggregates in human tissues affected by light chain amyloidosis: a FTIR microspectroscopy study. Sci Rep. 2016;6:29096.

298. Barlow DE, Dickinson GH, Orihuela B, Kulp III JL, Rittschof D, Wahl KJ. Characterization of the adhesive plaque of the barnacle Balanus amphitrite: amyloid-like nanofibrils are a major component. Langmuir. 2010;26(9):6549-56.

299. Barlow DE, Wahl KJ. Optical Spectroscopy of Marine Bioadhesive Interfaces. Annual Review of Analytical Chemistry. 2012;5:229-51.

300. Zou Y, Li Y, Hao W, Hu X, Ma G. Parallel β-sheet fibril and antiparallel β-sheet oligomer: new insights into amyloid formation of hen egg white lysozyme under heat and acidic condition from FTIR spectroscopy. The Journal of Physical Chemistry B. 2013;117(15):4003-13.

301. Tidy RJ, Lam V, Fimognari N, Mamo JC, Hackett MJ. FTIR studies of the similarities between pathology induced protein aggregation in vivo and chemically induced protein aggregation ex vivo. Vibrational Spectroscopy. 2017;91:68-76.

302. Haris PI. Probing protein–protein interaction in biomembranes using Fourier transform infrared spectroscopy. Biochimica et Biophysica Acta (BBA)-Biomembranes. 2013;1828(10):2265-71.

303. Glassford SE, Byrne B, Kazarian SG. Recent applications of ATR FTIR spectroscopy and imaging to proteins. Biochimica et Biophysica Acta (BBA)-Proteins and Proteomics. 2013;1834(12):2849-58.

304. Buch V. Molecular structure and OH-stretch spectra of liquid water surface. The Journal of Physical Chemistry B. 2005;109(38):17771-4.

305. Movasaghi Z, Rehman S, ur Rehman DI. Fourier transform infrared (FTIR) spectroscopy of biological tissues. Applied Spectroscopy Reviews. 2008;43(2):134-79.

306. Lewis R, Pohle W, McElhaney RN. The interfacial structure of phospholipid bilayers: differential scanning calorimetry and Fourier transform infrared spectroscopic studies of 1, 2-dipalmitoyl-sn-glycero-3-phosphorylcholine and its dialkyl and acyl-alkyl analogs. Biophys J. 1996;70(6):2736-46.

307. Venkataraman N, Vasudevan S. Characterization of alkyl chain conformation in an intercalated cationic lipid bilayer by IR spectroscopy. The Journal of Physical Chemistry B. 2002;106(32):7766-73.

308. Sigma Aldrich, Product Information, Bovine Calf Serum Sourced in USA, CATALOG NO. 12133C.

309. Chen RF. Removal of fatty acids from serum albumin by charcoal treatment. J Biol Chem. 1967;242(2):173-81.

310. Kaiden K, Matsui T, Tanaka S. A study of the amide III band by FT-IR spectrometry of the secondary structure of albumin, myoglobin, and γ-globulin. Applied Spectroscopy. 1987;41(2):180-4.

311. Sharma A, Ghosh KS, Singh BP, Gathania AK. Spectroscopic investigation of interaction between bovine gamma globulin and gold nanoparticles. Methods and Applications in Fluorescence. 2015;3(2):025002.

312. Segrest JP, Jackson RL, Morrisett JD, Gotto AM. A molecular theory of lipid—protein interactions in the plasma lipoproteins. FEBS Lett. 1974;38(3):247-53.

313. Balchin D, Hayer-Hartl M, Hartl FU. In vivo aspects of protein folding and quality control. Science. 2016;353(6294).

314. Maskiewicz VK, Williams PA, Prates SJ, Bowsher JG, Clarke IC. Characterization of protein degradation in serum-based lubricants during simulation wear testing of metal-on-metal hip prostheses. Journal of Biomedical Materials Research Part B: Applied Biomaterials. 2010;94(2):429-40.

315. Fink AL. Protein aggregation: folding aggregates, inclusion bodies and amyloid. Fold Des. 1998;3(1):R9-R23.

316. Ali MH, Imperiali B. Protein oligomerization: how and why. Bioorg Med Chem. 2005;13(17):5013-20.

317. LeVine III H. [18] Quantification of β-sheet amyloid fibril structures with thioflavin T. Methods Enzymol. 309: Elsevier; 1999. p. 274-84.

318. Rambaran RN, Serpell LC. Amyloid fibrils: abnormal protein assembly. Prion. 2008;2(3):112-7.

319. Sunde M, Serpell LC, Bartlam M, Fraser PE, Pepys MB, Blake CC. Common core structure of amyloid fibrils by synchrotron X-ray diffraction1. J Mol Biol. 1997;273(3):729-39.

320. Kirkitadze MD, Bitan G, Teplow DB. Paradigm shifts in Alzheimer's disease and other neurodegenerative disorders: the emerging role of oligomeric assemblies. J Neurosci Res. 2002;69(5):567-77.

321. Levine III H. Thioflavine T interaction with synthetic Alzheimer's disease β-amyloid peptides: Detection of amyloid aggregation in solution. Protein Sci. 1993;2(3):404-10.

322. Nilsson KPR, Åslund A, Berg I, Nyström S, Konradsson P, Herland A, et al. Imaging distinct conformational states of amyloid-β fibrils in Alzheimer's disease using novel luminescent probes. ACS Chem Biol. 2007;2(8):553-60.

323. Sauer M, Hofkens J, Enderlein J. Basic principles of fluorescence spectroscopy. Handbook of Fluorescence Spectroscopy and Imaging: From Single Molecules to Ensembles. 2011:1-30.

324. Albani JR. Fluorescence Spectroscopy Principles. Principles and Applications of Fluorescence Spectroscopy. 2008:88-114.

325. Naiki H, Higuchi K, Hosokawa M, Takeda T. Fluorometric determination of amyloid fibrils in vitro using the fluorescent dye, thioflavine T. Anal Biochem. 1989;177(2):244-9.

326. Camacho Dejay R. Polarization portraits of lightharvesting antennas: from single molecule spectroscopy to imaging: Lund University; 2014.

327. Khurana R, Coleman C, Ionescu-Zanetti C, Carter SA, Krishna V, Grover RK, et al. Mechanism of thioflavin T binding to amyloid fibrils. J Struct Biol. 2005;151(3):229-38.

328. Dzwolak W, Pecul M. Chiral bias of amyloid fibrils revealed by the twisted conformation of Thioflavin T: an induced circular dichroism/DFT study. FEBS Lett. 2005;579(29):6601-3.

329. Biancalana M, Koide S. Molecular mechanism of Thioflavin-T binding to amyloid fibrils. Biochimica et Biophysica Acta (BBA)-Proteins and Proteomics. 2010;1804(7):1405-12.

330. Stsiapura VI, Maskevich AA, Kuzmitsky VA, Uversky VN, Kuznetsova IM, Turoverov KK. Thioflavin T as a molecular rotor: fluorescent properties of thioflavin T in solvents with different viscosity. The Journal of Physical Chemistry B. 2008;112(49):15893-902.

331. Gade Malmos K, Blancas-Mejia LM, Weber B, Buchner J, Ramirez-Alvarado M, Naiki H, et al. ThT 101: A primer on the use of thioflavin T to investigate amyloid formation. Amyloid. 2017;24(1):1-16.

332. Nakashima K, Sawae Y, Murakami T. Study on Wear Reduction Mechanisms of Artificial Cartilage by Synergistic Protein Boundary Film Formation. JSME International Journal Series C Mechanical Systems, Machine Elements and Manufacturing. 2005;48(4):555-61.

333. LeVine H. Thioflavine T interaction with amyloid β-sheet structures. Amyloid. 1995;2(1):1-6.

334. Harvey R, & Ferrier, Denise R. Biochemistry (5th ed., International ed., Lippincott's illustrated reviews). Philadelphia, Pa: London: Wolters Kluwer Health/Lippincott Williams & Wilkins; 2011.

335. Korduba L, Wang A. The effect of cross-shear on the wear of virgin and highly-crosslinked polyethylene. Wear. 2011;271(9-10):1220-3.

336. Firkins P, Tipper J, Ingham E, Stone M, Farrar R, Fisher J. A novel low wearing differential hardness, ceramic-on-metal hip joint prosthesis. J Biomech. 2001;34(10):1291-8.

337. Simkin PA. The human knee: A window on the microvasculature. Tissue Barriers. 2015;3(1-2):e970465.

338. Binette J, Schmid K. The proteins of synovial fluid: A study of the α1/α2 globulin ratio. Arthritis & Rheumatism: Official Journal of the American College of Rheumatology. 1965;8(1):14-28.

339. Hames BD. Gel electrophoresis of proteins: a practical approach: OUP Oxford; 1998.

340. Wishart DS, Tzur D, Knox C, Eisner R, Guo AC, Young N, et al. HMDB: the human metabolome database. Nucleic Acids Res. 2007;35(suppl_1):D521-D6.

341. Clark A, Saunderson D, Suggett A. Infrared and laser-Raman spectroscopic studies of thermally-induced globular protein gels. Int J Pept Protein Res. 1981;17(3):353-64.

342. Byler DM, Purcell JM, editors. FTIR examination of thermal denaturation and gel-formation in whey proteins. 7th Intl Conf on Fourier Transform Spectroscopy; 1989: International Society for Optics and Photonics.

343. Egan MS, Goldenberg DL, Cohen AS, Segal D. The association of amyloid deposits and osteoarthritis. Arthritis & Rheumatism: Official Journal of the American College of Rheumatology. 1982;25(2):204-8.

344. Ladefoged C. Amyloid in osteoarthritic hip joints: deposits in relation to chondromatosis, pyrophosphate, and inflammatory cell infiltrate in the synovial membrane and fibrous capsule. Ann Rheum Dis. 1983;42(6):659.

345. Sørensen KH, Christensen H. Local amyloid formation in the hip joint capsule in osteoarthritis. Acta Orthop Scand. 1973;44(4-5):460-6.

346. Mohr W. Amyloid deposits in the periarticular tissue. Z Rheumatol. 1976;35(11-12):412-7.

347. Goffin Y, Thoua Y, Potvliege P. Microdeposition of amyloid in the joints. Ann Rheum Dis. 1981;40(1):27.

348. Ravid M, Gafni J, Sohar E, Missmahl H-P. Incidence and origin of non-systemic microdeposits of amyloid. J Clin Pathol. 1967;20(1):15-20.

349. Wright JR, Calkins E. Amyloid in the aged heart: frequency and clinical significance. J Am Geriatr Soc. 1975;23(3):97-103.

350. Fowler DM, Koulov AV, Balch WE, Kelly JW. Functional amyloid–from bacteria to humans. Trends Biochem Sci. 2007;32(5):217-24.

351. Schleeger M, Deckert-Gaudig T, Deckert V, Velikov KP, Koenderink G, Bonn M. Amyloids: From molecular structure to mechanical properties. Polymer. 2013;54(10):2473-88.

352. Smith JF, Knowles TP, Dobson CM, MacPhee CE, Welland ME. Characterization of the nanoscale properties of individual amyloid fibrils. Proceedings of the National Academy of Sciences. 2006;103(43):15806-11.

353. Mostaert AS, Giordani C, Crockett R, Karsten U, Schumann R, Jarvis SP. Characterisation of amyloid nanostructures in the natural adhesive of unicellular subaerial algae. The Journal of Adhesion. 2009;85(8):465-83.

354. Mostaert AS, Higgins MJ, Fukuma T, Rindi F, Jarvis SP. Nanoscale mechanical characterisation of amyloid fibrils discovered in a natural adhesive. J Biol Phys. 2006;32(5):393-401.

355. Gebbink MF, Claessen D, Bouma B, Dijkhuizen L, Wösten HA. Amyloids—a functional coat for microorganisms. Nature Reviews Microbiology. 2005;3(4):333.

356. Cobb A, Schmalzreid T. The clinical significance of metal ion release from cobalt-chromium metal-on-metal hip joint arthroplasty. Proceedings of the Institution of Mechanical Engineers, Part H: Journal of Engineering in Medicine. 2006;220(2):385-98.

357. Mishina H, Kojima M. Changes in human serum albumin on arthroplasty frictional surfaces. Wear. 2008;265(5-6):655-63.

358. Smith S, Dowson D, Goldsmith A. The effect of diametral clearance, motion and loading cycles upon lubrication of metal-on-metal total hip replacements. Proceedings of the Institution of Mechanical Engineers, Part C: Journal of Mechanical Engineering Science. 2001;215(1):1-5.

359. Jay GD. Characterization of a bovine synovial fluid lubricating factor. I. Chemical, surface activity and lubricating properties. Connect Tissue Res. 1992;28(1-2):71-88.

360. Sipe JD, Cohen AS. History of the amyloid fibril. J Struct Biol. 2000;130(2-3):88-98.

361. Nilsson MR. Techniques to study amyloid fibril formation in vitro. Methods. 2004;34(1):151-60.

10 Appendices

10.1 Code of Practice 470 Contaminant Level 2

Introduction

Biotribology laboratory 470 is used only by authorised members of the tribology group. There is security card access to the outer laboratory doors and room 470.

An area at the end of the lab 470 will be allocated for the handling human synovial fluid. These fluids are potentially infected with hazard group 2 and 3 pathogens. During test work a warning notice will be posted on the door of room 470 and access restricted to Academic staff only.

Samples used are unscreened and have to be handled as potentially infectious (as with all bodily fluids). It is very unlikely these samples will contain group 3 pathogens (e.g. TB/HIV/HepB) more likely that they would contain skin bacteria or hazard group 2's, if they infectious at all.

Personal protective equipment

Lab coats

It is compulsory to wear lab coats in the laboratory. These should remain fully buttoned at all times. Each person working biological samples will have two separate coloured lab coats for work on this only. These lab coats will be taken in a sealed bag for washing in room 709, City and Guilds building, every two weeks or if fluid is spilled on coat.

Gloves

Disposable nitrile gloves will be used to prevent skin exposure and are stored at the entrance of the lab. They must be changed regularly and as soon as possible after a potential exposure to any hazardous agent (biological, radiological or chemical).

Safety glasses

Safety glasses are worn at all times in 470.

Hand Washing

Hands should be washed with Hibiscrub disinfectant hand wash after removing protective clothing and before leaving the laboratory.

Transportation within/between laboratories

All samples that are transported within the lab (i.e. from freezer to work bench and from work bench to sink) will be carried in screw top containers.

All samples must be double contained when moving outside the lab. When transporting samples between campuses or departments they must be, at least, doubly contained, closed and sealed. This prevents the need to wear gloves or lab coats in non-lab areas. Please see below for response to spillage during transportation.

Decontamination and Disinfection

Contaminated material will be decontaminated via soaking in Pursept for 30 minutes in a sealed container. This will be carried out on a designated area of the work bench top made of stainless steel. This will be also covered in an orange biohazard sheet to absorb any spillages. Surfaces will be routinely cleaned with Pursept followed by 70% ethanol after use.

Waste treatment and disposal

Liquid waste will be treated with pursept to a final concentration of 2% and left for 30 minutes in a sealed container after which they can be disposed of through the sink.

Heavily soiled solids will be disposed of in an orange clinical waste bag and placed in a designated waste container in freezer ME470/01. At the end of each day these will then be transported (following guidelines above) and placed in the yellow bucket in freezer 8, room 709 (City and Guilds building) where they will be disposed via specialist waste contractor.

Lightly soiled solids for example nitrile gloves, Kimwipe blue roll, plastic pipettes etc will be placed in an orange clinical waste bag. When full this bag will be taken to room 709 and placed in the bin for incineration.

Spillages and incidents

Kimwipe blue roll will be used to take up spilled liquid. All tissues are then collected in an orange clinical waste bag. Purspect is then used to disinfect area (10 minutes contact time) followed by a wipe down of 70% ethanol.

Samples will be transported in a secondary containment and hence protected. If the tubes break or open inside this containment, the secondary containment can only be opened within the designated

area of the biotribology laboratory (room 470 City and Guilds building) and dealt with as described above.

If in contact with eyes or mouth wash out with water. If in contact with skin wash with soapy water. Encourage bleeding of a puncture wound and afterwards cover with a sterile dressing. See occupational health.

All incidents must be reported to Mechanical engineering building manager (Guy Fairhurst) and the safety officer (Steve Greenwood). An incident report form must be filled out for all unplanned events.

http://www3.imperial.ac.uk/safety/subjects/reportingaccidents (via SALUS)

Storage of samples

Samples should be fully labelled with all appropriate information and stored in a locked -32°C freezer. The room is only accessible by swipe card and freezer secured with a 4-digit combination lock. The code is only known by people directly working on project.

Samples in freezers will be included into sample database so the sample origin can be tracked, and any potential hazards associated with it. If freezers fail there should be emergency freezer space.

Health surveillance

All workers that are directly involved with the project must be registered with the occupational health unit.

Responsible PI's

Dr Philippa Cann
Room 668,
City and Guilds Building
South Kensington Campus,
Imperial College London,
Exhibition Rd,
London,
SW7 2AZ
p.cann@imperial.ac.uk

Details on training, supervision and competence assessment

All work performed in 470 will have to follow approved work practices, decontamination and emergency protocols listed in the relevant Bio1 form.

All users must have and received a laboratory induction by Dr Judith Thei. A list of authorised individuals will be available upon request to j.thei@imperial.ac.uk. The working area will be clearly cornered off and only those authorised to work with biological samples will be allowed to pass.

All those working with hazard group 2 material will receive training from a competent trainer (nominated by the Principle Investigator). Only those considered competent to work on the individual projects as assessed by the nominated trainers can work unsupervised with pathogens.

A template providing minimum requirements for training at contaminate level 2 is included below. Each individual being trained by an authorised trainer needs to illustrate that they are competent in the various techniques and control measures before they are considered to be competent to work at containment level 2 unsupervised.

Competence requirements to work unsupervised at containment level 2

Health issues – explanation of the following to be given by the trainer, followed by description of the requirements by the trainee back to the trainer:
Issues that would preclude working with hazardous biological material (e.g. undergoing a course of antibiotic treatment, pregnancy, illness, immune deficiencies etc) Signs and symptoms of disease caused by the hazardous biological agents being used and handled Route of exposure associated with hazardous biological agents being used and handled (e.g. inhalation, ingestion, through or on the skin, splashes in the eyes etc)
Laboratory techniques – practical supervision to be given by the trainer followed by demonstration by the individual to ensure individual has appropriate level of competence and understands the control measures associated with the techniques and hazardous material:
All laboratory members are expected to observe the local safety requirements and to respect the cleanliness and maintenance of laboratory and office equipment. A minimum requirement is the maintenance of your personal safety folder to include your shadowing (laboratory training) record, a copy of the risk assessments and MSDS data specific to your research. These records must be initialled and dated as and when you have read them. Your safety folder must be available for inspection whenever required by local or Institutional safety personnel.

Shadowing: This is an essential component of laboratory training. No laboratory member is authorised to perform any procedure unsupervised until such time as that procedure has been demonstrated by a named trainer. All laboratory members will keep a record of procedures they have received training in.
Emergency procedures - describe and then ask the trainee to explain back to the authorized trainer emergency procedures to be followed to minimise exposure to themselves and others in the event of an accident:
What to do in event of an exposure What to do in event of small spillage (< 5mls) inside and outside equipment What to do in event of large spill (>5mls) inside and outside of equipment Decontamination procedures Specific first aid procedures Reporting accidents and near misses
Disposal procedures – describe the disinfectants in use, their preparation, required contact times and routes for disposal of solid waste (autoclaves etc.). Ask trainee to demonstrate preparation of disinfectants and use of waste routes
Validated disinfectants Disposal of solid waste Disposal of liquid waste

10.2 Bio1 Form

Imperial College London

For Safety Dept use only	Activity I.D.: v	If updated, date of first consent:	
	Consent date for this version:	CL with derogation ☐	GM Class

BIO1 FORM

PROJECT REGISTRATION AND RISK ASSESSMENT FOR WORK INVOLVING BIOLOGICAL MATERIAL



PLEASE READ THIS CAREFULLY

This form acts to register projects involving the use of Biological Agents and / or Genetically Modified Micro-Organisms, or of materials (such as cells and tissues) that may be contaminated with these agents. It also allows assessment of the hazards and risks associated with the project as well as in identifying those at risk and the measures necessary for preventing, or controlling these risks. Please ensure that sufficient detail is provided when completing this form and that the relevant written protocols are referenced where required. Note that the written protocols (e.g. Code of Practice (CoP) or Standard Operating Procedures (SOPs)) containing details of the working procedures must accompany these risk assessments at submission for work requiring Containment Level 2 or above. Once completed and approved, all risk assessments plus the protocols must be held together and supplied to all those working within this project, or who may otherwise be at risk from exposure.

Any queries during the preparation of these documents should be directed to your Safety Officer or directly to the BioSafety Team before submission. This form plus protocols should be reviewed in the first instance by your FSM/CSM and then must be submitted to biosafety@imperial.ac.uk

The work described within this Project Registration must not commence until the Principal Investigator has received a completed Biological Project Certificate.

Any changes to the work, or the persons involved, must be notified via the above email address. All changes requested must be incorporated within an amended version of this form as well as within the Code of Practice plus details of what has been changed recorded within the risk assessment change control form (Form C).

Principal Investigator	
Name: Dr Philippa Cann	CID: 924 Other employee no:
Department / Section: Mechanical Engineering	
Faculty: Tribology	

Details of person conducting the risk assessment	
☐ Same as PI Name: Harriet Stevenson	CID: 00647222 Other employee no:
Department / Section: Mechanical Engineering	
Faculty: Tribology	

The activity
Title: Investigation of the lubrication mechanisms of synovial fluid

Change history *(list all previous versions of this risk assessment)*	
Date	Risk Assessment ID and version no.

The following declaration must be completed by the PI responsible for this project

- ☒ All information contained in this form is accurate and comprehensive.
- ☒ All workers involved will be instructed that their work must remain within the boundaries of this Project Registration.
- ☒ It is understood that this Registration does not comprise operating protocols or all risk assessment required for specific tasks. Such written protocols and risk assessments of individual tasks is still required. Where these must be submitted with this form is indicated within the relevant sections.
- ☒ All changes to the work covered by this form will be reassessed and the changes submitted to biosafety@imperial.ac.uk before those changes are made to the work.
- ☒ All workers have been given, or will be given before they become involved, this risk assessment, adequate training and where necessary, their competency assessed and recorded.
- ☒ All workers have, or will be before their involvement begins, enrolled with Occupational Health for health clearance where necessary.
- ☒ It is understood that this risk assessment shall not be transferred to a third party without the PI named in this form either taking responsibility for the new activities, or ensuring that a new proposal is submitted to Safety Department.

GUIDANCE ON THE COLOUR SCHEME FOR THIS FORM:				
Blue fill = mandatory for all work	No fill = for all work above CL2 only	Pink fill = tissues, cells, etc specific	Green fill - non-GM biological agents specific	Orange fill – GMM specific

I INTRODUCTION	This section must be completed in all cases	
	1.1 Background and aim of the project	The chemical composition of synovial fluid will be analysed along with its lubricating properties and resultant wear in an investigation of joint disease. Joint swelling can be a debilitating resulting in pain, stiffness and loss of function. This is distressing to patients, leads to hospital admission, considerable expense and absence from work. Many conditions can cause a painful, swollen joint including infection, osteoarthritis, gout and rheumatological disease. The final stage treatment is joint arthoplasty which can be carried out on a variaty of joints, the hips, knees, shoulder and ankles for example. In most cases these implants require to survive millions of loading cycles. The objective of this research is to understand the role of synovial fluid chemistry in determining the lubrication and wear of artifical implant materials. Excessive wear and the formation of inflammatory wear particles (metal or polymer) is linked to early failure of artificial joints. Most studies have only considered material effects and there is little information on the role of patient SF chemistry. The focus of the current research is to: • Develop small scale rubbing tests run under physiological conditions which allow the study of prototype materials and human SF. • Measure friction/wear for different SF and material combinations, analysis of surface films and wear debris. • 25% w/w bovine calf serum (BCS) used as reference fluid, initial tests with proteins as they are the most abundant species in SF The long term goal is to identify whether some synovial fluid chemistries promote wear and hence the risk of revison. With this in mind we would like to identify optimum material combinations for specific synovial fluid chemistries allowing surgeons to make an informed choice and reduce risk of revision.
	1.2 Description of the experimental procedures	1. Receipt and storage of biofluids -32oC storage 2. Friction and wear tests using HFRR 3. Removal of biofluid from test. Store for futher analysis. 4. Anaysis of deposits on test specimens *List all aspects of the work, including any proposed movement of the biological agents, or derivatives thereof, out of containment eg for imaging, FACS, sequencing, etc.*
	1.3 Where will this work be carried out? *List all areas to be used e.g. the main lab, CBS, shared incubator rooms, shared storage facilities*	Rooms or area(s): South Kensington campus: 4th floor, room 470 Building(s): City and Guilds Building Campus: South Kensington
	A brief background to the project provides the reviewer a better understanding of the aims of the work. For Q1.2, the author is encouraged to cover as much of their activities with a particular agent or material as possible within this form. The intention of this Project Registration is primarily to agree the scope of the proposed works, and not to focus on the risk assessment of individual procedures. Note however that risk assessment of specific procedures remains essential and must be carried out.	

2 NATURE OF WORK AND BASIC HAZARD IDENTIFICATION

If this material is to be used then all relevant parts of this section must be completed

TISSUES, CELLS, BODY FLUIDS OR EXCRETA

2.1	If human or animal tissues, cells, body fluids or excreta will NOT be used then hatch here ☐ and proceed to Q2.9		
2.2	List all the tissues, cells, body fluids or excreta to be used (species, type, where obtained)	Human joint fluid - Clinically sampled. The main bulk of samples are paitients undergoing elective or emergency joint surgury. The remaining samples are taken from patients with swallon joints. *Details on the source of the material must be included*	
2.3	Describe what infectious agents this material has been screened for	Clinical information is taken from patients prior to samples being taken. No samples will be taken if they have any known communicable diseases.,	
2.4	Will any clinical history or veterinary screening (if relevant) be provided?	Yes ☒ No ☐	N/R ☐
	If no, or N/R, explain why:		N/R ☒
	If yes, detail what this will include:	Medical History	N/R ☐
	If yes, will a policy of rejection of samples from diseased donors be adopted? Explain:	Any patients with known communicable disease will be excluded	
	If yes and for human material, how will the information be disseminated in the course of the project?	Samples will be anomised and medical history recorded as appropriate in sample database	N/R ☐
	If yes and for human material, will this information be anonomised?	Yes ☒ No ☐	N/R ☐
2.5	What is the likelihood of infection of any of this material? Please consider the worse case in this answer if multiple tissues, cells, etc are being used.	Medium risk ☐ High risk ☐ If medium or high risk of infection go to next question	None ☐ Low risk ☒ *If none or low risk proceed to Question 2.10*

2.6	If medium or high risk of infection name and classify the biological agents this material could be infected with	Tissue, cell, fluids or excreta	Name of agent	ACDP/defra classification
2.7	Describe the type and severity of the disease that can be caused to humans or animals by each of the agents that could be present			
2.8	Do any of the materials listed require a licence or a permit before work commences?	*For example, IAPPO1, SAPO, defra, or FERA licenses? If yes, please list these and attach them with this form.*		

BIOLOGICAL AGENTS

2.9	If non-Genetically-Modified Biological Agents will NOT be used then hatch here ☒ and proceed to Q2.13			
2.10	List the non-GM biological agents to be used *(Use numbering system to match agents with strains)*	Name of agent(s)	Strain(s)	ACDP/defra classification

2.11	Describe the type and severity of the disease that can be caused to humans, animals or plants by each of the agents, and if relevant, the particular strains in use	
2.12	Do any of the organisms listed require a licence or a permit before work commences?	*For example, IAPPO1, SAPO, defra, or FERA licenses? If yes, please list these and attach them with this form.*

GENETICALLY MODIFIED MICRO-ORGANISMS

2.13 If Genetically-Modified Micro-Organisms (GMMs) will NOT be used then hatch here ☒ and proceed to Question 3.1

2.14	Provide an overview of the different types of GMM that will be used. Please ensure that the scope and boundaries of the work are made clear	
2.15	List all recipient species and strains to be used, their ACDP or defra classification	
2.16	List of vector systems to be used and their functional properties	
2.17	List the names and functional properties of all altered or inserted genes	
2.18	Identify the most hazardous GMM(s) to be constructed giving consideration both to human health and the environment	

3 DECLARATION

This section must be completed in all cases

3.1	Are you confident that any non-GM organism, tissue, cell, blood, body fluid or any component of any GMM covered by this assessment cannot potentially pose a threat to humans or the environment?	Yes ☐ *Hatch here if you believe that this project comprises work requiring only Containment Level 1 proceed to Q5.1 of this form*	No ☒ *Hatch here if you believe that Containment Level 2 (or higher) is required and then answer Q3.2 and proceed to Q4.1 of this form*
3.2	Do any of the materials contain pathogens or toxins covered by the Anti-Terrorism (Crime and Security Act)?	Yes ☐ No ☒ *A list of the agents and toxins is available at the Safety Dept website. If yes, then Section 4 must still be completed even if only Containment Level 1.*	

PLEASE READ THIS CAREFULLY

You must only answer 'YES' to Q3.1 if you believe that you have sufficient information to classify the project as requiring only Containment Level 1, as defined in the Genetically Modified Organisms (Contained Use) Regulations or by COSHH. In order to do this you must be confident that even in the event of a total breach of containment all the biological agents, genetically modified organisms or cultured material would be of no, or of negligible, risk to human health, or to the environment.

For ALL projects requiring Containment Level 2, or higher, or those covered by the Anti-Terrorism (Crime and Security) Act, submissions of this form must be accompanied by a Code of Practice, or at the very least, all the SOPs relevant to the work.

4 FURTHER ASSESSMENT

All relevant parts of this section must be completed if you answered 'No' to Q3.1

TISSUES, CELLS, BODY FLUIDS OR EXCRETA

4.1	If human or animal tissues, cells, body fluids or excreta will NOT be used then hatch here ☐ and proceed to Q4.8		
4.2	Will any culturing of the material described in Q2.2 take place? If yes, describe which cell(s) will be cultured and under what conditions.	Yes ☐ No ☒	
4.3	If culturing, could HIV permissive cells be present? If yes, describe the cells and for how long these cultures will be allowed to grow.	Yes ☐ No ☐	N/R ☒
4.4	If culturing, what is the maximum volume of culture grown?	Per flask: Number of flasks:	N/R ☒
4.5	Will the tissues, cells, body fluids or excreta be manipulated in any way that could result in the concentration of any adventitious biological agent present? If yes, explain.	Yes ☒ No ☐ Samples to be centrifuged to remove cellular material before arrival at south kennsington campus	
4.6	What will the most hazardous procedure involving the use of this material be?	Sample preparation	
4.7	Will any of the fluids, tissues or cells be donated by you or your colleagues?	Yes ☐ No ☒	
	If yes, detail who will provide these		N/R ☒
	If yes, explain the special risks associated		N/R ☒
	If yes, provide justification for not using material from another safer source e.g. National Blood Service		N/R ☒
	If yes, how will confidentiality be assured?		N/R ☒
	If yes, has written consent been obtained from the donor?		N/R ☒
4.8	Has Ethics Committee approval been obtained?	Yes ☒ No ☐	N/R ☐
		If yes, provide Ethics Committee Ref: 15/LO/0388	

BIOLOGICAL AGENTS

4.9 If non-Genetically-Modified Biological Agents will NOT be used then hatch here ☒ and proceed to Q4.14

4.10 Describe ALL the route(s) of infection	Name of agent	Route(s) of infection	Minimum infectious

	(relevant to the laboratory setting) and the minimum infectious dose(s), if known			dose
	4.11 What is the highest concentration and volume of agent(s) to be worked with?	Per experiment: Total stored:		
	4.12 Are there any known drug resistances amongst the strains to be used? If yes, explain what these are and the consequences			
	4.13 What forms of the agent will be used e.g. spores, vegetative forms and are there any issues over the robustness of these particular forms e.g. resistance to disinfectants or increased stability on dry surfaces			
	4.14 What will the most hazardous procedure involving the use of this material be?			
	GENETICALLY MODIFIED MICRO-ORGANISMS			
	4.15 If GMMs will NOT be used then hatch here ☒ and proceed to Q5			
	4.16 Identify the hazards to human health or to the environment of the recipient microorganism(s)			
	4.17 Identify any of the hazards to human health or to the environment associated directly with the vector systems in use			
	4.18 Identify all of the known or potential hazards associated with all the GMMs to be used. It is important that the boundaries of this project are clearly explained here			
	4.19 Describe the likelihood and consequences of the modifications being transferred to related microorganisms			
	4.20 Identify the most hazardous GMM(s) to be constructed giving consideration both to human health and the environment			
	4.21 Describe ALL the potential route(s) of infection (relevant to the laboratory setting) of the GMM(s)	Name of agent	Route(s) of infection	Minimum infectious dose
	4.22 What is the highest concentration and volume of the GMM(s) to be worked with?	Per experiment: Total stored:		

5	All questions in this section must be answered and further details supplied when indicated NOTE that a Code of Practice (CoP) or Standard Operating Procedure (SOP) reference must be provided for CL2 or higher

work, or work covered by the Anti-Terrorism (Crime and Security) Act			
Risk		If yes, how will this be controlled?	Ref for SOP, CoP other written protocol providing details on usage, training, decontamination, etc.
5.1 Might infectious droplets or aerosols be created, either deliberately or by accident?	Yes ☐ No ☐	Will a safety cabinet or any other form of Local Exhaust Ventilation be required? If yes, provide details for type of cabinet and when this will be used. No Does the room have inward airflow? Yes Is the room ventilation performance monitored and can users check this before entry? Yes For CL3 work only, is the room extract HEPA filtered?	Code of Practice lab 470 containment level 2
5.2 Will material be transported within the laboratory?	Yes ☒ No ☐	Cultures will be transported from the freezer and the work bench area and from the work bench to the sink for disposal in its disenfected state. They will always be transported in screw top containers. *For example, cultures being transported between the safety cabinet and the incubator must be double contained so as to prevent spillage if dropped*	Code of Practice lab 470 containment level 2
5.3 Will the material be transported locally on campus but outside of the laboratory?	Yes ☒ No ☐	All biological samples will be packed and labelled as necessited by the safety instructions on the website of the College. The packaging will consist of a sealed plastic box that will enclose sealed sample vials/tubes. *For example, material transported from the primary laboratory to CBS must be double contained so as to prevent spillage if dropped, adequately labelled and no gloves must be worn outside of the laboratory*	Code of Practice lab 470 containment level 2 - Transported to biochemistry (SAF)
5.4 Will this material be shipped elsewhere in the UK or abroad?	Yes ☒ No ☐	All biological samples will be packed and labelled as necessited by the safety instructions on the website of the College. The packaging will consist of a polystyrene box filled with dry ice and smaller leakproof secondary plastic containers that will enclose the samples vials/tubes. The packages will also feature labels for the dry ice and biological contents. *Provide details of material to be shipped and the packing instructions to be followed. For example, MTb cultures shipped as Category A infectious substance in PI620 packaging. Further guidance is available on the Safety Dept website*	Code of Practice lab 470 containment level 2 - Transported from St Marys Hospital
5.5 Will this material be received from elsewhere?	Yes ☒ No ☐	All biological samples will be packed and labelled as necessited by the safety instructions on the website of the College. The packaging will consist of a polystyrene box filled with dry ice and smaller leakproof secondary plastic containers that will enclose the samples vials/tubes. The packages will also feature labels for the dry ice and biological contents. *Provide details of material to be received, how this will be arranged and what steps will be taken to ensure that the material is correctly packaged. Further guidance is available on the Safety Dept website*	Code of Practice lab 470 containment level 2 - Transported from St Marys Hospital
5.6 Will this material be stored?	Yes ☒ No ☐	-32oC freezer Room 470, Freezer ME470/01 City and Guilds Building, South Kensington Campus Long-term storage Charing Cross Site 7L34 *Provide details of how, where and in what this material will be stored.*	Only persons within the group have access to the padlock code

			If stored in Liquid Nitrogen describe the additional precautions in place	
	5.7 Will infectious material be centrifuged?	Yes ☐ No ☒	Will the primary containers be sealed? Will sealed rotors or sealed buckets be used? *Evidence of leak tightness for the centrifuge, rotors or buckets is required if the centrifuge is intended for use with biologically hazardous materials. This evidence should be provided by the manufacturer or supplier in the form of a Test certificate*	
			Where will these rotors be opened? *For example, within a safety cabinet*	
			Describe the procedures in place to deal with leaks or spillages in the centrifuge or rotor	
	5.8 Are biological samples to be cultured in an incubator?	Yes ☐ No ☒	*What type of incubator (e.g. shaking or static shelf) is this? Describe the measures to be used to prevent and contain any spillages.* *For shaking incubators, describe what system is in place to secure vessels to the platform (clamps/sticky tape or pads), what vessels are used and how are they lidded (glass/plastic, screwed top, secondary containment).* *At all times the manufacturers recommendations should be adhered to.*	
	5.9 Are sharps or potential sharps, e.g. glass pasteur pipettes, to be used at any stage during this activity?	Yes ☐ No ☒	*Describe the sharps, justify their use and describe the precautions in place to protect the user and others from injury*	
	5.10 Are animals to be used as part of this project?	Yes ☐ No ☒	What procedures will be undertaken?	
			Where will this aspect of the work be undertaken?	
			Is shedding of biological agent or GMMs by the infected animals possible? *If yes, detail routes of shedding, risk periods for such shedding and the additional precautions required to control exposure. Include a description on how the animals will be held after intection.*	
			Who will perform the inoculations/exposure of the animals? *What training will they have received and where will this be recorded*	
			Provide details on any additional training required for those handling these animals	
			Provide details on any additional precautions necessary	
	5.11 Will the pathogen be cultured on a large scale or will a fermenter be used?	Yes ☐ No ☒	What will the maximum volume be and are any supplementary containment measures required, for example, the use of a safety cabinet or spill tray?	
			What size and type is the fermenter, where is it located and who is in charge of the area?	
	5.12 Is there any stage within	Yes ☐	If yes, how will this be done and what will then happen to the material?	

	the experimental procedures when the infectious material is inactivated in order that it can be processed, imaged, sequenced or otherwise handled?	No ☒	If yes, describe what conditions or restrictions are placed on the material by the receiving laboratory with regards to its potential infectivity?	
	5.13 Are any of the following to be used in conjunction with this project? If yes provide details and the SOP/CoP reference		Liquid Nitrogen ☒ Radioactive materials ☐ Carcinogens ☐ Mutagens ☐ Toxins ☐ Lasers ☐ Fieldwork ☐ FACS analysis or sorting ☐	Used in FTIR Sectrometer. To be handeled by lab technician only. Cryogenic Liquids Policy PC-21, Guidance note 015 (Liquid Nitrogen – storage, use and transportation within College premises)

6 PPE & HYGIENCE

All questions in this section must be answered in all cases

NOTE that a Code of Practice (CoP) or Standard Operating Procedure (SOP) reference must be provided for CL2 or higher work, or work covered by the Anti-Terrorism (Crime and Security) Act

Control measure	Details	Reference for SOP, CoP other written protocol
6.1 When will gloves be worn?	All the time when handling clinical samples. Insulating gloves to be work when dealing with dry ice or liquid nitrogen.	Code of Practice lab 470 containment level 2
6.2 What type are these and where will they be stored?	Purple powder free nitrile gloves for sample handling available in the laboratory next to the hand washing facilities. Temperature protection gloves available next to the FTIR	Code of Practice lab 470 containment level 2
6.3 When will laboratory coats be worn and what type are these?	Standard Laboratory coats to be worn at all times within the laboratory	Code of Practice lab 470 containment level 2
6.4 Where will the lab coats be stored and what are the arrangements for cleaning or disposal?	Lab coats will be stored nect to the door in room 470. Each person working directley with biological samples will have two separate coloured coats soley for biological work. These coats will be washed every two weeks or if a sample is spilled on coat. They will be placed in a sealed orange clinical waste	Code of Practice lab 470 containment level 2

		bag and taken to the washing machine in room 709.	
	6.5 Is any other type of personal protective equipment to be used? If yes, provide details	Protective Eye wear to be worn when handling samples	Code of Practice lab 470 containment level 2
	6.6 Describe the lab hygiene facilities	Full hand washing facilities and bench cleaning materials available in the sample handling laboratory	Code of Practice lab 470 containment level 2

7 WASTE

All questions in this section must be answered in all cases

NOTE that a Code of Practice (CoP) or Standard Operating Procedure (SOP) reference must be provided for CL2 or higher work, or work covered by the Anti-Terrorism (Crime and Security) Act

7.1 How will waste be treated prior to disposal?

(Note that all differently treated wastes must be included e.g. if some liquid is autoclaved, but others not, then describe both)	Treatment prior to disposal *(note, that if for GM Class 1 work, waste will not be pre-treated before disposal then you must explain why this is acceptable)*	SOP/CoP/ protocol
Liquid waste	All human waste or liquid that may be contaminated with human waste to be disposed will be decontaminated with purspet in a sealed container for a minimum of 30 minutes. This can then be poured down the sink.	Code of Practice lab 470 containment level 2
Solid waste	All containated waste and equipment is to be placed in yellow waste bag. Once full this is then taken to room 709, City and Gulids, and disposed of to clinical waste bins for incineration.	Code of Practice lab 470 containment level 2
Other waste (specify):		

7.2 If waste is to be autoclaved confirm the following:

All cycles have been validated for the actual load types used	Yes ☐	No ☒	*N/R*
The successful completion of every load is checked prior to disposal?	Yes ☐	No ☒	

7.3 How will liquid waste be disposed of?

To drain?	Yes ☒	No ☐	Code of Practice lab 470 containment level 2
As solid waste?	Yes ☐	No ☒	
Other (specify)?	Yes ☐	No ☒	

7.4 How will solid waste be packaged and disposed of?

Categorisation	Colour code	Disposal method	SOP/CoP/ protocol
☐ Sharps	Yellow	Yellow sharps bin > autoclave sterilisation if known or potentially infected >clinical waste disposal (incineration)	
☒ Human body parts, organs including blood bags and blood preserves and excreta (unless identified as medium or high risk or known infected in Q2.5 of this assessment in which case they must be pre-treated before disposal)	Yellow	Yellow rigid one way sealed tissue bins > clinical waste disposal (incineration) * Human tissue waste must be placed in separate containers from non-human waste and labelled 'HTA waste'	Code of Practice lab 470 containment level 2
☐ Animal body carcasses or recognisable	Yellow	Yellow rigid one way sealed tissue bins >	

	parts (unless identified as medium or high risk or known infected in Q2.5 of this assessment in which case they must be pre-treated before disposal)		clinical waste disposal (incineration)	
	☐ Potentially or known infected lab wastes (including sharps) of Hazard Group 2, GM Class 2, DEFRA Category 2 or higher, that have not been pre-treated before leaving site	Special case – contact Safety Department	This is not a route of preference and is subject to special requirements	
	☐ Infected or potentially infected lab wastes, other than sharps or recognisable tissues, that have been pre-treated before leaving site	Orange	Disinfection or sterilisation in the laboratory suite > orange clinical waste bags > clinical waste disposal	
	☐ Infected or potentially infected animal or human body parts, organs or excreta that have been pre-treated before leaving site	Yellow	Disinfection or sterilisation in the laboratory suite >yellow one way sealed tissue bins > clinical waste disposal (incineration) * Human tissue waste must be placed in separate containers from non-human waste and labelled 'HTA waste'	
	☐ Packaging material that has been used for the importation of animal products subject to Defra licenses	Yellow	Yellow clinical waste bags > clinical waste disposal (incineration or alternative treatment as described in the licence	
	7.5 Where is the waste stored after treatment or packaging prior to final disposal?		Room 709 City and Guilds Building waste bin	
	7.6 Describe the procedures for the removal of the waste from the building?		waste is taken out weekly to the designated waste disposal point next to SAF (sk) by a member of staff	

8 MAINTENANCE

All questions in this section must be answered for all work at CL2 or higher, or work covered by the Anti-Terrorism (Crime and Security) Act. In all cases the SOP/CoP or protocol reference is required.

8.1 List the maintenance regimes for all the following lab equipment

	Maintenance frequency	Maintenance carried out by	SOP/CoP/ protocol	N/R
Centrifuge(s)				☒
Safety cabinets				☒
Autoclaves				☒
Shaking incubators				☒
Other (specify)				☒

9 TRAINING

All questions in this section must be answered for all work at CL2 or higher, or work covered by the Anti-Terrorism (Crime and Security) Act. In all cases the SOP/CoP or protocol reference describing the training procedures is required.

9.1 Confirm that training to all workers is providing in at least the following aspects of this work

	Training frequency	Training carried out by	Competency assessed by	SOP/CoP/ protocol	N/R
Hazards associated with this work	At start		Dr Philippa Cann	Code of Practice lab 470 containment	☐

					level 2	
	Safe working practices as described in this risk assessment	At start		Dr Philippa Cann	Code of Practice lab 470 containment level 2	☐
	Spillage response within the safety cabinet	At start		Dr Philippa Cann	Code of Practice lab 470 containment level 2	☐
	Spillage response within the centrifuge					☒
	Spillage response elsewhere	At start		Dr Philippa Cann	Code of Practice lab 470 containment level 2	☐
	Post-exposure protocols	At start		Dr Philippa Cann	Code of Practice lab 470 containment level 2	☐

10 EMERGENCY PROCEDURES

All questions in this section must be answered for all work at CL2 or higher, or work covered by the Anti-Terrorism (Crime and Security) Act. In all cases the SOP/CoP or protocol reference is required.

10.1 Describe the procedures in place for dealing with spillage of infectious or potentially infectious material

	Procedure	SOP/CoP/ protocol	N/R
Within the safety cabinet			☒
Within the centrifuge			☒
Within the laboratory but outside of any primary control measure e.g. safety cabinet	Use tissue (blue roll, Kim wipes) to take up spilled liquid. Use 1% Pursept followed by 70% ethanol and tissues to disinfect area,. All tissues are then collected in an orange clinical waste bag.	Code of Practice lab 470 containment level 2	☐
Outside of the laboratory	Potential CL2 samples will only be transported in secondary containers. If primary container breaks, sample will be transported back to CL2 lab and opened carefully and decontaminated with pursept followed by 70% ethanol.	Code of Practice lab 470 containment level 2	☐

10.2 Describe the procedures in place for an accidental exposure

Immediate action	Wash out with water (if eye or mouth) or soapy water (if wound or on skin). Encourage bleeding of puncture wound. Cover with sterile dressing afterwards. See Occupational Health 020 7594 9401 (work should be restricted to normal working hours)	Code of Practice lab 470 containment level 2	☐
When and to whom to report the incident	Report to Stephen Greenwood (Safety Officers), Head of Section, Occupational Health and on SALUS	Code of Practice lab 470 containment level 2	☐

11 ACCESS

All questions in this section must be answered for all work at CL2 or higher, or work covered by the Anti-Terrorism (Crime and Security) Act. In all cases the SOP/CoP or protocol reference is required.

		SOP/CoP/ protocol

	11.1 Is the lab(s) adequately separated from other areas (e.g. offices)	*Yes* ☒ *No* ☐ *If no, explain:*	
	11.2 Is/are the lab(s) or other work areas shared with other users not involved in this project	Yes ☒ No ☐ If yes, explain who and what procedures are in place to control any risk to them: Biotribology department - separate working areas but all users are aware of the work being carried out. Labels will be used to warn colleagues of the nature of the prep work.	
	11.3 Describe the measures in place to ensure that the infectious material is secured	No known infectious materials used. Closed containers, double contained samples when not in use. Labs have swipe card access and freezers are lockable with access only to those working on this project.	
	11.4 Are the laboratories in use for this work labelled with biohazard signage?	*Yes* ☒ *No* ☐ If no, explain:	N/R
	11.5 What access colour code do the rooms used have?	Red ☐ Amber ☐ Yellow ☒	

12 OCCUPATIONAL HEALTH

This section will be completed by the Occupational Physician for deliberate work with biological agents or GMMs in Hazard Group 2 or higher and for work with unscreened human tissues taken from a population with unusually high prevalence of transmissible infection.

This section will be completed by a Safety Department Biological Safety Officer, if for other work at Containment Level 2.

Note that where pre-activity requirements are identified, it is the responsibility of the Principal Investigator to ensure that these are carried out for all individuals working on this project, before they actually start work

THE PRINCIPAL INVESTIGATOR MUST ENSURE THAT THE INFORMATION DESCRIBED IN THIS SECTION IS UNDERSTOOD BY ALL THOSE THAT WORK ON THIS PROJECT

12.1 Medical risk assessment	
12.2 Pre-activity requirements	
select one	*Details:*
select one	*Details:*
select one	*Details:*
12.3 Periodic health surveillance requirements	
12.4 Post exposure action	
12.5 Antibiotic treatment or chemoprophylaxis	
12.6 Additional notes or comments	

13 LONE WORKING

This section must be completed in all cases

13.1 Does any aspect of this activity present an overt risk to the lone worker due to any of the following factors:

		Details including additional precautions to be implemented	SOP/CoP/ protocol
Can a lone worker safely enter and exit the facility? Including donning and removing PPE?	Yes ☒ No ☐	If no, describe why and any additional precautions necessary for lone working:	

	Can all equipment be used safely by the lone worker?	Yes ☒ No ☐	If no, describe why and any additional precautions necessary for lone working:	
	Does any substance used present a risk of rapidly incapacitating a lone worker?	Yes ☐ No ☒	If yes, describe why and any additional precautions necessary for lone working: The only risk of rapid incapacitation is posed by liquid nitrogen. However, even though this activity will involve work with FTIR filled with liquid nitrogen, actual handling of liquid nitrogen will not be performed by the lone worker.	
	Will a lone worker be able to safely deal with a spillage or other emergency e.g. malfunctioning equipment	Yes ☒ No ☐	If no, describe why and any additional precautions necessary for lone working:	
	Is it possible to observe occupants of the room at all times from the outside?	Yes ☒ No ☐	If yes, describe how: Window in door though which people can easily be observed If no, describe why this acceptable:	
	Will lone work take place in a secure or restricted access facility?	Yes ☐ No ☒	If yes, describe why and any additional precautions necessary for lone working:	
	13.2 Is lone working permitted for this activity?	Yes ☒ No ☐		
	13.3 Is specific consent required for lone working?	Yes (each lone working activity) ☐ Yes (but not for each specific instance) ☐ Specific consent is not required for lone working ☒		
	13.4 If lone working will take place, are there any restrictions as to when lone working can take place?	Yes ☒ No ☐ N/A ☐	If yes or no, describe the restrictions and why these are in place: During 'normal' working hours	

14 CONTAINMENT LEVEL

This section must be completed in all cases

14.1 Confirm what Containment Level can be assigned to each aspect or component of this project. If different aspects of this work merit different Containment Levels, then all must be listed. Include where, for example, the biological agents, GMOs or tissues, and material derived therefrom, are to be sent for sequencing, FACS, or other analysis, imaging or processing.

Project aspect	Where work will be carried out	Containment Level (as required under COSHH or GMO (Contained Use) Regs	With extra controls (list these, if relevant. If required seek advice from your DSO or the College BSO)	With derogation from certain controls (list these, if relevant. If required seek advice from your DSO or the College BSO)
Sample Collection	Imperial College NHS Trust	CL1	N/A	N/A
Sample Preparation and testing	4th floor, City and Guilds Room 470	CL2	N/A	N/A
Sample Disposal	7th floor, City and Guilds, room 709	CL2	N/A	N/A

15 GM

This section must be completed for work with Genetically Modified Micro-organisms only

15.1 Confirm the class of all GMMs in use

Project aspect	GM Class



10.3 Peak Positions from Deconvoluted Micro IRRAS Spectra

Table 10.1 - Summary of IR peaks for untested 25BCS and 25salBCS for 1750-1450 cm^{-1}. (Bold type represents most intense peak)

Peaks	Wavenumber (cm^{-1})		Assignment
	25BCS	25salBCS	
Amide I	1659	1659	α-helix/random coil
	1651	1651	α-helix/random coil
	1641	1641	N-β
	1632	1632	N-β
Amide II	1559	1558	
	1548	1548	
	1535	1535	
	1516	1514	
	1509	1509	

Table 10.2 - Summary of IR peaks from deconvolution and secondary structure assignment for untested 25salBCS, mBCS, mH, mOA and mPP for 1750 - 1450 cm^{-1}. (Bold type represents most intense peak)

Peaks	Wavenumber (cm^{-1})					Assignment
	25salBCS	mBCS	mH	mOA	mPP	
Amide I	1659	1659	1655	1659	1659	α-helix/random coil
	1651	1651	1647	1650	1651	α-helix/random coil
	1641	1641	1640	1643	1642	N-β
	1632	1632	1631	1632	1632	N-β
Amide II	1560					
	1548	1545	1548	1545	1548	
	1535	1537	1540	1537	1540	
	1514	1517	1516	1516	1516	
	1509	1501	1507	1501	1507	
A/G	0.8	0.8	2	1.5	3	

Table 10.3 - Summary of IR peaks from deconvolution and secondary structure assignment for untested 25salBCS + DPPC, mBCS + DPPC, mH + DPPC, mOA + DPPC and mPP + DPPC for 1750 - 1450 cm^{-1}. (Bold type represents most intense peak)

Peaks	Wavenumber (cm^{-1})					Assignment
	25salBCS + DPPC	mBCS + DPPC	mH + DPPC	mOA + DPPC	mPP + DPPC	
Ester	1735	1735	1735	1737	1737	N/A
Amide I	1659	1658	1658	1658	1659	α-helix/random coil
	1650	1649	1649	1649	1651	α-helix/random coil
	1641	1641	1640	1642	1642	N-β
	1632	1631	1632	1632	1632	N-β
Amide II	1558	1557	1556	1556	1557	
	1548	1548	1545	1546	1547	
	1538	1536	1536	1537	1537	
				1516	1517	
				1501	1500	
A/G	0.8	0.8	2	1.5	3	

Table 10.4 - Summary of IR peaks from deconvolution and secondary structure assignment for tested black and rainbow deposits for model fluids in the region 1800 - 1450 cm^{-1}. (Bold type represents most intense peak, ^{w} denotes a weak peak)

Peaks	Wavenumber (cm^{-1})						Assignment
	25BCS	25salBCS	mBCS	mH	mOA	mPP	
Amide I							
Black	1659	1658	1659	1659	1659	1659	α-helix/random coil
	1650	1650	1651	1650	1650	1650 (s)	α-helix/random coil
	1643	1642	1641	1642	1642	1643	N-β
	1632	1632	1632	1632	1632	1633	N-β
	1612 ^{w}	1612 ^{w}	1613	1612	1613	1613	F-β
Rainbow	1659	1658	1660	1658	1659	1659 (s)	α-helix/random coil
	1651	1650	1652	1650	1651	1651	α-helix/random coil
	1643	1643	1643	1641	1642	1641	N-β
	1632	1633	1632	1632	1632	1632	N-β
	1613 ^{w}	1612 ^{w}	1612	1611	1612 ^{w}	1612	F-β
Amide II							
Black	1547	1546	1544	1543	1544	1542	
	1537	1537	1536	1536	1535	1532	
	1517		1518	1517	1517	1516	
		1510	1510	1510	1510^{w}	1508	
			1501	1500	1500	1500	
Rainbow	1542	1543	1541	1542	1545	1540	
	1536	1537	1533	1534	1537		
			1515		1517	1517	
		1511		1510	1510^{w}	1509	
	1501		1500	1500	1502	1500	
A/G	0.8	0.8	0.8	2	1.5	3	

Table 10.5 - Summary of IR peaks from deconvolution for tested mOA black and rainbow deposits for 3000 - 2800 cm^{-1}. (Bold type represents the most intense CH_2/CH_3 peak, no bold indicates similar peak heights)

Peaks	Wavenumber (cm^{-1})				
	25 BCS	mBCS	mH	mOA	mPP
CH_3 (ν_{asym})					
Black	2959	2959	2959	2960	2960
Rainbow	2959	2960	2959	2960	2960
CH_2 (ν_{asym})					
Black	2930	2928	2929	2928	2929
Rainbow	2932 2916	2929	2933	2931	2929
CH_3 (ν_{sym})					
Black	2872	2870	2871	2871	2872
Rainbow	2869	2870	2870	2871	2872
CH_2 (ν_{sym})					
Black	2851	2850	2850	2850	2850
Rainbow	2850				

Table 10.6 - Summary of IR peaks from deconvolution and secondary structure assignment for model fluids for both black and rainbow deposits in the range 1800 - 1450 cm^{-1}. (Bold type represents most intense peak, ^{w} denotes a weak peak)

Peaks	Wavenumber (cm^{-1})					Assignment
	25salBCS + DPPC	mBCS + DPPC	mH + DPPC	mOA + DPPC	mPP + DPPC	
Ester						
Black	1735	1735	1734	1735	1735	C=O
Rainbow	-	-	-	-	-	
Amide I						
Black	1659	1659	1658	1657	1658	α-helix/random coil
	1651	1651	1648	1648	1651	α-helix/random coil
	1641	1641	1640	1640	1642	N-β
	1632	1631	1630	1631	1632	N-β
	1612^{w}	1611^{w}	1612	1612^{w}	1611	F-β
Rainbow	1659	1659	1658	1656	1659	α-helix/random coil
	1651	1650	1651	1649	1651	α-helix/random coil
	1641	1640	1641	1640	1641	N-β
	1631	1631	1631	1631	1632	N-β
	1612^{w}	161 ^{w}	1613	1611^{w}	1612	F-β
Amide II						
Black	1558	1558	1559	1558	1558	
	1543	1541	1541	1541	1541	
	1519	1515	1516	1517	1515	
	1510	1509^{w}	1508	1510	1510	
	1503	1500		1500	1502	
Rainbow	1558			1558	1558	
	1542	1558	1500	1541	1540	
	1510	1542	1558	1510	1508	
	1503	1510	1541	1500	1500	
		1501	1508			
			1500			

Table 10.7 - Summary of IR peaks from deconvolution for tested model fluids with DPPC for both black and rainbow deposits in the range 3000 - 2800 cm^{-1}. (Bold type represents the most intense CH_2/CH_3 peak, no bold indicates similar peak heights)

Peaks	Wavenumber (cm^{-1})					
	DPPC	25salBCS + DPPC	mBCS + DPPC	mH + DPPC	mOA + DPPC	mPP + DPPC
CH_3 (ν_{asym})						
Black	2958	2957	2959	2960	2959	2958
Rainbow		2959	2958	2959	2959	2960
CH_2 (ν_{asym})						
Black		2928	2927	2928	2929	2930
	2918	2917	2916	2917	2917	2916
Rainbow		2828	2927	2931	2929	2930
		2917	2917	2916	2917	2917
CH_3 (ν_{sym})						
Black	2871	2871	2870	2870	2870	2872
Rainbow		2871	2869	2871	2870	2872
CH_2 (ν_{sym})						
Black	2850	2850	2849	2851	2852	2850
Rainbow		2849	2849	2848	2849	2850

Table 10.8 - Summary of IR peaks from deconvolution and secondary structure assignment for all untested HSF fluids and 25BCS in the range 1800 - 1450 cm^{-1}. (Bold type represents most intense peak, ^{w} denotes a weak peak)

Peaks	Wavenumber (cm^{-1})									Assignment
	25BCS	HSF 041	HSF 077	HSF 110	HSF 113	HSF 135	HSF 145	HSF 156	HSF 164	
Amide I		1667	1666	1666		1666	1666	1666	1667^{w}	Turns and bends
	1659	1659	1659	1658	1658	1659	1661	1658	1658	α-helix/random coil
	1651	1650	1650	1649	1650	1650	1649	1649	1650	α-helix/random coil
	1641	1642	1642	1641	1642	1642	1642	1642	1643	N-β
	1632	1633	1632	1631	1632	1632	1632^{w}	1632^{w}	1632	N-β
Amide II	1559	1563	1564	1565	1564	1564	1562	1564	1564	
			1555	1555		1555	1555	1554	1554	
	1548	1548	1546	1545	1545	1545	1548	1548	1548	
	1535	1537	1536	1536	1536	1536	1537	1537	1536	
	1516				1517					
	1509									

Table 10.9 - Summary of IR peaks from deconvolution and secondary structure assignment for all tested HSF samples for both black and rainbow deposits in the range 1800 - 1450 cm^{-1}. (Bold type represents most intense peak, ^{w} denotes a weak peak)

Peaks	Wavenumber (cm^{-1})									Assignment
	25BS	041	077	110	113	135	145	156	164	
Ester										
Black		1735		1735				1735	1737	C=O
Rainbow		1735								
Amide I										
Black	1659	1659	1660	1657	1660	1658	1659	1659	1658	α-helix/random coil
	1650	1651	1651	1649	1651	1650	1651^{w}	1651	1649	α-helix/random coil
	1643	1643	1643	1641	1642	1639	1642	1642	1642	N-β
	1632	1631	1632	1631^{w}	1632	1630	1630	1632	1633	N-β
	1612^{w}	1612^{w}			1612			1612^{w}	1612^{w}	F-β
Rainbow										
	1659	1659	1660			1660	1660	1660	1559	α-helix/random coil
	1651	1651	1651			1651	1653	1651	1652	α-helix/random coil
	1643	1640	1642			1640	1642	1644	1644	N-β
	1632	1631	1632			1631	1632	1632	1632	N-β
	1613^{w}	1612	1612^{w}			1612				F-β
Amide II										
Black		1564		1563					1564	
		1556	1556	1554	1558	1558	1558	1556	1549	
	1547	1542	1542	1544	1542	1544	1543	1542	1541	
		1535		1536			1531	1534		
				1528	1522				1516	
	1537*						1508*			
	1517									
Rainbow		1560				1560	1560	1557	1564	
	1542	1546				1542	1541	1542	1542	
	1536	1538								
		1530								
						1508*	1508*		1515	

Table 10.10 - Summary of IR peaks from deconvolution for all tested HSF samples for both black and rainbow deposits in the range 3000 - 2800 cm^{-1}. (Bold type represents the most intense CH_2/CH_3 peak, no bold indicates similar peak heights)

Peaks	Wavenumber (cm^{-1})								
	25BS	041	077	110	113	135	145	156	164
CH_3 (ν_{asym})									
Black	2959	2960	2961	2960	2960	2959	2960	2959	2958
Rainbow	2959	2959	2961			2960	2960	2959	2958
CH_2 (ν_{asym})									
Black	2930	2916	2917	2916	2917	2920	2916	2918	2919
Rainbow	2932 2916	2931	2930			2930	2929	2932	2930
CH_3 (ν_{sym})									
Black	2872	2871	2870	2870	2870	2871	2870	2871	2870
Rainbow	2869	2871	2871	2870	2870	2871	2870	2871	2870
CH_3 (ν_{sym})									
Black	2851	2850	2850	2851	2850	2851	2850	2851	2851
Rainbow	2850	2852	2850	2851	2851	2850	2851	2852	2850